Title

Dielectric Elastomers for Actuation and Energy Harvesting

Author

Brochu, Paul

Publication Date

2012

University of California
Los Angeles

Dielectric Elastomers for Actuation and Energy Harvesting

A dissertation submitted in partial satisfaction
of the requirements for the degree
Doctor of Philosophy in Materials Science and Engineering

by

Paul A Brochu

2012

Abstract of the Dissertation

Dielectric Elastomers for Actuation and Energy Harvesting

by

Paul A Brochu

Doctor of Philosophy in Materials Science and Engineering
University of California, Los Angeles, 2012
Professor Qibing Pei, Chair

Dielectric elastomers are an emerging transducer technology that fit an interesting niche. They are soft and compliant by nature, and can be stretched, either via mechanical or electrically-induced means, to very large strains. They are capable of large strains, high energy densities, and low costs, while possessing the additional advantages of being light weight and conformable. Dielectric elastomers are well suited for both actuator and generator applications, with the actuators being heralded as artificial muscles. There remains, however, several issues that prevent the widespread adoption of dielectric elastomer technology. Each applications has its set of technical issues; for actuator purposes, the primary issues are that the driving voltage required for high performance is in excess of 2000 V for most dielectric elastomer actuators, and that the lifetime when operated at high performance levels is rather short. The requirement to prestrain the elastomers to achieve high performance actuation in most cases can also add significant bulk and mass to the actuator as well as reduce its shelf-life. Thus, materials capable of high-strain performance without the requirement for prestrain are sought after. The ability to operate over a wide range of temperatures and environmental conditions, as well as operate over a wide range of frequencies, is also very important for most actuator applications.

The first part of this dissertation looks to tackle the aforementioned issues. Silicone materials are chosen as the base dielectric elastomer material as they are generally capable of operating over wide ranges of temperature and frequency and are generally unaffected by moisture and have good environmental stability. The work focuses on free-standing linear soft silicone actuators as this configuration is the most relevant for real applications. A particular soft silicone has been isolated a good candidate and was extensively tested in a free-standing linear actuator configuration to determine the effects of pre-stretch and the application of mechanical loads on its actuation performance. It is shown that when the mechanical loads are properly applied, large linear actuation strains of 120% and work density of 0.5 J/cm^3 can be obtained. Furthermore, we demonstrate that when coupled with single wall carbon nanotube (SWNT) compliant electrodes, fault-tolerance is introduced via self-clearing leading to significantly improved operational reliability. Driven at moderate electric fields, the actuators display relatively high linear actuation strain (25%) without degradation of the electromechanical performance even after 85,000 cycles.

An issue related to the use of soft silicone actuators is that the work density is not very high when compared with many of the high-performance dielectric elastomer materials available. It is shown that the force output and work density of soft silicone actuators can be significantly enhanced by the addition of high permittivity titanium oxide nanoparticles. The nanocomposites are capable of maintaining the actuation strain performance of the pure silicone at relatively low electric fields while increasing the force output and work density due to the additive effects of mechanical reinforcement and permittivity enhancement.

The high performance of the aforementioned soft silicone actuators requires the application of rather large levels of prestrain. In order to eliminate this requirement a novel all-silicone prestrain-locked interpenetrating polymer network (S-IPN) elastomer was developed. The elastomer is fabricated using a combination of two silicones: a soft room temperature vulcanizing silicone that serves as the host elastomer matrix, and a more rigid high temperature vulcanizing silicone that acts to preserve the prestrain in the host network. The free-standing prestrain-locked silicones show a more than twofold performance improvement over standard free-standing silicone films, with a linear strain of 25% and an area strain of 45% when tested in a diaphragm configuration.

The S-IPN procedure was leveraged to improve electrode adhesion and stability as well as improve the interlayer adhesion in multilayer actuators. It is demonstrated that strongly bonded SWNT electrodes are capable of fault tolerance through self-clearing, even in multilayer actuators. The fault-tolerance and improved interlayer adhesion was used to fabricate prestrained free-standing silicone actuators capable of stable long life actuation (>30,000 cycles at >20% strain and >500 cycles at ∼40% strain) while driving a load. Issues related to gradual electrode degradation are also addressed through the use of quasi-buckled electrodes. For generator purposes, the primary concerns are ensuring environmental stability, increasing energy density, lowering losses, and determining effective methods to couple the dielectric elastomer to natural energy sources. The factors that affect the energy density and efficiency are explored and it is found that energy density can be increased by applying larger mechanical strains and using stiffer materials. Increasing the permittivity of the material and bias voltage can also improve the energy density but reach a peak and decrease the energy density thereafter. The efficiency is shown to depend primarily on the shape of the stress-strain curve of the material, the applied strain, and a lumped parameter containing the stiffness, permittivity and nominal bias electric field. For a particular applied strain, the efficiency shows a peak at a particular value of the lumped parameter. Increasing stiffness shifts the location of the peak to higher values, and thus higher required electric fields, while increasing permittivity shifts it to lower values, and thus to lower electric fields.

Using the results of this analysis, two material systems are explored: VHB acrylic elastomers at various prestrains and with various amounts of a stiffening additive, and a high energy density silicone-TiO_2 nanocomposite elastomer with various amounts of additive. It is shown that increasing prestrain in the VHB acrylic system increases the energy density, while the stiffening additive has the effect of making the acrylic stiffer but results in increased losses, result in poorer performance. The silicone TiO_2 composite demonstrates an increase in permittivity and stiffness with increasing additive while maintaining very high dielectric breakdown strength values. These increases are partially offset by small increases in mechanical and electrical losses. Calculations based on a simple model show that the generator energy density can be improved by a factor of 3 for a 20wt.% TiO_2 loading at a strain of 50% in area. The calculated generator energy density values exceed the maximum values measured experimentally for highly prestrained VHB4910 acrylic elastomers.

The focus on high energy density materials ignores the fact that not all applications require such a material, and that some applications may, in fact, benefit from the use of a softer material that is less intrusive. However, for lower energy density materials, parasitic losses due to electrode resistance and viscoelasticity play a larger role as relative energy gains are lower. With this is mind, a soft silicone single walled carbon nanotube composite is developed. The composite is very soft, has low viscoelastic losses, and is capable of being stretched up to >150% strain with only a marginal increase in resistance. The composite is also capable of being repeatedly stretched at up to 120% strain for over 1000 cycles without any appreciable change in resistance and is capable of being stretched at strain rate up to 100%/s or higher without affecting the performance of the electrode.

Two applications for dielectric elastomer actuators are also explored. A pressure-based ocean wave energy harvesting concept was introduced that does not use any moving parts. A footfall energy harvester concept is also developed capable of being deployed inside the sole of a shoe or as a flexible floor tile.

The dissertation of Paul A Brochu is approved.

Bruce Dunn
Jenn-Ming Yang
Christopher Lynch
Qibing Pei, Committee Chair

University of California, Los Angeles
2012

Dedicated to my family who supported me through these years and to my lovely girlfriend Jennifer Chou. Without your help and support this would not have been possible.

Table of Contents

List of Figures

List of Tables

ACKNOWLEDGMENTS

I would foremost like to thank my advisor, Professor Qibing Pei, for his guidance and help. Professor Pei's leadership and ingenuity have not only motivated and encouraged me throughout my work at UCLA, but also inspired me to become a better researcher, a better leader, and a better person.

I would like to thank my committee members, Professor Bruce Dunn, Professor Christopher Lynch, Professor Jenn-Ming Yang, and Professor H. Thomas Hahn for spending time serving on my committee and for their valuable suggestions.

I would like to thank my collaborators from different research groups, Kin Wai Leung from Professor Xiaolin Zhong's research group at UCLA as well as Siarhei Vishniakou and Brian Lewis from Prof. Deli Wang's research group at UCSD.

I am grateful to my labmates in the Soft Materials Research Laboratory, both past and present, for sharing their knowledge and expertise throughout my time at UCLA. A special thanks goes to former students Dr. Soon-Mok Ha, Dr. Wei Yuan, and Dr. Zhibin Yu for laying the groundwork for the many advances our lab has produced and for helping to guide me and many other graduate students; without their pioneering work I would not have been able to do any of this. I would also like to send a special thanks to Dr. Hristiyan Stoyanov who helped me put form to much of my work at UCLA and helped me immensely in my final year at UCLA; without his help my last year at UCLA would have been much more difficult. Many thanks to Xiaofan Niu whose tireless efforts in the lab helped make everyone's work easier, and to Zhi Ren for helping to prepare and test nanocomposite films for energy harvesting purposes. I also greatly appreciate the efforts of undergraduates Ryan Chang, Brandon Salazar, and Christopher Lai, and high school student Julian Capen for helping me with my research efforts and helping me develop some leadership and management skills. I would furthermore like to thank Vahagn Hokhikyan, Huafeng Li, Dr. Sung Ryul Yun, Chaokun Gong, Han Zhang, David McCoul, Wei (Maggie) Hu, Weili Hu, Tuling Lam, Qi

Chen, Dr. Dongjuan Xi, and Dr. Jiajie Liang who all helped me reach this goal.

A special thanks goes to my family and lovely girlfriend Jennifer Chou. Their love and support helped to carry me though the tough times when I was strugling with poor results, and to keep me confident and motivated. I would especially like to thank my parents, Lynda and Serge Brochu, for their invaluable support throughout my entire life.

I would also like to extend my appreciation to my friends Kannan Goundan for his help with Python, Kitty Cha for her help taking SEM images, Stephanie Reed for her help with tensile testing and 3D printing, Dr. Ankit Kumar for helping me get through the prelims, and Kenneth Wei for his help with modeling.

A big thanks also goes to all of my friends who helped keep my time at UCLA fun and lighthearted. You all helped me to keep things in perspective and maintain a reasonable stress level.

I would like to thank GM, the UC Discovery program, and the NSF for financial support through grants and to Qualcomm for financial support through their Qualcomm Innovation Fellowship.

Vita

2005	B.ASc. Nanoengineering, University of Toronto.
2008	M.S. Materials Science and Engineering, UCLA.
2008	Imagineering Intern, Disney, Glendale, California, USA.
2007-2010	Teaching Fellow, Department of Materials Science and Engineering, UCLA.
2011	Qualcomm Innovation Fellowship.
2007-2012	Research Assistant, Department of Materials Science and Engineering, UCLA.

Publications and Presentations

P. Brochu, H. Stoyanov, R. Chang, and Q. Pei, ”Highly stretchable silicone-carbon nanotube composite electrodes for capacitive energy harvesting and strain sensing,” In preparation.

P. Brochu, H. Stoyanov, X. Niu, and Q .Pei, ”All silicone prestrain-locked interpenetrating polymer network elastomers: free-standing silicone artificial muscles with improved performance and robustness,” In preparation.

P. Brochu, Z. Ren, H. Stoyanov, X. Niu, and Q. Pei, ”High energy density silicone nanocomposites for energy harvesting,” In preparation.

H. Stoyanov*, P. Brochu*, X. Niu, C. Lai, S. Yun, and Q. Pei, "Long lifetime, fault-tolerant freestanding actuators based on a silicone dielectric elastomer and self-clearing carbon nanotube compliant electrodes," In preparation.
**equal contribution*

H. Stoyanov*, P. Brochu*, X. Niu, E. Della Gaspera, and Q. Pei, "Dielectric elastomer tranducers with enhanced force output and work density," Applied Physics Letters 100 (2012) 262902.
**equal contribution*

P. Brochu and Q. Pei, "Dielectric elastomers for actuators and artificial muscles." In: L. Rasmussen (Ed.) "Electroactivity in Polymeric Materials, " Springer Science+Business Media, New York, 2012.

P. Brochu, H. Stoyanov, X. Niu, and Q. Pei, "Energy conversion efficiency of dielectric elastomer energy harvesters under pure shear strain conditions," Proceedings of the SPIE 8340 (2012) 83401W.

S. Yun, X. Niu, Z. Yu, W. Hu, P. Brochu, and Q. Pei, "Compliant silver nanowire-polymer composite electrodes for bistable large strain actuation," Advanced Materials 24 (2012) 10.

P. Brochu, X. Niu, and Q. Pei, "Acrylic interpenetrating polymer network dielectric elastomers for energy harvesting," Proceedings of the SPIE 7976 (2011) 797606.

P. Brochu and Q. Pei, "Advances in dielectric elastomers for actuators and artificial muscles," Macromolecular Rapid Communications 31 (2010) 10.

P. Brochu, H. Li, X. Niu, and Q. Pei, "Factors influencing the performance of dielectric elastomer energy harvesters," Proceedings of the SPIE 7642 (2010) 76422J.

W. Yuan, H. Li, P. Brochu, X. Niu, and Q. Pei, "Fault-tolerant silicone dielectric elastomers," International Journal of Smart and Nano Materials 1 (2010) 40.

W. Yuan, P. Brochu, S.M. Ha, and Q. Pei, "Dielectric oil coated single-walled carbon nanotube electrodes for stable, large-strain actuation with dielectric elastomers," Sensors and Actuators A: Physical 155 (2009) 278.

Z. Yu, W. Yuan, P. Brochu, B. Chen, Z. Liu, and Q. Pei, "Large-strain, rigid-to-rigid deformation of bistable electroactive polymers," Applied Physics Letters 95 (2009) 192904.

L. Hu, W. Yuan, P. Brochu, G. Gruner, and Q. Pei, "Highly stretchable, conductive, and transparent nanotube thin films." Applied Physics Letters 94 (2009) 161108.

P. Brochu, Energy conversion efficiency of dielectric elastomer energy harvesters under pure shear strain conditions, SPIE Conference 8340, Electroactive Polymer Actuators and Devices (EAPAD) XIV, San Diego, CA, USA, March 11-15, 2012.

P. Brochu, Acrylic interpenetrating polymer network dielectric elastomers for energy harvesting, SPIE Conference 7976, Electroactive Polymer Actuators and Devices (EAPAD) XIII, San Diego, CA, USA, March 6-10, 2011.

P. Brochu, Factors influencing the performance of dielectric elastomer energy harvesters, SPIE Conference 7642, Electroactive Polymer Actuators and Devices (EAPAD) XII, San Diego, CA, USA, March 8-11, 2010.

P. Brochu, Dielectric Elastomers for Direct Wind-to-Electricity Power Generation, ASME 2009 Conference on Smart Materials, Adaptive Structures & Intelligent Systems (SMASIS), Oxnard, CA, USA, September 21-23, 2009.

Part I

Dielectric Elastomer Actuators

CHAPTER 1

Introduction

The ability to mimic the muscles in our own human bodies, both for the advancement in our well-being and for our amusement, has been a topic of great interest for some time. Natural muscle has a number of properties that make it difficult to match in terms of performance. The energy density of muscle is on the order of 150 J/kg and can peak at around 300 J/kg, [1] while displacements are relatively large with typical strains ranging from 20 - 40% and peaking at 100%. [2–4] By these measures alone, electromagnetic (EM) motors and combustion engines should be able to match or exceed the performance of natural muscle. [5] However, as it is made obvious by current leading-edge robots (e.g., Hondas Asimo) [6], the real world performance of conventional-actuator-based robotics is limited. [2, 7] The shortcoming lies on several fronts. First is the power supply: natural muscle relies on chemical energy that is supplied to living organisms through the ingestion of food, while EM motors rely on heavy battery pack and capacitor banks that must be recharged frequently. These large power sources contribute to the overall mass of the robotic device and reduce the effective energy density as well as limit range and mobility. Second is the requirement for gearing systems: EM motors operate best at high rotational speeds; these must be reduced significantly through the use of gearing systems that can significantly increase mass and reduce energy density. Third is the ability to recover energy: tendon and flesh, as well as muscle itself, are capable of absorbing and storing a large percentage of the impact energy that can be translated back to motion. Additionally, muscles possess other salient properties that allow them to operate as motors, brakes, springs, and struts, permitting better stability control and impact energy absorption. [8] EM motors also generate more noise and heat than natural muscle, which is not welcome for certain applications, and cannot be effectively operated in large magnetic fields.

Pneumatic systems operate linearly like natural muscle; pneumatic artificial muscles (McKibben artificial muscles) in particular are intrinsically compliant and can thus provide the ”give” that natural muscle attains. Unfortunately, these systems require air compressors that are neither light nor small, and their response speed is limited by the ability to pump air into and out of the actuators. Several ”smart materials” have been proposed as artificial muscles. These include shape memory alloys (SMA), magnetostrictive alloys (MSA), and piezoelectrics. [2, 9] SMAs are capable of producing relatively large linear displacements and can be actuated relatively quickly using resistive heating. What limits their applicability to artificial muscle applications is the time it takes to cool the alloy and return to the rest position. In order to obtain good operating frequencies, the SMA must be actively cooled, increasing the bulk, complexity and cost of the system. Magnetostrictive alloys and piezoelectric ceramics both suffer from small strains and high stiffness. These materials are thus not particularly suited to artificial muscle applications.

Polymers present an interesting alternative to conventional technologies. They possess inherent compliance, are lightweight, and are generally low cost. Electroactive polymers (EAPs) are an emerging type of actuator technology wherein a lightweight polymer responds to an electric field by generating mechanical motion. [1, 10, 11] Their ability to mimic the properties of natural muscle has garnered them the moniker ”artificial muscle”, though the term electroactive polymer artificial muscle (EPAM) is more appropriate and descriptive.

The concept of electroactive polymers can be dated back to 1880 in a paper by Roentgen. [12] In his experiments, he observed that a film of natural rubber could be made to change in shape by applying a large electric field across it; this was the first observation of actuation of a dielectric elastomer material.

Today the number of electroactive polymers has grown substantially. There currently exists a wide variety of such materials, ranging from rigid carbon-nanotubes to soft dielectric elastomers. A number of reviews and overviews have been prepared on these and other materials for use as artificial muscles and other applications. [1, 2, 7, 11, 13–29] The next section will provide a survey of the most common electrically activated EAP technologies and provide some pertinent performance values. The remainder of the paper will focus specifically on dielectric elastomers. Several actuation properties for these materials are summarized in Table 1.1 along with other actuation technologies. It is important to note that data was recorded for different materials under different conditions so the information provided in the table should only be used as a qualitative comparison tool.

1.1 Survey of Electroactive Polymer Technologies

EAPs can be broadly divided into two categories based on their method of actuation: ionic and field-activated. Further subdivision based on their actuation mechanism and the type of material involved is also possible. Ionic polymer-metal composites, ionic gels, carbon nanotubes, and conductive polymers fall under the ionic classification. Ferroelectric polymers, polymer electrets, electrostrictive polymers, bistable electroactive polymers, and dielectric elastomers fall under the electronic classification.

1.1.1 Ionic Electroactive Polymers

1.1.1.1 Ionic Polymer-Metal Composites

Ionic polymer-metal composites (IPMCs) consist of a solvent swollen ion-exchange polymer membrane laminated between two thin flexible metal (typically percolated Pt nanoparticles or Au) or carbon-based electrodes. [1,30,31] Application of a bias voltage to the device causes the migration of mobile ions within the film to the oppositely charged electrode, causing one side of the membrane to swell and the other to contract resulting in a bending motion. [32] Over time the actuator will relax slightly due to the built-up pressure gradient. A schematic representation of the actuation mechanism is shown in Figure 1.1. Typical membrane ma-

Table 1.1: Comparison of actuator materials

Type (Specific)	Maximum Strain (%)	Maximum Pressure (MPa)	Specific Elastic Energy Density (J/g)	Elastic Energy Density (J/cm^3)	Coupling Efficiency k^2 (%)	Maximum Efficiency (%)	Specific Density	Relative Speed (Full-Cycle)
Dielectric Elastomer (Prestrained Acrylic) [2,3,41] 2,3,166	380	7.2	3.4	3.4	85	60-80	1	Medium
Dielectric Elatomer (Prestrained Silicone) [41]	63	3	0.75	0.75	63	90	1	Fast
Dielectric Elastomer (Silicone – Nominal Prestrain) [3]	32	1.36	0.22	0.2	54	90	1	Fast
Bistable Electroactive Polymer (PTBA) [42,43]	335	3.2	1.2	1.2	–	–	1	Medium
Electrostrictive Polymer (P(VDF-TrFE)) [3]	4.3	43	0.49	0.92	–	~80 (est.)	1.8	Fast
Electrostatic Devices (Integrated Force Array) [4,41,44]	50	0.03	0.0015	0.0025	50 (est.)	> 90	1	Fast
Electromagnetic (Voice Coil) [4,44]	50	0.1	0.003	0.025	–	> 90	8	Fast

Continued on next page

Table 1.1 – *Continued from previous page*

Type (Specific)	Maximum Strain (%)	Maximum Pressure (MPa)	Specific Elastic Energy Density (J/g)	Elastic Energy Density (J/cm^3)	Coupling Efficiency k^2 (%)	Maximum Efficiency (%)	Specific Density	Relative Speed (Full-Cycle)
Piezoelectric Ceramic (PZT) [44]	0.2	110	0.013	0.1	52	> 90	7.7	Fast
Piezoelectric Single Crystal (PZT-PT) [44]	1.7	131	0.13	1	81	> 90	7.7	Fast
Piezoelectric Polymer (PVDF) [44]	0.1	3.8	0.0013	0.0024	7	–	1.8	Fast
Shape Memory Alloy (TiNi) [44]	> 5	> 200	> 15	> 100	5	< 10	6.5	Slow

terials include Nafion and Flemion [21] with anionic side groups or polystyrene ionomers with anionic-substituted phenyl rings. [1,2,30] Wang et al. have recently shown that IPMCs based on a sulfonated poly(styrene-b-ethylene-co-butylene-b-styrene) ionic membrane are capable of high speed bending actuation under constant voltages and give excellent harmonic responses under sinusoidal excitation. [33] Since the membrane materials contain anionic species, they will be negatively charged, so cationic species are added to the solvent in the membrane to balance the charge. The ionic segments of the chains form hydrophilic clusters whereas the surrounding areas are hydrophobic; as such, the mobile ions accumulate near the ionic segments. Channels through the hydrophobic regions allow for ion and solvent migration. [34] Driving voltages are typically on the order of a few volts or less and actuation strains and stresses of > 3 % [31,35] and 30 MPa [30,34] have been reported. Several studies have demonstrated that IPMCs are well suited for use as soft actuators for bending and sensing. [36–38] Potential applications include mechanical grippers, metering valves, micropumps, and sensors. [1,31,39] Eamax, Japan has developed a commercially available fish robot that uses IPMC actuators. [40] Due to the low strains and the nature of their actuation, their applications for artificial muscle may be limited.

1.1.1.2 Ionic Gels

Ionic polymer gels consist of a crosslinked polymer, typically a polyacrylic gel acid, in an electrolyte solution. These materials are a class of hydrogels, a type of network polymer that swells in water. Hydrogels have been of interest for use as actuators for some time. [45–48] A hydrogel placed into an aqueous solution can change in shape and volume by a change in the polymer-liquid interaction, and hence the degree of swelling. This change can be brought about by a number of stimuli; the mostly commonly used is a change in pH. Polyacrylic gel acids will ionize in response to an increase in the pH, causing them to swell. [49] The change in pH can be induced by chemical means; however, this approach is impractical as it relies on a fluid-pumping system. Ionic gels also respond to electrical fields. [50] Application

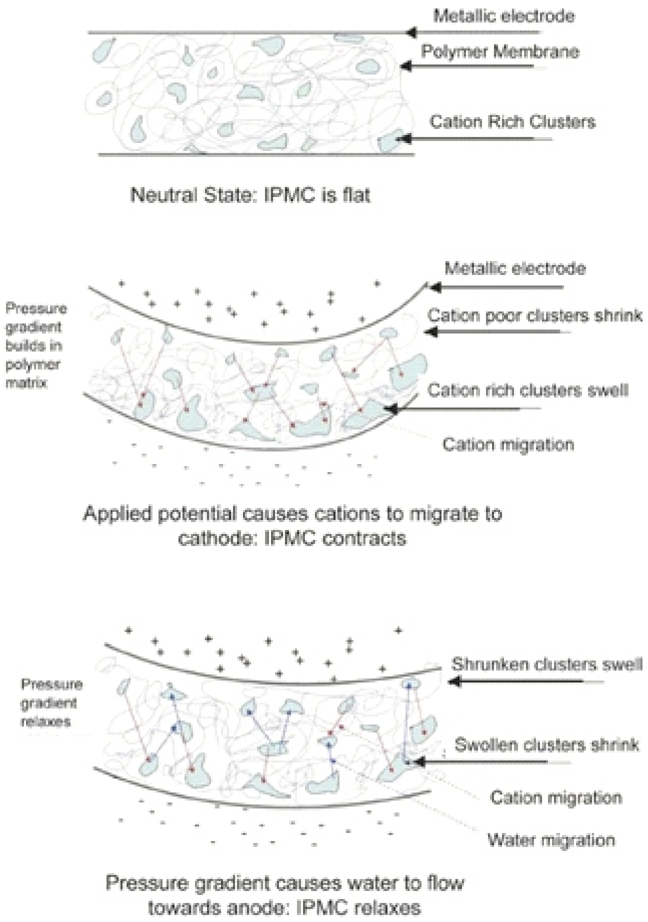

Figure 1.1: Schematic representation of the actuation mechanism for an IPMC actuator. Application of a bias voltage causes mobile ions to migrate to one of the electrodes. The concomitant migration of solvent causes thecion rich region to swell, generating a bending motion. Over time the actuator relaxes due to the built-up pressure gradient. [2] IEEE 2004, reprinted with permission.

of an electric field to the gel causes the migration of hydrogen ions out of or into the gel resulting in a change in pH. The change in pH results in a reversible shift between swollen and contracted states. Actuators tend to bend in response to a DC field, which is caused by the difference between ion diffusion rates in the gel and in the electrolyte solution. [51] While bending may be useful for some applications, it is not particularly useful for artificial muscle applications. Calvert and Liu have reported on the swelling of layered gels, consisting of crosslinked polyacrylamide layers stacked on polyacrylic acid layers. [52, 53] When the pH is decreased to create a basic environment, the polyacrylic acid layers swell strongly; however, the polyacrylamide layers do not. The result is that the stacks expand with only marginal bending. Since the actuation depends on the diffusion of ionic species and the presence of a liquid electrolyte, actuation rates tend to be slow and encapsulation is an issue. These materials are still in the exploratory stages as artificial muscles. Recent work by Tondu et al. has probed the possibility of combining ionic gels with McKibben artificial muscles. [54] The intention is to replace the conventional pneumatic system with a chemical actuation mode with the goal of improving the response speeds and reducing system complexity.

1.1.1.3 Carbon Nanotubes

Since their discovery by Iijima, [55] carbon nanotubes (CNTs) have garnered a great deal of interest thanks to their intrinsic mechanical and electrical properties and the ability to functionalize them and incorporate them in composite materials. Individual CNTs possess a high tensile modulus near that of diamond (640 GPa) and their tensile strength is thought to be 20 - 40 GPa, an order of magnitude larger than any other continuous fiber. [56] The mechanical properties of CNT bundles typically used in actuator tests tend to be much lower since they are held together by relatively weak van der Waals forces. [57] CNTs suspended in an electrolyte are capable of expanding in length due to double-layer charge injection. [2] When a bias is applied between the CNTs and a counter electrode, ions migrate to the surface of the CNTs. The resulting charge buildup must be offset by a rearrangement in the electronic charge within the tubes. The resulting actuation is due to these effects and to Coulombic forces. [2, 25] Figure 1.2 shows a schematic representation of the actuation mechanism. At low charge injections the quantum mechanical charge redistribution effects can predominate while at moderate to high levels the Coulombic effects dominate. [57] This mechanism does not require ion intercalation so lifetime and actuation rate is higher than for most ionic EAPs. CNTs possess low actuation voltages (∼1 V), high operating loads (26 MPa), high effective power to mass ratios of 270 W/Kg, and a response speed in the millisecond range. [58] They should also be capable of work densities per cycle that are higher than any other current actuation material due to their high modulus. Strains are typically < 2 % [2] since CNTs are stiff and as such they would require strain amplifiers to be used as artificial muscles. Creep is also an issue, and can negatively affect the measured work densities. [59] CNTs also suffer from very poor electromechanical coupling. This can be partly attributed to the disparity in modulus between individual nanotubes and nanotube bundles. [53] Related work on polymer nanofibers has shown that the elastic modulus increases exponentially from bulk materials to nanofibers with diameters in the range of tens of nanometers. [60] Multi-wall CNTs tend to have lower strains than single-wall CNTs since they have a lower exposed surface area to capture ions; [2] however, Hughes and Spinks have shown that strains in excess of 0.2% are possible in multi-wall CNT mats. [61] Cost and manufacturing difficulties are issues that are currently being addressed. [62, 63]

Aliev et al. have recently reported on novel giant-stroke, super-elastic CNT aerogel muscles. [64] The CNT aerogel sheets are fabricated from highly ordered CNT forests and are capable of anisotropic linear elongations of 220 % and strain rates of 3.7x104 %/s at temperatures from 80 to 1900 K. The actuation decreases the aerogel density and the strain can be permanently frozen in. Unlike conventional CNT actuators, no electrolyte is required and the actuation results from applying a positive voltage with respect to a counter electrode. The actuators have gas-like density and highly anisotropic mechanical properties, with Poissons ratios reaching 15.

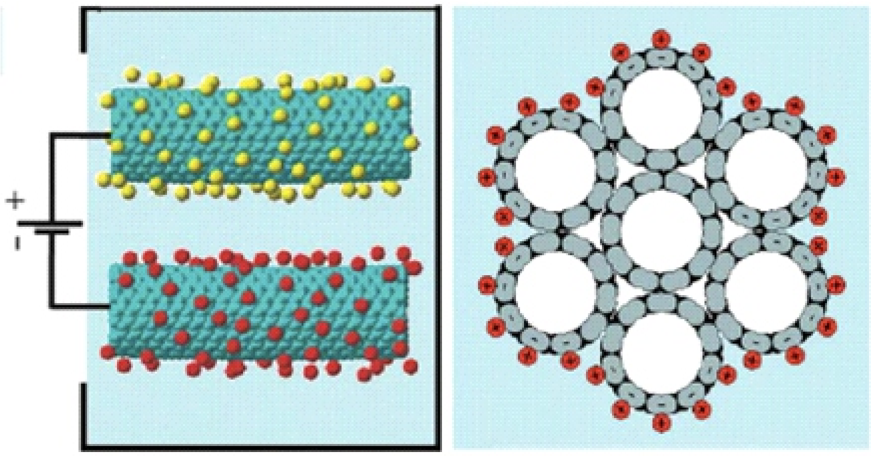

Figure 1.2: Schematic representation of the actuation mechanism for a CNT actuator. When a bias is applied to CNTs that are submerged in an electrolyte, ions will migrate to the surface of the CNTs, which is offset by the rearrangement in their electronic structure. This phenomenon, coupled with Coulombic effects, results in actuation. [7] Materials Today 2007, reprinted with permission.

1.1.1.4 Conductive Polymers

Actuators based on conductive polymers (CPs) were first proposed by Baughman et al. in 1990. [65–67] Much of the exploratory work was subsequently reported by Pei and Ingans, and Smela, Ingans and Otero et al. [68–71] CPs actuate due to the uptake of counter-ions during electrochemical redox cycling, with the majority of the expansion occurring perpendicular to the polymer chain direction, indicating that ions and solvent are incorporated between the polymer chains. [66, 69, 72, 73] Changes in oxidation state result in a charge flux along the polymer chain and counter ions in the electrolyte migrate to balance the charge. [1, 2, 7, 21, 74, 75] For polymers doped with moderately sized counter anions, the oxidized state causes the polymer chains to expand due to the presence of the counter anions; in the reduced state the ions migrate away and the polymer chains relax. In polymers doped with bulky counter anions, the reduction involves uptake of cations into the polymer. The reduced polymer is in the expanded state. [69, 75, 76] Since both states are stable, these actuators are bistable. The most commonly used CPs for actuation purposes are polypyrrole and

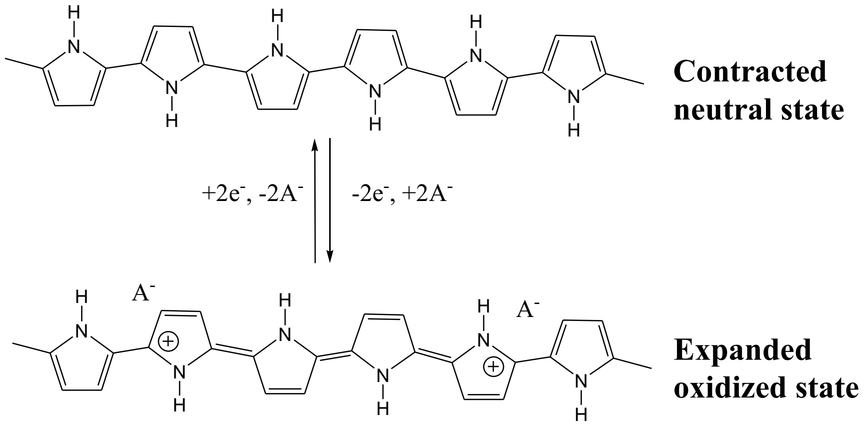

Figure 1.3: Schematic representation of a polypyrrole chain in its oxidized and reduced states. Actuation results from the intercalation and deintercalation of ions between the chains.

polyaniline. [74, 77] Figure 1.3 shows a schematic representation of a polypyrrole chain in its oxidized and reduced state. Actuation voltages are typically low (1-2 V) [68] and the materials are biocompatible. Strains are typically a few percent but can range from 1 to ∼40 %. [2, 7, 78–82] Force densities up to 100 MPa are achievable [83] and values up to 450 MPa may be possible. [68] Conductive polymers suffer from a very low operating efficiency of ∼1 % and electromechanical coupling under 1 %. [2] In addition, actuation speeds are limited since the mechanism relies on the migration of ions [21] and due to internal resistance between the electrolyte and polymer. [4] Due to the requirement of an electrolyte, most CP actuators must be encapsulated, [36] though work has been performed on developing solid electrolytes that would remove this restriction. [84] Application of these materials for artificial muscles may be limited due to their poor coupling efficiencies and relatively slow actuation speeds (which would be exacerbated in large devices), though other potential biomimetic and human-interface applications exist that include blood vessel reconnection, dynamic Braille, valves, and catheters. [85–87]

1.1.2 Field Activated EAPs

1.1.2.1 Ferroelectric Polymers

Ferroelectric polymers have a non-centro-symmetric structure that exhibits permanent electric polarization. These materials possess dipoles that can be aligned in an electric field and maintain their polarization. The induced polarization can be removed by applying a reverse electric field or by heating above the materials Curie temperature. They exhibit non-linear polarization curves demonstrating pronounced hysteresis. The polymers exhibiting these properties are limited mainly to poly(vinylidene difluoride) (PVDF), some PVDF copolymers, certain odd-numbered polyamides such as Nylon 7 and Nylon 11, [88] and blends thereof. [89, 90] In order to display ferroelectric behavior, polymers not only require polar side groups, they must also maintain molecular configurations in which the polarity does not cancel out. Thus, polymers such as poly(vinyl chloride) that has a polar carbon-chloride bond will not display ferroelectric behavior as it must arrange itself in a helical conformation due to steric effects from the relatively large van der Waals radius of the chloride atoms. Additionally, the polymer chains must be able to crystallize in a manner in which the polarization does not cancel. As an example, PVDF has four crystal structures, [91, 92] a non-polar alpha phase, its polar analog (the delta phase), a highly polar beta phase, and a polar gamma phase. The morphology of the crystals must also be considered as they can have pronounced effects on the Curie temperature, remnant polarization, and other properties.

For commonly used poly(vinylidene fluoride trifluoroethylene), abbreviated as P(VDF-TrFE), copolymers with a VDF content ranging from 50 to 85 mole%, the ferroelectric beta phase is stable at room temperature, and a transformation to the paraelectric alpha phase occurs above the Curie point but below the melting point. [93] Above the Curie temperature, a transition between the paraelectric and ferroelectric phases can be brought about by applying an electric field. [94,95] The change in phases results in an extremely large change in lattice constant, resulting in large bulk strains. [96] The Curie point decreases with

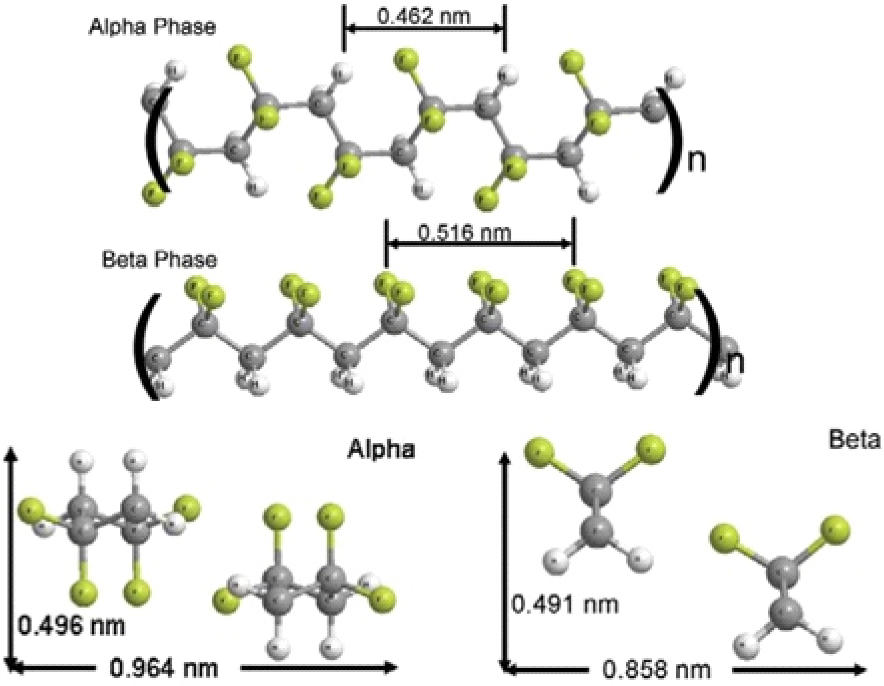

Figure 1.4: The alpha and beta phases of the ferroelectric polymer PVDF. The beta phase is stable at room temperature but can be reversibly changed to the alpha phase by heating above the Curie temperature. Above the Curie temperature, an electric field can be used to induce a change between the alpha and beta phases. For ferroelectric relaxor polymers, the Curie temperature is below room temperature so the alpha phase is stable. A change to the beta phase can be induced by an electric field.

decreasing crystallite size and can also be influenced by mechanical stress. [19] The induced change between the ferroelectric beta phase and paraelectric alpha phase is represented schematically in Figure 1.4.

These materials have shown piezoelectric responses after appropriate poling. [19] Their piezoelectric actuation properties are typically worse than ceramic piezoelectric crystals; however, they have the advantages of being lightweight, flexible, easily formed, and not brittle. Additionally, while ceramics are limited to strains on the order of 0.1 %, ferroelectric polymers are capable of strains of 10 % [95] and very high electromechanical coupling efficiencies. [97]

Recent advances in PVDF-based materials have led to the elimination of the hysteretic behavior characteristic of ferroelectrics. For this reason, these PVDF-based materials are classified as relaxor ferroelectric polymers; they will be discussed under the "Electrostrictive Polymers" heading.

1.1.2.2 Polymer Electrets

Early work by Eguchi on wax electrets [98] paved the way to the development of commercially viable low cost polymer electrets, with applications including microphones, sensors, transducers, and filters. [19] Electrets are insulating materials that display piezoelectric effects due to a non-uniform space charge distribution. [99, 100] Modern polymer electrets consist of a highly porous polymer with a polarization gas in the pores. The porous films are subjected to corona charging with voltages ranging from 5-10 kV. It is generally accepted that electrical discharging within the pores results in the build-up of charges at the polymer-gas interface. Positive and negative charges will lie on opposite sides of the pores according to the direction of the applied field, forming macroscopic dipoles. [19] Metal electrodes are applied to both sides of the film to act as contacts. Polymer electrets can be operated as sensors or actuators. Their operation is very similar to that of a piezoelectric material and their direct piezoelectric transducer coefficient (d_{33}) is higher than that of solid PVDF ferroelectric polymers. [101] If a compressive force is applied to the film, the pores will deform preferentially with respect to the polymer material. Unlike charges within the polymer will be pushed closer together and the potential measured at the contacts will change accordingly. Similarly, the application of a voltage across the electrodes will yield a change in thickness in the material. In order to meet increasing performance demands for electret applications, polymer electret blends are being explored. Lovera et al. have recently reported on tailored polymer electrets based on poly(2,6-dimethyl-1,4-phenylene ether) (PPE) and its blends with polystyrene (PS). [102] They obtained good electret performance with neat PPE and showed that it could be improved by blending with PS.

1.1.2.3 Electrostrictive Polymers

Electrostrictive polymers have a spontaneous electric polarization. Electrostriction results from the change in dipole density of the material. These polymers contain molecular or nanocrystalline polarizations that align with an applied electric field. PVDF copolymers with nano-sized crystalline domains, electrostrictive graft copolymers, and liquid crystal elastomers fall under this category.

Relaxor Ferroelectric Polymers Relaxor ferroelectric polymers are intimately related to the ferroelectric polymers described above. All known relaxor ferroelectric polymers are based on the P(VDF-TrFE) copolymer. As the name suggests, these polymers behave as relaxor ferroelectrics, which is distinguished by a broad peak in dielectric constant and a strong frequency dispersion. [103, 104] There are two major limitations of the P(VDF)-based ferroelectric actuators. First, the electrically induced paraelectric-ferroelectric transition that allows for actuation only occurs at temperatures above the Curie temperature, which is usually above room temperature. Second, the existence of strong hysteresis can make actuation more energy intensive and difficult to control. The Curie temperature of P(VDF-TrFE) copolymers can be lowered by introducing defects into the material, thereby reducing the size of the crystallites in the solid PVDF copolymer. [19] Having smaller crystallites also lowers the energy barrier required for the transition between paraelectric and ferroelectric states, which results in lower hysteresis. [105] For efficient room temperature operation, the Curie temperature must be reduced to around room temperature and the hysteresis must be suppressed. Zhang and others have shown this can be achieved by irradiating P(VDF-TrFE) with high-energy electrons or protons [95, 105–107] or adding bulky side groups to the copolymer, [95, 108–110] thus introducing polarization defects that destabilize the ferroelectric phase. Bulky side groups can be introduced though the formation of copolymers containing PVDF, TrFE and either chloride containing monomers such as cholorofluoroethylene (CFE) [95, 108] and chlorotrifluoroethylene (CTFE) [109, 110] or hexafluoropropylene

(HFP). [111–113] The actuation mechanism is essentially the same as for ferroelectric polymers; a transition between paraelectric and ferroelectric phases is induced by the application of a high electric field as represented in Figure 1.4.

Recent work by Bao et al has shown that P(VDF-TrFE) synthesized via reductive dechlorination from P(VDF-CTFE) exhibits ferroelectric relaxor behavior at high temperature (∼100 °C) with a melting point near 200 °C. [114] This result is important and it provides another avenue to study the relaxor phenomena which are still not completely understood. The high melting point coupled with the high dielectric response of these materials at high temperature makes them attractive for use in high-temperature capacitors.

These materials have shown thickness strains on the order of 5 % with fast response times. [19] Representative results are shown in Figure 1.5. As seen in the figure, the required fields are quite high as in most electronic EAPs. Strains tend to show a peak and decrease for stresses above and below the peak value. Reported values for irradiated P(VDF-TrFE) show peak strains at 20 MPa, dropping to 50% of the maximum value above 40 MPa and below 5 MPa. [115] Elastic moduli in the range of 0.3-1.2 GPa have been reported with energy densities around 1 MJ/m^3. [7] In order to compete as artificial muscles, strain values will have to be improved.

Electrostrictive Graft-Copolymers Electrostriction has also been obtained from graft copolymers wherein polar crystallites are grafted to flexible polymer backbones. The polar side groups aggregate to form crystalline regions which serve as the polarizable moieties required for actuation and as physical crosslinking sites for the flexible polymer as shown schematically in Figure 1.6. [116] When an electric field is applied to the copolymers, the polar crystallites reorient themselves which results in bulk deformation of the material. Strains and energy densities can be as high as 4 % and 247 J/kg. [117] Similar results have been reported for a graft copolymer consisting of chlorofluoroethylene and trifluoroethylene backbone with P(VDF-TrFE) side chains. [1] While the required electric fields are lower than for relaxor

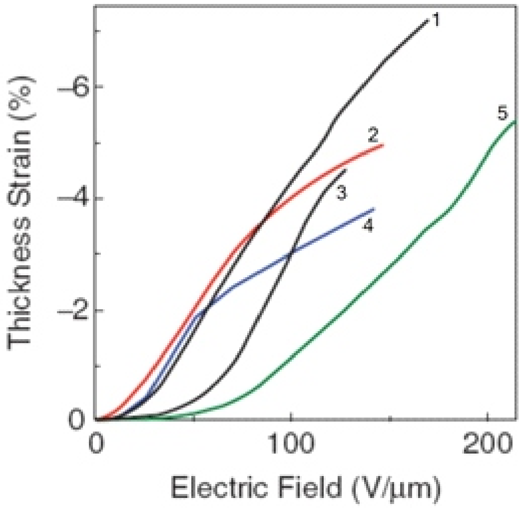

Figure 1.5: Actuation strain as a function of electric field for irradiated P(VDF-TrFE) copolymer (2), P(VDF-TrFE-CTFE) (4), P(VDF-CTFE) (5), and P(VDF-TrFE-CFE) (1 and 3, the two curves have different compositions). [19] Materials Research Society 2008, reprinted with the permission of Cambridge University Press.

ferroelectrics, the strains are lower and the actuation rates are slower due to the size of the polar crystallites. Unimorph and bimorph bending actuators have been demonstrated. [117]

Liquid Crystal Elastomers As the name suggests, liquid crystal elastomers (LCEs) combine the orientational ordering properties of liquid crystals with the elastic properties of elastomer networks. [118] As early as 1975, de Gennes predicted that the reorientation of mesogens in liquid crystals during a phase transition could result in bulk stresses and strains. [119] LCEs were first proposed for use as artificial muscles by de Gennes in the late 1990s. [120] LCEs consist of mesogens attached to one another via a networked elastic polymer. The polymer network permits sufficient motion to allow for the rotation of the mesogens while maintaining a solid shape and preventing free flow. LCEs can be divided into two categories depending on the phases present: nematic and smectic. The actuation mechanism for these two systems is different. Here we will briefly describe the nematic system since it is the focus of the majority of the current research in the field; the interested reader can consult refer-

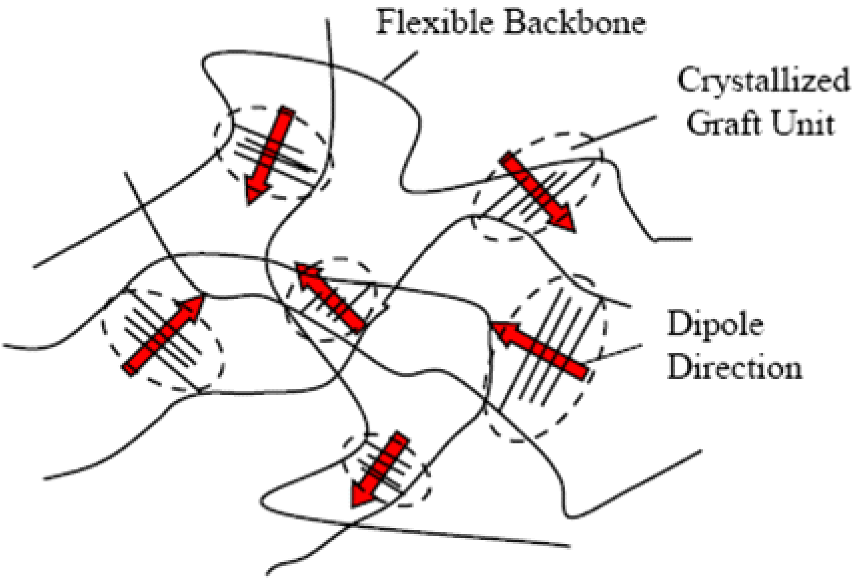

Figure 1.6: Electrostrictive graft copolymer consisting of P(VDF-TrFE) main chains and PVDF grafts. Polar PVDF units (pink) aggregate and form crystallites that serve as polarizable moieties for actuation and as physical crosslinks between elastomer chains. [116] J. Su 2003, reprinted with permission.

ences [121–123] and [124] for a detailed look at the nematic and smectic systems respectively. In nematic polymer systems where the mesogens are incorporated directly into the backbone, the chains will elongate in their nematic phase when all of the mesogens are aligned [125–127] and will relax when the polymer is in the isotropic state and the chains are allowed to coil up into their entropically favored positions. [128] Similar effects are observed when the mesogens are attached as grafts to the elastomeric backbone. The change in orientation can be effected via thermal and electrical stimuli. [119, 121, 124, 129–135] Thermally activated LCEs display length changes as high as 400% but their response speed is limited due to the requirement for heat diffusion. [120, 136] Several strategies have been investigated for improving the thermal diffusivity [132, 137] of LCEs but thermal relaxation is still an issue. The thermal response can be generated from a number of stimuli, including optical, electrical, and direct magnetic through the incorporation of appropriate additives. [138] Electrically activated LCEs have intrinsically polarized mesogens that can realign in the presence of an electric field to generate bulk stress and strain as shown schematically in Figure 1.7. [119] Electrically activated LCEs have much faster response speeds (10 ms) [124] than the thermally activated variety and the required fields (1.5-25 MV/m) are lower than for most other field activated EAP technologies; however, the actuation strains are relatively small (< 10 %). Recent results have shown 4 % strain at 133 Hz with a field strength of 1.5MV/m. [124] The combination of small to moderate strains with low moduli means that the work densities of these materials will be relatively low. The use of stiffer polymers yielded strains of 2 % at 25MV/m and a work density of 0.02 MJ/m^3. [134] Additional improvements in strain and work density will be required if LCEs are to compete as artificial muscles. Recent results have shown that the application of a high electric field across a smectic LCE results in a large electroclinic effect with reasonable rates at relatively low voltages that can be used for actuation. [139, 140]

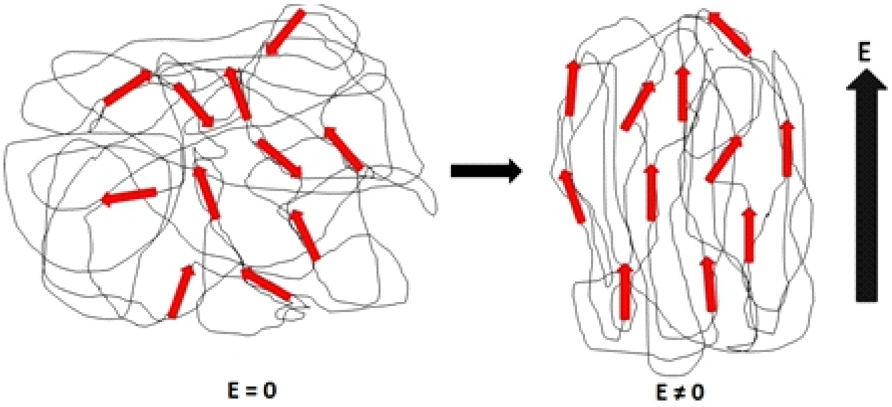

Figure 1.7: Actuation mechanism of a liquid crystal elastomer. The application of an electric field results in the realignment of intrinsically polarized liquid crystal mesogens. The mesogens are either grafted to elastomer chains or incorporated within them. The elastomer chains prevent the free flow of the mesogens and couple their motion to bulk stresses and strain.

1.1.2.4 Bistable Electroactive Polymers

Bistable electroactive polymers (BSEPs) are a new class of electroactive polymer developed in 2009 by Yu et al. [42] BSEPs combine the properties of dielectric elastomers (described in the following section) and shape memory polymers (SMPs). As with SMPS, BSEPs behave as rigid plastics below their glass transition temperature (T_g) and soft elastomers above their T_g. If a thin film of the material is sandwiched between compliant electrodes, it can behave as a capacitor in the rigid state and as a compliant variable capacitor in the elastomeric state. If a voltage is applied across the BSEP film in the softened state, the resulting electrostatic forces will act to compress the film in thickness and expand it in area. In the rigid state, the modulus of the film is too large to be electrostatically deformed. If the film is actuated in the softened state, then cooled to below its T_g, it will retain the actuated shape indefinitely without the requirement for an applied voltage. In addition, because of the transition to a rigid glassy state, the material is able to support relatively large loads. When reheated, the film returns to its rest position. Because the strain is electrically controlled, BSEPs can be reversibly actuated and locked in to any position between the rest state and their maximum

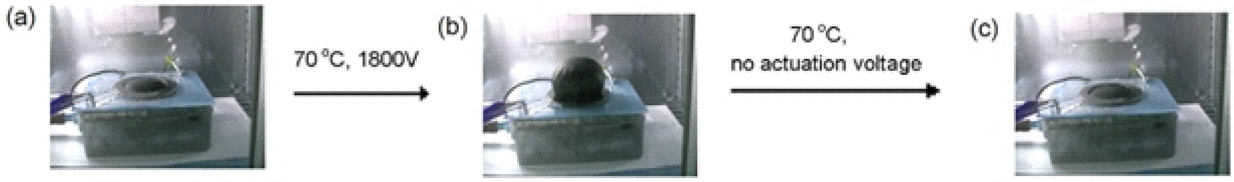

Figure 1.8: Diaphragm actuator with a BSEP film and conductive carbon grease coated on both surfaces as the compliant electrodes. (a) Initial device at room temperature or 70 °C; (b) Applying 1.8 kV at 70 °C followed by cooling to room temperature and removal of the actuation voltage; (c) raising temperature to 70 °C without any external voltage being applied. [42] Appl Phys Lett 2009, reprinted with permission.

deformation state. Figure 1.8 shows an example of a BSEP being actuated in a diaphragm configuration. The film is heated to 70 °C and actuated to a high strain state; it is then cooled to room temperature to lock in the strain and the driving voltage is removed. Upon reheating to 70 °C, the film returns to its original state.

Poly(tert-butyl-acrylate) (PTBA) has been extensively studied as a BSEP material. [42, 43] It exhibits a relatively sharp glass transition at 50°C. At room temperature PTBA has a storage modulus of 1.5 GPa and a loss factor, tan δ, of 0.03. At 70°C, the bulk modulus is reduced to 0.42 MPa with a loss factor of 0.8. PTBA also exhibits excellent strain fixity (ability to retain its actuated shape upon cooling) and strain recovery. In its softened state PTBA also possesses excellent actuation properties with a breakdown field strength in excess of 250 MV/m, a maximum strain of 335% in area, a maximum actuation stress of 3.2 MPa and an energy density of 1.2 J/cm^3, values that rival even the best of the conventional dielectric elastomer materials. The BSEP is the first active material that possesses bistable actuation with high strain and specific power density.

The ability to lock in strain is very important for applications wherein the device must hold its actuated state for an extended period of time. Conventional dielectric materials consume energy when actuated due to current leakage through the film, and can succumb to

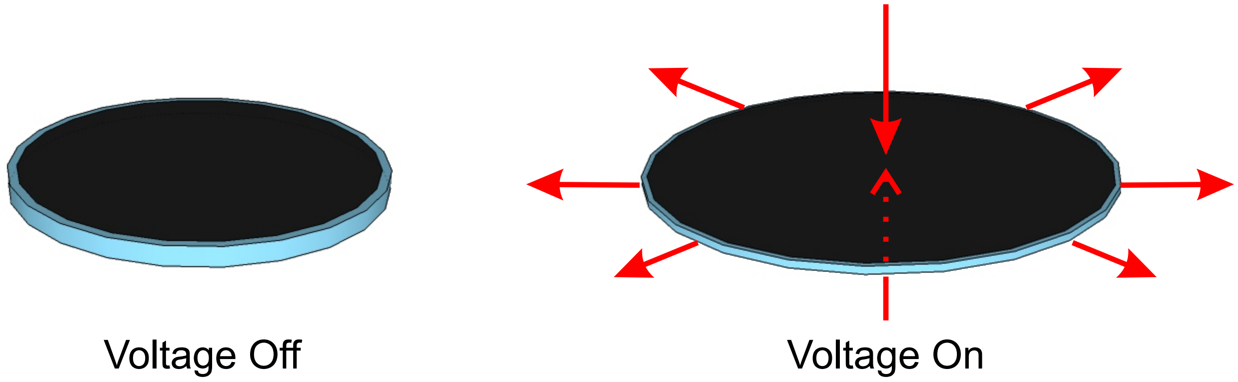

Figure 1.9: Dielectric elastomer operating principle. When a bias voltage is applied across an elastomer film coated on both sides with compliant electrodes, Coulombic forces act to compress the film in the thickness direction and expand it in plane.

premature breakdown when held at high strain for an extended period of time. By locking in the actuated shape, BSEPs can hold their actuated shape without draining power and can maintain that shape indefinitely without failure. This combination of properties places BSEP materials at the forefront in terms of electroactive polymer materials for artificial muscle applications.

1.1.2.5 Dielectric Elastomers

Dielectric elastomer (DE) actuators are essentially compliant variable capacitors. They consist of a thin elastomeric film coated on both sides by compliant electrodes. When an electric field is applied across the electrodes, the electrostatic attraction between the opposite charges on opposing electrode and the repulsion of the like charges on each electrode generate stress on the film causing it to contract in thickness and expand in area (Figure 1.9). Most elastomers used are essentially incompressible, so any decrease in thickness results in a concomitant increase in the planar area.

Typical operating voltages for DE films 10-100 μm in thickness range from 500 V to 10 kV. The area expansion can be readily measured if the films are subjected to tensile

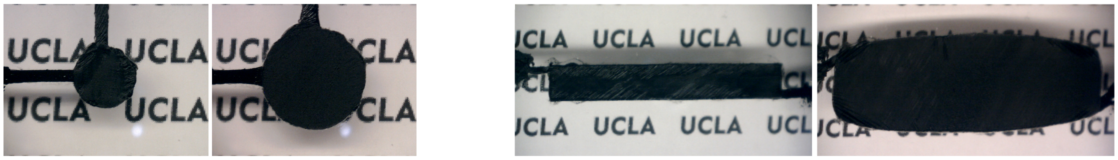

Figure 1.10: Actuation of dielectric elastomer devices with biaxial and uniaxial prestrain. Uniaxial prestrain results in preferential in-plane strain in the direction perpendicular to the applied prestrain direction.

prestrain: the non-active areas in tension surrounding the active area pulls the expanded active area and keeps it flat (Figure 1.10).

The driving currents are very low and the device is electrostatic in nature, so it will theoretically only consume power during an active area expansion (thickness reduction) and no power will be consumed to maintain the DE at a stable actuated state. Furthermore, some of the energy can be recovered after the actuation cycle is complete. In practice, however, there will be some leakage current through the dielectric, the amount of which will depend on the material and its thickness, and thus the DE will consume a small amount of power when maintained in a stable actuation state. Viscoelastic effects may also play a role in reducing efficiency.

Output stress varies quadratically with electric field; however, due to the inherent compliance of the materials, the force that can be coupled to a load will decrease with increasing strain for a particular electric field. Maximum force is available at zero strain and at maximum strain the elastomer will not generate any output forces. Note also that for a given strain, the output force, and thus the stiffness, can be modulated by varying the applied field. This is an important feature for artificial muscle applications as it allows the DE actuators to "brace" themselves as natural muscles do to maintain stability or prevent damage.

1.2 Modeling of Dielectric Elastomer Materials

The actuation of DEs can be approximated as the lateral electrostatic compression and planar expansion of an incompressible linearly elastic material where the electrical component is treated as a parallel plate capacitor. [141] The incompressibility constraint can be expressed as:

$$Az = P \tag{1.1}$$

where A is the area of the electrodes, z is the thickness of the elastomer film between electrodes, and P is a constant. The stored electrical energy on the DE is given by the stored energy on a parallel plate capacitor:

$$U = 0.5\frac{Q^2}{C} = 0.5\frac{Q^2 z}{\epsilon_r \epsilon_0 A} \tag{1.2}$$

where Q is the charge on the electrodes, C is the capacitance, ϵ_r is the relative permittivity and ϵ_0 is the permittivity of free space. The electrostatic pressure across the electrodes is then given by the Maxwell pressure:

$$p = \epsilon_r \epsilon_0 E^2 \tag{1.3}$$

This is exactly twice the pressure across a parallel plate capacitor. The factor of two is due to the incompressibility of the elastomer film. Charges on opposite electrodes will attract one another, resulting in a reduction in thickness as well as a concomitant increase in area since the material is incompressible. Likewise, like charges on each electrode will also repel each other, causing an increase in area and a concomitant reduction in thickness.

Using the linear-elasticity and free boundary approximations used in the early work in the field, which is only valid for small strains (< 10 %), the change in thickness is given by: [141]

$$s_z = -\frac{p}{Y} = -\frac{\epsilon_r \epsilon_0 E^2}{Y} = -\frac{\epsilon_r \epsilon_0 \left(V/z\right)^2}{Y} \tag{1.4}$$

where V is the applied voltage and Y is the elastic modulus.

Krokovsky et al. provided a good derivation of this linear small-strain case and extended these derivations to include the effects of electrostriction that may be important for certain materials. [142] Pelrine et al. showed that for the small strain case, the actuator energy density is given by: [3, 44]

$$e_a = -p s_z = \frac{\left(\epsilon_r \epsilon_0\right)^2 E^4}{Y} = \frac{\left(\epsilon_r \epsilon_0\right)^2 \left(V/z\right)^4}{Y} \tag{1.5}$$

This equation considers both the expansion and contraction in an actuation cycle can exert work. Similarly, the elastic energy density is given by:

$$e_e = -\frac{1}{2} p s_z = \frac{1}{2} \frac{\left(\epsilon_r \epsilon_0\right)^2 E^4}{Y} = \frac{1}{2} \frac{\left(\epsilon_r \epsilon_0\right)^2 \left(V/z\right)^4}{Y} \tag{1.6}$$

For larger strains, while maintaining the assumption that the material is linearly elastic, they showed that: [141]

$$s_z = \frac{2}{3} + \frac{1}{3}\left(f\left(s_{z0}\right) + \frac{1}{f\left(s_{z0}\right)}\right) \tag{1.7}$$

where:

$$f\left(s_{z0}\right) = \left(2 + 27 s_{z0} + \frac{\left(-4 + \left(2 + 27 s_{z0}\right)^2\right)^{1/2}}{2}\right)^{(2/3)} \tag{1.8}$$

and:

$$s_{z0} = -\epsilon_r \epsilon_0 \frac{V^2}{Y z_0^2} \tag{1.9}$$

In this case, the elastic energy density is: [3, 44]

$$e_e = Y\left(s_z - ln\left(1 + s_z\right)\right) \tag{1.10}$$

The preceding equations provided a reasonable foundation for predicting DE behavior. Indeed the assumption that DEs behave electronically as variable parallel plate capacitors still holds; however, the assumptions of small strains and linear elasticity limit the accuracy of this simple model. More advanced non-linear models have since been developed employing hyperelasticity models such as the Ogden model, [143–146] Yeoh model, [146, 147] Mooney-Rivlin model, [144, 145, 148, 149] and others (Figure 1.11). [146, 150, 151] Models taking into account the time-dependent viscoelastic nature of the elastomer films, [147, 149, 150] the leakage current through the film, [150] as well as mechanical hysteresis [152] have also been developed.

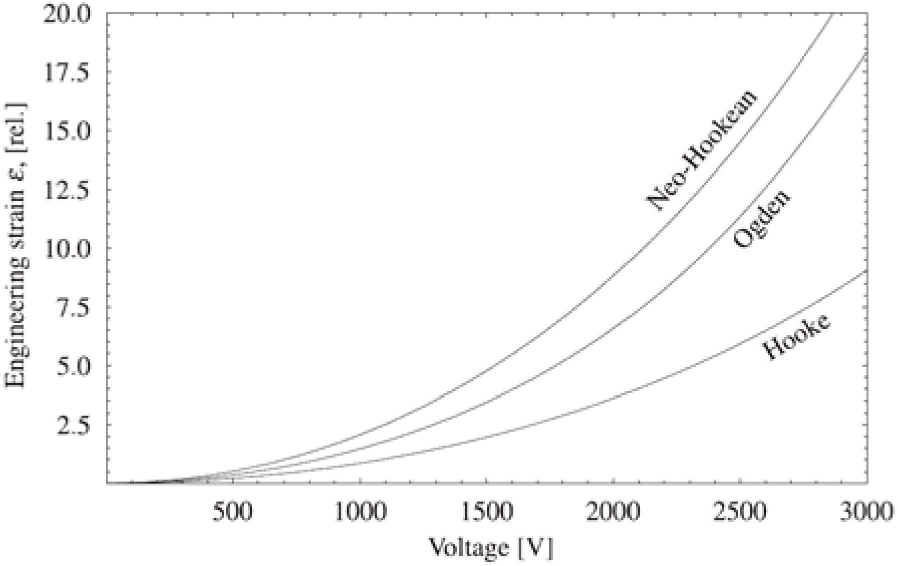

Figure 1.11: DE voltage-strain curves as predicted by various models. [146] G Kofod 2001, reprinted with permission.

Recently Zhao and Suo developed a thermodynamic model of electrostriction for elastomers capable of large deformation that helps elucidate the roles that different electrostrictive effects play at different strain levels. [153] Others have attempted to study dynamic effects for actuators subjected to time-varying voltage and pressure inputs. [154, 155]

Models have been used to study the failure modes and instabilities present in DEs, including the thermodynamic electromechanical instability (pull-in), [156–162] wrinkling/buckling, [157, 158] mechanical rupture, [158, 159] and dielectric breakdown [158, 159] for select actuator configurations. An improved understanding of these failure modes should allow for the design of actuators capable of operating in a safe regime, thus prolonging actuator lifetime.

The applicability of any of the models to a general case is suspect since the modeling parameters are strongly dependent on the testing conditions. Factors such as prestrain, mechanical loading, actuator configuration, humidity, and temperature can have a large effect on the parameters obtained. However, these studies have provided useful insight into the failure mechanisms present in DE actuators and provide tools for design engineers to develop new actuator configurations capable of large strains, high forces outputs, and long lifetimes.

1.3 Dielectric Elastomer Materials

In the late 1990s and early 2000s a large number of elastomer materials were tested, including silicones, polyurethanes, isoprene, and fluoroelastomers. [141, 142, 163, 164] Pertinent properties of these materials and several other dielectric elastomers described below are included in Table 1.2. Pelrine et al identified three particularly promising groups of materials: silicones, polyurethanes, and acrylics. Their actuation characteristics were promising; however, it was not until strains in excess of 100% in area in both silicone and acrylic elastomer films were reported that significant interest was garnered in the scientific community. [41, 44] The key to developing such large strains in these materials was prestrain. Though the exact mechanism by which actuation strains are improved is not known, it has been shown that prestrain enhances the breakdown field in certain acrylic elastomers and can reduce viscoelastic effects.

Of these materials, a commercially available 3M VHB acrylic elastomer (VHB 4910 and

Table 1.2: Comparison of dielectric elastomer material properties

Polymer (Specific Type)	Prestrain (%)	Energy Density (MJ/m^3)	Actuation Pressure (MPa)	Thickness Strain (-%)	Area Strain (%)	Young's Modulus (MPa)	Electric Field (V/μm)	Dielectric Constant	Dielectric Loss Factor	Mechanical Loss Factor	Coupling Efficiency k^2 (%)	Efficiency (%)
Silicone (Nusil CF19-2186) [3]	–	$0.22^{(e)}$	$1.36^{(f)}$	32	–	1	235	2.8	54	–	–	–
Silicone (Nusil CF19-2186) [41, 44]	(45, 45)	$0.75^{(e)}$	3	39	64	$1.0^{(g)}$	350	2.8	6.3	0.005	0.05	79
Silicone (Nusil CF19-2186)	(15, 15)	$0.091^{(e)}$	0.6	25	33	–	160	2.8	–	– [41, 44]	–	–
Silicone (Nusil CF19-2186) [41, 44]	(100, 0)	$0.2^{(e)}$	0.8	39	63 (linear)	–	181	2.8	–	–	–	–
Silicone (Dow Corning HS3) [3]	–	$0.026^{(e)}$	0.13	41	–	0.135	72	2.8	65	–	–	–
Silicone (Dow Corning HS3) [41, 44]	(68, 68)	$0.098^{(e)}$	0.3	48	93	$0.1^{(g)}$	110	2.8	79	0.005	0.05	82
Silicone (Dow Corning HS3) [41, 44]	(14, 14)	$0.034^{(e)}$	0.13	41	69	–	72	2.8	–	–	–	–
Silicone (Dow Corning HS3) [41, 44]	(280, 0)	$0.16^{(e)}$	0.4	54	117 (linear)	–	128	2.8	–	–	–	–
Silicone (Dow Corning Sylgard 186) [3]	–	$0.082^{(e)}$	$0.51^{(f)}$	32	–	0.7	144	2.8	54	–	–	–
Polyurethane (Deerfield PT6100S) [3, 165]	–	$0.087^{(e)}$	$1.6^{(f)}$	11	–	17	160	7	21	0.5	0.08 (@ 30 Hz)	–
Polyurethane (Estane TPU588) [166]	–	0.0025	0.14	8	–	–	8 (at max. strain)	6	–	–	–	–

Continued on next page

Table 1.2 – *Continued from previous page*

Polymer (Specific Type)	Prestrain (%)	Energy Density (MJ/m^3)	Actuation Pressure (MPa)	Thickness Strain (-%)	Area Strain (%)	Young's Modulus (MPa)	Electric Field (V/μm)	Dielectric Constant	Dielectric Loss Factor	Mechanical Loss Factor	Coupling Efficiency k^2 (%)	Efficiency (%)
Polyurethane-Carbon Powder Composite (Estane TPU588) [3, 165]	–	0.0043	0.14	12	–	–	8 (at max. strain)	6	–	–	–	–
Fluorosilicone (Dow Corning 730) [3]	–	$0.0055^{(e)}$	$0.39^{(f)}$	28	–	0.5	80	6.9	48	–	–	–
Fluoroelastomer (Lauren L143HC) [3]	–	$0.0046^{(e)}$	$0.11^{(f)}$	8	–	2.5	32	12.7	15	–	–	–
Isoprene Natural Rubber Latex [3]	–	$0.0059^{(e)}$	$0.11^{(f)}$	11	–	0.85	67	2.7	21	–	–	–
Dr. Scholl's Gelactive Tubing [167]	(140, 0)	–	0.0037	1.8	–	–	28	–	–	–	–	–
Acylic (3M VHB) [4]	–	$3.4^{(e)}$	7.2	79	380	–	–	–	–	–	–	60-80
Acylic (3M VHB) [41, 44]	(300,300)	$3.4^{(e)}$	7.2	61	158	$3.0^{(g)}$	412	4.8	90	< 0.005	0.18	80
Acylic (3M VHB) [41, 44]	(15, 15)	$0.022^{(e)}$	0.13	29	40	–	55	4.8	–	–	–	–
Acylic (3M VHB) [41, 44]	(540, 75)	$1.36^{(e)}$	2.4	68	215 (linear)	–	239	4.8	–	–	–	–
SEBS161 (5 - 30 wt.% copolymer) [168]	(300, 300)	0.141 - 0.151	–	62 - 22	180 - 30	0.007 - 0.163	32 - 133	1.8 - 2.2	92 - 53	–	–	–
SEBS161 (30 wt.% copolymer) [168]	Nominal	0.013	–	14	16.5	$1.3^{(h)}$	27	–	28	–	–	–

Continued on next page

Table 1.2 – *Continued from previous page*

Polymer (Specific Type)	Prestrain (%)	Energy Density (MJ/m^3)	Actuation Pressure (MPa)	Thickness Strain (-%)	Area Strain (%)	Young's Modulus (MPa)	Electric Field (V/μm)	Dielectric Constant	Dielectric Loss Factor	Mechanical Loss Factor	Coupling Efficiency k^2 (%)	Efficiency (%)
SEBS217 (5 - 30 wt.% copolymer) [169]	(300, 300)	0.119 - 0.139	–	71 - 31	245 - 47	0.002 - 0.133	22 - 98	1.8 - 2.2	88 - 40	–	–	–
SEBS217 (30 wt.% copolymer) [168]	Nominal	0.013	–	16	18.8	1.1	29	–	28	–	–	–
SEBS75 [168]	Nominal	0.0263 (@30 wt.%)	–	16 (@25 wt.%)	19 (@ 25 wt.%)	12 (@ 30 wt.%)	29 - 41	2.08-2.12	29	–	–	–
ACN Rubnber [170]	(60, 60)	0.084	0.3	20	–	4	50	14	–	–	–	–
IPN (VHB 4910-HDDA) [171, 172]	(0, 0)	–	–	70	233	2.5	300	–	–	–	–	–
IPN (VHB 4905-TMPTMA) [173]	(0, 0)	0.68	1.51	59.36	146	3.94	265.4	2.43	83.5	–	–	–
IPN (VHB 4910-TMPTMA) [173]	(0, 0)	3.5	5.06	74.97	300	4.15	418	3.27	93.7	–	–	–
BSEP (PTBA) [42]	(50, 50)	1.2	3.2	77	335	0.42 (@ 70 C)	260	5.4 (@ 70 C and 200 Hz)	–	0.8 (@ 70 C)	–	–

(a) Breakdown field unless otherwise stated. (b) At 1 kHz. (c) At 80 Hz unless otherwise stated. (d) At 80Hz. (e) Estimated via calculation.
(f) Calcualted Maxwell Pressure. (g) Effective Modulus. (h) Measured in compression

VHB 4905) appears to be the most promising in terms of strain performance, with strains in excess of 380% reported for highly prestrained films. [4] The theoretical energy density of this elastomer is an impressive $3.4MJ/m^3$ and coupling coefficients as well as efficiencies as high as 90% are possible.

Polyurethane films were pursued because of their larger force outputs and higher dielectric constant, allowing them to be actuated at lower electric fields. However, polyurethane films are limited in their ability to generate large strain.

Silicone elastomers have the advantage of lower viscoelasticity than acrylic films and can therefore be operated at higher frequencies with lower losses. Silicones show modest actuation strain when there is little to no prestrain and can be operated over a wide temperature range, making them more suitable to applications where temperatures are expected to vary significantly. They are also capable of strains in excess of 100% when prestrained but fall short of acrylics in this area. Silicones also possess a relatively low dielectric constant and thus require higher electric fields.

Carpi et al have reported on the actuation characteristics of another commercially available elastomer (Dr Scholls, Canada, Gelactiv tubing). [167] The material was capable of thickness strains of 1.8% at 27 MV/m with an actuation stress of 3.7 kPa at 24 MV/m.

It follows that many of the most exciting dielectric elastomer materials were discovered via exploratory testing. New formulations of commercially available elastomers are continually being developed and may well be worth exploring. However it is expected that research focusing on developing materials specifically for dielectric elastomer purposes from focused and directed research will provide the best candidates for improved performance in the years to come.

1.3.1 Effects of Prestrain

It has been found that prestrain can significantly improve the actuation performance of dielectric elastomer devices. [44,164] The observed improvements have been largely attributed to an increase in the breakdown strength, [159, 174, 175] which has been explained via a thermodynamic stability criterion. [160] Prestrain has the additional benefits of improving the mechanical efficiency [176] and response speed of most dielectric elastomers while causing a marginal decrease in the dielectric constant. [177] Prestrain can also be used to achieve preferential actuation in a certain direction by applying high prestrain in the direction perpendicular to the desired actuation direction and low prestrain along the actuation direction. [44]

The effects of prestrain on the actuation performance of dielectric elastomers have been widely studied from both a practical as well as theoretical perspective; [44,144,147,151,160, 164,174–184] however, the mechanism by which prestrain increases dielectric strength is still not completely understood. It is generally believed that premature DE failure is exacerbated by localized defects introduced during manufacture, processing, or through fatigue. The localized defects act to reduce the local breakdown strength in that area which can lead to localized or permanent device failure. Localized pull-in effects, viscoelastic behavior, and high leakage current can also reduce the usable electric field. It is likely that prestrain prevents pull-in effects. As shown in Figure 1.12 for a given material, a non-prestrained film will undergo a characteristic rapid increase in stress, then a plateau region, followed by a very steep rise in the stress until the film fails via the breaking of covalent bonds. The actuation stress/strain curve will follow the quadratic curve in the figure. For sufficiently high driving voltages, the reduction in film thickness and increase in electric field intensity form a positive feedback loop. The film will continue to be driven thinner and thinner until the local electric field exceeds the dielectric strength of the film, as indicated by the intersection of the quadratic curve and elastic stress curve. This induces the pull-in effect and possible eventual dielectric breakdown. If the film is prestrained, the origin of the actuation stress/strain curve will shift to O. The resulting actuation stress/strain curve will be less likely to intersect the elastic stress/strain curve; therefore the actuation will be more stable. Prestrain is very effective for acrylic films and is also effective in silicone and other elastomers. The effect varies from material to material.

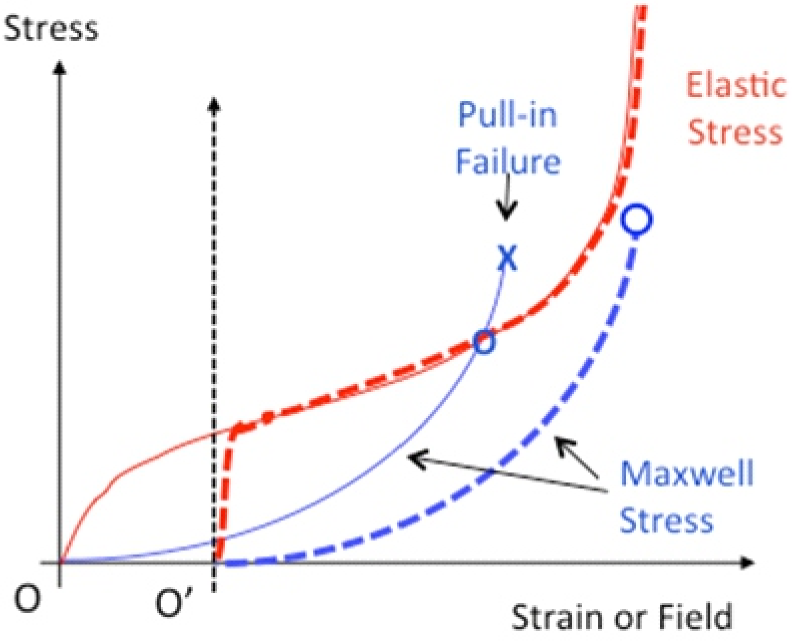

Figure 1.12: Characteristic stress of a dielectric elastomer film as a function of mechanical strain or electric field (constant voltage condition). The charts with origin at O are for a non-prestrained film and at O for the prestrained film. The cross (X) indicates dielectric breakdown and the bar () indicates stable actuation strain. Small o and large O represent the apparent breakdown field and actual breakdown strength, respectively.

Prestrain has the additional benefit of improving the frequency response of many elastomer films. The drop off in actuation strain with frequency is less pronounced for acrylic films that have been prestrained. The increased tension in the film increases the modulus and reduces the viscoelastic nature of the films.

Kofod used advanced materials models in an attempt to elucidate the effects that prestrain have on the actuation performance of a simple cuboid DE actuator. [185] The results are purely phenomenological; however, they indicate that in the special case of a purely isotropic amorphous material, prestrain does not affect the electromechanical coupling directly. The enhancement in actuation strain due to prestrain occurs through the alteration of the geometrical dimensions of the actuator. Kofod also determined that the presence of an optimum load is related to the plateau region in the forcestretch curve and that prestrain is not able to affect the location of this region.

The unfortunate drawback to prestraining films is that a rigid frame, or other structure, must be used to maintain the tension in the film. The added mass of the supporting structure increases the total mass of the DE device, which can significantly reduce the effective work density and power to mass ratio of the actuator. The prestrained films may also relax or fatigue over time. This reduces the shelf life of the DE devices.

1.3.2 Improved Silicone Films

A considerable amount of research has focused on reducing the operating voltages of DE actuators in order to increase their commercial viability and remove the dangers associated with high voltage. There are two basic methods of reducing the operating voltage: reducing the thickness of elastomer films so that the required field for high-performance actuation occurs at lower voltages; and increasing the dielectric constant of the elastomer films to reduce the required electric field intensity. Reducing of film thickness has the benefit of maintaining the dielectric breakdown strength and dielectric loss of the film but suffers from reduced output force and the increased importance of inhomogeneities that cause localized areas of high electric field and stress and result in premature breakdown. The output force can be scaled up through the use of multilayer actuators but doing so increases fabrication complexity.

A number of approaches have been explored for increasing the dielectric constant of elastomers for DEs. The most common approach involves the addition of high dielectric constant filler materials to an elastomer host. Silicone is of particular interest for this type of approach as it possesses good actuation properties to begin with, is readily available in gel form, and has a low dielectric constant. Results thus far do not appear particularly promising: increases in dielectric constant have been met with concomitant increases in dielectric loss and reductions in dielectric breakdown strength. [95, 186, 187] It has also been shown that the elastic modulus is affected by the addition of filler. [188]

Researchers have investigated the effects of adding various oxides including aluminum oxide, titanium oxide, and barium titanium oxide, [187–190] as well as various other fillers including organically modified montmorillonite (OMMT), [191] lead magnesium niobate-lead titanate (PMN-PT), [186, 189] copper-phthalocyanine oligomer (CPO), [189, 192] and PEDOT/PSS/EG. [193] Improvements appear limited at best as any meaningful increases in the dielectric constant are achieved at loadings near the percolation threshold and are met with increases in the leakage current. Research is still ongoing and some researchers believe that with some additional refinement real improvements can be achieved.

Carpi et al have recently developed silicone-based polymer blends that display enhanced electromechanical transduction properties. [190]] Their technique involves blending, rather than loading, the silicone elastomer with a highly polarizable conjugated polymer. They have reported very promising results for silicones loaded with very low percentages (1-6 wt.%) of poly(3-hexylthiophene) (PHT). The resulting blends yielded an increase in dielectric permittivity, with a relatively small increase in dielectric loss, and a reduction in tensile elastic modulus, which contribute synergistically to an improvement in electromechanical performance. The best performance was obtained for a blend with 1 wt.% PHT, achieving a transverse strain of 7.6% at a field of only 8 MV/m.

Chen et al. have developed an electrothermally actuated CNT-silicone composite. [194] They have been able to produce a maximal strain of 4.4% with an applied field of only 1.5 kV/m by incorporating a CNT network into the silicone elastomer. The mechanism of actuation differs strongly from that of conventional DEs. In these materials, the CNT loadings are such that conductivity through the specimen is possible. The flow of current through the CNT matrix causes joule heating, which raises the temperature of the silicone matrix, causing it to expand due to thermal effects.

Kussmaul et al. have established a novel method for enhancing the permittivity of DE actuators via molecular level modifications of the elastomer matrix. [195] They have grafted push-pull dipoles to the crosslinking molecules via a one-step process. The method effectively prevents agglomeration of the highly polarizable additive resulting in molecularly homogeneous films. The resulting films demonstrate a six-fold improvement in actuation sensitivity.

Researchers have also explored the use of conductive fillers encapsulated in an insulating polymer shell to overcome the issues of reduced breakdown fields and increased electrical losses. [196, 197] The silicone composites showed increases in permittivity, increased strain at break, and in some cases even an increase in the breakdown electric field. Proper tuning of the mechanical properties via crosslinking density optimization has to be performed to obtain significant improvement in actuation sensitivity [197].

1.3.3 Improved Acrylic Films

Conventional acrylic films, such as the VHB 4910 series of elastomers from 3M, possess excellent actuation strain, energy density, and coupling efficiency. However, in order to achieve these high performance values, the film must be prestrained. The addition of bulky support frames required to maintain the prestrain on the film significantly increases the mass of VHB acrylic based devices, reducing their effective energy densities to more pedestrian values. VHB acrylic films also suffer from viscoelastic effects, which limit their maximum response frequency to the 10 - 100 Hz range. The viscoelastic nature of these films also limits their overall efficiency and results in time dependent strain that can make their performance somewhat erratic.

Low molecular weight additives can increase the frequency response of VHB films. [198]

Representative results are shown in Figure 1.13. For the film without additives, the strain reduced to half its static value at 12 Hz; for the films with additives this frequency was pushed to over 100 Hz. These additives have the additional benefit of decreasing the glass transition temperature, thereby increasing the range over which the VHB films can be operated. When added in high concentrations, however, the additives reduce the mechanical stability of the films, making them easier to tear.

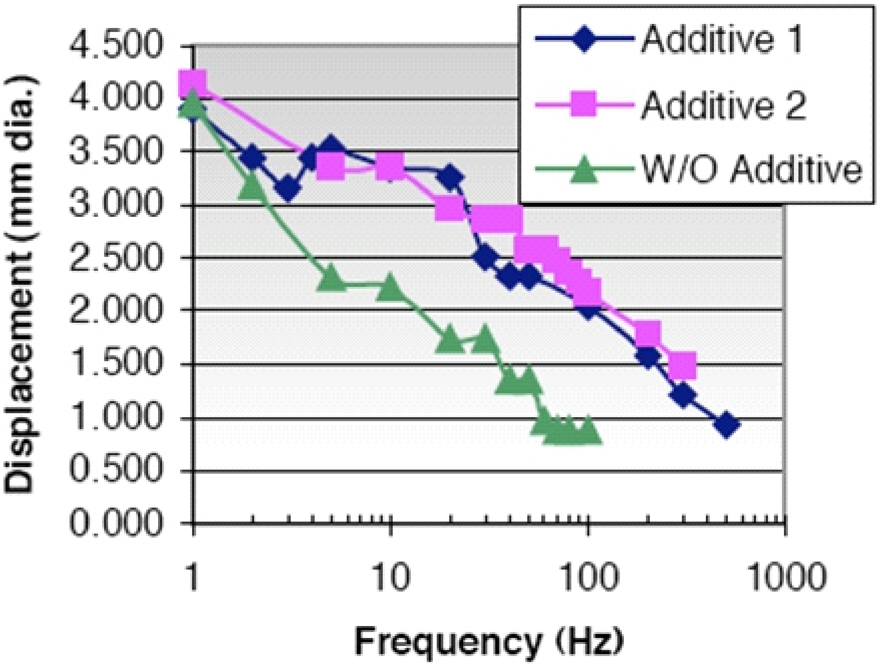

Figure 1.13: Improved frequency response of VHB acrylic elastomers via the addition of low molecular weight additives (plasticizers). [198] Proc SPIE 2004, reprinted with permission.

Interpenetrating polymer networks (IPNs) have been synthesized combining acrylic and silicone rubber materials. [199] These IPN films are synthesized by diffusing silicone chains into swollen acrylic rubber films in the presence of a co-solvent and then crosslinking the silicone chains. The resulting films display properties between those of acrylic and silicone films as expected. Such IPN films provide a simple and easy way to eliminate some of the disadvantages of acrylic films while maintaining high strain performance.

Much more promising results have been obtained in prestrain-locked VHB-based IPNs. [171–173, 200, 201] These IPNs are fabricated by first prestraining the VHB film to very high strains and spraying a multifunctional monomer onto the film along with an initiator, then allowing the monomer and initiator to diffuse into the film. The additive monomers are then polymerized and form a second network elastomer within the VHB elastomer host. Upon releasing the IPN film from its support, the additive network will resist the contraction of the VHB host, preventing it from returning to its unstrained state. The IPN film will thus remain in a state wherein the VHB film is locked in tension and the additive network is locked in compression. The process is outlined in Figure 1-14.

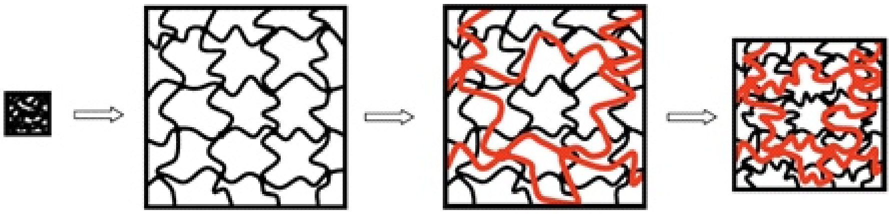

Figure 1.14: Fabrication steps for IPN elastomer films. The film is first prestrained, then an multifunctional monomer additive is sprayed onto the host film and polymerized forming an interpenetrating polymer network. Upon releasing the film it retains most of the applied prestrain, with the additive network being in compression and the host film in tension. [172]

The resulting films are capable of performance similar to prestrained VHB films without the need for a support frame. Ha et al. have reported results for IPNs incorporating bifunctional 1,6-hexandiol diacrylate (HDDA) [171, 200] and trifunctional trimethylolpropane trimethacrylate (TMPTMA) monomers. [172, 201] With no externally applied prestrain, these prestrain-locked IPN films have matched the performance of highly prestrained (300% by 300% biaxial prestrain) VHB4910 acrylic elastomers in terms of strain, electromechanical coupling factor, and energy density. [173] With no externally applied prestrain, the TMPTMA-based IPN films are capable of thickness strains as high as -75%, with an energy density of $3.5 MJ/m^3$, pressure of 5.1 MPa, and coupling efficiency of 94%, with a breakdown field of 420 MV/m. Figure 1.15 shows the actuation of VHB-based IPN films with HDDA and TMPTMA additives.

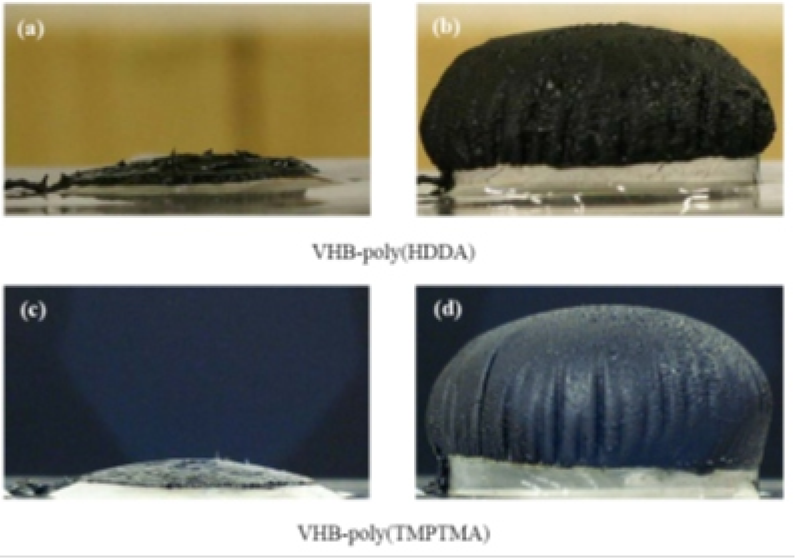

Figure 1.15: VHB-based IPN films before and after actuation for films with HDDA (a to b) and TMPTMA (c to d) additives in a diaphragm configuration with no externally applied prestrain. Only a small bias pressure was used in the diaphragm chamber as evidenced by the small bulge in the film prior to actuation.

IPN films have the added benefits of reducing viscoelasticity and enhancing mechanical stability as compared to regular VHB acrylic elastomers. [173] Reduced viscoelasticity has led to improvements in mechanical efficiency as seen in Figure 1.16. Further improvements have been made through the introduction of plasticizing agents. Zhang et al. have show that plasticizers can significantly improve the actuation temperature range, reducing the drop-off in performance at both high and low temperatures, and also improve the frequency response. [202]. The addition of the plasticizer has the additional benefit of reducing the modulus of the elastomer thereby reducing the required electric field for high strain actuation. These materials should open the door to a host of new actuator configurations and applications with minimal supporting structures and very high power-to-mass ratios.

1.3.4 Thermoplastic Block Copolymers

Thermoplastic block copolymeric elastomers are also of interest as dielectric elastomer materials. These polymers differ from conventional elastomers in that they possess physical crosslinks rather than chemical ones. In these polymers flexible elastic chain segments separate rigid segments. The rigid sections act as the binding points between chains, while the flexible segments allow for large deformations.

Recently, Shankar et al reported on nanostructured polystyrene-block-poly(ethylene-co-butylene)-block-polystyrene (SEBS) triblock copolymers swollen with a midblock sensitive oil. [168, 169] At relatively high oil concentrations, the thermoplastic elastomer behaves as a physical network where glassy styrene micelles serve as thermally reversible crosslinks. The glassy micelles are linked by rubbery ethylene-co-butylene midblocks swollen in the oil, giving the copolymer its elastomeric properties. Figure 1.17 shows a TEM image of a SEBS copolymer in midblock sensitive oligomeric oil with a concentration of 10 wt.% polymer; the inset is a depiction of the network linked by the glassy micelles. Actuation strains as high as 245% in area (71% thickness) were reported in highly prestrained actuators, exceeding the maximum reported values for silicone and rivaling those reported for VHB acrylic elastomers.

Attempts to increase the strain sensitivity of block copolymer has also been attempted through the addition of nanoparticle fillers. Stoyanove et al. [203] used neat and surface modified nanoparticles to enhance the permittivity of a block copolymer matrix. The dielectric properties were observed to increase, however, these increases were met with increases in the stiffness of the elastomer. Leakage current was also observed to increase with inceasing additive content. Surface modified nanoparticles showed larger improvements in overall performance due to improved guest-host interactions. The overall strain performance of the nanocomposite improved for loadings up to 15vol.% as the actuators retained the same level of performance while reducing the required electric field.

Because of the ability to tune the composition by varying the copolymer molecular weight

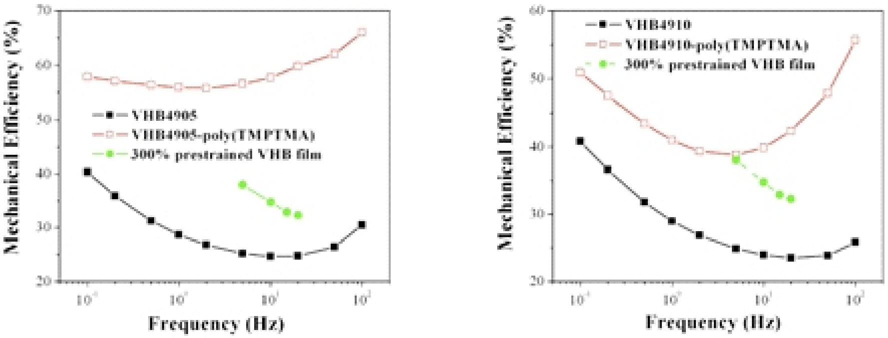

Figure 1.16: Improved mechanical efficiency for VHB-based IPN films over neat VHB films in both the highly prestrained and non-prestrained states. The improved efficiency over prestrained VHB acrylic elastomers is attributed to a reduction in viscoelasticity. [173]

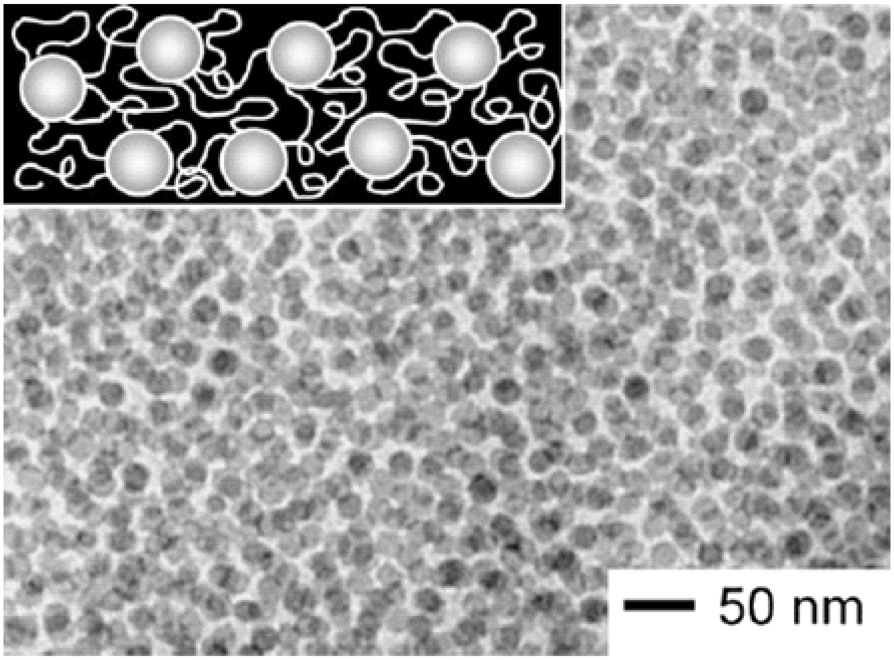

Figure 1.17: TEM image showing the presence of glassy micelles of a SEBS copolymer in midblock sensitive oil with a polymer loading of 10 wt.%. The inset is a depiction of the glassy micelle-stabilized polymer network. [25] Soft Matter 2007, reprinted with permission.

and the weight fraction of the polymer and oil, materials can be fabricated with tensile moduli ranging from 2 to 163 kPa with actuation strains being the highest for the low modulus variety and decreasing to 30% in area (22% thickness) at the high modulus range. Coupling efficiencies achieved were as high as 92% for low polymer loadings and lower molecular weight (161 kg/mol) and reduced to approximately 40% at high polymer loadings and higher molecular weight (217 kg/mol). A maximum energy density of $289kJ/m^3$ was achieved at intermediate polymer weight fractions for the higher molecular weight copolymer. A recent report showed that the materials are capable of blocking stresses as high as 442 kPa with a breakdown field of 203 MV/m at a polymer loading of 30 wt.%. [204] The material also exhibited low cyclic hysteresis. These nanostructured polymers also display favorable actuation characteristics in their non-prestrained state when compared with non-prestrained VHB acrylic elastomers. [25] Unfortunately it appears as though large strains require low polymer loadings, while high blocking stress and breakdown field are limited to higher polymer loadings. The issue is the requirement for a midblock sensitive oil to allow for easier chain movement in the ethylene-co-butylene midblocks. Without a high concentration of solvent, the chain mobility is reduced and strains are limited; however, as the concentration is increased, the breakdown field suffers and leakage current may increase, limiting the blocking pressure and reducing efficiency. Depending on the solvent used, there may also be leaching issues that can act to degrade the polymer over time.

Polyurethane (PU) also falls under the class of thermoplastic polymers. The electromechanical response of polyurethane is due to both Maxwell pressure and electrostriction. The Maxwell pressure has been found to have a significant contribution to the strain response of polyurethane films above the glass transition temperature. [165] While polyurethane films initially proved promising, they fell to the sidelines soon after due to the dramatic improvements in the actuation properties of silicone and acrylic films with prestrain. The majority of research since then has focused on polyurethane based composites. Cameron et al reported on their findings pertaining to graphite loaded polyurethane films. [205] They reported an increase in the actuation stress by a factor of over 500 and a relative permittivity beyond 4000 for graphite loadings near the percolation threshold. Unfortunately, such high loadings resulted in an increase in the dielectric loss factor by several orders of magnitude and an increase in modulus by a factor of 5. The result was a dramatic increase in the leakage current, power consumption, and a reduction in maximum actuation strain (due to the inability to reach high fields). Nam et al demonstrated the ability to tune the bulk permittivity and ionic conductivity of polyurethane-montmorillonite (MMT) nanocomposites by varying the gallery heights of the (MMT) nanoplatelets through the addition of different counter ions. [206] Resulting permittivity values were shown to vary from below that of pristine polyurethane for both low and high gallery heights, to above the value for intermediate gallery heights, indicative of an optimal gallery height for such composites.

Huang et al have demonstrated an all-organic, three-component polyurethane-based composite with a high electromechanical response. [207] By combining a high dielectric constant copper phthalocyanine oligomer (PolyCuPc) and conductive polyaniline (PANI) into a PU matrix, they have been able to achieve an electromechanical strain of 9.3% and elastic energy density of $0.4 J/cm^3$ under an electric field of only 20 MV/m. This approach overcomes issues associated with other percolative composites in which the loading of conductive filler must be near the percolation threshold in order to achieve meaningful increases in dielectric constant, which has a deleterious effect on the dielectric breakdown strength of the composite. In the composite, the PolyCuPc enhances the dielectric constant of the PU matrix; the two-component system also acts as the host for the conductive PANI that further enhances the dielectric response via a percolative phenomenon at much lower concentrations than in single component systems. Figure 1.18 shows the increase in thickness strain achieved in the three-component composite at different filler loadings.

Recent results have been reported on another polyurethane based composite film. [166, 208] A carbon nanopowder was added into a polyether-type thermoplastic (TPU5888 from Estane) at loadings up to 1.5 volume %. The maximum thickness strain of the composite

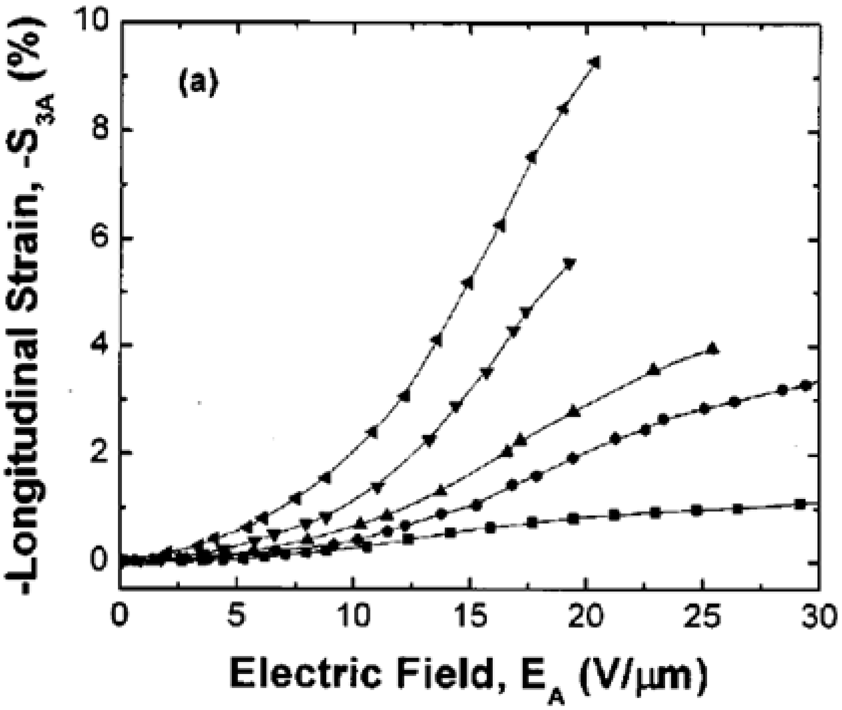

Figure 1.18: Thickness strain S3A as a function of the applied-field amplitude for composites of PANI/yPolyCuPc/PU (from lowest strain to highest strain): 0/0/100, 0/15/85, 4.6/15/85, 9.3/15/85, 14/15/85. [207] Appl Phys Lett 2004, reprinted with permission.

was 12% versus 8% in the pure polymer, with a maximum pressure of 0.14 MPa (unchanged), and a response speed in the ms time range under a driving field of 8 MV/m. The results may have been limited by the use of sputtered gold electrodes that can contribute to device stiffness and lose conductivity at moderate strains. The energy density of the composite was estimated using FEM simulations to be $4.3kJ/m^3$, a factor of approximately 1.7 increase over the pure polymer.

P(VDF-TrFE), a well-studied electrostrictive polymer, is also thermoplastic. By dispersing copper-phthalocyanine (CuPc), a high dielectric constant metallorganic compound, into a P(VDF-TrFE) matrix, the resulting composites maintained the flexibility of the matrix with a very high dielectric constant (425 at 1 Hz) and relatively low dielectric loss. [209] The dielectric constant was shown to vary with both electric field and frequency and was highest at high fields and low frequencies. The strain exhibited a quadratic dependence on electric field, as expected, and a thickness strain of -1.91% was achieved at a field of 13 MV/m with an elastic energy density as high as $0.13MJ/m^3$. The strain response of the material was attributed to a number of mechanisms, including Maxwell stress and electrostriction.

1.3.5 Other Engineered Elastomers

It is interesting to note that the elastomers that provide the best actuation characteristics (VHB acrylics and silicones) were not designed for use as dielectric elastomers. Their noteworthy performance is not the result of targeted materials developed, but rather a fortuitous coincidence. The development of new engineered dielectric elastomers has made slow progress; however, in recent years several new developments have been presented that indicate that research is moving toward improved materials with the targeted application of dielectric elastomer actuators for artificial muscle applications.

Jung et al have developed a synthetic elastomer composed of acrylonitrile butadiene rubber copolymer. [210, 211] The properties of the copolymer can be tuned by changing its composition. Reported data for dielectric constant, elastic modulus, and strain relaxation are promising (see Table 1.2). The synthetic elastomer provides some improvement over VHB and some silicone films under certain conditions; however, the tests were limited to low prestrain (60% radial), where the performance of VHB films is poor.

The same group has recently reported on the effects of a plasticizer (dioctyl phthalate (DOP)) and a high-K ceramic (TiO^2) on the actuating performance of their synthetic elastomer. [212] The addition of DOP showed the expected results of lower modulus, increased strain, and increased elastic energy density. The addition of TiO^2 had the effect of decreasing the modulus, increasing the dielectric constant, and increasing the strain and elastic energy density up to an optimal value, after which the values were seen to decrease. Maximum energy density of $1.2kJ/m^3$ was achieved for a synthetic elastomer with a DOP loading of 100 parts per hundred rubber (phr) with a radial strain of 1.62%. A maximum strain of 3.04% was reported for a DOP loading of 80 phr and a TiO^2 loading of 30 phr. The maximum dielectric constant achieved was 11.1 for DOP and TiO^2 loadings of 80 and 40 phr respectively, but strain and elastic energy density were limited to 1.7% and $0.5kJ/m^3$ respectively. The values, albeit lower than the peak performance of most conventional DE materials, were achieved at relatively low electric fields (20 MV/m or lower).

1.4 Compliant Electrode Materials

Identifying or developing a suitable compliant electrode is also a key factor in achieving good DE performance. A number of electrode materials have been explored. Original tests were performed using thin metal films. While these films provided good electrical conductivity, they limited strains to approximately 1%. Good compliant electrode materials should maintain high conductivity at large strains, have negligible stiffness, maintain good stability, and be fault tolerant. Common solutions include metallic paints (e.g. silver grease or paint), carbon grease, graphite, and carbon powder. Carbon grease electrodes are the most commonly used solution as they provide good conductivity even at very high strains, are cheap and easy to apply, and provide good adhesion to most DE materials while having minimal negative impacts on actuation performance. Dry graphite and carbon powder are also cheap, easy to apply, and have the additional benefit of being easy to handle. These dry electrode materials are better suited to multilayer devices where carbon grease electrodes result in slippage between adjacent layers which can eventually result in inhomogeneities in the electrode coverage; however, they tend to lose conductivity at high strains as the individual particles are pulled apart and lose contact. A comparative evaluation of some of the early electrode materials was performed by Carpi et al in 2003. [213]

Improved metal electrodes have been developed by Benslimane et al. [214] The electrodes are capable of achieving an anisotropic planar stain of 33% before losing electrical contact. The key to their design was patterning the surface of the elastomer itself prior to depositing a layer of silver. The films are able to expand in the corrugated direction, while expansion in the lateral direction is inhibited. Similarly, Lacour et al achieved 22% strain with gold electrodes by first applying a compressive stress to the elastomer film in order to create surface waves. [215]

Recent studies have been performed on alternative electrode materials. Nanosonic has developed low modulus, highly conducting thin film electrodes by molecular level self-assembly processing methods capable of maintaining conductivity up to strains of 100%. [216, 217] Recent developments have enabled the reduction of the modulus to less than 1 MPa and an increase in the strain to rupture to 1000%. [218] A version of the material is commercially available under the name Metal Rubber^{TM}. Delille et al have developed novel compliant electrodes based on a platinum salt reduction. [219] The platinum salt is dispersed into a host elastomer and immersed in a reducing agent. A maximum conductivity of 1 S/cm was observed and conductivity was maintained for strains up to 40%.

In order to fully exploit the scalability of DE actuators, it necessary to be able to pattern electrodes on the micro scale as well. Rosset el al have explored the use of ion implanted metal electrodes in PDMS. [220–223] Their results show that conductivity can be maintained for strains up to 175% and can remain conductive over 105 cycles at 30% strain. This is of particular importance for MEMS microfluidic devices where the DE micro-actuators could be used as micro-pumps. The ion-implanted films maintained high breakdown fields (¿ 100 MV/m) while the Youngs modulus increased by 50 to 200% depending on the dose.

Studies performed by Yuan et al. on conductive polyaniline (PANI) nanofibers, P3DOT, and CNT thin films show that all three are capable of forming highly compliant electrodes with fault tolerant behavior. [224] Nanowires and tubes are of particular interest since they are capable of maintaining a percolation network at large strains, thus reducing the required electrode thickness while still allowing for maximum strain performance.

Further investigations by Lam et al showed that PANI nanofibers films provided good actuation characteristics, provided fault tolerance, and had a negligible influence on the mechanical properties of the film but lost conductivity over time. [225] When tested on VHB 4905 films prestrained biaxially by 300 x 300%, the electrodes provided an maximum area strain of 97% at 3 kV and demonstrated self-clearing with a preserved strain of 91% after the first clearing event.

More recent results on CNTs were much more promising. [226, 227] Two types of CNT thin films were tested: functionalized P3-single walled nanotubes (SWNTs) and raw (non-functionalized) SWNTs. Both films provided excellent actuation characteristics (on par with carbon grease), had a negligible influence on mechanical properties of the film, and remained stable over longer periods of time. In addition, the carbon nanotube films could be made thin enough to remain optically transparent for use as transparent compliant electrodes. [228]

The ultrathin PANI and CNT thin films are capable of ”self-clearing”, a process wherein the electrode material is burnt off locally in the event of an electrical short through the dielectric film. [224–227] Dielectric failure is one of the leading causes for premature device failure of DEs and results in terminal failure in carbon grease, graphite, and carbon powder electroded devices. The fault tolerance of devices with CNT electrodes is demonstrated in Figure 1.19; in the tests a prestrained circular VHB acrylic actuator was punctured with a cactus pin and maintained very high actuation strains. In separate tests, the actuators were driven at a high field until the occurrence of a localized breakdown, the actuators "self-cleared" and recovered well from the local failures and retained high actuation strains. An SEM image of a "self-cleared" region is shown in Figure 1.20. The image shows that the CNTs in the region surrounding the short have been burnt off. The addition of self-clearing introduces fault tolerance to DEs and can dramatically increase device lifetime. Results for CNT-based electrodes have demonstrated increases in constant actuation lifetime over carbon grease electrode based devices by two orders of magnitude; and demonstrated the ability to withstand and recover from several localized dielectric breakdown events.

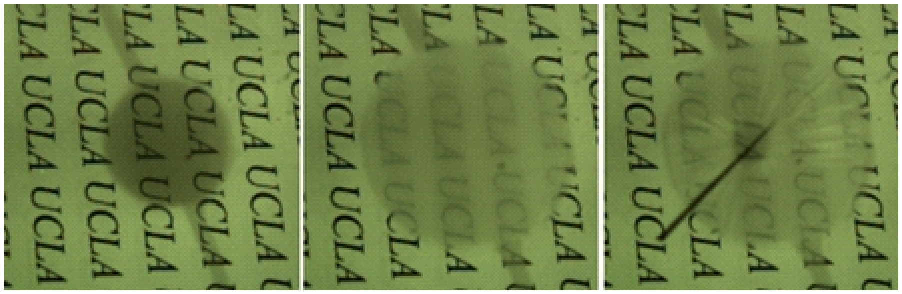

Figure 1.19: Fault-tolerance of CNT electrodes. DEAs with CNT electrodes are able to withstand puncture and maintain a high level of strain due to self-clearing of CNT around puncture. From left to right: prestrained VHB acrylic actuator with CNT electrodes; actuated; actuated with a cactus pin through the active area.

Further increases in operational lifetime have been achieved through the addition of a thin layer of dielectric oil over the CNT electrodes. [229] Due to the high field amplification at the CNT tips, corona discharging through the air is an issue. In P3-SWNT films, this results in a slow degradation of the electrode conductivity resulting in lower actuation strains over time. Raw-SWNT films suffer from unabated breakdown-clearing events, which persist until the film loses mechanical stability and fails. The dielectric oil fills in the gaps between adjacent nanotube tips and flows into the voids left behind after the clearing events, turning the corona discharging process into silent discharge. This results in fewer breakdown-clearing events and can prolong constant actuation life at high strains by over an order of magnitude.

Figure 1.20: Cleared area on a CNT electrode. Localized dielectric breakdown results in an electrical short through the film. Corona discharging burns away the CNTs in the area surrounding the short, isolating it from the rest of the electrode and allowing the device to continue operating.

With the improved fault tolerance and lifetime afforded by compliant carbon nanotube electrodes with dielectric oil, DE artificial muscle devices that are capable of providing high performance actuation reliably over an extended number of cycles should be possible and should push DE actuators and artificial muscles closer to commercialization.

1.5 DE Actuator Configurations

Because DEs are fabricated from conformable elastomers, they can be shaped into many actuator configurations over a wide range of dimensions. Most actuator designs use the area expansion of the DE film for actuation; however, multilayer stacked actuators exist wherein actuation is through a reduction in thickness. Typical designs incorporate support structures to maintain prestrain in the films, though materials and processing advances have allowed for frameless designs as well. The majority of the actuator configurations in use today were developed by SRI in the late 1990s and early 2000s. [156, 163, 230, 231] These include rolled (spring and core free), tube, unimorph, bimorph, stretched-frame, diaphragm, bowtie, spider, and extender. Carpi et al provide a detailed account of dielectric elastomer technology with an emphasis on actuator configurations and applications. [232]

A number of other actuator configurations have been developed, including a bidirectional framed actuator, [233] a multiple-degree-of-freedom double diaphragm-type actuator, [234] a tube-spring actuator (TSA), [235] a reinforced cylindrical actuator, [236] an active shell-based actuator, [237] a cone actuator, [238] a compound structure frame actuator, [239], an inflated bending actuator, [240] and thickness mode actuators that can be used in programmable deformable surfaces. [241] Additional efforts have been put into characterizing and modeling the performance of different actuator configurations. [242]

Yet another interesting DE actuator configuration, dubbed DEMES, which stands for Dielectric Elastomer Minimum Energy Structure, has been introduced by Kofod et al. [243, 244] and further developed by O'Brien et al. [245] This type of actuator relies on a thin bendable frame. The frames are designed such that, when a prestrained DE layer is fixed to the frame, the forces exerted by the prestrained DE layer will cause the frame to curl until the forces balance; the result is that the device is curved in the equilibrium rest state. Upon actuation the DE layer will relax causing the actuator to uncurl until it reaches the equilibrium actuated state, which will vary with the applied field.

Plante et al proposed using bistable binary actuator systems. [246] These actuators are capable of transitioning between two stable rest states and thus do need to be actuated continuously for extended periods of time, which can dramatically improve overall lifetime.

Artificial Muscle Incorporated (AMI) has developed a Universal Muscle Actuator (UMA) that has been proposed for use as an auto-focusing lens for camera phones. [247] This design relies on coupled prestrained circular framed actuators linked antagonistically and mechanically biased; they are spaced apart around the outer edge and connected at the center. Actuation of one of the films allows the other to relax, resulting in out-of-plane linear displacements.

From the perspective of artificial muscle design, the two most interesting device designs are the spring roll and stacked actuator. Both of them are able to effectively couple the deformations of DEs to provide linear actuation. Spring rolls are interesting from the perspective that they are capable of providing a combination of large linear strains (∼30% of the active area) with relatively large output forces (∼21 N for a cylindrical device measuring 65 mm in length and 12 mm in diameter). [179,248] The main drawback of spring roll actuators is that their design requires several passive or semi-active components such as a compression spring and end caps. A spring roll actuator can be seen in Figure 1.21 along with a schematic of the components. A DE/electrode/DE/electrode layered film strip is rolled around a spring compressed between two end caps. When released, the spring acts to maintain the prestrain in the film and prevent buckling. Reliability is an issue as the spring and end caps may generate areas of localized high stress that may result in premature failure.

Spring rolls capable of both bending and elongation have been reported by Pei et al.

[198, 249, 250] Bending is achieved by patterning the electrodes; for two and three degree-of-freedom actuators, two and three electrically isolated electrode pairs are required respectively. By actuating one electrode pair, only a portion of the actuator will elongate, causing the actuator to bend. These actuators are capable of bending angles as high as 90 degrees with lateral forces higher than 1.5 N for cylindrical devices measuring 9 cm in length and 2.3 cm in diameter. The ability to both bend and elongate opens up a number of new possibilities for multiple-degree-of-freedom spring rolls. These will be explored in the next section.

Stacked and folded configurations consist of tens to thousands of DE films stacked together and utilize the reduction in thickness rather than the area expansion of the DE film as the means of actuation. Employing a large number of layers amplifies the displacements. Several configurations have been proposed and tested. [190, 251–255] The simplest device consists of laminated layers of DEs sandwiching compliant electrodes. Several silicone-based actuators have been developed and have demonstrated linear strains in excess of 15%.

To reduce manufacturing difficulties and the likelihood of electrical shorts that may result from the presence of disjointed electrodes, a helical design was proposed where only two continuous electrodes were required. [190,252] The actuator was capable of a -5% compressive strain at a field of only 14 MV/m using a softened silicone. A third configuration has also been proposed wherein a single long strip of DE film with electrodes on either side is simply folded in such a way as to keep the opposing electrodes isolated. [253, 254, 256] This configuration is perhaps the easiest to fabricate and yielded compressive strains and stresses up to 15% and 6 kPa respectively, but may result in non-uniform displacements. The three stacked actuator configurations are shown in Figure 1.22.

Another method to reduce manufacturing difficulties was developed by Schlaak et al. [257,258] They implemented a process wherein the components of a thermally cured silicone elastomer were spin-coated and thermally cured while the electrodes were spray coated using a contact mask.

Recent efforts by Arora et al have led to the development of DE based fiber actua-

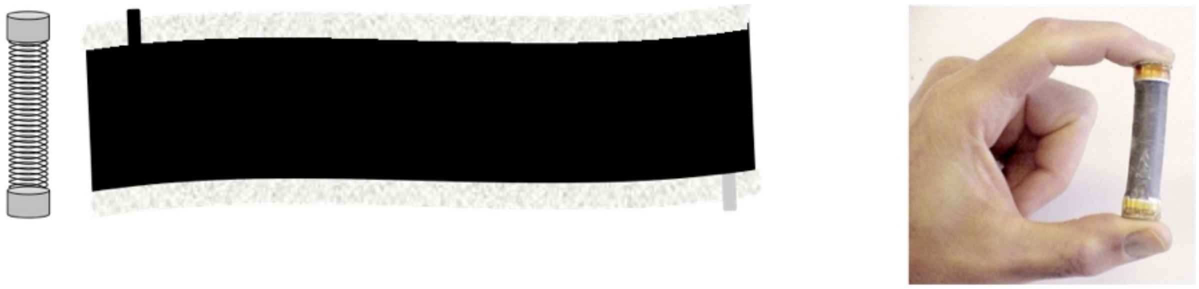

Figure 1.21: Spring roll DEA. Rolls are fabricated by compressing a spring between two end caps and rolling a DE/electrode/DE/electrode layered strip around it. Increasing the number of layers wrapped around the spring core increases the output force. [249] Proc SPIE 2003, reprinted with permission.

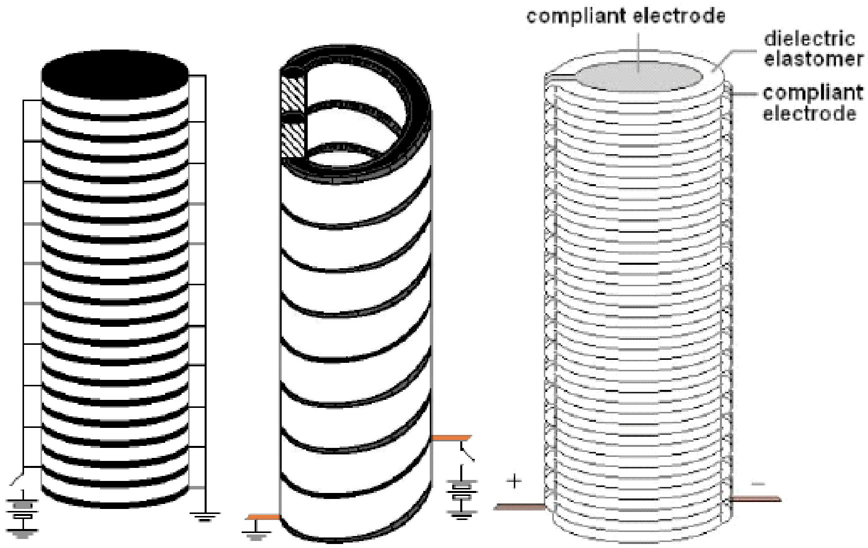

Figure 1.22: Stacked linear contractile actuator configurations. From left to right: Stacked device wherein alternating layers of elastomer and electrode are stacked together; helical device where two complementary helical elastomer strips and electrodes are interlocked; folded device where a single strip of elastomer with electrodes on the top and bottom is folded upon itself. [256] Proc SPIE 2007, reprinted with permission.

tors. [259] These actuators are essentially miniaturized tube actuators. In their work, prestrain was applied by both uniaxial elongation as well as inflation. These actuators may be of interest for artificial muscle applications since they mimic the fibular nature of natural muscle; however, unlike natural muscle, their method of actuation is through elongation and the maximum strains reported were limited to 7% in the axial direction. Cameron et al have performed similar work on co-extruded tube DE actuators. [260] Their co-extrusion process presents a fast, easy, scalable method to produce small diameter tubes, or hollow fibers, for use as DE actuators that would make these actuators very amenable to mass manufacturing. Strains, thus far, are limited to approximately 2%. Kofod et al. have also explored the fabrication of fiber-like actuators. [261] Their process involves a simple dip-coating technique whereby alternating layers of dielectric and conductive material are deposited. Actuators fabricated using this method are capable of strains up to 8%.

The use of IPN films, described in the Dielectric Elastomer Materials section, has enabled higher energy density actuators. VHB-based IPN films seem particularly suited to the stacked actuator configuration as they do not require pre-straining. Kovacs and During have recently reported on the fabrication of such an actuator. [262] They constructed two prototypes: one consisting of 280 layers with an active diameter of 16 mm, a total diameter of 18 mm, and a height of 18.3 mm; the second consisting of 330 layers, an active diameter of 16 mm, a total diameter of 20 mm, and a height of 21.2 mm. The actuators achieved 46% and 35% contractile strain respectively with both ends free, and 30% and 20% respectively with their ends fixed to rigid supports. The reduced strain performance for devices with fixed ends was attributed to the physical constraints imposed by the rigid end pieces. The results were obtained at voltages just above 4 kV. Maximum forces achieved were in excess of 30 N. IPN films have also been incorporated in core free rolled actuators. [263] Since the film is free standing, no spring core is needed to maintain prestrain in the film. As a result, the shelf and actuation lifetime, as well as the specific volume energy density of the device, have been improved.

1.6 DE Actuator Applications

When placed in an antagonistic arrangement, linear DE actuators have demonstrated the ability to mimic the motion of natural muscle. We are still some way off reliable reproduction of natural muscles performance; however, these preliminary results show a great deal of promise. When coupled with new advances in artificial skin and other related technologies that may reduce the performance requirements for artificial muscles, advances in DE actuators may allow for commercial applications sooner than would otherwise be anticipated. [264]

Perhaps the best example of both the promise that DE actuators and other EAP technologies show, and hurdles they must overcome, was the 2005 EAP arm wrestling competition organized by Bar-Cohen. Kovacs et al reported on the construction of one such robot as seen in Figure 1.23. [265]

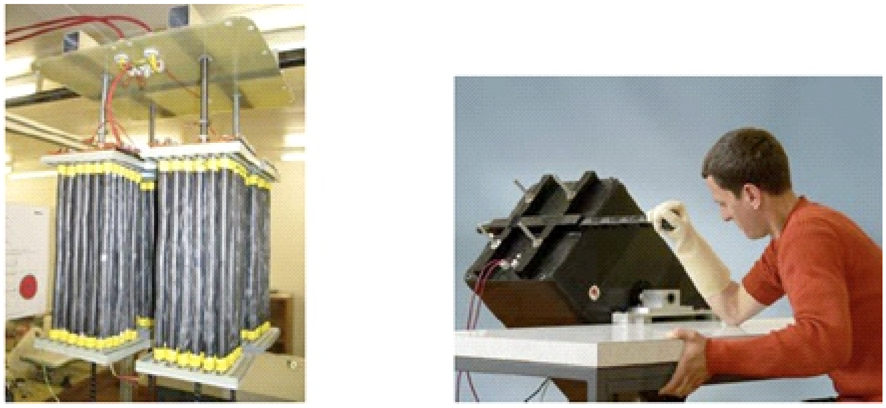

Figure 1.23: Arm wrestling robot using dielectric elastomer spring roll actuators. Left: actuator assemblies used in the device. Right: demonstration of the arm wrestling robot. [265] Smart Mater Struct 2007, reprinted with permission.

Other artificial muscle applications have been demonstrated as well. Carpi et al used helical contractile linear actuators and buckling actuators to actuate eyeballs for use in an android face. [255,266,267] Another eyeball actuator has been developed by Liu et al based on their inflated actuator design; their actuator is capable of generating eyeball rotations from -50 to 50. [240] Kornbluh et al have also reported on a mouth driven by a DE actuator. [4]

Biddiss and Chau have provided a good review on the challenges and opportunities of DE actuators for upper limb prosthetics. [268]

DE actuators have been used in a number of biomimetic robots ranging from simple hopping robots [269] and inchworm robots [4, 233, 270–272] to more complex walking robots, flapping-wing robots, and serpentine or octopus arm-inspired actuators. [4, 238, 239, 272–274] Two particularly interesting walking robots developed by SRI, dubbed Flex II and MERbot, can be seen in Figure 1.24. Utilizing spring roll actuators, Flex II was capable of a respectable 3.5 cm/s. [272] MERbot used multiple-degree-of-freedom spring rolls to achieve speeds in excess of 13 cm/s. [250]

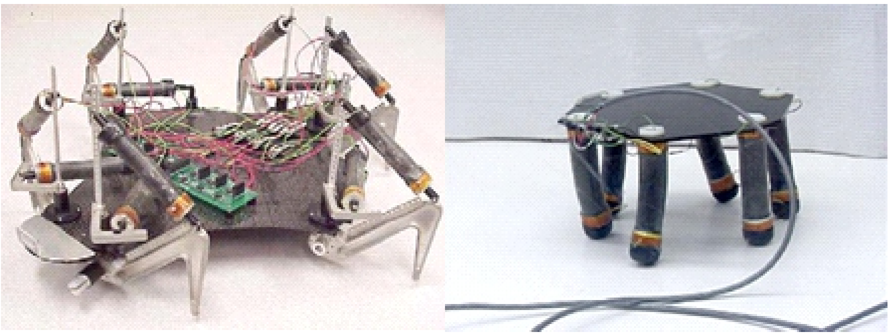

Figure 1.24: FLEX II and MERbot walking robots. FLEX II uses two dielectric elastomer spring roll actuators per leg while MERbot uses multiple-degree-of-freedom spring roll actuators. [250, 272]

Potential applications of DE actuators are by no means limited to artificial muscles. A plethora of other DE applications have been proposed and demonstrated that can potentially be used in humanoid devices. These include loudspeakers, [275–277] variable diffraction gratings, [276] tunable transmission gratings, [278] and micro-optical zoom lenses, [279] among others. These applications may find use in biomimetics as a method to bestow polymer robots with the abilities to speak and to focus their vision.

Outside of biomimetics, dielectric elastomers may still be of use in other human-related applications including refreshable Braille devices, [257, 280–282] hand rehabilitation splints, [283] MRI compatible machines, [150, 284–286] micro-fluidic devices, [287, 288] force feedback,

[248] and wearable tactile interfaces. [282,289] Other potential applications include actuators for lighter-than-air vehicles, [290,291] tunable phononic crystals, [292–294] and variable phase retarders. [295] Beck et al have also developed a sub-100 nm resolution total internal reflection fluorescence microscope using a tunable transmission grating and transparent phase shifters actuated by electroactive polymers. [296]

Lastly, the first DE product to actually make it to market is a force feedback device that can be attached to an iPod touch. [297] The device was developed by Artificial Muscle Incorporated, a division of Bayer Materials Science, and is capable of replicated various force feedback sensations in a way that conventional ”rumble packs” are unable to. The device has been released by Mophie under the name Mophie Pulse Game Enhancing Case.

1.7 Overview of this Part of the Dissertation

In this part of the dissertation we focus on improving the state of the art for dielectric elastomer actuators. Despite their excellent performance at room temperature and the advances in acrylic elastomer outlined above, it appears as though they are losing favor in the dielectric elastomer community. This can likely be attributed to two main factors: (1) their performance varies strongly with temperature, and (2) their viscoelasticity limits operation to a few Hz. The focus has instead turned to the use of silicones. Though their performance numbers are lower than those of the best acrylic elastomers, they are still capable of strains in excess of 100%, their performance does not generally degrade over the expected operating temperature range of most devices (-40 to 60 °C), and they can be operated at much higher frequencies.

As described above, a great deal of research has been poured into improving silicone dielectric elastomer materials with the primary goal of increasing the permittivity to bring down the required electric field for high performance actuation. Here we take a slightly different approach.

In Chapter 2 we explore the use of very soft silicone materials for high performance, long lifetime actuation. We choose a soft silicone as our base material and cast thin films to maintain a low driving voltage, with a goal of keeping it below 2000 V. We characterize the mechanical and electroactive properties of the material to determine the optimal operating conditions with respect to crosslink density, applied prestrain, and mechanical load. To improve the lifetime of the actuators we introduce self-clearing carbon nanotube electrodes to improve device lifetime. The result is that we are able to produce soft silicone free-standing linear actuators capable of actuation strains up to 120% and repeat actuation at approximately 20% strain for over 80,000 cycles.

In Chapter 3 we follow the lead of other researchers in the field by introducing nanoparticle fillers to the soft silicone elastomer. Our goal, however, is slightly different. Given the softness of the silicone we chose, the elastic energy density, and thus the work density, of the material is rather low. In order to improve this, we introduce PDMS coated TiO_2 nanoparticles to the silicone. The nanoparticles act to both increase the permittivity and the stiffness of the material. The additive effects of these increases means that the work density can be increased while the actuation performance at low voltages can be maintained.

In Chapter 4 we develop a method for preparing all-silicone prestrain locked interpenetrating polymer network elastomers (S-IPN). We choose a soft silicone host that cures at room temperature and a much stiffer silicone additive that cures at high temperature and co-dissolve them in a common solvent. By casting films and allowing the soft silicone to cure, then prestraining the film and curing the rigid component at high temperature, we are able to create free-stranding prestrain locked films. We measure the mechanical properties and actuation capabilities of the free-standing films and show a more than two-fold improvement in actuation strain over the pure soft silicone material.

In Chapter 5 we also demonstrate that the S-IPN preparation procedure can be used to improve the bonding force between the silicone and single walled carbon nanotube electrodes. Additionally, the technique can be leveraged to improve the interlayer bonding force between adjacent layers in a multilayer actuator, even in the presence of prestrain. We show that highly prestrained freestanding linear multilayer actuators fabricated using this technique are capable of over 30,000 actuation cycles at >20% strain and over 5,000 cycles at > 40% strain. Lifetime degradation issues are also explored; we observe a gradual lengthening of the actuator's active area with a time scale on the order of a few hours that can be attributed to viscoelastic creep and a gradual decrease in the peak strain that dominates at longer time scales that is attributed to a gradual increase in the resistance of the electrodes. We tackle the latter issue by using quasi-buckled electrodes made by applying excess prestrain in the actuation direction prior to applying the electrodes so that during actuation the electrode is never strained past its as-deposited state.

In Chapter 6 we summarize the work presented in this part of the dissertation and explore future work that can be done in the field. We believe a strong focus should be made on understanding the long-term degradation of dielectric elastomer actuators when operated under high performance conditions.

CHAPTER 2

Soft Silicone Actuators for High Performance Long Lifetime Actuation

Due to their ability to operate well over bread temperature and frequency ranges and generate actuation strains in excess of 100%, silicones have been gathering more and more interest as the field of dielectric elastomers pushes toward commercialization. In this chapter, the effects of mechanical properties, tuned via crosslink density and prestrain, on the actuation performance of a soft silicone elastomer are explored. The information is used to fabricate large strain linear actuators. Single walled carbon nanotubes are used to impart fault-tolerance to the actuators in order to improve device lifetime.

2.1 Materials and sample preparation

Wacker Silpuran 6000/10 is a high temperature vulcanizing (HTV) two part platinum catalyzed PDMS. Thin films for electromechanical characterization were prepared first by dissolving the PDMS in an isoparafinic solvent (ExxonMobil Chemical Isopar G), followed by drop-casting onto a glass substrate. After evaporation of the solvent, the films were cured at 160 °C to form the elastic network. Single wall carbon nanotubes (SWNTs) dispersed in chloroform (0.3 mg/ml) or dispersions of SWNTs functionalized with carboxylic acid (P3-SWCNTs, Carbon Solution, Inc.) in a combination of 80% isopropyl alcohol and 20% deionized water (0.5 mg/ml) were used to pattern the electrodes by spraying (Pasche airbrush, 20 PSI) through a contact mask. The SWNT dispersions were prepared by sonication for 3 hours in a 400W bath sonicator.

2.2 Mechanical characterization

The mechanical properties were characterized using a TA Instruments RSA3 dynamic mechanical analysis machine (DMA). Tensile test samples were prepared with a planar dog-bone shape with a gauge length of 12 mm and width of 2mm. Tensile tests were performed at a strain rate of 3.33 mm/s. Dynamic mechanical properties were characterized for samples in a pure shear actuator configuration under a dynamic load in the frequency range of 0.1 to 20 Hz at a strain of 1%, thus providing results that can be directly correlated to device performance.

2.3 Electromechanical characterization

Freestanding linear actuators were fabricated as follows: the silicone films were pre-strained by different stretches and attached to stiff frames in order to preserve the pre-stretch and to define a freestanding area with a width of 10 mm in the actuation direction and 60 mm in the width direction (schematically shown in Fig. 2.3(b) inset). To enable electric connection, adhesive aluminum strips were attached to both sides to the stiff frames. The linear actuation strain in constant force mode was measured by suspending a load from the bottom of the devices and applying a voltage ramp (Trek 10/10B-HS high voltage amplifier) at a rate of 20 V/s and monitoring the elongation of the active region using digital video and Labview software. Current-limiting resistor of 50 MΩ was connected in series, to protect the film from rupture in case of high current. Cycling actuation tests were performed on the same setup using a sine wave voltage signal at a frequency of 0.5 and 2 Hz.

Blocking force measurements were performed by loading the linear actuators in a DMA. The samples were preloaded to maintain the initial pre-stretch and allowed to stress relax for several hours prior to testing. A high voltage power supply built in-house was used to apply high voltage across the film from 0 V to failure using a 200 V step. The device was maintained under isostrain conditions and the blocking force was monitored using the DMA's load cell.

2.4 Results and discussion

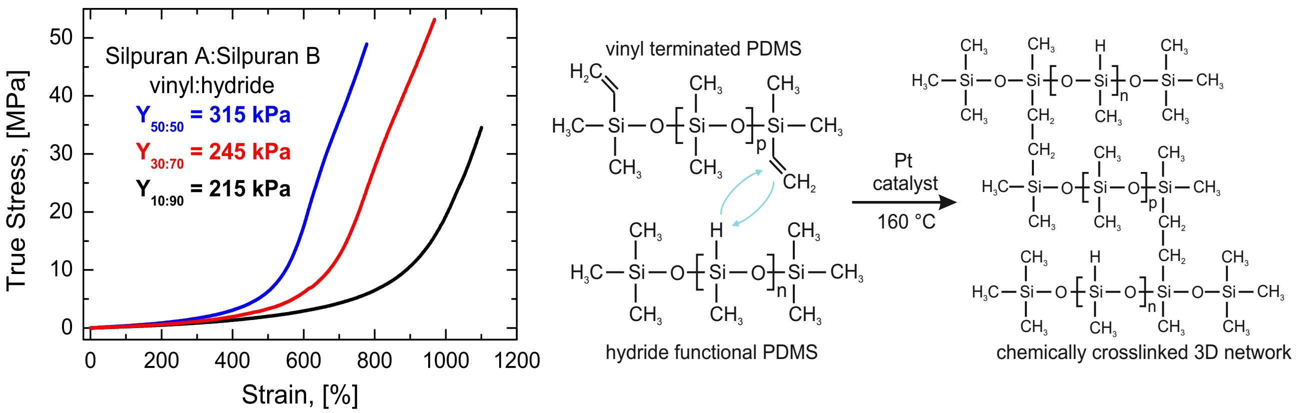

Figure 2.1: True stress-strain curves for different vinyl:hydride ratios and schematic representation of the elastic network crosslinking chemistry.

As shown in Ref. [185], prestrain plays a remarkable role in the nonlinear hyper-viscoelastic processes in dielectric elastomers. Through the application of prestrain, the stress-strain response of a dielectric elastomer material can be altered to prevent issues related to wrinkling and pull-in instabilities, [298] drastically changing the apparent breakdown strength of the materials and allowing for substantial improvements in peak performance. Through the appropriate choice of prestrain, the stress-strain response of the material can be made anisotropic, leading to large linear actuation strains in the direction of low prestrain. [44] Based on these observations, we feel it is safe to conclude that the performance of a dielectric elastomer actuator is primarily defined by its stress-strain response. Clearly, other factors play a large role, such as the bulk resistivity of the material and its inherent breakdown strength; however, these parameters are difficult to control beyond the basic choice of material components. The stress-strain response, on the other hand, can be influence by prestrain, crosslink density, and additive content, among other things.

In this work we consider a soft PDMS material: Wacker Silpuran 6000/10, a two part platinum catalyzed high temperature vulcanizing (HTV) liquid silicone rubber. The crosslinking chemistry is the hydrosilylation reaction between vinyl terminated PDMS and hydride functional PDMS on the Pt catalyst activated at 160 °C (Fig. 2.1). We begin our study by first testing the effects of crosslink density on the system. In order to vary the crosslink density, the two parts of the PDMS, one part vinyl-terminated and the other part hydride-functional, were mixed in unequal amounts. By altering the relative amounts of the two parts the crosslink density of the material can be reduced and the material can be made significantly softer. Fig. 2.1 shows the true stress-strain curves and the calculated Young's modulus (inset) of the different formulations. The materials display the non-linear hyper-elastic response typical of elastomers. Reducing the crosslinking density leads to significant softening from 315 kPa for the 50:50 vinyl:hydride ratio to 215 kPa for the 10:90 ratio and increase in maximum elongation (1100% for 10:90 ratio). Dynamic mechanical measurements (not shown) reveal that reducing the crosslinking density does not cause increase of the viscoelastic losses ($\tan \delta = 0.15$ at 1 Hz). All three formulations exhibit large elongation followed by steep stiffening when approaching the limiting stretch.

Although the stress-strain curves are monotonic under uniaxially applied forces, they might not be under deformation due to applied voltage which generally leads to pull-in. [299, 300] As shown in Ref. [299] the voltage induced stretch response is related to the stress-stretch curve ($\sigma(\lambda)$) as $\Phi = H\lambda^{-2}\sqrt{\sigma(\lambda)/\varepsilon}$, where H is the thickness, ε is the permittivity of the elastomer. Fig. 2.2 shows the voltage-stretch curves plotted by substituting the stress-strain data in the equation above and using the experimental values of $H = 40$ μm and $\varepsilon = 2.47 * 10^{-11}$ F/m. As voltage is increased, the silicone elastomer responds by increasing in stretch. Due to the large limiting stretch and relatively low increase of $\sigma(\lambda)$ at low to moderate strains the rate of decrease in λ^{-2} dominates; this leads to a voltage peak and a sudden drop at around 20% strain. A peak in the $\Phi - \lambda$ curve indicates the onset of pull in due to EMI caused by a positive feedback between a thinning of the silicone elastomer and a continuously increasing electric field [300]. As a result the maximum actuation strain would be significantly reduced when compared to the value that would be expected at the intrinsic electric breakdown strength of the material. In Fig. 2.2, $\Phi_b(\lambda) = E_b H/\lambda^2$ is plotted using an intrinsic breakdown value of 150 V/μm. As seen, actuation strain of around 130% is expected if EMI is eliminated. As recently demonstrated, [298,301] for free-standing linear actuators where horizontal pre-stretch is applied and the device is actuated in the short vertical direction the EMI is completely absent and the voltage-stretch curves are monotonic. This can be achieved by clamping the membrane between rigid clamps [298] or by constraining the horizontal deformation by using stiff fibers. [301]

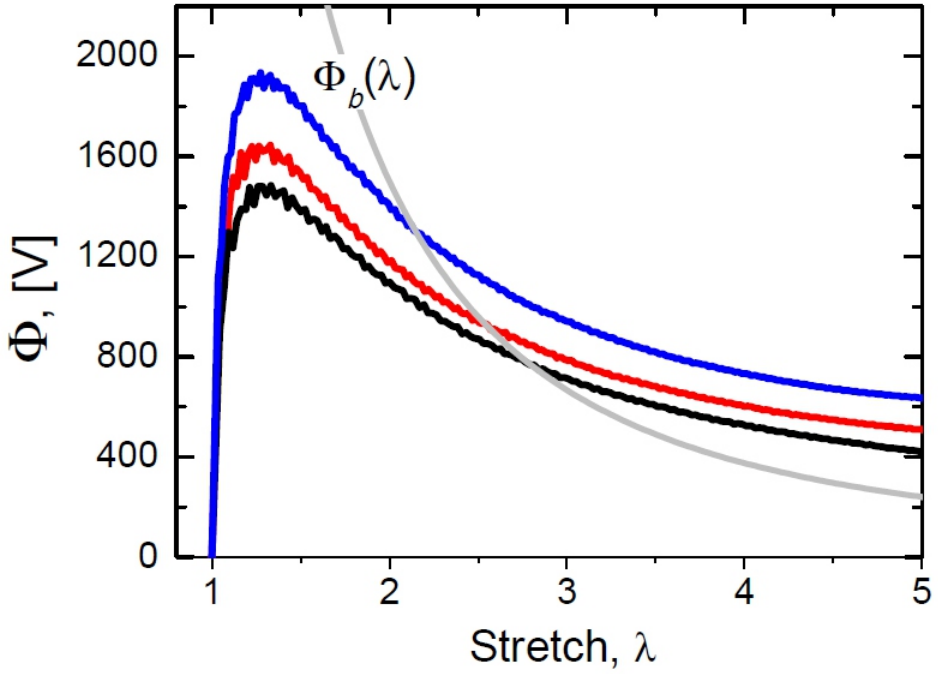

Figure 2.2: Voltage-stretch curves for the different formulations according to Eq.1 in Ref. [299].

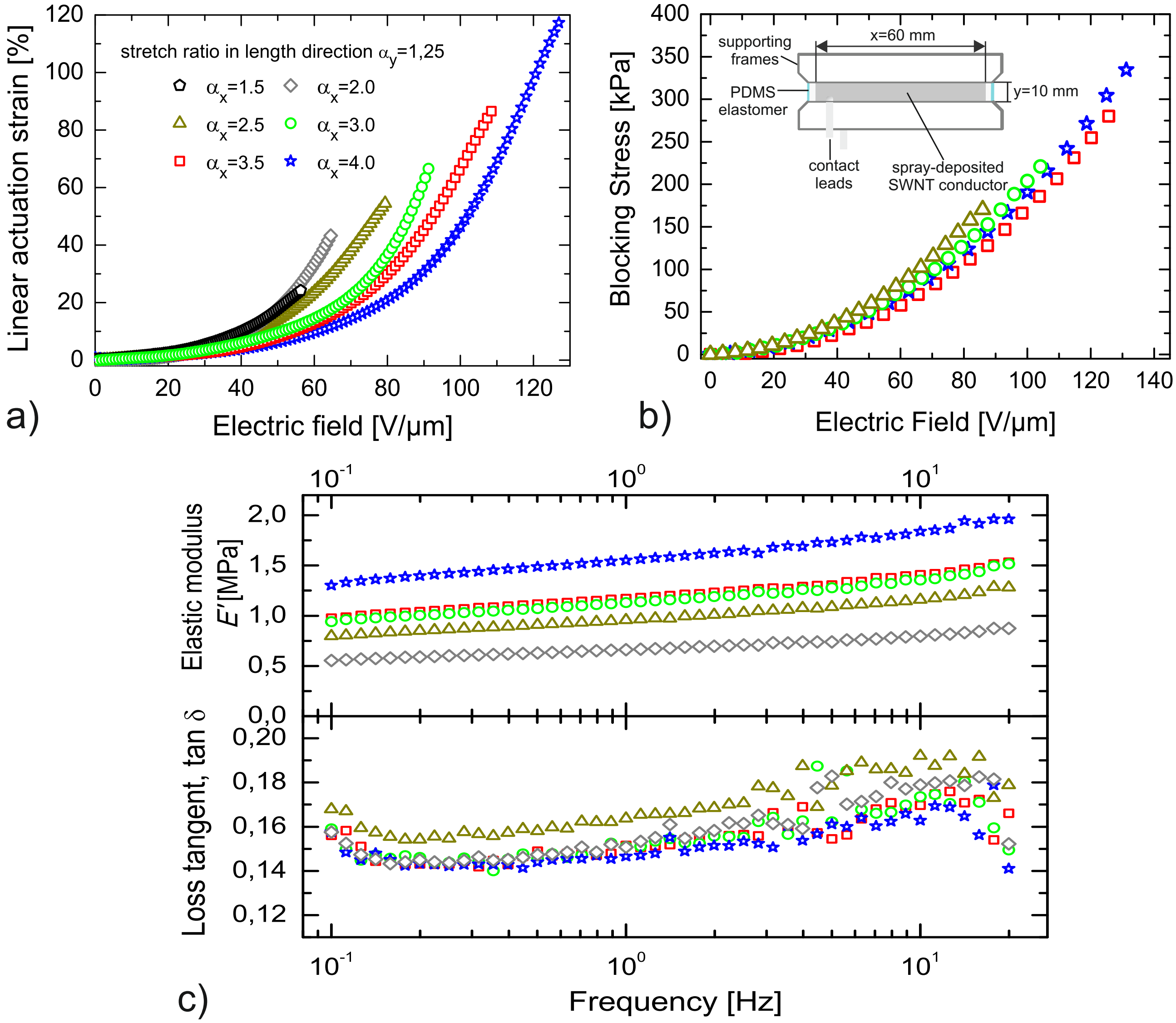

Figure 2.3: Linear actuation strain vs. electric field (a), blocking stress vs. electric field (b) and elastic modulus and mechanical loss tangent vs. frequency (c) for different pre-stretch ratios in horizontal direction. The vertical pre-stretch is fixed (α_y=1.25)

We explore the effect of pre-stretch in the horizontal direction on the electromechanical properties of actuators made using the soft PDMS by fixing the pre-stretch in actuation direction to $\alpha_y = 1.25$ and systematically varying the pre-stretch ratio in horizontal direction (α_x). Fig. 2.3 displays the actuation strain (a), blocking stress (b) and dynamic mechanical data for the different pre-stretch ratios (c). The linear actuator configuration is shown schematically in Fig. 2.3(b) inset. Increasing the horizontal pre-stretch shifts the electric breakdown to higher electric fields leading to higher actuation strain since the voltage-stretch curves are expected to be monotonic. For example, for a pre-stretch of $\alpha_x = 4$ an actuation strain of 120% is measured at electric field of 127 V/μm. Note that for simplicity, the nominal electric field is plotted. The apparent increase of the breakdown strength is due to the increase of the mechanical stiffness [302] caused by the increased pre-stretch (Fig. 2.3(c)). The elastic modulus measured at 1 Hz increases from 0.66 MPa for $\alpha_x = 2$ to 1.55 MPa for a pre-stretch of $\alpha_x = 4$. Interestingly, the viscoelastic loss (tan δ) does not change appreciably with prestrain in the range tested since the PDMS used is intrinsically a low loss material.

Fig. 2.3(b) shows blocking force measurements measured under isostrain conditions. Measurements were performed for pre-stretches of $\alpha_x = 2.5-4$. Since the blocking force measured is a function of the permittivity of the active material and geometry of the actuator, [174,303] the curves for the different pre-stretches are essentially overlapped and the maximum blocking stress is mainly determined by the electric field that the material can support. A maximum blocking stress of 335 kPa was measured for a prestretch of $\alpha_x = 4$ at 132 V/μm. Overlapping of the blocking stress curves is an indication that the dielectric constant of the material does not change significantly with the pre-stretch. We can therefore assume the dielectric constant remains constant during actuation and that the Maxwell stress is independent of the strain state.

To investigate the influence of the vertical pre-stretch on the electromechanical properties, we fixed the horizontal pre-stretch to $\alpha_x = 3$ and varied α_y. The results for vertical pre-stretch of 1.25, 1.5 and 1.75 are shown in Fig. 2.4. Based on our experiments, the maximum actuation strain does not change with the vertical pre-stretch; however, the breakdown field is slightly shifted to higher electric fields. This trend can be explained by the increase in material stiffness in the actuation direction. As the material become stiffer more force is required to deform it, while it also become more difficult to induce pull-in. The result is that actuators with higher prestrain in the vertical direction are capable of driving heavier loads. In the inset of Fig. 2.4 the work density calculated as $W = Fy_0 s_z/v$ (F is the applied load, v is the volume, s_z is the strain at given electric field and y_0 is the initial actuator length) is plotted for the different values of α_y. Due to the fact that the driving load increases from 0.51 N for $\alpha_y = 1.25$ to 0.88N for $\alpha_y = 1.75$, the actuator with a prestrain of $\alpha_y = 1.75$ shows the higher work density of 0.32 J/cm^3 at an electric field of 118 V/μm.

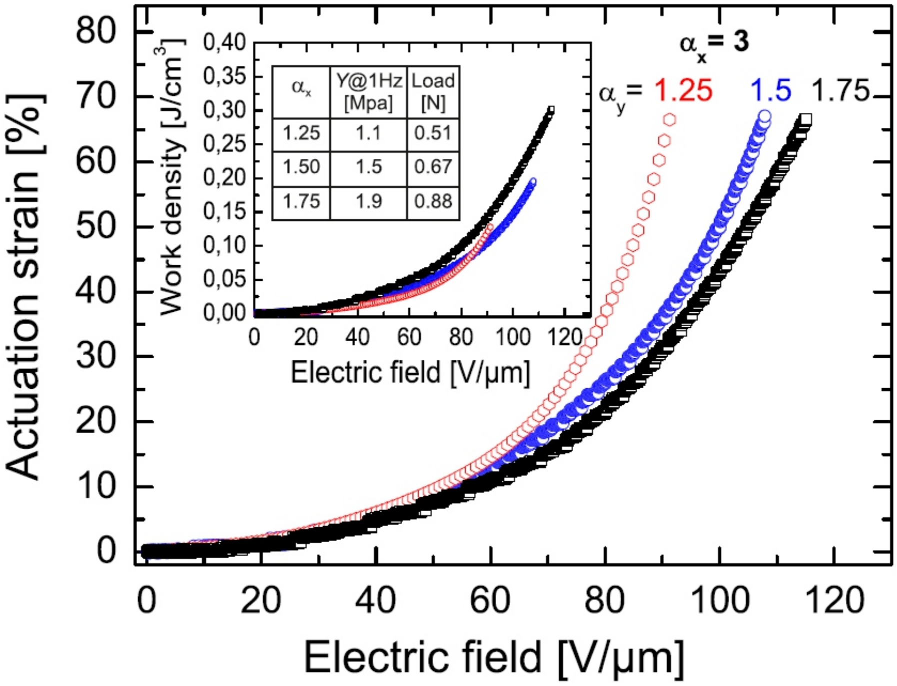

Figure 2.4: Actuation strain and work density (inset) as a function of electric field for fixed pre-stretch of $\alpha_x = 3$ in horizontal direction and different pre-stretch in vertical direction.

Freestanding linear actuator (schematically shown in Fig. 2.3(b) inset) with a prestrain of $\alpha_x = 3$; $\alpha_y = 1.5$ were chosen to test lifetime performance. Fig. 2.5 displays the cycling actuation tests at different actuation voltages using a sine wave signal at a frequency of 0.5

Hz. First the actuator was tested at a relatively low voltage of 1kV, far below the electrical breakdown of the material. Repeatable actuation strain of 13% was measured for 5000 cycles, corresponding to 2.7h of operation. After that, the voltage was increased to 1.4 kV and 5000 cycles were recorded at actuation strain of 20%. Increasing the voltage further to 1.6 kV resulted in actuation strain of 25% strain; however, the actuator suffered several breakdown events that were successfully self-cleared through the fault-tolerance of the electrodes. The actuator withstood more than 5000 cycles with occasional breakdown events. The durability of the actuator at higher voltages and correspondingly higher actuation strains was fairly poor. For example actuation at 1.8 kV and actuation strain of 35% resulted in less than 50 cycles before a dielectric breakdown event. It appears that 25% strain for this material formulation is the maximum stable actuation strain that can be obtained as a freestanding linear actuator driving a load. This underscores the importance of dynamic effects during actuation. Despite being capable of over 60% linear strain, the actuator is limited to less than half of that value when cycled repeatedly. Undoubtedly, both mechanical and electrical fatigue play a large role in device lifetime.

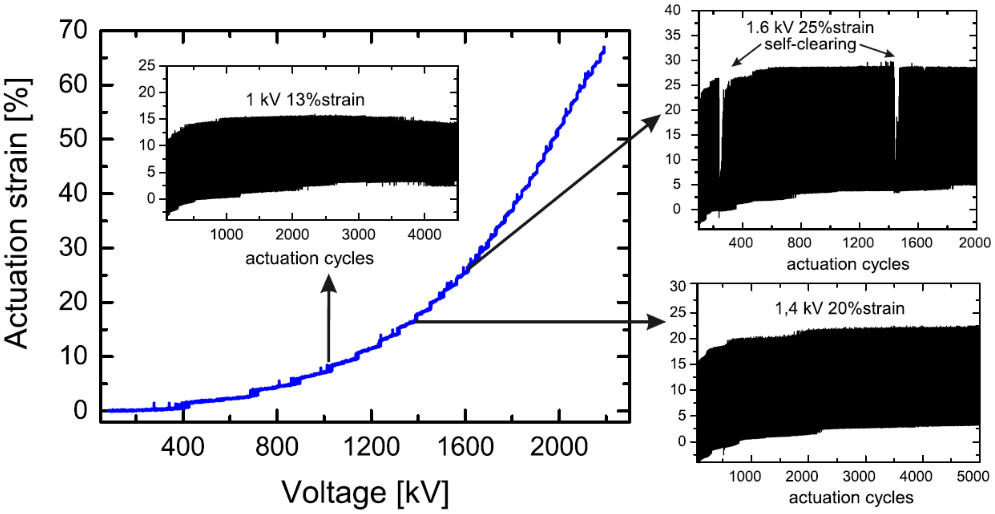

Figure 2.5: Cycling actuation tests for a freestanding linear actuator with a prestrain of $\alpha_x = 3$; $\alpha_y = 1.5$ at different operation voltages performed using sine wave signal at a frequency of 0.5 Hz.

To demonstrate that the combination of SWNT electrodes with the silicone is capable of repeatable and reliable fault-tolerance, localized dielectric breakdown events were intentionally introduced by operating the actuator in the unstable region as identified in the previous experiments. The ability of the electrodes to self-clear was tested in two different configurations: prestrained film with stretch ratios of $\alpha_x = 3$; $\alpha_y = 1.5$ actuated in the plane of the film and free-standing linear actuators driving a load. Fig. 2.6 displays the actuation strain vs. number of actuation cycles for an in-plane actuator with dimensions $w = 25$ mm and $l = 5$ mm. First, a 1.4 kV sine wave signal at a frequency of 2 Hz was applied to induce dielectric breakdown events for about 6000 cycles and after more than 25 self-clearing events, the voltage was reduced to 1.2 kV and the sample was then cycled for 20 000 more cycles showing stable actuation without any degradation of the performance. Inset of Fig. 2.6 shows an image of the actuator; the white dots are the self-cleared regions caused by local decomposition of the SWNT material around the electric breakdown sites. It is worth noting that the actuation strains obtained are slightly lower than for a freestanding actuator driving a load. This can be explained by the different boundary conditions and the absence of load to direct the actuation in the direction of low pre-stretch. Because of that and the absence of stiff frames to constrain the actuation in the lateral direction, the material tends to expand laterally as well.

Fig. 2.7 shows the cycling performance of a typical freestanding linear actuator. The actuator was cycled over 25,000 times at an actuation strain of 25% while driving a load, thus inducing multiple self-clearing events. The voltage was reduced to 1.2 kV and 20% strain respectively and the actuator was tested for an additional 10,000 cycles. To test the repeatability of the actuation performance, the actuator was then left overnight and a 2nd run of 25,000 cycles was performed, followed by 3rd run on the 3rd day of testing for an additional 25,000 cycles. To our knowledge this is the first demonstration of a free-standing linear dielectric elastomer actuator capable of maintaining such a high level of actuation strain for over 85,000 cycles. The ability to induce self-clearing events by operating at higher voltages is interesting from the perspective of removing potential failure points prior to deployment.

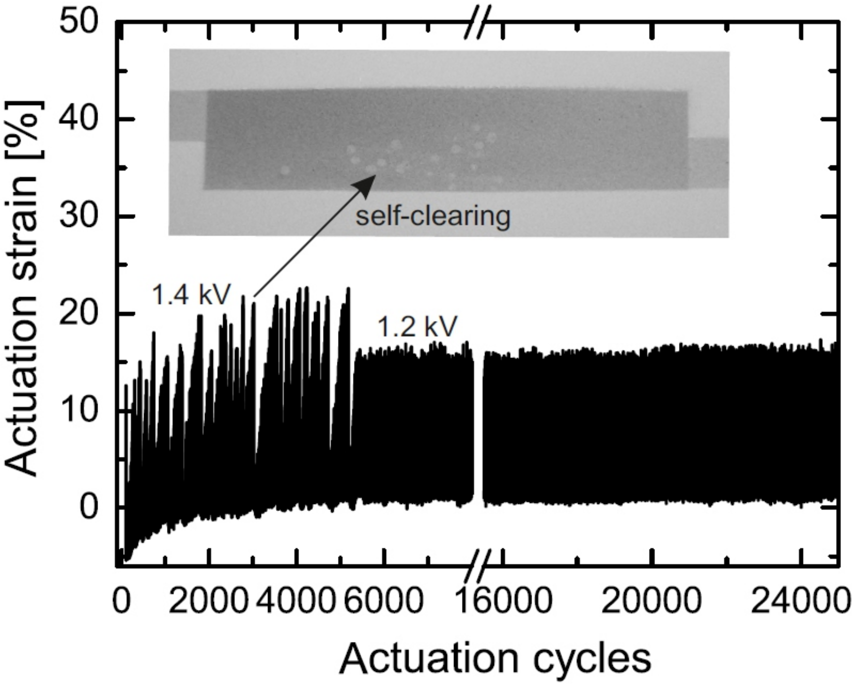

Figure 2.6: Fault-tolerance and cycling actuation tests of an in-plane actuator with a pre-stretch of $\alpha_x = 3$; $\alpha_y = 1.5$ using sine wave signal at a frequency of 2 Hz.

This process could be useful for commercial products using dielectric elastomer actuators. By pre-clearing potential defects, we would expect the reliability and repeatability of the actuator to improve substantially.

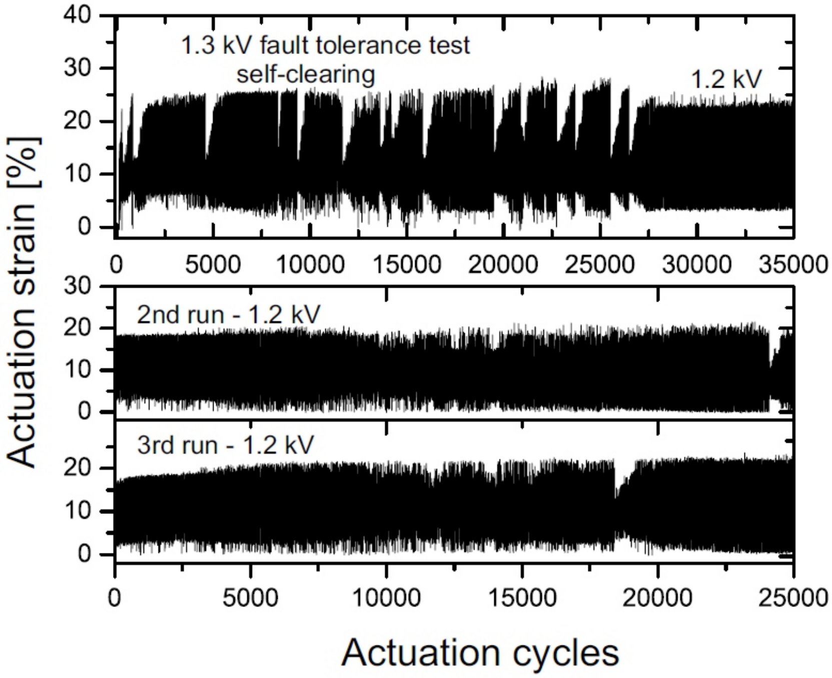

Figure 2.7: Fault-tolerance and cycling actuation tests of a freestanding linear actuator with a pre-stretch of $\alpha_x = 3$; $\alpha_y = 1.5$.

2.5 Conclusions

We have explored the non-linear stress-strain curves in terms of pre-stretch of an addition cure High Temperature Vulcanizing (HTV) silicone rubber to obtain large linear strain (120%) freestanding actuators. In addition, we demonstrated that when coupled with SWNT compliant electrodes, fault-tolerance is introduced, thus significantly improving the manufacturing yield and operational reliability. Cycling actuation tests showed that even after more than 30 self-cleared electrical breakdown events the actuators maintain high level of performance for more than 85,000 cycles.

CHAPTER 3

Silicone TiO_2 Nanocomposite for Enhanced Work Density

The high strain and long lifetime actuation performance of the soft silicone actuators presented in Chapter 2 can be further improved via the addition of nanoparticle filler. While most other attempts at improving the performance of silicone materials via the introduction of filler particles have centered on increasing the permittivity to reduce the required driving voltage [95, 195–197, 203, 212, 232, 261, 304, 305], our approach is different. Reducing the required electric fields is indeed a noble and perhaps necessary task, dielectric elastomers also require high strain, high force, and high work density to compete with current state of the art technologies. A higher work density allows for a reduction in the size, mass, and intrusiveness of actuator devices. We approach the issue from a different perspective: rather than focusing solely on attempting to reduce the driving voltage by increasing the permittivity, we choose a soft elastomer host that can produce relatively high strains at low to moderate electric fields, and use the nanoparticle composite approach to increase the force output and work density. The mechanical reinforcement and increase in permittivity, caused by the addition of the nanoparticles to the elastomer host, work in tandem to increase the overall performance of our composite material. We show that indeed, this nanocomposite approach leads to significant enhancements of the actuator blocking force and work density while maintaining relatively low electric field operation, high actuation strains, and high breakdown fields.

3.1 Material Preparation

For the host elastomer we selected a high temperature vulcanizing (HTV) two part platinum catalyzed PDMS with a low elastic modulus (Wacker Silpuran 6000/10). In order to prevent aggregation of the nanoparticles, we have selected 20nm rutile TiO_2 nanoparticles ($\varepsilon_r = 128$) that have been functionalized with short PDMS chains. The tendency of the nanoparticle filler to reinforce the PDMS was offset by decreasing the crosslink density of the PDMS. This was achieved by mixing unequal parts of the two part silicone, the optimal ratio to produce the softest host was a 1:9 ratio of part A to part B. Composites were prepared by dissolving the two silicone parts in isopar G (ExxonMobil), adding the TiO_2 nanoparticles to part B and sonicating in a 400W bath sonicator for 1 hour. The solutions were cooled and the part A solution was added and briefly sonicated to homogenize the mixture. The solutions were drop cast onto glass and cured at 160°C for 30 minutes.Linear actuators were fabricated by prestraining the resulting films by stretches $\alpha_x = \alpha_y = 1.75$ to prevent any issues related to electromechanical instability [160, 306] and attaching them to rigid frames as seen in Figure 3.3 (top inset) on page 80. Electrodes were patterned by spraying a dispersion of single walled carbon nanotubes (P3-SWCNTs) in a combination of 80% isopropyl alcohol and 20% deionized water through a contact mask. The resulting freestanding linear actuators were used for electromechanical characterization including blocking force measurements, dynamic mechanical analysis, and constant load linear actuation tests.

3.2 Results and Discussion

Blocking force measurements were performed by loading the linear actuators in a TA Instruments RSAIII dynamic mechanical analysis machine (DMA). The samples were preloaded to maintain the initial prestrain and allowed to stress relax for several hours prior to testing. A high voltage power supply built in-house was used to apply high voltage across the film from 0 V to failure using a 200 V step. The device was maintained under isostrain conditions

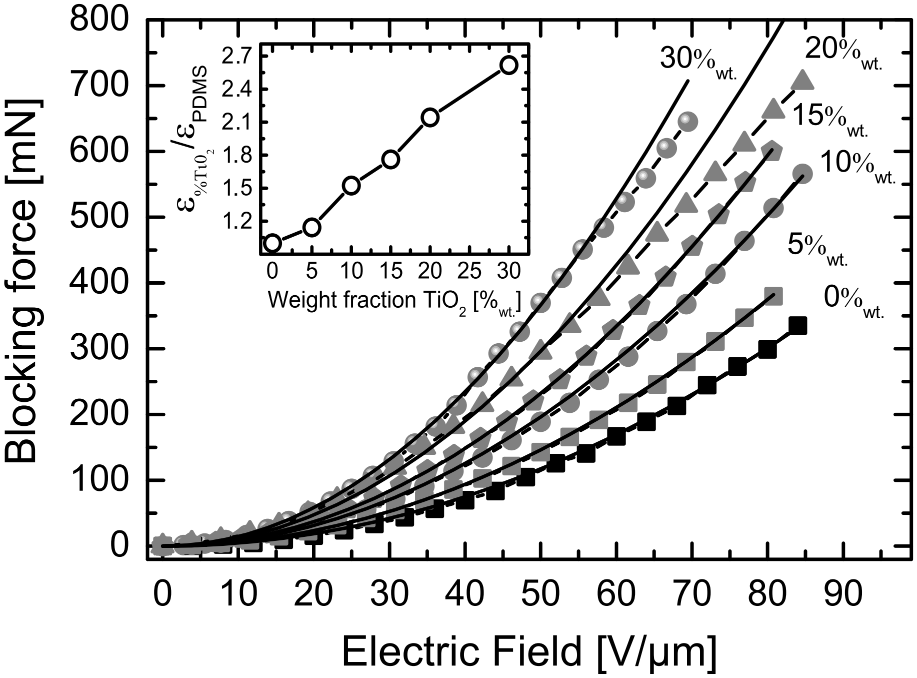

Figure 3.1: Blocking force as a function of electric field measured at room temperature for varying TiO_2 loadings.

and the blocking force was monitored using the DMA's load cell. Figure 3.1 on page 76 presents the blocking force measured at different electric fields for systematic variation of the nanoparticle content. The blocking force is observed to progressively increase with TiO_2 loading, reaching a value of 705 mN for $20\%_{wt}$ which corresponds to 2.2 times increase compared to the pure PDMS (320 mN). Importantly, no decrease in the breakdown field strength was observed up to a loading of $20\%_{wt}$. This is important as both electrostatic pressure and strain vary with the square of the electric field and the energy density varies with the fourth power of electric field [307].

The blocking force measured in the direction perpendicular to the applied electric field (F_y) is directly related to the Maxwell pressure generated in the thickness direction and for pre-strained actuators can be derived for physically measurable quantities as shown and experimentally validated by Kofod et al. [174]:

$$F_y = \frac{x_0 z_0}{\alpha_y} \varepsilon_o \varepsilon_r E^2 = \frac{x_0}{z_0} \alpha_x^2 \alpha_y \varepsilon_o \varepsilon_r V^2 \tag{3.1}$$

Where x_0 is the actuator width, z_0 is the film thickness before pre-strain, α_x and α_y are the stretch ratios in width and length direction, respectively, ε_o is the vacuum permittivity, ε_r is the relative permittivity of the dielectric film, E is the electric field and V is the applied voltage. The blocking force is a function of the applied voltage, permittivity of the active material, and geometry of the actuator only. It provides an efficient way to determine the permittivity of the composites at high electric field, since all other parameters are known. In order to determine the change in permittivity of the composite, the blocking force data was fit with the force equation (Figure 3.1 (black lines)). The results of the fit are plotted in the inset of Figure 3.1 as a relative increase over the pure PDMS. A substantial increase of 2.7 times is observed for relatively low volume fractions. The advantage of using this method to determine the permittivity of the composite over other standard methods, such as dielectric spectroscopy and LCR meters, is that the measurements are made at high electric fields (0-300 V/μm compared to 0.001 to 0.1 V/μm for standard methods) under normal operating conditions for dielectric elastomers and thus provide results that can be directly correlated to device performance. As reported previously, dielectric permittivity is a complex parameter and measurements made at low electric fields for composite materials can give misleading results due to increases in the dielectric loss ($\tan\delta$) related to Maxwell-Wagner polarization or increased conductivity which leads to substantial decreases in the electric field that the material can support and thus greatly reducing overall performance [308].

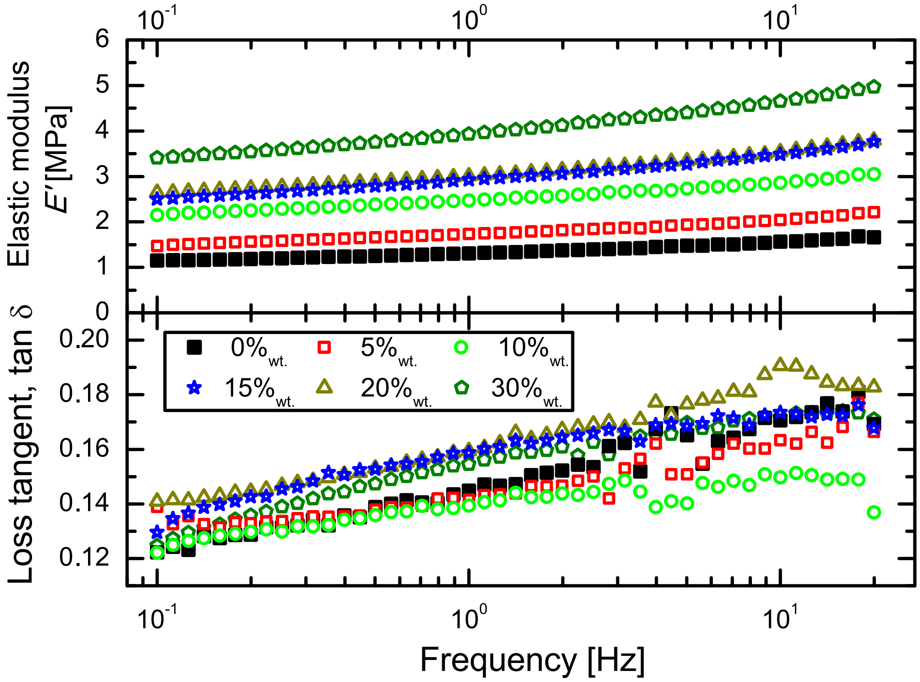

Figure 3.2: Elastic modulus and mechanical loss tangent $\tan\,\delta$ in the frequency range of 0.1 to 20 Hz.

The mechanical properties of the material were characterized using the same setup and actuator configuration under a dynamic load in the frequency range of 0.1 to 20 Hz at a strain of 1% (Figure 3.2 on page 78). As expected the stiffness increases with TiO_2 nanoparticle loading as the nanoparticles act to restrict chain motion by effectively acting as physical crosslinking sites. The elastic modulus is seen to increase from 1.3 MPa at 1Hz for the pure material to 3.9 for the composite with $30\%_{wt}$ loading. Importantly, the loss tangent is observed to remain essentially unchanged from the neat PDMS up to loadings of $30\%_{wt}$ (and perhaps higher), indicating that the TiO_2 had no effect on the viscoelastic behavior of the material.

The actuation strain was measured by suspending a load from the bottom of the devices and applying a voltage ramp at a rate of 20 V/s and monitoring the elongation of the active region using digital video and Labview software. The results of the actuation tests (Figure 3.3 top) show an increase in the actuation strain sensitivity for loadings of $5\%_{wt}$ and $10\%_{wt}$ over the pure PDMS, indicating that at low loadings the influence of the nanoparticles on the permittivity of the composite outweighs their influence on the mechanical properties. Above $10\%_{wt}$ the added mechanical reinforcement begins to dominate and the strain response is slightly reduced. At higher loadings the composites are still capable of respectably high linear actuation strains, reaching 19.5% at 80 V/μm for $15\%_{wt}$ and 16.8% at 81 V/μm for $20\%_{wt}$.

The mechanical reinforcement of the materials due to the presence of the nanoparticles leads to significant increase in the load that the actuators are capable of driving (bottom inset of Figure 3.3) which, in combination with the enhanced permittivity, leads to significant improvements in the work density. The work density of the material was calculated as the work carried out by the actuator divided by the volume and since the actuator drives a constant load the work carried out can be written as:

$$W = \int F dx = F y_0 s_z, \tag{3.2}$$

Where F is the applied load, y_0 is the initial actuator length and s_z is the strain at given electric field. The data plotted in Figure 3.3 (bottom) shows clearly the beneficial effect of the nanoparticles on the actuators work density. Although the max. actuation strain is slightly reduced for the $20\%_{wt}$ nanocomposite compare to the pure PDMS, the driving load is increased by 3 times thus leading to significant improvement of work density. The increase in work density is very valuable for most actuator applications as it decreases the required size and mass of the actuator device to perform a task, allowing for small, lighter weight, and less intrusive devices.

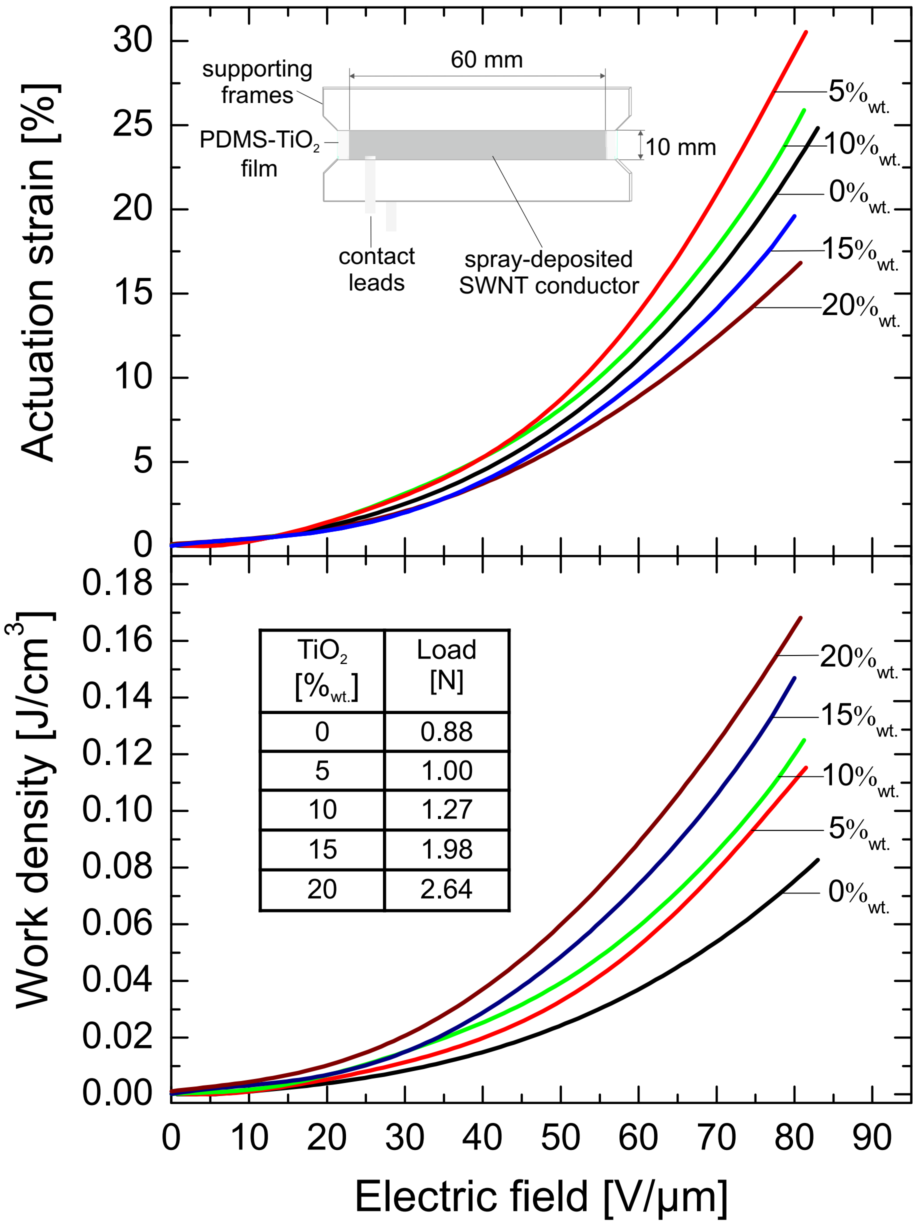

TiO$_2$ [%$_{wt.}$]	Load [N]
0	0.88
5	1.00
10	1.27
15	1.98
20	2.64

Figure 3.3: Linear actuation strain (top) and calculated work density (bottom).

3.3 Conclusions

We have demonstrated that the addition of high permittivity nanoparticle fillers to a soft high breakdown strength silicone host can yield high work density and high strain actuation at relatively low electric fields. This approach seems well suited for the development of dielectric elastomer artificial muscle actuators for biomedical and mobile robotic applications where low mass, small size, and low intrusiveness are of the utmost importance.

CHAPTER 4

Prestrain-Locked Freestranding Silicone Interpenetrating Polymer Network Elastomers

The silicone actuators presented in chapters 2 and 3 have demonstrated the ability to actuated to linear strains over 100% with work densities in excess of 100 J/g and long lifetime actuation at strain in excess of 20%. These values compare favorably to the best DE materials; however, such high strains and energy densities require the use of mechanical prestrain to enhance the breakdown strength of the elastomer material and to mitigate the electromechanical instability that limits strains of conventional relaxed elastomers. [160]. Prestrain-locked interpenetrating polymer network elastomers (IPNs) based on 3Ms VHB^{TM} 4910 series of adhesive acrylic elastomers have been able to circumvent the requirement of a mechanical prestrain by locking in prestrain in the host elastomer using a more rigid additive network. [171, 172, 202]. These acrylic IPNs have successfully mitigated issues related to the electromechanical instability [309] and have opened the door to a number of applications with minimal support structures and high power-to-mass ratios. [262] No similar solution has yet to be presented for silicone actuators.

Here we present a novel prestrain-locked interpenetrating polymer network elastomer consisting entirely of silicone elastomers (S-IPN) that is capable of overcoming the aforementioned issues. We use a soft room temperature vulcanizing (RTV) silicone as the host elastomer and a more rigid high temperature vulcanizing (HTV) silicone as the support network to lock in the prestrain applied to the host network. Prestrain is applied to the RTV silicone host material and the HTV silicone is then cured. Subsequently releasing the film from the prestrain support frame allows the tension in the host RTV silicone to relax; however, as the host silicone network relaxes, the additive network is compressed. The tensile and compressive forces eventually balance in a new equilibrium state preserving some of the applied prestrain. [171] The result is free standing silicone film with a higher breakdown field, higher energy density, and improved actuation strains as compared to the soft RTV silicone. The technique can also be leveraged to lock in the electrodes if the electrodes are applied prior to curing the HTV silicone component. Multilayer actuators with enhanced interlayer adhesion can also be fabricated by applying electrodes and laminating the films together prior to curing the HTV silicone.

4.1 Material Design

The process we use to prepare the films is shown in Figure 4.1. In our approach we use two commercially available silicones, a condensation cure RTV silicone and an addition cure HTV silicone. The RTV silicone acts as the host elastomer and the mechanical and electrical properties of the composite will be largely influenced by the properties of this component. The RTV silicone is used as an additive with the primary purposes of retaining prestrain in the host elastomer and limiting the large stress-strain plateau characteristic of most soft elastomer materials. As such, a soft silicone known to have high dielectric elastomer performance (Dow Corning HSIII) [44] is selected as the host and a more rigid silicone with a lower maximum elongation (Dow Corning LR3003/70) is selected as the additive network. The two silicones are mixed in a co-solvent and drop-cast onto polystyrene-sulfonate (PSS) treated glass. The RTV silicone is allowed to cure while the excess solvent evaporates. The film is then gently peeled off of the glass substrate, prestrained biaxially by 100x100% onto a metal frame, and heat treated at an elevated temperature to cure the HTV silicone. We have explored the use of a condensation cure organotin catalyzed RTV liquid silicone rubber (LSR) and an addition cure platinum catalyzed HTV LSR with an extended room temperature pot-life. The organotin catalyst used in our RTV silicone is dimethyl tin dineodecyl ester and the silicone cures via an alkoxy condensation reaction. The HTV silicone cures via the addition route common for LSR Pt-catalyzed silicones.

After the curing process, the films are released from the metal frames. The tension in the host silicone network causes the film to contract; however, this contraction is impeded by the compression of the additive silicone network. The film will therefore contract into a new equilibrium position where the tensile and compressive forces are equal. [171] The resulting films are optically transparent and homogeneous as confirmed by cross-polarization microscopy. Maintaining homogeneity in these composite materials is important to ensure even and stable actuation across the entire active portion of the film.

4.2 Experimental Details

Prestrain-locked silicone IPNs were fabricated by first dissolving Dow Corning HSIII in an isoparafinic solvent (ExxonMobil Chemical Isopar G) and centrifuging the solution to remove the beige pigment found in HSIII. The centrifuged Dow Corning HSIII was then mixed with Wacker Elastosil LR 3003/70 at various concentrations in Isopar G. Dow Corning 83NW curing agent was added to the solutions in a HSIII to catalyst ratio of 20:1 and the solvent was drop cast on a poly(styrene sulfonate) (PSS) treated glass. The solutions were left for 2 days to allow the excess solvent to evaporate and for the HSIII silicone to cure. The resulting films were peeled from the glass substrate and prestrained equibiaxially by 100x100%. The films were then heated in an oven at 180°C for 20-30 minutes to cure the Elastosil LR 3003/70. After the heat treatment the films were released from the support structure and allowed to fully relax. The amount of preserved prestrain was calculated from the final dimensions after relaxation with respect to the sample size before prestrain was applied. Thus, the listed preserved prestrain values represent the actual prestrain on the HSIII host elastomer.

The mechanical properties of the fully relaxed S-IPN films were characterized using a

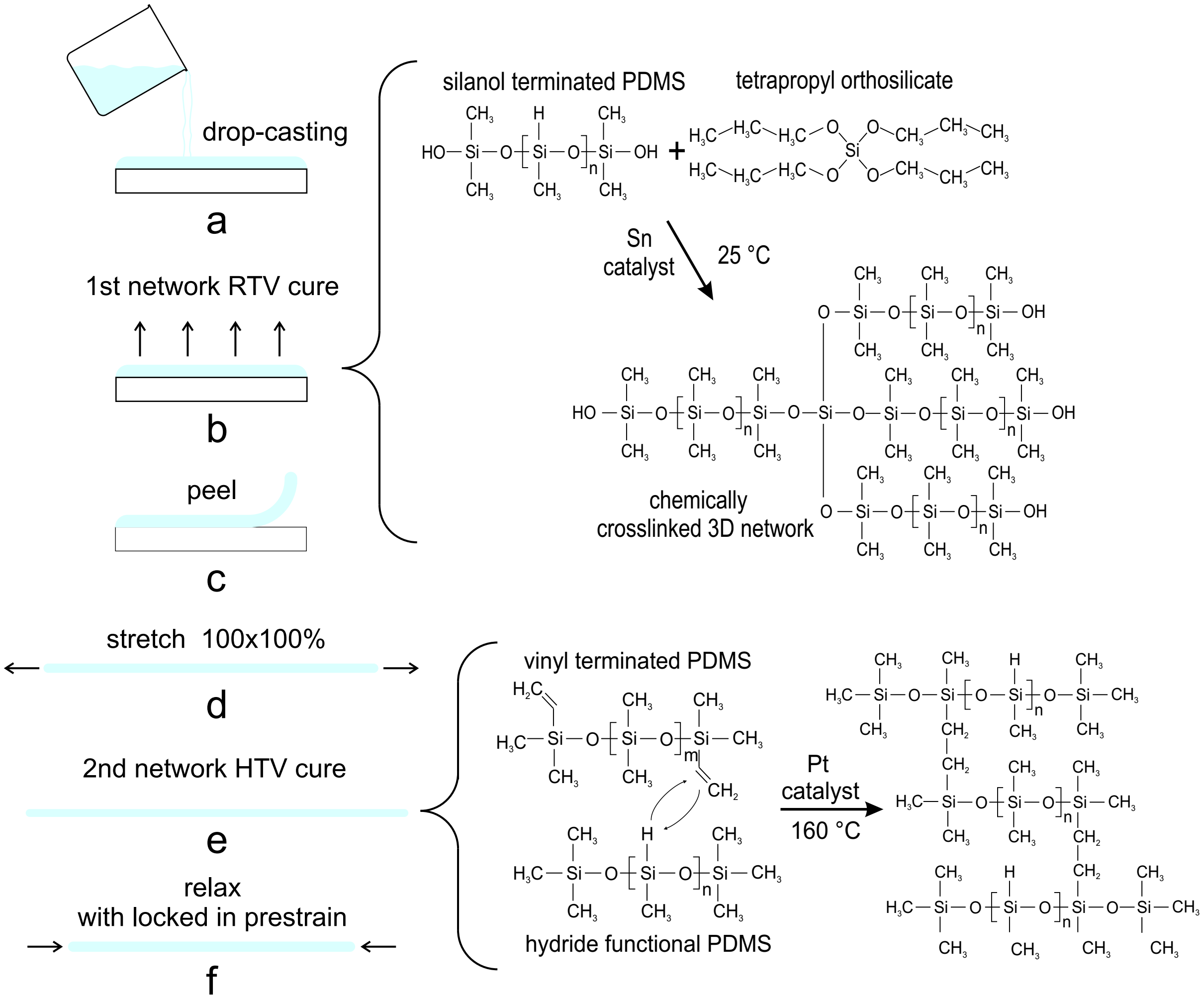

Figure 4.1: Process for preparing S-IPN films; (a) film is drop cast from solution onto treated-glass, (b) solvent is allowed to evaporate and RTV silicone cures at room temperature, (c) film is peeled off of the glass substrate, (d) film is stretched biaxially by 100x100%, (e) HTV silicone is cured at 180 °C for 30 minutes, (f) film is relaxed and some prestrain is preserved.

TA Instruments RSA3 dynamic mechanical analysis machine. The sample thickness was measured using a Mituyo micrometer with a precision of 1 micron. Tensile test samples were prepared with a planar dog-bone shape with a gage length of 12 mm and width of 2mm. Tensile tests were performed on the samples at a strain rate of 25%/s.

Actuation tests were performed on samples with a square active area with an edge length ranging from 16 to 22mm (dependent on the degree of relaxation). Carboxyl-group functionalized single walled carbon nanotube (SWNT) electrodes were spray deposited using a Pasche airbrush at approximately 20 PSI from a dispersion in isopropanol and deionized water at a concentration of 0.2mg/mL. The SWNT dispersion was prepared by sonication for 3 hours in a 400W bath sonicator. The resulting dispersions were opaque black and remained properly dispersed for several hours. The actuation strain was monitored using a USB microscope camera and the high voltage was applied using Trek 10/10B-HS high voltage amplifier using LabView software and a National Instruments USB-6009 digital acquisition module. For high frequency actuation tests, a high speed camera was used to record the samples during actuation at a frame rate of 1200 fps. The nominal electric field was calculated based on the applied voltage and the initial thickness. Linear actuation samples were clamped using a plastic frame at either end with a free-hanging mass of 1.1 g pulling in the direction of actuation. Diaphragm actuation samples were adhered to an air chamber and a small air pressure was applied to cause the film to deform in the desired direction.

4.3 Results and Discussion

4.3.1 Preserved Prestrain and Mechanical Properties

Prestrain-locked all silicone IPN films were successfully fabricated and tested for the HSIII-LR 3003/70 system for LR3003/70 contents of 10, 15, 20 wt.%. The resulting films were clear, free of visible defects and had uniform thickness. The amount of prestrain preserved for each sample is shown in Figure 4.2a. Due to the higher stiffness and lower maximum elongation of the additive silicone network, relatively large values of preserved prestrain can be achieved at low additive loadings. The amount of preserved prestrain is observed to increase from 41% at 10wt.%, to 54% at 15wt.% and 66% at 20wt.%. Figure 4.2b shows the results of the tensile tests for the IPN samples; a regular HSIII film was tested for comparison. The results show a marked increase in the stiffness of the IPN samples throughout the entirety of the stress-strain curve. The large plateau region seen in the HSIII film is effectively eliminated for all IPN samples as desired. At higher additive contents the increase in the effective stiffness of the IPN films is caused by an increase in preserved prestrain and an increase in the relative amount of the stiffer additive network. The frequency response of the neat and IPN silicones were also tested in the range of 0.1 to 20 Hz with a 10% offset strain to prevent buckling and an oscillatory strain of 1% (Figure 4.2c). All materials show a flat response with low losses across the frequency range tested, indicating low viscoelasticity. The mechanical loss factor (tan) for all additive concentrations remains in the range of 0.01 to 0.1. At a frequency of 1 Hz the loss factor is approximately 0.03 for all materials. For comparison the mechanical loss factor for acrylic IPN materials at 1Hz measured at room temperature is 0.42 while fully relaxed VHB has a loss factor of approximately 0.64.

The temperature response of a 15% S-IPN film was also measured (Figure 4.2d) from -50 to 120°C. The material shows low losses across the entire temperature range, maintaining a mechanical loss factor between 0.01 and 0.1 with the largest losses occurring at low temperatures. The material also shows a slight increase in modulus across the range tested. In the expected operational temperature range (-40°C to 80°C) the modulus increases from 0.52 MPa to 0.62 MPa, with relative changes of -4% and 15% with respect to the value at room temperature (0.54 MPa). This increase in modulus and reduction in mechanical loss factor is expected for elastomers as they display entropic elasticity, and higher temperatures result in an increase in the elastic restoring force. For comparison, the modulus and loss factor for acrylic IPN materials change drastically with temperature due to the glass transition of such materials lying close to 0°C. As a result, the actuation performance of acrylic IPN materials varies drastically with temperature. [310]

4.3.2 Actuation Tests

Linear actuation results obtained by applying a voltage ramp at 20 V/s are shown in Figure 4.3a. Note the increase in the apparent breakdown strength and actuation strain of the S-IPN materials over the standard HSIII. This trend follows from the expected suppression of the electromechanical instability due to the preservation of prestrain in the S-IPN composite films [311, 312]. Figure 4.3b top and bottom show a representative actuator in the rest and actuated state respectively. Note the appearance of wrinkles in the film oriented along the actuation direction. Due to the lack of prestrain in the lateral direction and the rigidity of the top and bottom frames, expansion in the lateral direction is inhibited and the film is forced into a wrinkled shape.

All S-IPN actuators demonstrated roughly the same maximum linear actuation strain of 25%, a 100% improvement over the actuation strain for standard HSIII silicone. The actuation sensitivity for the different composites is observed to change with additive loading as well due to the increased stiffening effects at higher additive contents. This is important as it allows us to tune the material to provide high force output or operate at low electric fields without any loss in strain performance.

Additional actuation tests were performed on HSIII and 15wt.% films in a diaphragm configuration with a very small bias air pressure applied to cause the film to actuate in the desired direction. The area strain (s_A), was calculated according to the following equation [171]:

$$s_A = \frac{(h^2 + r^2) - (h_0^2 + r_0^2)}{(h_0^2 + r_0^2)} \tag{4.1}$$

Where h and h_0 are the height and original height of the active area respectively, and r and r_0 are the radius and original radius of the active area. Results of the diaphragm actuation

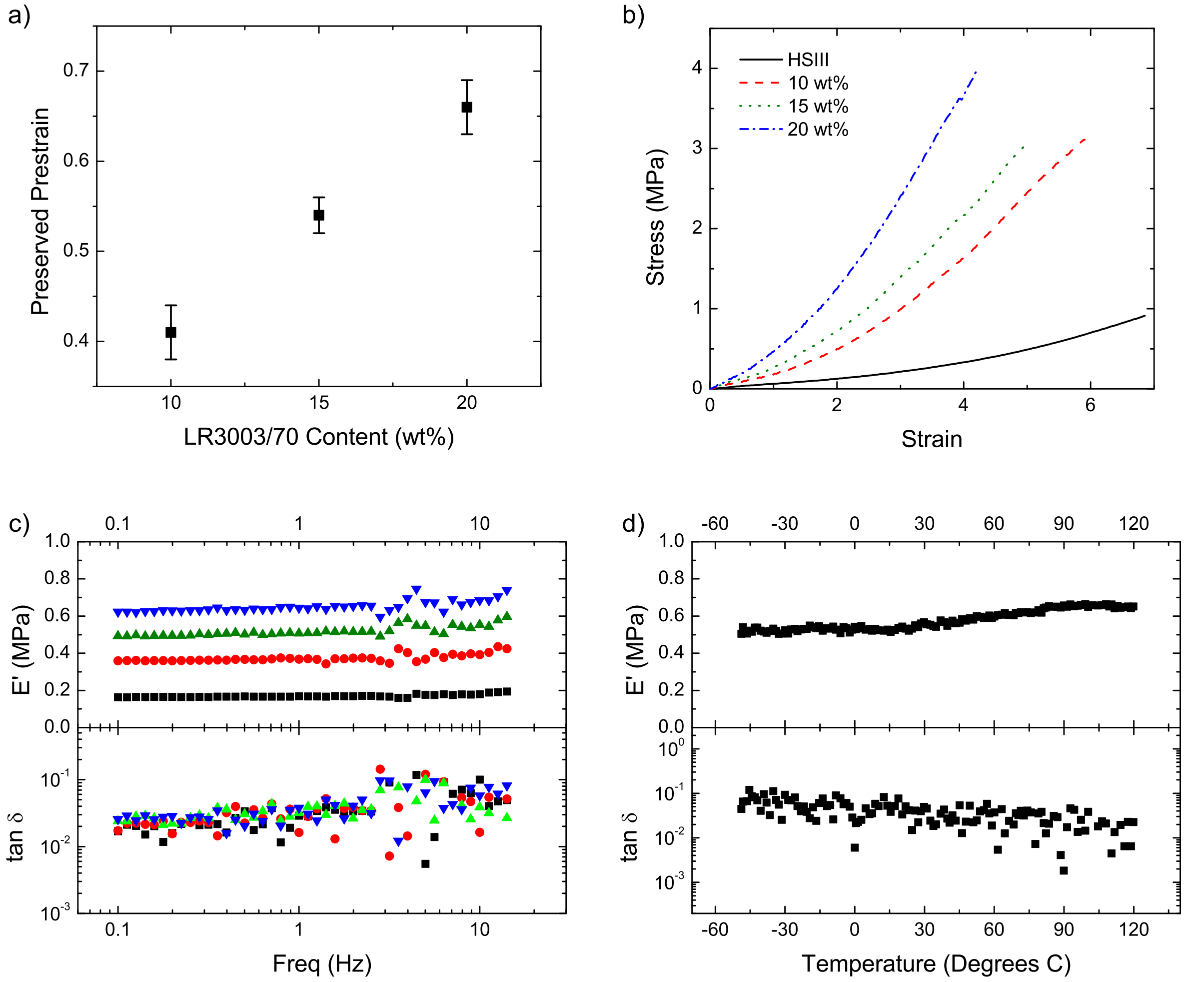

Figure 4.2: (a) Tensile test and (c) frequency sweep results and for standard HSIII and S-IPN films with different LR3003/70 contents with (b) different preserved prestrains. (d) Temperature sweep from -50 to 120 °C for an S-IPN film with 15wt.% LR3003/70.

tests are shown in Figure 4.3c. A peak strain of 45% was measured for the silicone IPN material, a 276% improvement over the standard HSIII silicone. Figures 4.3d top, middle, and bottom show the actuator at rest, in an intermediate actuated state and actuated to 45% area strain respectively. The actuation strain of the S-IPN actuator once again shows a large improvement over the standard HSIII film, confirming the increase in actuation performance, likely due to the suppression of the electromechanical instability through preserved prestrain. From the images it appears as though the strain in the highly actuated state is in excess of 45%; however, due to issues with the non-uniform shape and wrinkling of the actuator due to the low bias pressures used it is difficult to obtain a better measurement. The value of 45% area strain therefore represents the lower bound of what the actuator is capable of.

Actuation speed tests were performed on planar circular actuator samples prestrained biaxially by a small amount to prevent loss of tension. A square wave high voltage signal was applied to the devices using a Trek 10/10B-HS high voltage amplifier with a frequency ranging from 1 to 400 Hz. A high speed camera was used to record the samples during actuation at a frame rate of 1200 fps. The voltage was chosen such that the strain at 1Hz was 10%; the voltage was kept constant across the entire frequency range. The results show no degradation in actuation performance over the entire range tested, confirming the conclusion from the frequency sweep tests that the material has low viscoelasticity (Figure 4.4). In comparison, acrylic IPN materials show a large drop-off in performance with actuation frequency. [310]

4.4 Conclusions

Prestrain-locked all-silicone IPN films were successfully fabricated by co-dissolving a soft RTV silicone and a rigid HTV silicone in a common solvent, drop casting the resulting solution, allowing the RTV silicone to cure at room temperature, prestraining the partially cured composite, then heating it to cure the HTV silicone. The resulting films were homoge-

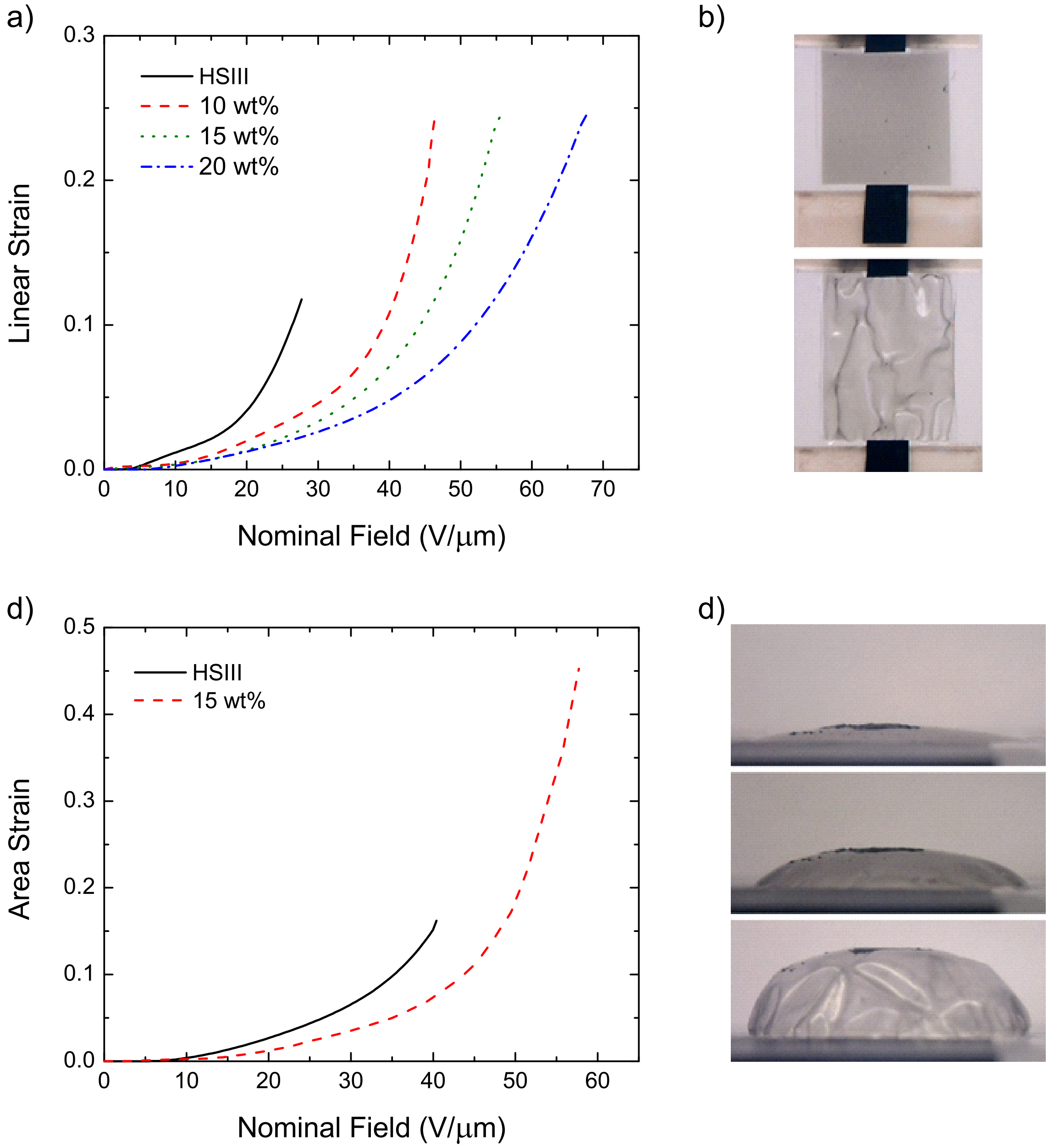

Figure 4.3: (a) Linear actuation tests for HSIII and S-IPN films with different LR3003/70 contents with images of the actuator in the (b top) rest and (b bottom) highly actuated states. (c) Diaphragm actuation tests for an HSIII film and an S-IPN film with a 15wt.% LR3003/70 loading with images of the actuator in the (d top) rest, (d middle) intermediate actuated state, and (d bottom) highly actuated state.

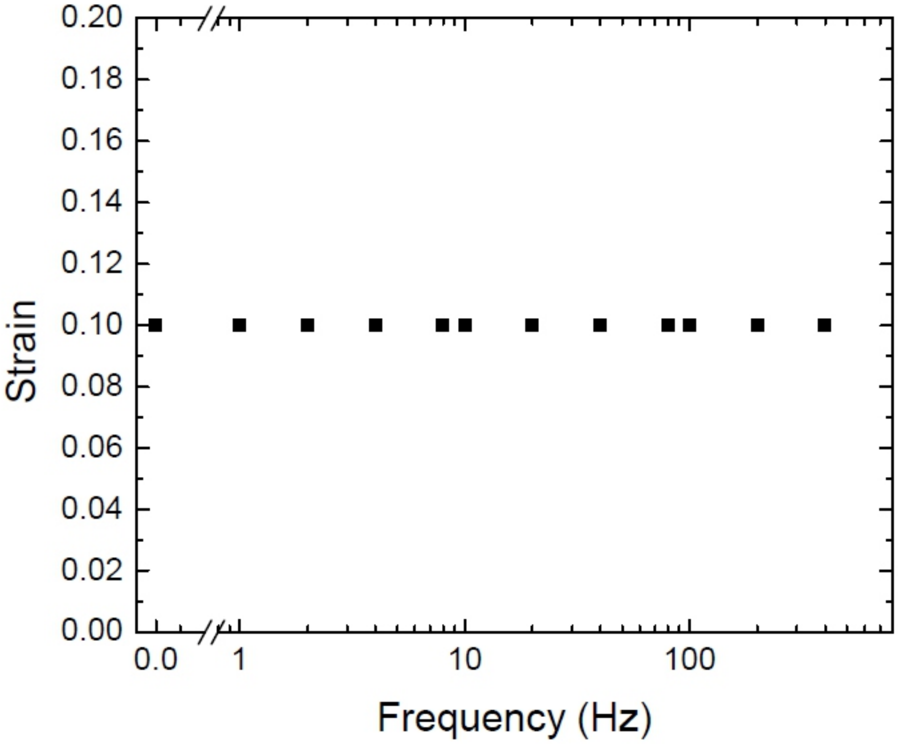

Figure 4.4: Actuation strain as a function of frequency for a planar S-IPN actuator

neous and transparent indicating good compatibility between the silicone components. The films demonstrated improved performance as both linear and diaphragm-style actuators in a non-prestrained state. Linear actuation performance was improved by over 100% while the performance of diaphragm actuators was improved by over 250%. The actuation performance that could be tuned to higher electric field, and thus higher force output, or lower electric field, thus requiring lower operating voltages. Additionally, the materials demonstrated good mechanical and actuation stability over a wide temperature and frequency range.

CHAPTER 5

Highly Prestrained Silicone Interpenetrating Polymer Network Elastomers with Improved Robustness and Muscle-like Performance

Chapter 4 discussed the preparation and actuation characteristics of a novel pre-strain locked all-silicone interpenetrating polymer network elastomer for use in dielectric elastomer actuators. This technique can also be leverage to produce additional benefits for dielectric elastomer actuators. The unreacted additive silicone present in the host silicone after the room temperature curing process has been completed causes the silicone to be tacky. The sticky nature of the film surface can be used to improve adhesion between the silicone and electrode materials and the unreacted chains at the surface of the film can also be used to improve bonding between films. In fact, if films are laminated together prior to curing the additive network, the adhesion between adjacent layers increases significantly both with and without the presence of an electrode between the layers. This technique can be used in prestrained and non-prestrained actuator configurations alike.

The result is that strongly bonded robust multilayer actuators with and without prestrain can be fabricated. Coupled with self-clearing single walled carbon nanotube electrodes, prestrained actuators are capable of linear strains in excess of 60%, and can be actuated for over 30,000 cycles at >20% strain and over 5000 cycles at >40% strain while driving a load. From Chapter 4, the strain performance remained stable up to 400 Hz (limited by equipment) so peak strain rates in excess of 8000%/s are expected. Coupled with the natural softness of the silicone, its ability to vary its stiffness with voltage, and its small form factor and low mass, these actuators compare quite favorably with real skeletal muscle.

5.1 Experimental Details

Electrode adhesion was determined by pressing a piece of 3M Scoth Tape firmly onto the electroded portion of the sample and then peeling it off. The electrodes were then quantitatively examined to determine if any electrode material was removed from the silicone surface and if any of the electrode material was transfered to the adhesive tape. The resistance of the electrodes was also measured using a multimeter to determine any quatitative changes in electrode resistance.

Interfilm adhesion tests were performed on a TA Instruments RSA3 dynamic mechanical analysis machine using a modified T-Peel test on 10mm wide samples with a bonded region length of 15mm at a rate of 250 mm/minute.

Highly prestrained actuators were fabricated by prestraining the films after the initial curing step by 200% in the lateral direction and 25% in the actuation direction. SWNT electrodes were spray deposited as described above using a contact mask to pattern electrodes measuring 60mm in the 200% prestrain direction and 10mm in the 25% prestrain direction. Films were then laminated together while still attached to their prestrain support frames and placed in a vacuum environment to remove any trapped air. The films were then heated at 180C for 30 minutes to cure the additive network. Rigid rectangular frames measuring 65 by 10 mm were attached across the top and bottom the active area to clamp the stacked actuators and preserve prestrain in the lateral direction. The films were then cut from the prestrain support frames. A mass was hung from the actuator in order to return the actuator to the original 25% applied strain in the actuation direction. The actuation strain was monitored using a USB microscope camera and the high voltage was applied using Trek 10/10B-HS high voltage amplifier using Labview software and a National Instruments USB-

6009 digital acquisition module. For lifetime tests, a half-sine voltage signal with a frequency of 0.5 Hz was used. In the case of quasi buckled electrodes, the same procedure was followed except that the film was originally prestrained by 75% in the actuation direction.

5.2 Improved Electrode Adhesion

An additional benefit of this method for forming S-IPN films is that the electrode materials can be strongly bonded to the surface layer of the silicone by applying the electrode material before curing the additive silicone. In our case, we use single walled carbon nanotubes (SWNTs) due to their high aspect ratio, allowing for high strain actuation, and their ability to self-clear on acrylic films. Prior to curing the additive network, the films are tacky due to the presence of unreacted PDMS resin. The tacky nature of the film allows the SWNTs to adhere well to the surface of the silicone. After the curing process, the SWNTs are partially embedded in the surface of the S-IPN films. [313] Scotch tape peeling tests were performed on samples where SWNT electrodes were deposited after curing the additive network and on samples where the electrodes were deposited before curing the additive network. Images of the electrodes in the as-deposited state and after a tape test are shown in Figure 5.1. In the case of materials cured before application of the electrodes, the majority of the electrode material was removed, resulting in an entirely non-conductive electrode as seen in the second image in Figure 5.1. For samples where the electrode was applied before curing the additive network, the majority of the electrode material was retained after multiple adhesion tests. For thin to moderately thick electrode coatings, no change in the resistance of the electrodes was observed. For thicker electrode coatings, the resistance was observed to decrease. It is expected that in the case of thick electrodes, the upper layer of SWNTs is not in direct contact with the S-IPN films but instead sits on top of the more strongly bonded SWNTs underneath.

Following the work of Yuan et al. [227] the SWNT electrodes were also tested for their ability to self-clear on the S-IPN films, a process by which the electrode materials around a fault are burnt away and the actuator is able to regain its high strain performance. Figure 5.2 shows the results of a strain cycling test, wherein an S-IPN linear actuator with SWNT electrodes is actuated using a half-sine voltage signal. A localized dielectric breakdown event was induced in the sample by first applying a higher voltage; the sample was then cycled at a lower voltage to demonstrate the self-clearing capabilities of the electrodes. The sample regains its full performance after 3 cycles. The inset shows a region of an actuator that underwent several successful self-clearing events at high operating voltages. The localized breakdown sites are marked with arrows while the cleared regions can be discerned by the color change in the electrode surrounding the breakdown sites.

The incorporation of strongly bonded fault-tolerant SWNT electrodes should greatly enhance the actuation lifetime and ruggedness of S-IPN dielectric elastomer actuators. The ability of the electrodes to self-clear allows the actuators to maintain a high level of performance despite the presence of defects in the film, something that cannot be avoided during large scale production, even in cleanroom environments. Small faults due to dust particles or material inhomogeneities are among the leading causes of terminal device failure in DEAs without fault-tolerant electrodes. Secondly, by strongly bonding the SWNTs to the surface layer of the silicone film, the integrity of the SWNT electrode is maintained even during rough contact. As seen in the images above, standard electrodes can be severely damaged by direct contact which can result in permanent loss of conductivity or device failure.

5.3 Improved Multilayer Adhesion

If dielectric elastomer actuators are to gain any significant market share in any industry, multilayer actuators will be required in order to produce sufficient actuation force while maintaining low operating voltages. Strong interlayer adhesion is a requisite for good multilayer actuators. Without good adhesion, individual layers may delaminate over time resulting

Figure 5.1: SWNT electrodes on S-IPN film. Left to right: as deposited, post-cure electrode after one adhesion test, pre-cure electrode after multiple adhesion tests.

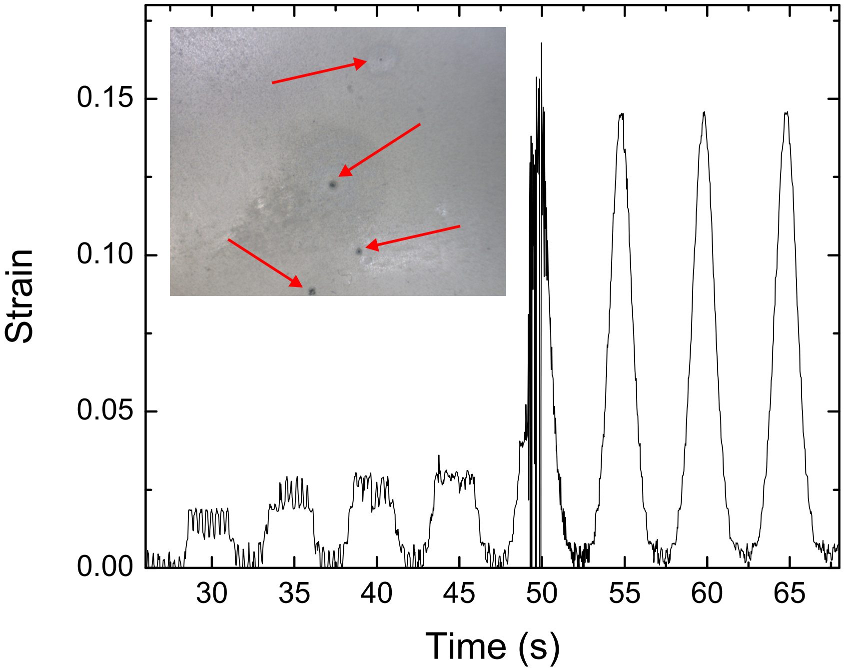

Figure 5.2: Electrode self-clearing. A breakdown event was induced in the actuator by applying a higher voltage. The sample was then actuated using a repeat half sine voltage signal at a slightly lower voltage. The induced breakdown site was successfully cleared on the 4th actuation cycle. The inset of the figure shows a region of the actuator that underwent several breakdown-clearing events. The location of the breakdown sites are marked by arrows.

in changes in device performance and perhaps terminal failure. Silicone elastomer films used for DE applications that were cured separately generally display poor bonding to most materials, including other silicones; this issue may be exacerbated with the presence of electrode materials between adjacent silicone films.

Using the S-IPN approach strong interlayer adhesion may be achieved. If individual films are first coated with electrodes and laminated to one another before curing, the interfilm bonding force is improved by a factor of ∼10, even in the presence of SWNT electrodes between adjacent silicone films (Figure 5.3). Measurements were made using a modified T-Peel test as described in the experimental section. In order to ensure a fair comparison, the HSIII sample was placed in vacuum to remove any trapped air and given the same heat treatment as the S-IPN films.

The improvement in electrode and interlayer bonding is attributed to the presence of the additive network. During the curing process at elevated temperatures, the thermal diffusion rate of the oligomeric chains can be enhanced. [314] Surface interpenetration of the oligomeric chains into the adjacent cured silicone films and SWNT electrodes is made more significant. Covalent bonds can therefore be formed in between the two films after curing, in addition to Van der Waals force, improving the surface adhesion. It is also expected that the additive silicone chains will physically entangle the SWNT electrode material, partially embedding or trapping them to the surface of the film. This technique offers an alternative to plasma treatment that requires special equipment and may cause unwanted damage to the silicone or electrode materials.

5.4 Multilayer Actuator Performance

This approach is not limited to fully-relaxed films; it can be used to improve the interlayer bonding force in highly-prestrained actuators as well, where delamination and issues related to pinholes introduced during self-clearing or tears due to mechanical fatigue may cause

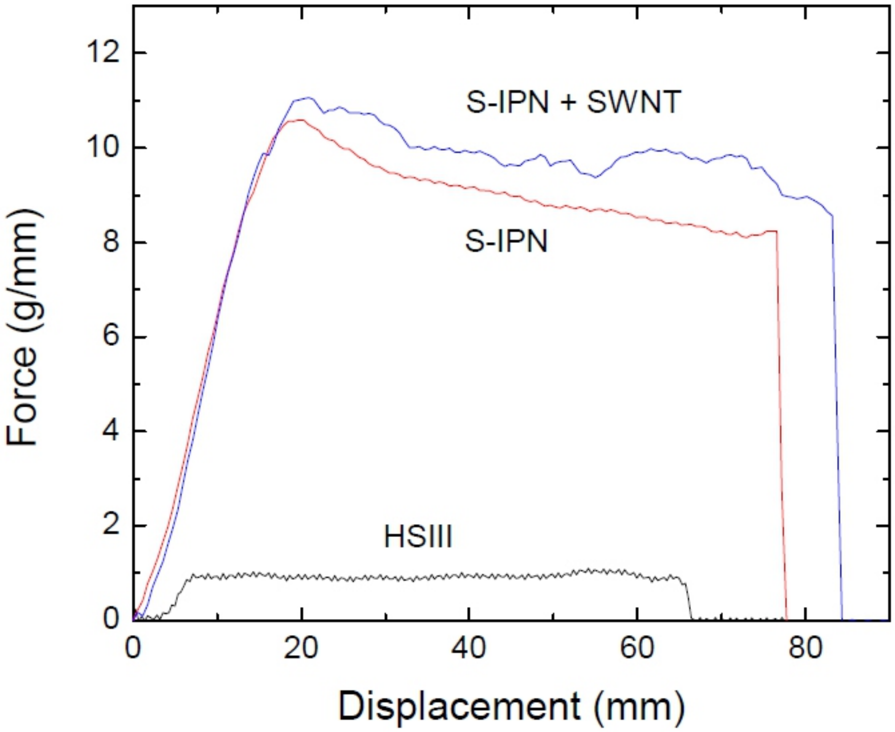

Figure 5.3: T-peel test results for two layers of HSIII, S-IPN and S-IPN with SWNT electrodes. The S-IPN samples were prepared by curing the additive network after the electrode material had been applied (for the sample with SWNT electrodes) and after the films had been laminated together. In order to ensure a fair comparison, the HSIII samples were placed in vacuum to remove any trapped air bubbles and annealed at high temperature prior to testing.

individual films to separate from their neighbors resulting in changes in performance or device failure. The improved bonding between highly prestrained layers prevents issues related to delamination and anchors films in place in the event of localized dielectric breakdown events or fatigue-induced defects.

To demonstrate the performance of prestrained multilayer actuators fabricated using this method, multilayer S-IPN devices were prepared by prestraining S-IPN films by 200x25% prior to curing the second network, spray depositing electrodes, laminating several films together, and curing the second network. The actuators were tested in the 25% prestrain direction using a voltage ramp at 20 V/s while driving a load. Figure 5.4a shows representative results for a 2 layer actuator. A schematic representation of the actuator is shown in the inset of Figure 5.4a. A maximum actuation strain in excess of 60% is possible which compares favorably with other high performance DE materials as well as natural muscle. [2–4, 307].

Cycle testing was also performed on the prestrained actuators; Figure 5.4b shows representative results, with a 3 layer film using a half-sine wave signal at a frequency of 0.5 Hz carrying a load of 83g. The actuator was cycled over 30,000 times at over 20% linear actuation strain while driving a load. To our knowledge this is the first demonstration of a free-standing multilayer dielectric elastomer actuator capable of maintaining such a high level of performance over so many cycles. It is important to note the several self-clearing events were observed during actuation, indicating that self-clearing is still possible even with a completely buried DE layer.

Dielectric elastomer actuators are often heralded as artificial muscles as they possess several muscle-like properties [Bar-Cohen2004, Brochu2010]. In Figure 5.4a we demonstrated that multilayer S-IPN actuators can be actuated to strains in excess of 65% which compares well with the peak performance of natural skeletal muscle; however, natural muscle is also capable of repeated strains in excess of 40%. [2, 44] In order to determine if true muscle-like performance is indeed possible, several actuators were tested at 40% strain. Figure 5.4c shows results for a 2 layer actuator being cycled using half-sine input signal carrying a load

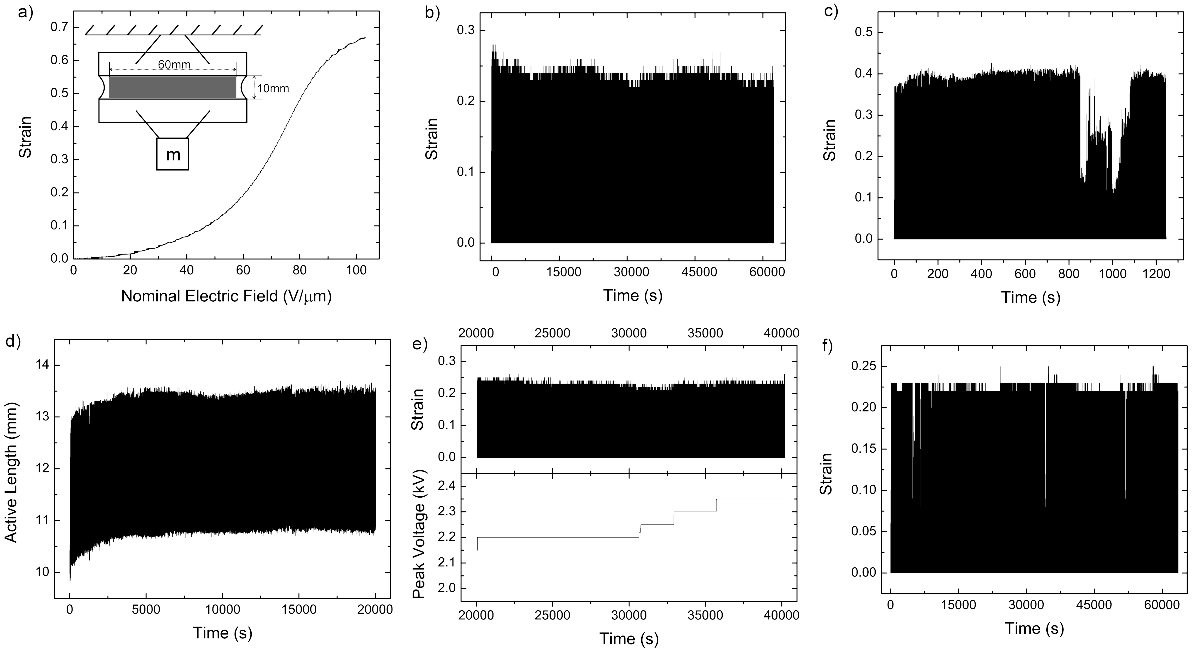

Figure 5.4: a) Actuation strain curve for a 2-layer prestrained S-IPN actuator with a schematic of the actuator shown in the inset. b) Cyclic testing of a 3-layer S-IPN actuator at >20% strain using a half-sine voltage signal at 0.5Hz and driving a load of 83g showing more than 30,000 cycles. c) Cyclic testing of a 2-layer S-IPN actuator at ∼40% strain using a half-sine voltage signal at 0.5Hz and driving a load of 57g. d) Demonstration of the effects of creep on the length of the active area; the actuator gradually lengthens over time and is most prevalent at short to moderate time scales. e) Example of a gradual loss in strain performance with time as a result of electrode degradation. In order to maintain the same level of actuation strain the applied voltage must be increased to compensate for the increase in resistance of the electrodes. f) Cyclic testing of a 2-layer S-IPN actuator with quasi-buckled electrodes using a sinusoidal voltage signal at 0.5Hz. The peak actuation voltage was maintained at 1.85 kV for the duration of the test and no loss in performance was observed over more than 30,000 cycles.

of 57g. The actuator was capable of 500 cycles at 40% strain and also demonstrated the ability to recover full actuation strain after several persistent breakdown and self-clearing events. The actuator lost function shortly after the timeframe shown, but the results indicate that repeated actuation cycles matching the strain performance of natural muscle are indeed possible and that fault-tolerance is preserved at these high strains.

For most long-lifetime actuation tests, a gradual reduction in the apparent strain was observed. The reduction in strain can be attributed to two main factors that affect the strain in different manners. The first factor is creep which manifests itself as a gradual increase in the passive length of the actuator with time (Figure 5.4d). This is most pronounced in the early stages of actuation since the time-scale for creep is relatively short (on the order of minutes or hours). The second factor is a gradual increase in the electrode resistance with time. As the material is strained and relaxed and current flows across the electrodes, their resistance increases gradually. The resistance increase results in an increased drop in the potential being applied across the electrodes, thus reducing the electric field across the elastomer film. Figure 5.4e shows typical results for the multilayer actuators tested. As the number of cycles increases the strain gradually drops, necessitating an increase in the applied voltage to maintain the strain performance. Eventually, higher applied voltages can lead to an increased probability of corona discharge and dielectric breakdown.

Localized dielectric breakdown also plays a critical role in the long-lifetime actuation stability of these actuators as well. In the event of a dielectric breakdown, the electrodes around the fault must be cleared away before the actuator can resume its normal functionality. The primary issue with self-clearing in general is that successive clearing events reduce the functional part of the active area and generate small holes in the film itself. After a sufficient number of clearing events the actuator begins to drop in actuation strain and the probability of failure due to tearing increases.

While self-clearing of dielectric breakdown events is advantageous for long lifetime operation, there also exists the possibility of corona discharge along the electrodes without the presence of a breakdown event. Corona discharge is the result of partial breakdown of the air around the electrode at the points of highest electrical stress. It has been observed numerous times, largely in the event of a dielectric breakdown event and is characterized by a buzzing noise and blue flashes. A faint smell of ozone may also result from continued corona discharging. Corona discharging along the surface of an electrode can damage the electrode and reduce conductivity, and in some cases can damage the underlying elastomer which may result in a dielectric breakdown event. Based on numerous observations of this phenomenon and the previous work by Yuan et al. on the subject [227, 229] it is believed that corona discharge along the surface of the electrode is the result of a drop in the conductivity of the electrodes, which is more prevalent at high strains or after a large number of cycles. As the electrode degrades and resistance increases the likelihood that the charge on the electrode will find a less resistive path through the air is more likely. The likelihood of corona discharge is further exacerbated by the field amplifying nature of carbon nanotubes. Due to their high aspect ratios and sharp tips, SWNTs can amplify the electric field. Yuan et al. [229] showed that corona discharge between parallel SWNT electrodes across a 4 mm gap can take place at 6 kV when operated in open air.

5.4.1 Quasi-Buckled Electrodes

In order to alleviate the issues related to gradual electrode degradation and corona discharge along the electrode surface, the use of quasi-buckled electrodes was implemented. This work was motivated by the results from Chapter 12 in which stretchable electrodes for energy harvesting purposes were prepared by spraying electrodes onto highly prestrained S-IPN films prior to curing the additive network. The additive was then cured at high temperature which effectively locks in the electrode and the films were allowed to relax. The electrodes could then be stretched to their original length with only negligible increases in resistance and could be cycled several thousands of times without an increase in resistance. When stretched beyond their original length, a large resistance increase was observed and the change was partially irreversible.

For actuator testing, samples were prestrained 200% in the transverse direction and 75% in the actuation direction with dimensions of 65mm and 10mm in the transverse and actuation directions respectively. Prior to actuation, the films were relaxed in the actuation direction to approximately 7-7.5mm, maintaining 22-30% prestrain, thus allowing for between 30 and 40% strain to reach the initial length of 10mm.

Results for a 2 layer actuator with quasi-buckled electrodes cycled using a sinusoidal voltage input with a peak value of 1.85 kV and a frequency of 0.5 Hz are shown in Figure 5.4f. The actuation strain remained stable for over 30,000 cycles despite the occurrence of several dielectric breakdown events. These results indicate a drastic improvement in the long-lifetime stability of the electrodes which will allow for improved repeatability and stability during long-lifetime actuation.

5.5 Conclusions

It has been demonstrated that the S-IPN technique can be leveraged for preparing films with strongly bonded SWNT electrodes, improving electrode adhesion and enabling self-clearing. Improved adhesion between adjacent layers in multilayer actuators has also been demonstrated. These improvements have been used to fabricate multilayer actuators with improved robustness and performance. A prestrained three-layer actuator fabricated using this process demonstrated over 30,000 cycles of actuation at over 20% strain while driving a load and a two-layer actuator demonstrated over 500 cycles at $\sim$40% strain. Issues related to a gradual degradation in strain performance were also addressed. It was found that by employing quasi-buckled electrodes the peak strain of the multilayer S-IPN actuators can be maintained for over 30,000 cycles at $>$20% strain.

CHAPTER 6

Summary and Future Directions of this Work

6.1 Conclusions

Dielectric elastomers are a promising actuator technology with the potential for providing high strain, high energy density, robust actuation in a soft, flexible, stretchable and cost effective package. There are still, however, several hurdles that must be overcome if dielectric elastomers are to break into the commercial market in a significant way.

In this part of the dissertation, it was demonstrated that long lifetime actuation can be achieved in Wacker Silpuran 6000/10 soft silicone actuators at moderate performance values. The effects of crosslink density, prestrain and mechanical load on actuation strain were explored. It was found that decreasing crosslink density results in a decrease in modulus while maintaining the ability for high strain actuation. Increasing prestrain in the transverse direction increases the maximum actuation strain while increasing the required electric field. Increasing prestrain in the actuation direction increases the required electric field but also increases the load that the actuator can carry and therefore increases the work density. In order to maintain a low electric field requirement while maximizing performance a prestrain of 200x25% was selected. It was shown that when combined with self-clearing single walled carbon nanotube electrodes, the prestrained soft silicone actuators are capable of over 85,000 cyles at 20%.

It was shown that nanocomposites consisting of Silpuran 6000/10 silicone and TiO_2 nanoparticles coated with short PDMS chains are capable of increasing the work density of the actuators while maintaining the same actuation performance as for the neat silicone. The TiO_2 nanoparticles serve to increase both the permittivity of the composite and the stiffness by acting as physical crosslink points. These increases combine to boost the work density while offsetting one another to maintain high strain performance and relatively low driving voltages.

Silicone interpenetrating polymer network elastomers (S-IPNs) were prepared using a room temperature vulcanizing (RTV) liquid silicone rubber (LSR) in conjunction with a high temperature vulcanizing (HTV) LSR. The RTV host and HTV were comixed at various ratios in a co-solvent. The solution was then drop cast onto treated glass and the solvent was allowed to evaporate. Following that the RTV silicone was allowed to cure, the film was then peeled from the glass and prestrained onto a rigid frame, then heat treated to cure the HTV component. The films were then relaxed and part of the applied prestrain was preserved in the resulting free-standing all silicone interpenetrating polymer network elastomer. The films demonstrated a large improvement in actuation strain in both freestanding linear actuation and diaphragm actuation configurations than the pure host elastomer.

The S-IPN process was also leveraged to improve the bonding force between the elastomer film and single walled carbon nanotube (SWNT) electrodes as well as improve the bonding force between adjacent layers in multilayer actuators. The technique was used to fabricate highly prestrained freestanding silicone actuators capable of over 60% linear strain and a cycle life of over 30,000 cycles at 20-25% strain and 500 cycles at 40% strain. The strongly bonded SWNT electrodes also demonstrated the ability to self-clear in the event of a localized dielectric breakdown, which contributed to the long-lifetime performance of the actuators. Improved electrodes utilizing a quasi-buckled structure were implemented to help reduce issues relating to a gradual increase in resistivity of the electrodes during long-lifetime testing. These improvements lead to improved actuation longevity and stability making these dielectric elastomer actuators more interesting for commercial applications.

6.2 Future Work

6.2.1 Fatigue Testing

Long-lifetime actuation at high strains is the goal for dielectric elastomer actuator. Gaining a better understanding of the fatigue mechanisms that play a part in device degradation and failure would play an important role in reaching that goal. The fatigue lifetime study of dielectric elastomers could be approached using four concurrent testing procedures: (1) electromechanical fatigue testing wherein a free-standing actuator with a load is actuated electrically; (2) electrical fatigue testing wherein an in-plane actuator is driven at a constant voltage; and (3) mechanical fatigue testing wherein a dielectric elastomer is cyclically stretched mechanically. Coupling the results from these tests with creep and stress relaxation data, it should be possible to discern the relative importance of mechanical and electrical components to material degradation. By monitoring the resistance of the electrodes during these tests at regular intervals it should be possible to determine if electrode degradation plays any significant role in the reduction in performance with time or terminal device failure.

6.2.2 S-IPN Formulation

The S-IPN formulation presented here was designed to minimize the required driving field through the selection of a very soft host elastomer. The drawback of this approach is that the work density is not very high. Preliminary attempts to combine the S-IPN approach with TiO_2 proved unsuccessful. It is likely that the TiO_2 nanoparticles act to inhibit the curing process for the RTV host silicone. The choice of a different host silicone with different curing chemistry may help eliminate this issue.

Different host and additive elastomers may also be good candidates. Preliminary results on hard silicone rubber (HSR) peroxide cured silicones as additive had mixed results. The composites were able to preserve prestrain; however, some phase segregation was observed as the HSR silicone fell out of solution and aggregated during solvent evaporation. The resulting films were translucent and the properties were poorer than those reported in chapter 4. The use of a more rigid silicone host would result in improved work density which may be worth examination. The choice of a different silicone host elastomer may also result in improvements to the maximum actuation strain. In order to eliminate issues related to pull in, the choice of a materials system that has a monotonically increasing stress-strain relationship would be ideal.

The introduction of high-polarization groups onto the host or additive network would help to improve the strain sensitivity of the actuators assuming they do not affect the polymerization of either silicone network.

6.2.2.1 S-IPN Fabrication

The use of a UV curable additive would improve both the throughput and yield of the S-IPN fabrication process. The thermal stresses introduced during high temperature curing cause many films to break around the edges of the metal frames.

In addition to altering the curing process, it may be beneficial to prestrain the S-IPN prior to curing the additive by different amounts. Increasing the applied prestrain will likely result in increased locked-in prestrain in the free-standing films, though care must be taken to ensure that the level of applied prestrain does not result in a decreased yield.

6.2.3 Improved Electrode Stability

The incorporation of quasi-buckled electrodes improved the durability of the carbon nanotube electrodes by ensuring that they are not stretched beyond their as-deposited state. However, issues relating to electrode damage due to corona discharge and dielectric breakdown are still problematic in the long term. Yuan et al. showed that these issues can be partially alleviated by coating the surface of the electrodes with a dielectric oil which serves to quench the corona discharging. [229] In order to determine if this is possible for silicone actuators we have attempted to coat the silicone with the same dielectric oil; however, the oil did not wet the surface of the silicone or electrode sufficiently to have any tangible effect. Silicone oil was tested in place of the dielectric oil but caused the silicone elastomer to swell resulting in damage to the electrode material. Silicone gel materials were also tested for top-coating the electrodes; however, no improvement was observed in this case either. It is possible that during a dielectric breakdown event, the thin top-coated layer can be burnt off resulting in exposure of the electrodes to air, thereby allowing corona discharging to occur. Additional materials can be tested to determine if they are effective at quenching corona discharge for silicone actuators with carbon nanotube electrodes.

Part II

Dielectric Elastomer Generators

CHAPTER 7

Introduction

While hydraulic, pneumatic, and electromechanical systems are mature and proven energy harvesting technologies, they are not without their limitations. Many of the systems can be relatively complex and consist of many moving parts that can become damaged in harsh conditions. Robust designs capable of withstanding marine environments will be expensive. Alternative approaches toward energy conversion may provide benefits over these mature technologies and open the door to newer, more effective designs. It has been proposed that smart materials such as piezoelectric ceramics and electroactive polymers can be used to harness mechanical energy. Piezoelectric materials have demonstrated the ability to harness ambient vibrations for use as sensors and generators [315–317] and have been incorporated into several energy-scavenging designs including human motion harvesting backpacks. [318, 319] The main limitations imposed by piezoelectric ceramics are their stiffness, brittleness, and cost. They are suitable for applications where the ambient energy is in the form of small-amplitude high-frequency vibrations, essentially precluding them from use in many applications. The term electroactive polymers refer to the broad class of polymeric materials capable of responding to electrical stimuli and includes the subcategories of polymer electrets, polymer piezoelectrics, electrostrictive polymers, ionic polymer-metal composites, conducting polymers, and dielectric elastomers among others. [20, 320] These materials possess the general advantage of being mechanically flexible, lightweight, and easily processable. A number of electroactive polymers have been explored for use as generators. Electrostrictive polymers have been shown to possess output electrical energy densities as high as 39mJ/cm^3 and mechanical-to-electrical conversion efficiencies of about 10%. [321–323] However, these materials are not particularly suited for use in many applications as they are limited by high stiffness and small deformations.

Recent advances in dielectric elastomer (DE) technology could enable a new generation of energy harvesting devices with high efficiency and low cost. DEs consist of a thin elastomer film sandwiched between compliant electrodes, essentially forming an elastic variable capacitor. The capacitance (C) across the elastomer can be varied by adjusting the area (A) and the distance between the two electrodes (z):

$$C = \epsilon_r \epsilon_0 \frac{A}{Z} \tag{7.1}$$

where ϵ_r is the relative dielectric constant of the elastomer (typically between 2 and 10) and ϵ_0 is the permittivity of free space.

Table 7.1 shows a brief comparison of DE generators with other typical energy harvesting technologies. DE generators are capable of outperforming both piezoelectrics and electromagnetic generators in terms of specific energy density and display relatively high efficiency values. Issues related to reliability, control circuitry, and coupling to many energy sources still remain; however, their soft and compliant nature presents an interesting contrast to other generator technologies and with some additional work, DE generators should be capable of finding applications in certain niche markets and can perhaps supplant electromagnetic and piezoelectric generators in other areas.

7.1 DE Generator Fundamentals

The generator mode of dielectric elastomers is essentially the reverse of the actuator mode; in the generator mode an input of mechanical energy, coupled to deform the dielectric elastomer, results in an increase in electrical energy. DEGs can be operated in several energy harvesting cycles, the simplest and easiest to implement is the constant charge cycle. If a mechanically stretched DE film is loaded with a fixed amount of charge and the film is subsequently

Table 7.1: Comparison of Energy Harvesting Technologies [324]

Technology	**Stiffness Range**	**Specific Energy Density (J/g)**	**Frequency Range**	**Maximum Efficiency**
Dielectric Elastomer	0.1 - 10 MPa	0.4 (active material only) 0.05 typical	Low to Mid	>50%
Electromagnetic	N/A	0.004	Mid to High	<20%
Piezoelectric ceramic	50-100 GPa	0.01	Mid to High	>50%

allowed to relax without allowing any charge to escape, like charges will be brought closer together and opposite charges will be pulled further apart, resulting in an increase in the electronic potential energy of the system. The difference in potential between the stretched and relaxed states can be used to produce useful energy. Figure 7.1 illustrates the two states.

Owing to their near-incompressibility, a change in the area of the DE results in a concomitant change in the thickness. Depending on the generator configuration, this means that the capacitance can vary with the strain (if stretched uniaxially with the length longer than the thickness), with the strain squared (is stretched biaxially or uniaxially in a pure shear mode), or at some intermediate value. Typically it is advantageous to have capacitance change with strain squared, so that care must be taken when designing a DE energy harvesting device.

The electrical energy (e) stored on the film at any given time is given by:

$$e = 0.5CV^2 = 0.5\frac{Q^2}{C} = 0.5QV = 0.5\frac{Q^2 P}{\epsilon_r \epsilon_0 A^2} \tag{7.2}$$

where Q is the charge on the electrodes, and P = Az = constant (the volume of the

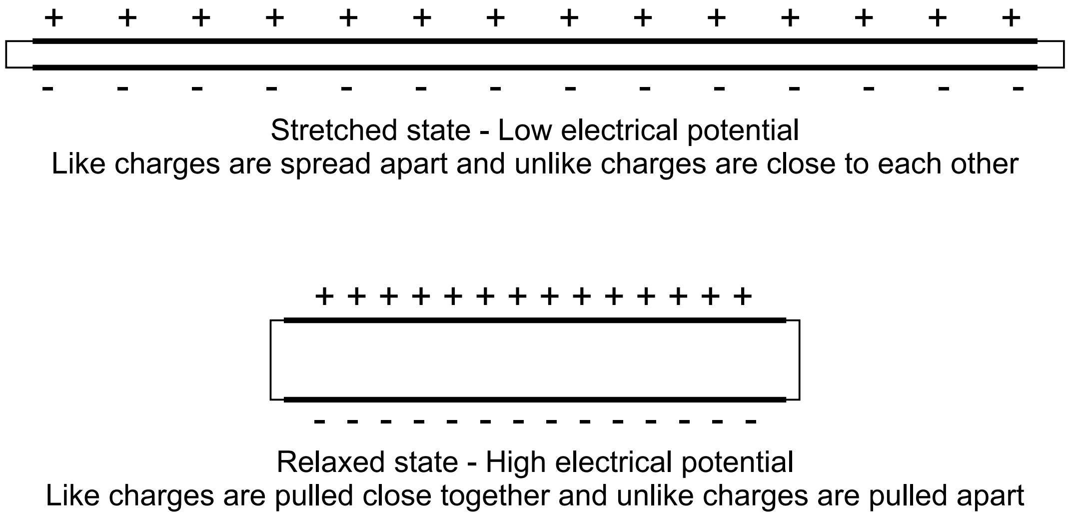

Figure 7.1: Basic mechanism of dielectric elastomer generator mode.

film). The electrical energy produced per cycle (e_{gen}) can be found by taking the difference in potential between the contracted and stretched states:

$$e_{gen} = e_u - e_s = 0.5\frac{Q^2 P}{\epsilon_r \epsilon_0}\left(\frac{1}{A_u^2} - \frac{1}{A_s^2}\right) = 0.5 C_s V_b \left(\frac{C_s}{C_u} - 1\right) \tag{7.3}$$

where the subscript u refers to the relaxed (unstretched) state and s to the stretched state. Vb is the bias voltage applied to the film in the stretched state. The energy output will thus depend strongly on the change in area between the stretched and relaxed states and on the bias voltage.

Other DEG energy harvesting cycles also exist:

- The constant voltage cycle - the voltage is kept constant during relaxation and energy is generated though the flow of charge onto and off of the film.
- The constant field cycle the electric field is kept at a constant value during relaxation and energy is generated by both the flow of charge onto and off the film and the increase in electrical potential of charges on the film.

The different energy harvesting cycles are represented in Figure 7.2. For each cycle, the

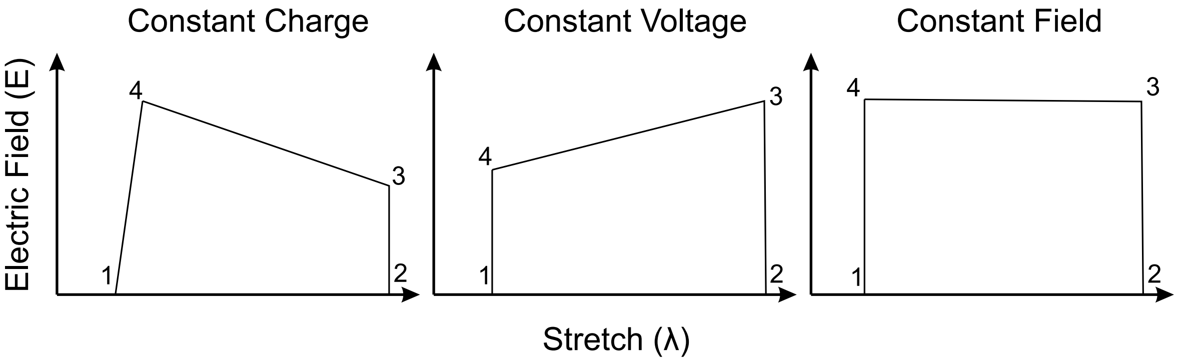

Figure 7.2: Energy harvesting cycles for constant charge, constant voltage, and constant field.

elastomer goes through 4 phases: 1) the dielectric elastomer is stretched mechanically with zero charge on the film; (2) charge is injected onto the film; (3) the film is allowed to contract while either the charge, voltage or electric field is kept constant; (4) once the film reaches the field-supported regime, charge is gradually removed to return it to its zero charge, zero strain state. Graf and Maas [325] have shown that of the three energy cycles, the constant field cycle is capable of generating the most energy while the constant charge cycle minimizes losses. They have shown that the relative energy output of their systems can be related to the area change ($\alpha = A_{min}/A_{max}$) of the DEG in the following ways:

Constant Charge:	$e_{gen,Q} \propto (1-\alpha^2)$
Constant Voltage:	$e_{gen,V} \propto (1-\alpha^2)$
Constant Field:	$e_{gen,E} \propto 2ln\left(\frac{1}{\alpha}\right)$

In considering the selection of the energy harvesting cycle, we must also consider the complexity of the power electronics. For the constant charge cycle, simple switches or transistors can be used to connect and disconnect the DEG from the charging electronics and discharging electronics. For the constant field cycle, the control system would be much more complex. We will therefore focus our initial efforts on the constant charge cycle with the knowledge that performance improvements can be achieved by increasing the complexity of the power system.

From the above equations we can see that DEGs produce the most energy at high strains (large change in capacitance) and at high bias voltages (larger amount of charge on the film). The amount of energy harvested by a DEG is limited by 4 main factors:

1. Dielectric breakdown a material property that limits the maximum applied field (or bias voltage).
2. Maximum elongation the maximum strain that the elastomer can withstand prior to breaking.
3. Electrostatically-induced stresses Electrostatic Maxwell stresses induced by the increase in electric field during the relaxation step of the constant charge cycle can prevent the elastomer from fully relaxing, which limits the change in capacitance and reduces the output energy.
4. Parasitic losses losses due to leakage current through the elastomer film, resistive losses on the electrodes, and viscoelastic losses during stretching and relaxation.

7.2 Materials

Very little research has gone into the development of materials specifically for DE generator purposes. Materials developed with actuation in mind may not be suitable for generator purposes. For DE generators, certain material parameters are of greater importance, including the resistivity of the dielectric and resistance of the electrodes. The ideal DE material will have high energy density, low viscoelastic loss, and overcome dielectric and mechanical failure as a result of fatigue after repeated deformation. Prestrain has been found to effectively increase the dielectric energy density of acrylic elastomers to the unprecedented high value of 3 J/g in such soft, highly deformable materials. Prestrain, however, necessitates the use of a rigid frame that adds significant parasitic mass. Previous results from our lab demonstrate that the use of an interpenetrating network (IPN) of elastomers can eliminate the need for such frames [172, 201]. The IPN films are based on highly prestrained acrylic elastomers combined with an additive network. The tension in the acrylic network is internally balanced by the compression in the additive network. Thus, the advantages of prestrain are preserved within the acrylic elastomer without requiring an external frame.

Silicone materials also show promise for energy harvesting purposes as they generally possess a wide operating temperature range, which is important for most applications, low viscoelasticity, and are generally resistant to many environmental factors, including moisture. Silicone materials, however, are known to have lower energy densities owing to their lower breakdown fields when compared to highly prestrained VHB acrylic elastomers.

Electrode materials are also of paramount importance in dielectric elastomer generators as they must maintain a relatively low resistance up to strain in excess of 100% and must be capable of remaining conductive after thousands of stretch-relaxation and charge-discharge cycles. A high resistance will impact the ability of the DE generator to harvest energy in two ways: (1) increased RC charging time ($\tau = RC$) which may prevent the DE from fully charging, and (2) increased resistive losses across the electrodes, causing additional electrical energy to be lost due to resistive heating. Factor (1) above is especially important in cases of large capacitance, such as large scale DE generator devices, or in cases of moderate to high frequencies, when the time available to charge the DE is limited.

The ability of the electrode material to self-clear, as described in Chapter 1 of Part 1, is also of paramount importance. Intrinsic defects introduced during material preparation and device fabrication, as well as fatigue-induced defects, may result in a region of reduced electrical breakdown strength. Once the fault reaches a critical size, the device will suffer from a localized dielectric breakdown event, resulting in an electrical short through the dielectric. An electrode material that is capable of self-clearing will neutralize the fault. This is typically accomplished using thin metal coatings or thin carbon-based electrode materials that can burn off when subjected to high leakage currents. Single walled carbon nanotube electrodes are a good example of a self-clearing electrode material and they possess the additional advantage of having a large aspect ratio, allowing them to remain in contact with one another when stretched to high strains.

A more detailed review of DE materials and electrodes can be found in Chapter 1.

7.3 Energy Harvesting Circuitry

7.3.1 Equivalent Circuit

Dielectric elastomers are typically modeled as perfect capacitors. Unfortunately, the elastomer materials used in DE devices are not perfect insulators, and some energy is lost via charge leakage through the elastomer layer. Additionally, the resistance of the electrodes is typically too large to ignore, especially when the DE is in a high strain state. To accurately model the electrical behavior of a DE generator, an equivalent circuit for the DE is required. Figure 7.3 shows the equivalent circuit for a DE device. R_{E1} and R_{E2} represent the resistance of the electrodes. As the device is stretched, the resistance of the electrodes will typically increase. In some cases this increase can be several order of magnitude. The elastomer itself can be treated as a capacitor in parallel with a resistor. C_{DE} represents the capacitance of the device and increases with strain as the electrode overlap area increases and the distance between the electrodes decreases. R_{DE} represents the resistance of the elastomer and also varries with the stretch state of the elastomer. The finite resistance of R_{DE} means that some charge is lost by leakage through the dielectric. For some materials, these leakage losses can be significant.

7.3.2 Basic Energy Harvesting Circuitry and Current Issues

Since dielectric elastomer generators operate as capactive energy harvesters, a voltage source is required in order to harvest energy. The most basic circuit requires a high voltage input source, two switches and a load (Figure 7.4). If efficiency is not important, the switches can be replaced with diodes. For a constant charge cycle, when the DE is in a high strain, high

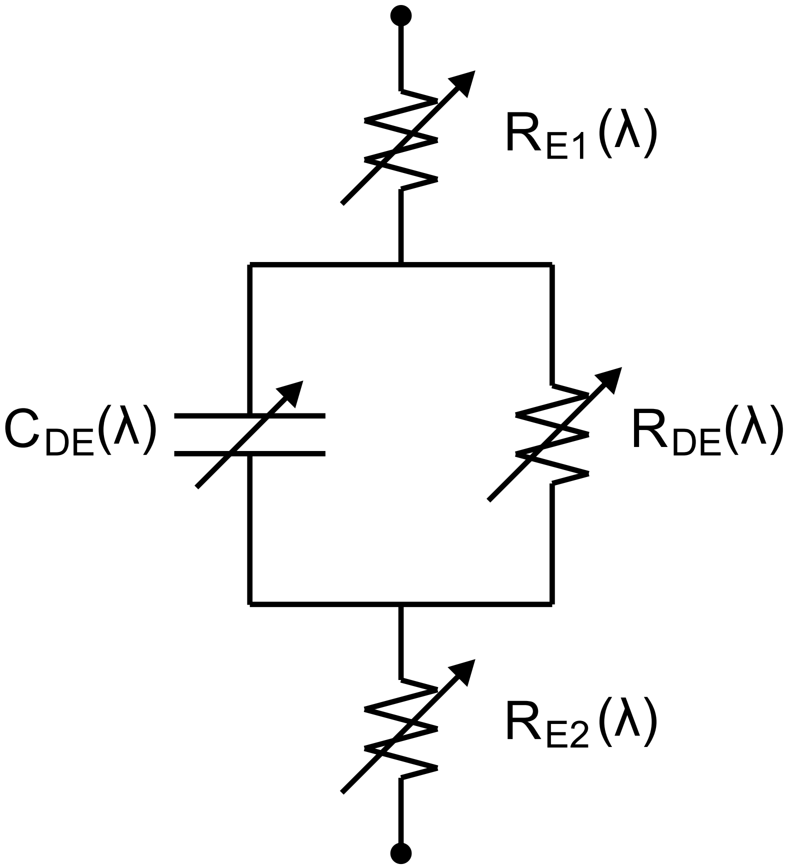

Figure 7.3: Equivalent circuit for a dielectric elastomer. R_{E1} and R_{E2} represent the resistance of the electrodes, C_{DE} and R_{DE} represent the capacitance and resistance of the elastomer. All values are dependent on the stretch state (λ) of the DE; R_{E1} and R_{E2} both increase as the DE is stretched, C_{DE} increases with stretch and R_{DE} decreases with stretch as area increases and thickness decreases.

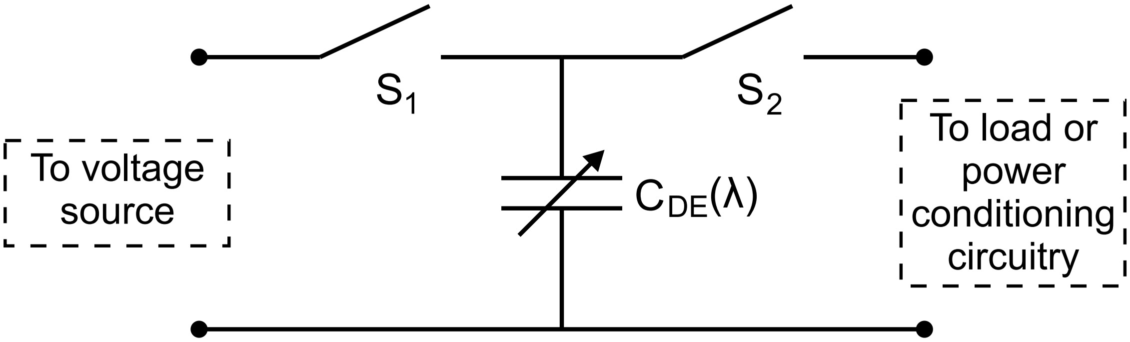

Figure 7.4: Basic energy harvesting circuit for a dielectric elastomer generator. A bias voltage is supplied by a voltage source through switch S_1 when the DE is in the stretched state. After the DE has relaxed, switch S_2 is closed and the charge flows to a load or power conditioning circuitry.

capacitance state, switch S_1 is closed and the DE is charged by a voltage source. After the DE has relaxed, switch S_2 is closed and the charge is collected by a load or power conditioning circuitry.

The same circuitry can be used to implement a simple constant voltage energy harvesting cycle. The primary issue with such a simple circuit is that the state of the DE must be known or be easily predictable. Unfortunately, this will not be the case for most applications and some form of feedback system is required to control the switches.

More complex energy harvesting circuitry is also possible that can approach the performance limits of dielectric elastomers and harvest a larger portion of the available energy with the implementation of a true constant field cycle being the ultimate goal. Such a control system, however, requires more complex control circuitry, an issue that is further exacerbated by the variability in most energy sources.

Increased circuit complexity leads to additional costs and additional power requirements. In some cases these requirements are justified while in other they may make the device economically non-viable or consume more power than they save.

The choice of appropriate energy harvesting circuitry is made more difficult by a relative dearth in available electrical components. Very few applications require the high voltage and low leakage current that DE devices require. The result being that components may be very expensive or are entirely unavailable. These issues appear to be improving, however, there is still significant progress that can be made.

SRI has developed comprehensive energy harvesting and conditioning circuitry with an efficiency of 78%. [324, 326], though details have not been published.

7.3.3 Self-Priming

DEGs require a seed charge in order to function; they are not capable of harvesting energy from any source without first being biased by an external electrical source. The DEG then increases the potential energy of the seed charge. This seed charge can be provided by any external source such as a capacitor, battery, an external connection to the grid, a solar panel, etc. As described above, the energy produced by a DEG increases with increasing applied bias. For efficient and high power operation a bias between 1000 and 5000 V may be required. To achieve potentials this high a high voltage power conversion unit is often required. The loss of charge due to leakage through the DEG itself or through external circuitry must also be compensated.

McKay et al. have developed a method by which a DEG is able to boost the applied seed voltage without the requirement for an external high voltage power conversion unit. [327–329] By making use of the voltage-boosting capabilities of the DEGs themselves, McKay et al. have developed a self-priming circuit through which the DEG can replenish charge lost through leakage and external circuitry and boost the bias of the seed charge. A basic self-priming circuit, illustrated in Figure 7.5, consists of a pair of capacitors and three high voltage diodes. When the DEG is in a high-voltage state (i.e. following relaxation in the constant charge cycle), the equivalent circuit consists of the two capacitors in series. In this state the current flows from node A to node B and the DEG transfers energy to the self-priming circuit. When the DEG is returned to the stretched state, the self-priming circuit will charge the DEG. In this case the equivalent circuit consists of the two capacitors in

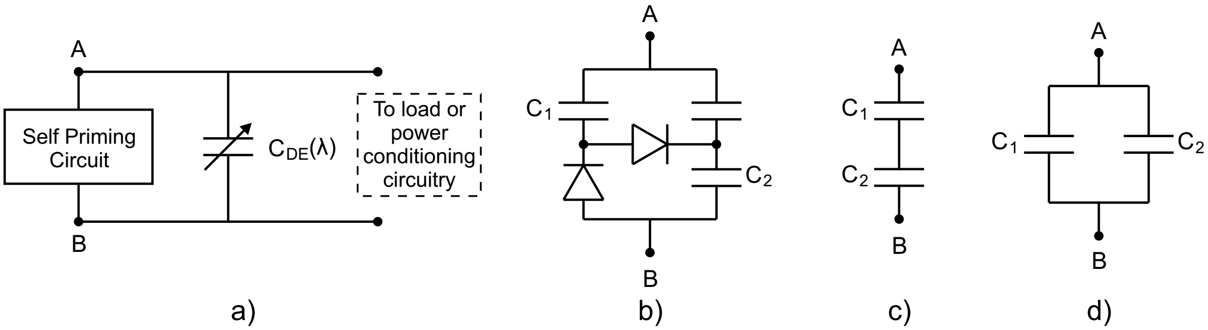

Figure 7.5: Self-priming circuit. [327] The circuit is connected in parallel with the DEG and load as seen in (a). A simple self-priming circuit (b) can be formed using two capacitors and three high-voltage diodes. The circuit toggles between high voltage (c) and high charge (d) states.

parallel; this is a high charge configuration and energy flows from the self-priming circuit to the DEG, replenishing the charge on the film.

In order to transfer charge between the self-priming circuit and the DEG, the voltage gain on the DEG during relaxation must be greater than then change in voltage when the self-priming circuit toggles between series and parallel configurations. If C1 and C2 in the circuit above are equal, then the voltage across the DEG must double for self-priming to occur. Increasing the complexity of the system can reduce this requirement. [327]

The requirement for external circuitry can be further reduced by employing the concept of dielectric elastomer switches. [330] These switches are fabricated by applying a low aspect ratio electrode material in a zig-zag pattern on the surface of the DE film. If the DE is stretched, the electrode resistance can increase by several orders of magnitude, effectively preventing any charge from flowing. This eliminates the requirement for external diodes or switches. The external capacitors can also be replaced by additional DE components that can be arranged in an antagonistic manner so that they alternate between high and low capacitance states. [328] The DE switch concept was used to create ”self-contained” DE generators that only need to be connected to an external circuit to provide a small seed charge and to collect the higher potential charge once it reaches a sufficiently high potential. [329]

7.4 Applications

The flexible form factor permitted by dielectric elastomers means that they are not limited to a particular shape or size and can thus be tailored to meet different application requirements, often being incorporated into existing structures without the need for constructing costly support structures. Several dielectric elastomer-based generators have been demonstrated to date including a boot generator [324,326,331,332], a polymer engine [333], a hand-pumped small-scale power-generation device [276], a knee-movement energy harvester [334], and wave power generators [324,326,332,335,336]. Recently, SBM offshore have unveiled an impressive prototype of an ocean wave energy harvester for large scale energy production that they hope to deploy off the coast of France. [337]

Of these applications, harvesting energy from ocean waves and human motion, particularly from walking, appear the most promising. Dielectric elastomers operate best at relatively high strains and low to moderate frequencies and are thus optimally suited to wave energy harvesting. Energy harvesting is also most efficient at relatively high electric fields, in the range of 100 V/μm. For a typical film thickness of 20 μm this works out to be 2 kV. The higher voltage will allow for more efficient transmission of power back onshore without the need for onboard transformers.

For harvesting energy from human motion, lower operational voltages are preferred. Thanks to the breadth of elastomers available, it is possible to select a material and tune its properties to effectively harvest energy from human motion. By selecting softer materials, the energy density may decrease, but the optimum voltage will also be lowered, as will the burden placed on the user to stretch the material. Harvesting energy from walking, jogging, or running is particular interesting as large forces are transmitted during each footstep. A device embedded into a shoe, such as the device demonstrated by SRI [324,326,331,332], or incorporated into the flooring of a high pedestrian traffic area could produce sufficient energy to recharge portable electronics, or power local electronic devices, such as lights, signs, and guides.

7.5 Overview of this Part of the Dissertation

This part of the dissertation focusses on modeling the performance of dielectric elastomer energy harvesters with the goal of determining what material and operational factors influence device performance in terms of generator energy density and energy conversion efficiency. Based on the results of this analysis, an attempt is made to develop materials that are better suited for energy harvesting purposes. Finally, novel designs for harvesting energy from ocean waves and human footsteps are explored.

In Chapter 8 a simplified dielectric elastomer energy harvesting model is developed to explore the effects of various materials and operating parameters on both the amount of energy generated and the efficiency of dielectric elastomer generators. It is shown that high energy output and efficiency can be obtained in various materials systems. The amount of energy generated increases with increasing values of bias voltage and applied stretch while the efficiency is shown to depend strongly on bias voltage but only weakly on stretch. Increasing the dielectric constant can have significant impacts on the amount of energy generated in certain systems and that stiffening the elastomer has the main effect of shifting the regions of high efficiency to lower strains and larger voltages. Using these results as a basis, one particular material system is explored experimentally and compared with the results from our model. The impacts of electrode resistance and elastomer viscoelasticity are also explored.

In Chapter 9 a simple analytical relationship for the efficiency of a constant charge dielectric elastomer energy harvesting cycle is derived for the case of pure shear. The relationship takes into account the non-linear nature of elastomer materials and the effects of electrically induced strains during relaxation. It is explicitly shown that efficiency is dependent on the applied strain, the shape of the stress-strain curve, and on a lumped parameter (Z') containing the applied electric field, stiffness and permittivity. Any term in the lumped parameter can be offset by the other terms; thus a stiff material may require a higher permittivity or electric field to attain the same efficiency as a similar soft material.

Based on the results from Chapter 8 and 9, stiffer elastomers should be capable of higher energy densities; the increased stiffness of the elastomer films should results in lower Maxwell pressure induced strains, and thus allow the elastomer to relax further, resulting in a larger swing in capacitance and larger energy gains. With this in mind, in Chapter 10 the use of VHB-based acrylic interpenetrating polymer network dielectric elastomers with a trimethylolpropane trimethacrylate (TMPTMA) additive network is explored for energy harvesting purposes. It is shown that increasing the amount of the TMPTMA additive increases the stiffness of the network. Films with varying additive content are tested and their performance is compared with highly prestrained VHB acrylic elastomers. By increasing the additive content, Maxwell induced strains can be suppressed and larger energy gains can be achieved at higher bias fields. Moreover, the introduction of the additive network stabilizes the highly prestrained acrylic elastomers mechanically, thereby increasing their mechanical robustness. However, the interpenetrating polymer network films suffer from an increase in viscoelastic behavior that hinders their overall performance. The result is that the highly prestrained VHB outperforms on the films with additive in terms of energy density.

In Chapter 11 another attempt is made at synthesizing an elastomer material with improved performance. A high breakdown strength silicone material is chose as the host in this case as silicones generally display more stable performance across a broad temperature and frequency range and are typically resistant to moisture, making them more suitable for most energy harvesting applications. In order to increase the energy density of the host silicone, TiO_2 nanoparticles coated with short PDMS chains are added. The resulting films show in increase in both stiffness and permittivity with only marginal increases in the mechanical loss factor (tan δ) and electrical losses (dissipation factor). The nanocomposite materials also retain high dielectric breakdown strengths, an important material parameter for high performance operation. Based on simplified calculations, the generator energy density increases by a factor of 3 for a nanocomposite with 20wt.% TiO_2 over the pure host silicone. The results exceed the experimental results obtained for highly prestrained VHB, though the simplified calculation ignores electrical and mechanical losses.

In Chapter 12 a silicone/carbon nanotube composite is introduced based on the S-IPN concept from Chapters 4 and 5. As mentioned above, electrode materials capable of maintaining relatively low resistances at high strains and long lifetimes are important for efficiency DE generator operation. A sheet resistance under 2 $k\Omega/\square$ can be achieved. The composite is capable of being stretched to over 150% strain with a minimal increase in the baseline resistance and excellent recovery of electrical properties upon relaxation. The electrode displays excellent stability, withstanding over 1000 cycles at 120% strain and a total of over 17000 cycles with strain rates up to 100%/s at strains between 10% and 120% with minimal change in resistance. The technique can be used to pattern electrodes onto both sides of the silicone for use in soft dielectric elastomer energy harvesters. When stretched the capacitance change is repeatable and can be made linear for sensor purposes or superlinear for improved energy gains as an energy harvester. We demonstrate that the material is capable of harvesting over 7 mJ/cm^3 of active material when subjected to a strain of 50%. Due to the softness of the composite, it is suitable for applications such as harvesting energy from human motion.

In Chapter 13, two potential applications for dielectric elastomer generators are explored. A novel pressure-based wave energy harvester is presented and the potential capacity to harvest energy is explored. In its most basic form, the proposed device consists of a simple hollow tube with a DE stack at one end. The tube is partially submerged under water with air trapped inside. As waves pass by, the change in water height causes a change in the air pressure inside the tube, causing the DE stack to deform. A concept for a floor tile energy harvester is also introduced. Due to the compliant nature of DEs, the floor tile can be made entirely flexible for improved conformability to curved surfaces and easy deployment and storage.

Chapter 14 outlines the conclusions of this part of the dissertation and explores future work that can be done based on the material presented.

CHAPTER 8

Factors Influencing the Performance of Dielectric Elastomer Energy Harvesters

8.1 Modeling

We wish to determine how certain materials parameters, such as dielectric constant, sample parameters, such as film thickness, and operating parameters, such as bias voltage and applied stretch, affect the amount of energy generated and the energy conversion efficiency of a DE generator. As such, we make the assumptions that the material is hyperelastic, has no viscosity, and the electrode resistance and leakage current through the film are negligible. It is possible to incorporate the viscoelastic nature of the film as well as the electrical losses into the model but they would only serve to complicate the calculations and the overall conclusions would remain unchanged. The model also accounts for the 4 main failure criterion described above.

We explore two materials systems in this study: VHB4905-based IPN films and PolyPower InLastor Pull silicone films. In order to model the stress-strain characteristics of the materials we use data published in the literature. [172, 173, 338] We use the Mooney-Rivlin strain energy density function to model the PolyPower system since strain is limited to relatively low values, and the Yeoh strain energy density function to model the IPN films. The parameters used for each material are listed in Table 8.1. The strain at rupture is limited to an area increase of 185% in the case of the IPN film. While strains in excess of this are possible, it is not feasible to operate safely at such high strains due to issues with fatigue. In

Table 8.1: Material parameters

	IPN	**PolyPower InLastor Pull**
Dielectric Constant	2.43	3.1
Breakdown Strength (MV/m)	265	35
Strain to Rupture (area increase)	185%	35%
Initial Thickness (m)	50	60
C1 (MPa)	0.6891	0.07
C2 (MPa)	-7.112 10^{-8}	0.04
C3 (MPa)	3.062 10^{-2}	–

practice, a more practical limit on strain would likely lie around or below 100% and would depend on a number of environmental factors.

In our model we assume a constant charge cycle and a pure shear strain state. The four steps in the energy harvesting cycle are outlined below:

8.1.1 Step 1 - Stretching

The film is stretched to a value λ along the longitudinal direction, we assume that the materials are incompressible in nature, so that:

$\lambda_1 = \lambda$ $\quad$ $B_1 1 = \lambda^2$ $\quad$ $I_1 = \lambda^2 + 1/\lambda^2 + 1$

$\lambda_2 = 1$ $\quad$ $B_2 2 = 1$ $\quad$ $I_2 = \lambda^2 + 1/\lambda^2 + 1$

$\lambda_3 = 1/\lambda$ $\quad$ $B_2 2 = 1/\lambda^2$

For the case of the IPN film, the strain energy density is calculated using the Yeoh equation:

$$W = \sum_{i=1}^{3} C_i \left(I_1 - 3\right)^i \tag{8.1}$$

And in the case of the PolyPower film, the strain energy density is calculated using the

Mooney-Rivlin equation:

$$W = C_1 \left(I_1 - 3 \right) + C_2 \left(I_2 - 3 \right) \tag{8.2}$$

The mechanical energy (e_{mech}) is calculated by multiplying the strain energy density function by the volume of the sample, which can be defined arbitrarily. In both cases the principal stresses along directions 1 and 3 are:

$$\sigma_1 = -p + 2\frac{\partial W}{\partial I_1} B_{11} - 2\frac{\partial W}{\partial I_1} B_{11}^{-1} \tag{8.3}$$

$$\sigma_3 = 0 = -p + 2\frac{\partial W}{\partial I_1} B_{33} - 2\frac{\partial W}{\partial I_1} B_{33}^{-1} \tag{8.4}$$

Solving for p and then σ_1 we obtain:

$$\sigma_1 = 2\left(\frac{\partial W}{\partial I_1} + \frac{\partial W}{\partial I_2}\right)\left(\lambda^2 - \frac{1}{\lambda^2}\right) \tag{8.5}$$

8.1.2 Step 2 - Charging

The film is charged, but we maintain a constant strain on the film. The Maxwell stress is given by:

$$\sigma_{Maxwell} = -\epsilon_r \epsilon_0 \left(\frac{V_b}{t_s}\right)^2 \tag{8.6}$$

Where t_s is the thickness of the DE film in the stretched state. If the Maxwell stress is greater than the applied stress then the device has transitioned from the generator mode of operation to the actuator mode; the strain on the film will begin to increase and no energy will be harvested. If the applied field exceeds the breakdown field, the device will fail. The capacitance, charge, and energy stored on the film are calculated as:

$$C_s = \epsilon_r \epsilon_0 \left(\tfrac{A_s}{t_s}\right) \qquad Q = C_s V_b \qquad e_s = \tfrac{1}{2} C_s V_b^2$$

8.1.3 Step 3 - Relaxing

The film is allowed to relax; the charge on the film remains constant but the capacitance decreases and thus the voltage must increase. The stress state on the film is now given by:

$$\sigma_1 = 0 \tag{8.7}$$

$$\sigma_3 = -\sigma_{Maxwell} = -2\left(\frac{\partial W}{\partial I_1} + \frac{\partial W}{\partial I_2}\right)\left(\lambda_u^2 - \frac{1}{\lambda_u^2}\right) \tag{8.8}$$

Where λ_u is the stretch in the unstrained state caused by the Maxwell stress. Solving for stretch:

$$\lambda_u = \left(\frac{\frac{\sigma_{Maxwell}}{2(\partial W/\partial I_1 + \partial W/\partial I_2)} + \left(\frac{\sigma_{Maxwell}^2}{4(\partial W/\partial I_1 + \partial W/\partial I_2)^2} + 4\right)^{1/2}}{2}\right)^{1/2} \tag{8.9}$$

The capacitance, voltage, and energy stored on the film are calculated as:

$$C_u = \epsilon_r \epsilon_0 \left(\frac{A_u}{t_u}\right) \qquad V_u = \frac{Q}{C_u} \qquad e_u = \frac{1}{2} C_u V_u^2$$

The Maxwell stress and all other values must be solved iteratively until the solution converges. Again, if the applied field exceeds the breakdown field, the device will fail.

8.1.4 Step 4 - Discharging

The film is discharged and the device returns to the original state. The energy generated (e_{gen}) is given by $e_u - e_s$ and the energy conversion efficiency is taken as e_{gen}/e_{mech}.

8.2 Experimental

8.2.1 Generator Design

The generator design consists simply of a rectangular elastomer sheet with electrodes covering the majority of the film, held in place by rigid plastic frames along the transverse edges and free along the longitudinal edges. Additional reinforcing elastomer strips are added along the edges of the plastic frames to prevent tearing. Forces are coupled to the rigid bars and result in strains along the longitudinal direction. An image of a completed single-sheet generator is shown in Figure 8.1. One issue that may arise is a type of pull in along the longitudinal sides: when the film is stretched the sides will be pulled inward. We use elastic strips along the longitudinal edges to partially mitigate this issue.

8.2.2 Testing Apparatus

The testing apparatus is shown on the left of Figure 8.2. The apparatus is capable of variable frequency and displacement and is designed such that friction and lateral motions are minimized. The sample is attached to an upper plate held a distance away from a lower place where the driving motor is attached. The driving motor rotates an off-center shaft, which pulls on a cord that is attached to the bottom of the sample through a load cell. The load cell can be used to measure the load applied to the film during testing. The displacement can be adjusted by changing the length of the off-center shaft. Frequency is controlled by the revolution rate of the motor.

In order to charge and discharge the DE generator and make the necessary measurements we use the simple circuit shown on the right of Figure 8.2. A high voltage power supply is used to charge the DE, which we can treat as a variable capacitor, $C_{DE}(x)$, at a bias voltage VB when switch S_1 is closed. When switch S_2 is closed, the DE is discharged through the load resistor R_L. The voltage across the DE is measured using an oscilloscope.

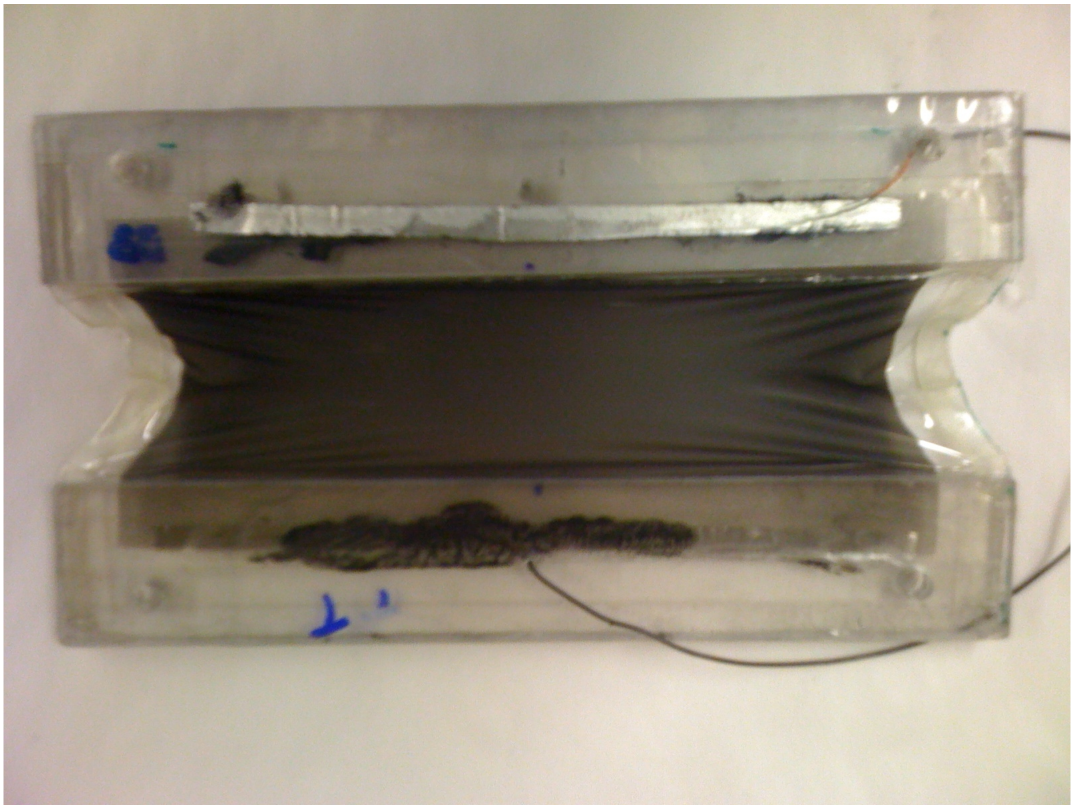

Figure 8.1: Sheet generator. The generator consists of an electroded elastomer film clamped at the transverse ends with rigid end pieces and free along the longitudinal sides. Due to the elastic nature of the film, some pull in along the longitudinal sides is inevitable. This can be partially mitigated by adding an elastic material along the edges.

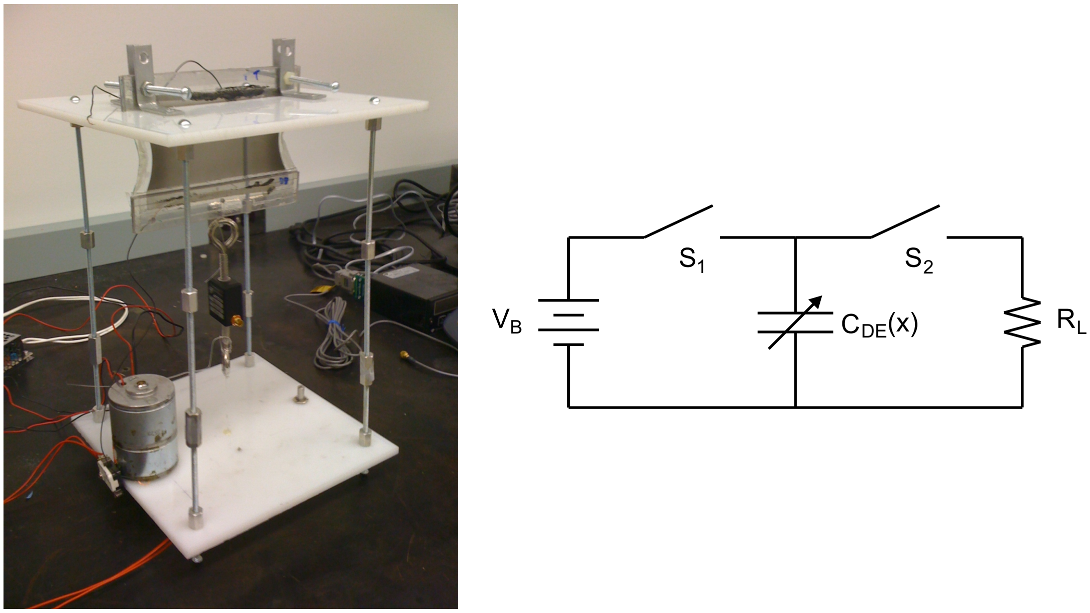

Figure 8.2: Left: Generator testing apparatus. The sample attaches to the upper plate, the motor rotates an off-center shaft that pulls on a cord attached to the sample through a load cell that can be used to measure the applied load during testing. Right: Simple energy harvesting circuit. S1 and S2 can be closed to charge the DE from the high voltage power supply or drain it through the load resistor respectively.

8.2.3 Materials

For this study we use a VHB4905-based interpenetrating polymer network (IPN) film. The IPN films were prepared using trimethylolpropane trimethacrylate (TMPTMA) by first prestraining a 3M VHB4905 film to 400x400% onto a rigid frame and spraying a solution of TMPTMA monomers with a thermally activated free radical initiator onto the film using an airbrush. The films were left overnight to allow the monomers to diffuse into the film and the solvent to evaporate. The monomers were polymerized in a vacuum oven at 80C for several hours. Upon removal, electrodes were applied to the films. In the proposed generator configuration, the IPN film will relax slightly in the longitudinal direction; however, due to the presence of the second network, the relaxed film will maintain the majority of the prestrain. The IPN preparation process is described in more detail in References [171, 172].

Carbon powder and carbon nanotubes (CNTs) were used as electrode materials. For all cases a contact mask was used to pattern the electrodes. Carbon powder was rubbed on using a cotton applicator. CNTs were sprayed from a dispersion in chloroform using an airbrush.

8.3 Results and Discussion

The results of the simulations for the 2 materials systems can be seen in Figures 8.3 and 8.4 for energy generated per cm^3 of active material and energy conversion efficiency respectively. The data is plotted as a function of both the strain applied to the film (measured as the thickness strain) and the applied bias voltage.

From the energy density plots we can conclude that in both cases the amount of energy generated will increase with increasing strain and bias voltage until failure. The IPN film is capable of much higher energy densities because both the maximum strain and breakdown field are much higher. This is not surprising since higher strains lead to higher capacitance changes and higher applied voltages lead to more charge being stored on the films. The maximum amount of energy generated for both materials is achieved at the highest strain value tested. At these high strain values, the voltage is limited by the breakdown strength of the polymer. The results for the mechanical-to-electrical energy conversion efficiency are more interesting. Both materials systems have maximums near 50%: the maximum for the IPN system lies at a strain of 1.0% in area and a voltage of 1.8 kV while the maximum for the PolyPower system lies at 1.5% area strain and a voltage of 0.9 kV. Unfortunately, at such low values of strain, the harvested energy is also very low. In systems where parasitic viscoelastic, resistive, and leakage losses are taken into account, the actual efficiencies will be much lower. Fortunately, as seen in the figures, efficiencies in excess of 45% can be achieved at higher values of strain where the energy output is more reasonable and the impact of parasitic losses is lower.

In order to determine the impact that materials parameters such as the dielectric constant and stiffness have on efficiency and generated energy, 2 additional hypothetical materials systems are explored: an IPN-type film with wherein the dielectric constant is 8, and a PolyPower-type film with increased stiffness (Mooney-Rivlin fitting parameters C1 and C2 are doubled). The results are displayed in Figures 8.5 and 8.6 for the energy harvested per cm^3 of active material and the efficiency respectively.

A comparison of the results for the IPN film and the IPN-like film with higher dielectric constant shows that the maximum efficiencies are essentially unchanged but occur at lower voltages. In terms of the energy harvested per cm^3, the IPN-like film with higher dielectric constant showed a marked improvement with improvements across the board occurring at lower voltages. This change can be attributed to the increased capacitance of the film. The 3.3x increase in dielectric constant translates to a roughly 1.7x increase in the maximum energy harvested, which occurs at nearly the same values of strain and bias voltage as for the regular IPN films. This type of increase is likely to occur for stiffer elastomers where the effects of Maxwell pressure are less pronounced. For softer films, like silicones, the increase in dielectric constant may increase the Maxwell pressure in the relaxed charged state to a

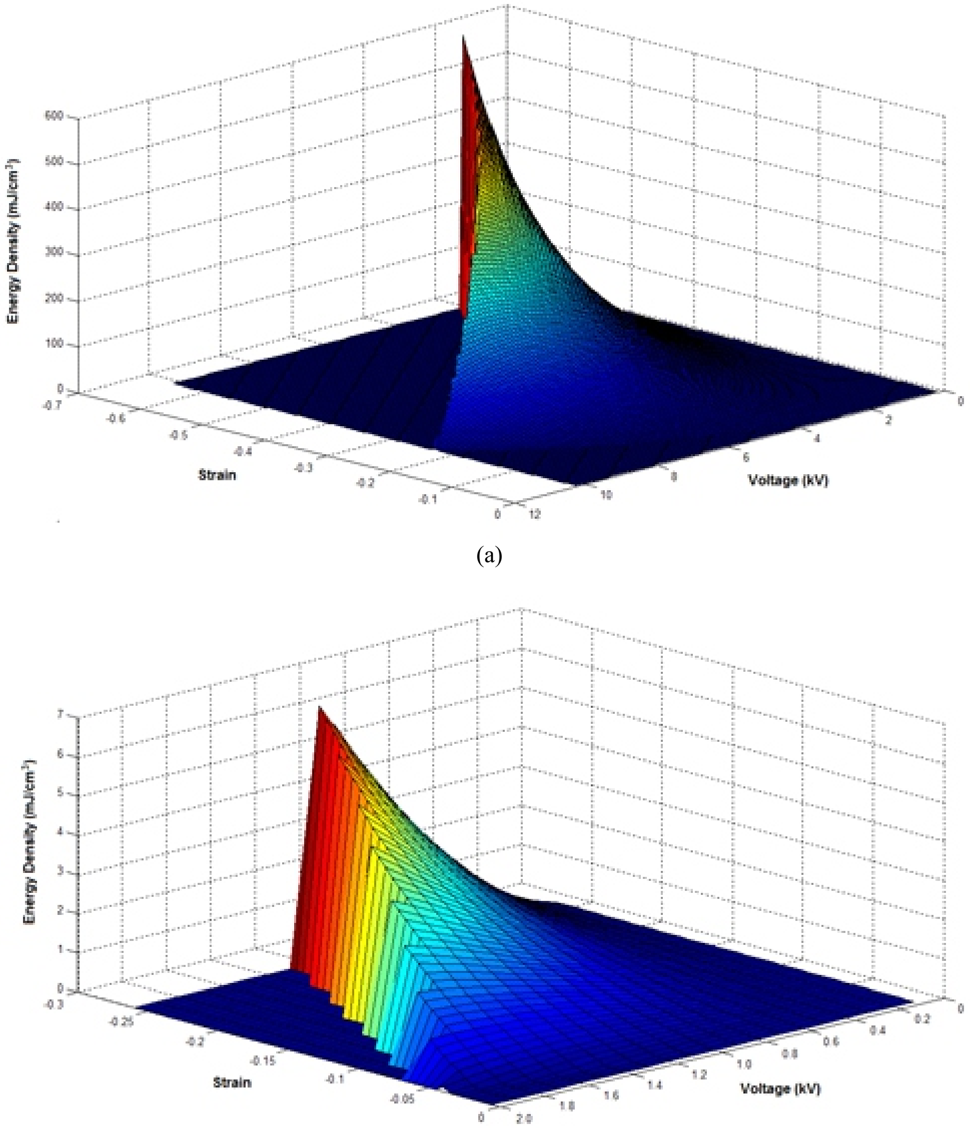

(a)

(b)

Figure 8.3: Modeled energy generated per cm^3 of active material for (a) an IPN film and (b) a PolyPower InLastor Pull film. The energy generated increases for both strain and bias voltage up to failure.

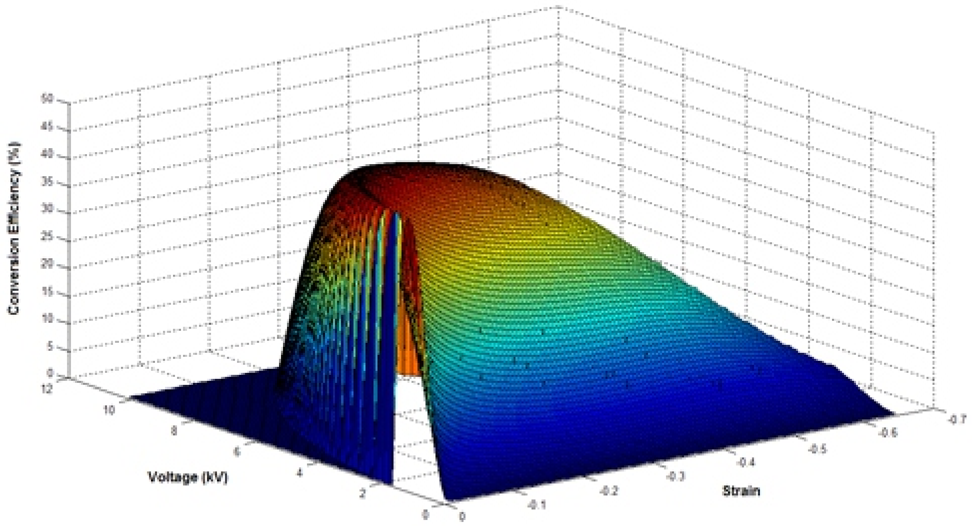

(a)

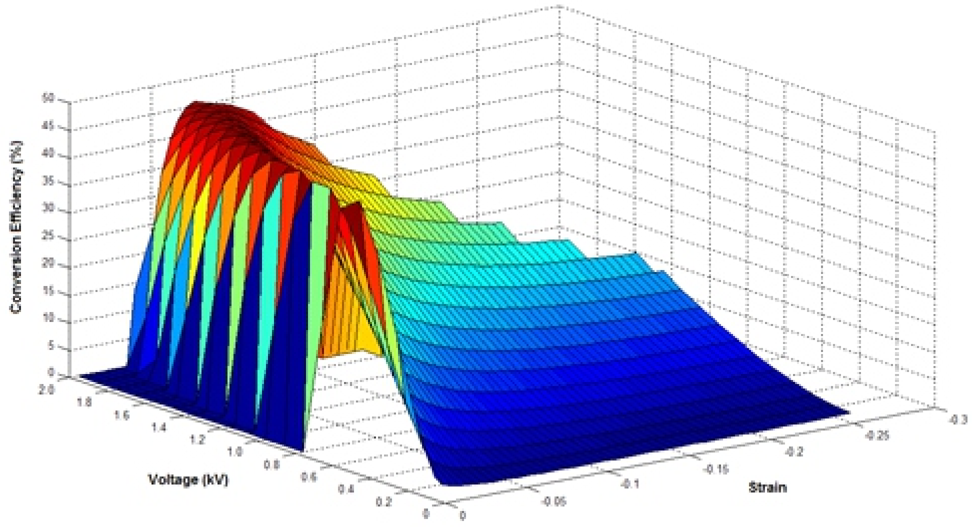

(b)

Figure 8.4: Modeled energy conversion efficiency for (a) an IPN film and (b) a PolyPower InLastor Pull film. The efficiency for both materials peaks near 50%. As strain increases, the voltage required to convert energy at high efficiency increase quickly then levels off.

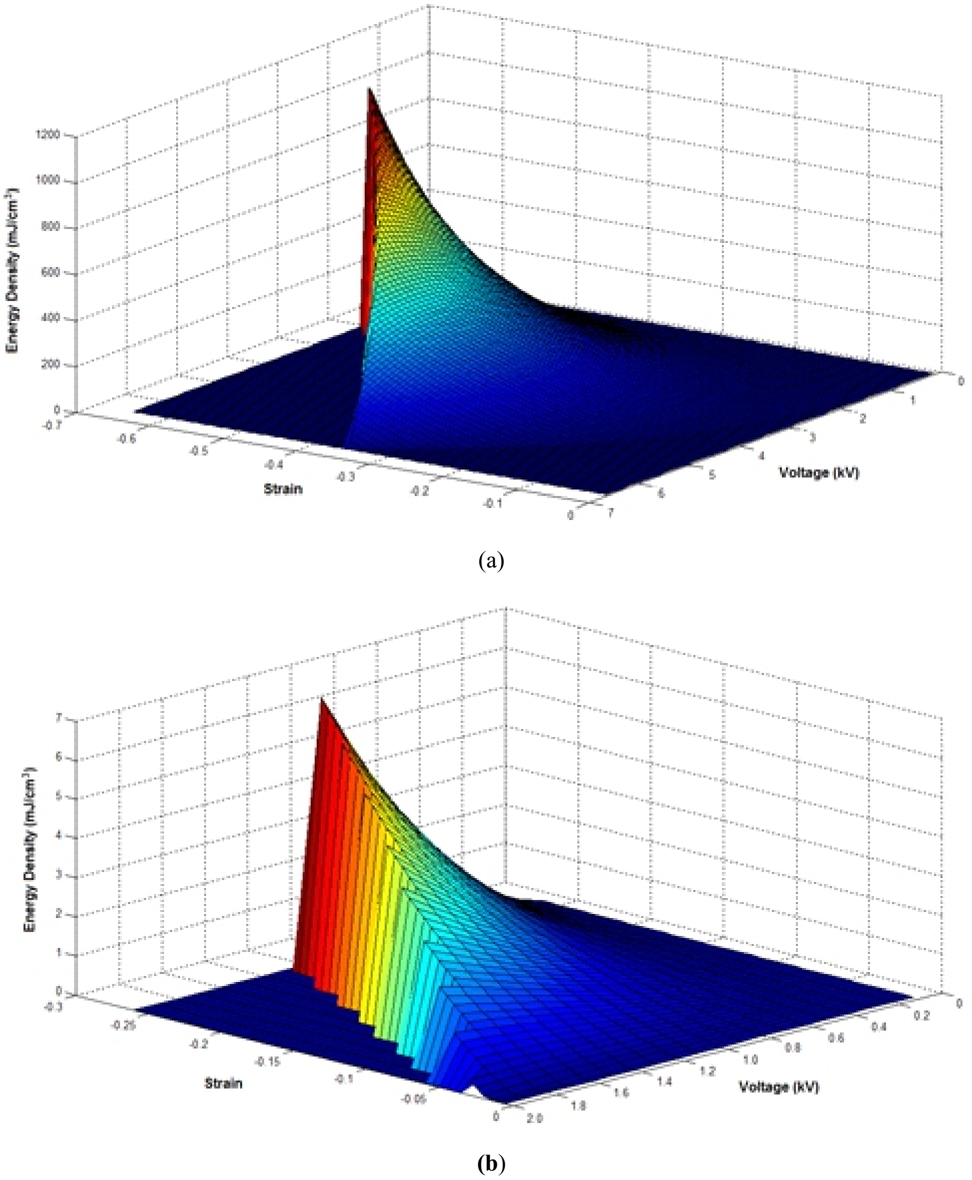

Figure 8.5: Modeled energy generated per cm^3 of active material for (a) an IPN-like film with a dielectric constant of 8 and (b) a PolyPower-like film with increased stiffness.

point where the transition between generator and actuator mode becomes an issue.

Referring to Figures 8.5 (b) and 8.6 (b) for the stiffened PolyPower-like film we observe that the energy harvested per cm^3 remains essentially unchanged while higher efficiencies are shifted to lower strains and higher voltages. The lack of change in terms of energy generated is due to the fact that the limiting factor for generated energy is the breakdown field; thus the effect of the increased stiffness is very small in this particular system. In terms of the efficiency, however, a shift to a stiffer material means an increase in the strain energy required to stretch the film. This has obvious ramifications in terms of the amount of energy that must be applied to stretch the material, thus the shift to lower strains seen in Figure 8.6 (b), but it also has the effect of reducing the strains due to Maxwell stress in the relaxed state, thus higher efficiencies can be obtained at low strains and higher voltages since the Maxwell induced strain will be small.

The results of the experimental test on the IPN sheet generator with CNT electrodes are shown in Table 8.2. Additionally, the sheet generator was tested at 3 different frequencies at 2.8 kV: 0.28, 0.78, and 1.85 Hz. The frequency range and bias voltage were limited by the experimental setup.

The measured strain applied to the film was observed to decrease from the start of testing. This phenomenon can be attributed to the mechanical hysteresis of the material. The data for the different frequency ranges clearly shows the effects of parasitic losses: at low frequencies the generated energy decreases due to leakage current through the film but the efficiency remains the same due to a reduction in the necessary applied force to stretch the film. At higher frequencies the viscoelastic nature of the film affects the results. Accounting for these losses, the experimental results match quite well with the model.

Another factor that cannot be ignored is the effect of the electrode resistance. Figure 8.7 shows the voltage scans for two IPN sheet generators, one with carbon powder electrodes and the other with CNT electrodes. The one with carbon powder electrodes displays a rapid drop in voltage at the start of the relaxation step that is not present in the sample with CNT

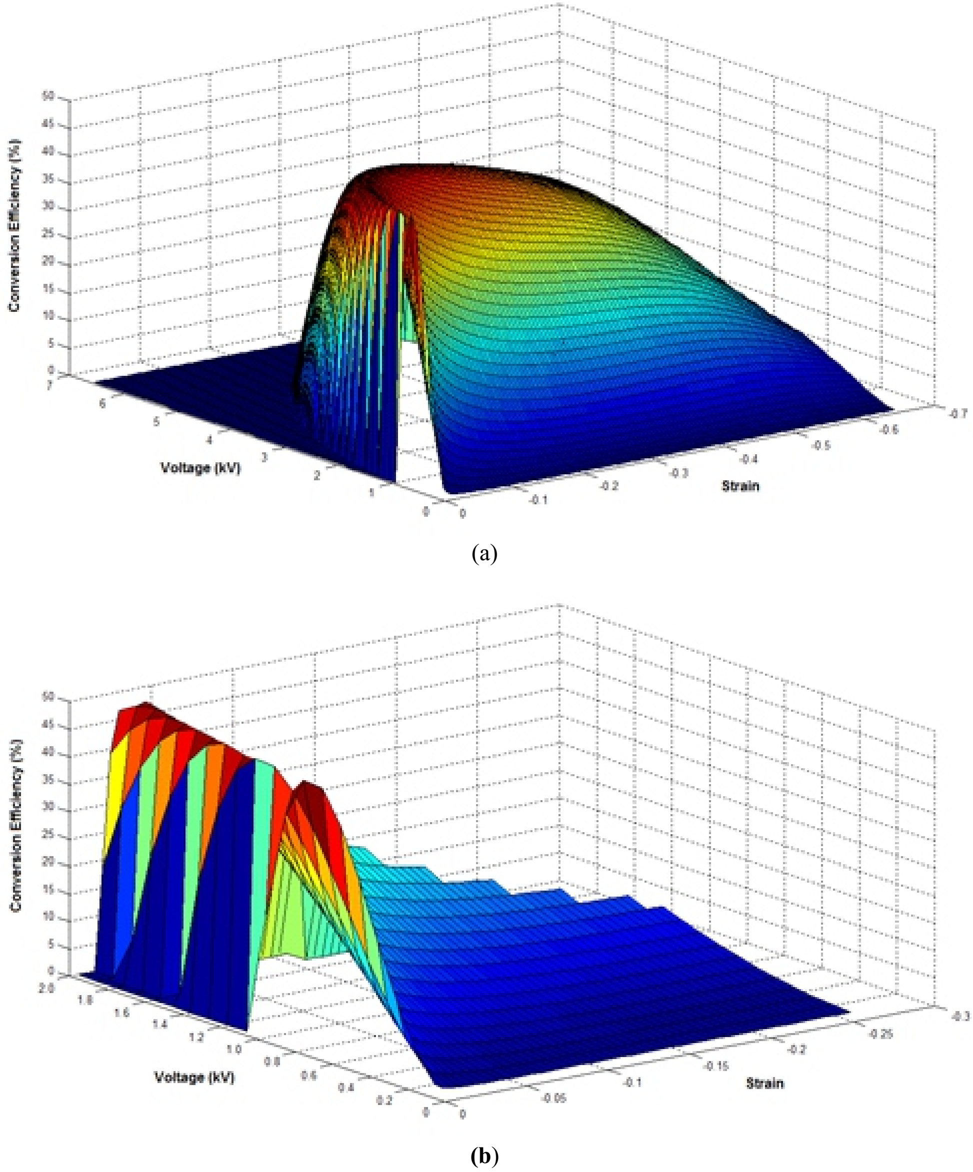

Figure 8.6: Modeled energy conversion efficiency for (a) an IPN-like film with a dielectric constant of 8 and (b) a PolyPower-like film with increased stiffness.

Table 8.2: Experimental Data

Bias Voltage (kV)	**Strain**	**Frequency (Hz)**	**Energy Harvested (mJ)**	**Efficiency**
0.65	41%	0.78	0.60	1%
1.14	39%	0.78	1.95	4%
1.7	38%	0.78	4.01	9%
2.26	38%	0.78	5.30	12%
2.8	35%	0.78	5.87	13%
2.8	40%	0.28	4.94	13%
2.8	32%	1.85	5.55	12%
0.67	57%	0.68	1.03	1%
1.2	57%	0.68	3.27	4%
1.72	57%	0.68	5.69	7%

electrodes. This drop can be attributed to arcing along the carbon powder electrode in the strained state. The carbon powder particles begin to lose contact at high strains, causing resistance to increase sharply. At the same time, when the elastomer relaxes, the voltage on the dielectric elastomer increases. In this case, the resistance of the carbon powder electrodes was sufficiently high that arcing through the air provided a lower resistance pathway than conduction through the carbon powder particles. This presents the extreme cases where a large drop in potential results from arcing. In less extreme cases, the increased resistance will still contribute to a loss in the electrical potential and will also result in longer charging and discharging times as the RC time constant increases. The high aspect ratio of the CNTs, however, allows them to maintain relatively high conductivity, even at high strains. One aspect of the PolyPower devices that provides an advantage over other systems is the high conductivity of their electrodes, which essentially eliminates the issue of parasitic resistive losses and reduces the RC time constant so that large area devices can be operated at relatively high frequencies.

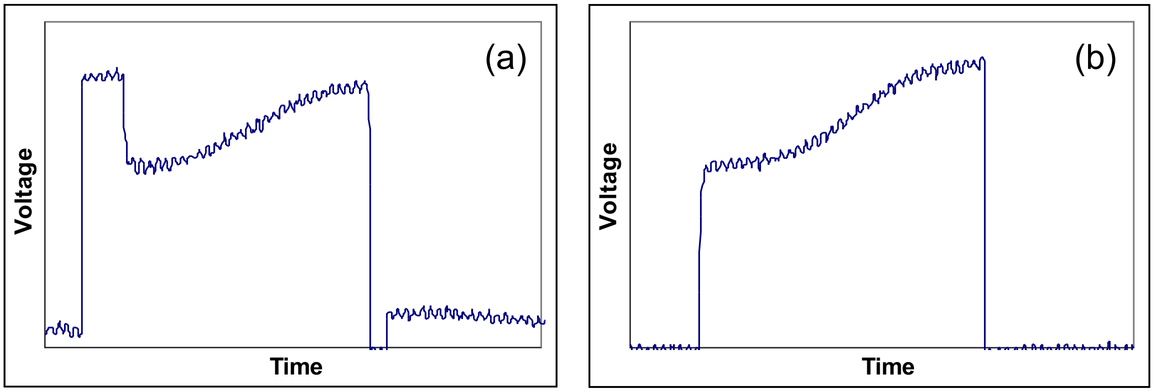

Figure 8.7: Voltage scans for (a) an IPN sheet generator with carbon powder electrodes and (b) an IPN sheet generator with CNT electrodes tested under similar conditions. The higher resistance of the carbon powder electrodes, especially at high strains, leads to potential arcing, parasitic resistive losses, and issues charging the film.

8.4 Conclusions

We have presented a simplified DE generator model capable of accurately describing the effects of several materials and operational parameters and have validated our model with experimental results. The model shows that the amount of energy generated increases for both the applied stretch and the bias voltage. The dependency of efficiency on stretch and bias voltage is more complex. High efficiencies can be obtained over a wide range of stretch and bias voltage. The energy generated and the efficiency are bounded by dielectric breakdown and Maxwell forces in the relaxed state. The energy generated is also limited by the stretch to rupture of the material. We have shown that in certain materials systems, an increase in dielectric constant can cause a substantial increase in the energy generated and can reduce the necessary bias voltage for high energy-high efficiency operation. Stiffening the material has the main effect of pushing high efficiency to lower strains and larger bias voltages.

Using experimental results, we have demonstrated the effects of parasitic losses such as viscoelastic losses, leakage current, and resistive losses. Viscoelastic losses play a more important role at higher frequencies, while losses due to leakage are more pronounced at lower frequencies due to the increased time the charge spends on the DE film. Resistive losses are directly related to the choice of electrode material and can be significant, particularly in systems where resistance is high at high strains. In extreme cases, electrical arcing may occur, resulting in significant losses in electrical potential and possible damage to the electrode and underlying elastomer.

CHAPTER 9

Dielectric Elastomer Generator Efficiency

In our search to better understand the nature of our surrounding, the models we develop invariably become more and more complex which can yield more accurate results but can also obfuscate some rather simple conclusions that would otherwise be apparent and obvious. This is also true in the world of dielectric elastomer transducers, where complex hyperviscoelastic models are oft ignored, to be replaced with simple equations with clear relationships. Though these relationships may not provide the same accuracy or precision in all cases, they provide good estimates and an excellent method for the comparison of different materials. Indeed, in the field of dielectric elastomer actuators, the following equations for Maxwell stress (p), strain in the thickness direction (s_z), and energy density(e) are still used as the cornerstones for material comparisons [3, 44]:

$$\begin{aligned}
&p = -\epsilon_0\epsilon_r E^2 \\
&s_z = \tfrac{p}{Y} = \tfrac{\epsilon_0\epsilon_r E^2}{Y} \\
&e = \tfrac{1}{2}ps_z\tfrac{\left(\epsilon_0\epsilon_r E^2\right)^2}{Y}
\end{aligned}$$

Models to describe the power density and efficiency of DEGs have recently been developed that can help elucidate the roles of certain materials properties, such as stiffness, dielectric constant, and breakdown field, as well as operational parameters such as strain, strain rate, and bias voltage [339,340]. Though these models are capable of relatively accurately describing the energy harvesting capabilities of DEGs, they are rather cumbersome to deal with and make comparative analyses difficult to undertake.

In a relatively simple model based on a DEG in a constant charge cycle, Kang et al. [341] inferred that the power generation efficiency depends on the thickness, charging voltage, effective stiffness, permittivity, and relative deformation and that the power generation efficiency is inversely proportional to the effective stiffness. While their model provides the simplicity necessary for easy comparisons it lacks sufficient grounding to provide correct general conclusions. Here we develop analytical relationships for the energy density and power generation efficiency of a constant charge energy harvesting cycle taking into account the non-linear stress-strain behavior and electrostatic pressure induced strains during relaxation. The resulting relationships can be expressed as a simple equation that can provide easy insights into how to improve the operation of DEG materials and devices. We show that the energy that can be harvested from a DEG per unit volume depends on material parameters such as dielectric constant, stiffness, and breakdown filed as well as operational parameters such as applied strain and bias voltage. We show that efficiency is a function of a lumped parameter (Z') containing the combination of applied electric field, stiffness and permittivity, and that the maximum efficiency is governed by the shape of the stress-strain curve and applied strain.

9.1 Derivation

For our analysis we make the assumptions that the elastomer materials are isotropic and incompressible and that the material is stretched in either a pure shear mode. Following the work of Kang et al, we define the power generation efficiency as the ratio of energy harvested (J_E) to the mechanical work used to deform the film (J_M):

$$\eta = \frac{\Delta J_E}{J_M} \tag{9.1}$$

We characterize the elastomers stress-strain response in the configuration that the device will be operated in; as such, for pure shear operation the material would be characterized under pure shear conditions, for a diaphragm configuration, the material would be characterized under those conditions.

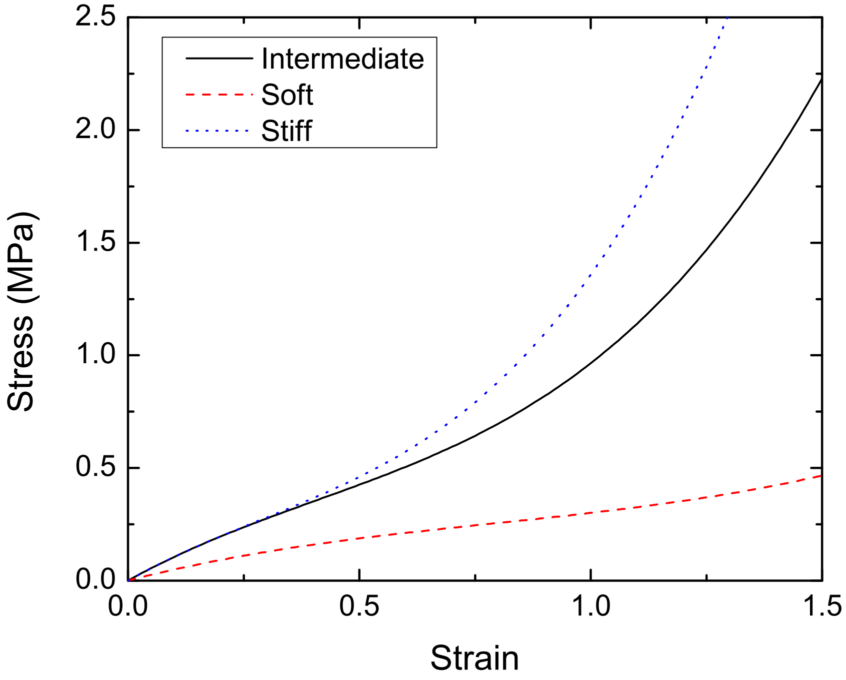

Figure 9.1: Stress-strain responses for three typical elastomer materials.

Figure 9.1 shows typical stress-strain responses for three fully relaxed elastomers under pure shear conditions, the stiff and intermediate films are silicones while the stiff film is a prestrain locked acrylic interpenetrating polymer network elastomer [171]. For relatively small strains (<20%) we can treat the elastomer as a linearly elastic material [44], and the stress-strain relationship is given by:

$$\sigma = Ys \tag{9.2}$$

Where σ is stress, s is strain, Y is the Youngs modulus. For the case of higher strains, the non-linear behavior of the elastomer material cannot be ignored. It is possible to accurately describe the non-linear stress-strain response up to reasonably high strains using a hyperelastic constitutive equation such as the Yeoh, Ogden and Mooney-Rivlin models.

Here we use the Yeoh model, thus, the mechanical work becomes:

$$J_M = AdW = A_0 d_0 \sum_{i=1}^{3} C_i \left(I_1 - 3\right)^i = A_0 d_0 Y \sum_{i=1}^{3} c_i \left(I_1 - 3\right)^i \tag{9.3}$$

Where A and A_0 are the area and original area respectively, d and d_0 are the thickness and initial thickness respectively, W is the strain energy function, C_i and c_i are constants, and I_1 is the first strain invariant. We maintain the Youngs modulus as an effective stiffness while c_1, c_2, and c_3 are constants that depend on the material system. Under the assumptions of incompressibility and pure shear strain, the equation becomes:

$$\begin{aligned} J_M = A_0 d_0 Y \Bigg[& c_1 \left(\lambda_{A,M}^2 + \frac{1}{\lambda_{A,M}^2} - 2\right) \\ & + c_2 \left(\lambda_{A,M}^2 + \frac{1}{\lambda_{A,M}^2} - 2\right)^2 + c_3 \left(\lambda_{A,M}^2 + \frac{1}{\lambda_{A,M}^2} - 2\right)^3 \Bigg] \\ = A_0 d_0 Y \lambda' & \end{aligned} \tag{9.4}$$

Where $\lambda = s + 1$, $\lambda_{A,M}$ is the area stretch due to external mechanical forces, and λ' represents the terms in the square brackets. To derive the electrical energy that can be harvested for the case of a constant charge cycle we compare the energy stored on the elastomer in the stretched and relaxed states when it is biased with a charge, Q:

$$\Delta J_E = J_{Er} - J_{Es} = \frac{1}{2} C_r V_r^2 - \frac{1}{2} C_s V_b^2 \tag{9.5}$$

Where C_r and C_s are the capacitance in the relaxed and stretched state respectively, V_b is the applied bias voltage, and V_r is the voltage in the relaxed state, which can be expressed as the bias voltage plus an additional generated voltage, $V_r = V_b + V_g$. For a constant charge energy harvesting cycle, the charge on the film remains constant during relaxation, thus:

$$Q = constant = C_s V_b = C_s \left(V_b + V_g\right) \tag{9.6}$$

Following the assumptions above, the capacitance can be represented as:

$$C = k\frac{A}{d} = k\frac{A_0}{d_0}\lambda_A^2 = k\frac{A_0}{d_0}\frac{1}{\lambda_3^2} \tag{9.7}$$

Where $k = \epsilon_r\epsilon_0$ is the permittivity, and λ_3 is the stretch in the thickness direction.

From these results the electrical energy harvested can be rewritten as:

$$\Delta J_E = \frac{1}{2}C_s V_b V_g = \frac{1}{2}k\frac{A_0}{d_0}\frac{1}{\lambda_{3,M}^2}V_b^2\left(\frac{\lambda_{3,E}^2}{\lambda_{3,M}^2} - 1\right) \tag{9.8}$$

Where the subscripts E and M refer to the electrically and mechanically induced strains. Noting that because the voltage increases faster than the film thickness when the film is relaxed, the electric field will increase which will increase the electrostatic pressure across the elastomer and may prevent the film from relaxing fully. Since dielectric elastomers are isotropic and can be treated as incompressible, the electrostatic pressure is given by the Maxwell pressure [44]:

$$p_{3,E} = -k\left(\frac{V_b + V_g}{d}\right)^2 = -k\left(\frac{\lambda_{3,E}}{\lambda_{3,M}^2}\frac{V_b}{d_0}\right)^2 \tag{9.9}$$

Assuming this electrostatic pressure induced strain is small (<20%) we can treat the elastomer as being linearly elastic, thus the strain is given by:

$$s_{3,E} = -\frac{1}{Y}k\left(\frac{V_b + V_g}{d}\right)^2 = -\frac{1}{Y}k\left(\frac{\lambda_{3,E}}{\lambda_{3,M}^2}\frac{V_b}{d_0}\right)^2 \tag{9.10}$$

Noting that $\lambda_{3,E} = 1 + s_{3,E}$ and solving for $\lambda_{3,E}$ we obtain:

$$\lambda_{3,E} = \frac{-1 + \sqrt{1 + 4Z}}{2Z}, Z = \frac{k}{Y}\left(\frac{V_b}{d_0}\right)^2\frac{1}{\lambda_{3,M}^4} = \frac{k}{Y}E^2\frac{1}{\lambda_{3,M}^2} \tag{9.11}$$

Thus the electrical energy harvested becomes:

$$\Delta J_E = \frac{1}{2}k\frac{A_0}{d_0}\frac{1}{\lambda_{3,M}^2}V_b^2\left(\frac{\left(\frac{-1+\sqrt{1+4Z}}{2Z}\right)^2}{\lambda_{3,M}^2}-1\right) = \frac{1}{2}A_0 d_0 ZY\left(\frac{\left(\frac{-1+\sqrt{1+4Z}}{2Z}\right)^2}{\lambda_{3,M}^2}-1\right) \tag{9.12}$$

Combining (12) with equation (4) into equation (1) while noting that the strain in equation (4) represents a tensile strain while the stretch terms represent the corresponding stretches in the thickness direction, the efficiency becomes:

$$\eta = \frac{1}{2}Z\frac{1}{\lambda'}\left[\frac{\left(-1+\sqrt{1+4Z}\right)^2}{4Z^2}-\lambda_{3,M}^2\right] \tag{9.13}$$

Rewriting equation (13) to remove strain dependence from the constant Z:

$$\eta = \frac{1}{2}Z'\frac{1}{\lambda_{3,M}^2}\frac{1}{\lambda'}\left[\frac{\left(-1+\sqrt{1+4Z'/\lambda_{3,M}^4}\right)^2\lambda_{3,M}^6}{4Z'^2}-1\right], Z' = \frac{k}{Y}\left(\frac{V_b}{d_0}\right)^2 \tag{9.14}$$

Figure 9.2a shows efficiency curves for the three elastomer materials shown in Figure 9.1 for strains of 10% and 30%. Note the efficiency curves for the soft and intermediate material essentially overlap completely. To elucidate the cause for this, the normalized stress, calculated as the stress divided by the elastic modulus for strains <20%, is plotted in Figure 9.2b. The curves for the soft and intermediate films overlap almost completely while the stiff film shows an increase in stiffness with strain, indicating that it is the shape of the stress-strain response and not the elastic modulus that has an impact on the efficiency. This can be seen in equation (14) by noting the dependence of efficiency on the inverse of the non-linear components of the stress-strain response. The efficiency for a material that stiffens in the strain range of interest (0-40%) will have a lower efficiency than a material that softens as it stretches.

Note that the data is plotted against the parameter Z' that contains the combination of permittivity, modulus, and nominal electric field; thus changing any of the parameters will have no impact on the shape of the efficiency curve. The peak in efficiency is determined by the shape of the stress-strain curve and applied strain only, though the ability of the material to reach the peak efficiency will depend on the parameters within Z'. A high stiffness material will require either a high permittivity or a high breakdown field if it is to reach its peak efficiency while a softer material will be able to operate at peak efficiency at lower, and perhaps more manageable electric fields.

In order to provide a more qualitative picture of the derivation, a visual determination of the maximum efficiency for the intermediate elastomer at a strain of 30% is shown in Figure 9.3 assuming a dielectric constant of 3. The elastic stress is shown as a solid black line and the elastic energy per unit volume, taken as the integral of stress with respect to strain, is shown as the dotted blue line. In this case, the material is stretched to 30% strain and held there, resulting in an input of 0.0442 J/cm^3 of elastic energy into the system (show as the red diamond). A nominal electric field equal to 47.9 MV/m (corresponding to the value that results in the peak efficiency) is applied to the elastomer, resulting in an input of 0.0515 J/cm^3 of electrical potential energy and an electrostatic pressure (Maxwell stress) of 0.10 MPa. The mechanical stress is then removed and the material relaxes to the point where the Maxwell stress is equal to the elastic stress of the material (red circle). At this point, the electrical energy has increased to 0.0664 J/cm^3 (red square). This energy is then collected and the material is allowed to relax fully. The efficiency is taken as the peak in electrical energy minus the input electrical energy over the mechanical energy (0.0664-0.0515)/0.0442 = 33.7%.

9.2 Conclusions

The equation derived provides a simple and useful tool for predicting the efficiency of dielectric elastomer energy harvesters and can not only be used to predict the maximum efficiency that a material is capable of, but can also be used for determining the operating parameters required to achieve that efficiency. The analysis underscores the importance of electrostatic pressure induced strains caused by the increasing electrical potential across the elastomer films during the relaxation phase of a constant charge energy harvesting cycle. Assuming the elastomers strain response is linear up to 20% strain, the equation can accurately predict the maximum efficiency and optimal material and operating parameters up to an applied strain of approximately 40% depending on the shape of the stress-strain curve. Beyond this value it begins to deviate but can still provide a useful approximation for determining the optimal performance values for high efficiency operation. We note that the maximum attainable efficiency for a particular strain is dependent upon the lumped parameter $Z^{'}$ and the shape of the stress strain curve.

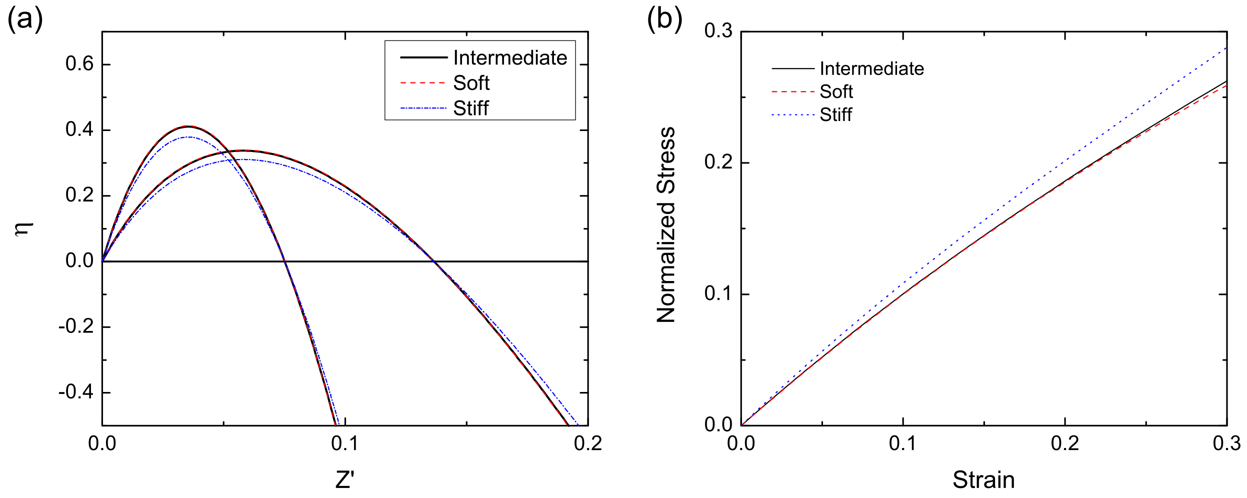

Figure 9.2: (a) Efficiency of the three elastomers from Figure 9.1 as a function of Z' for 10% and 30% strain. Note the results for the soft and intermediate elastomers overlap despite having very different stiffness. (b) Normalized stress for the three elastomers in Figure 9.1 showing that the shape of the stress-strain curves for the soft and intermediate films are almost identical.

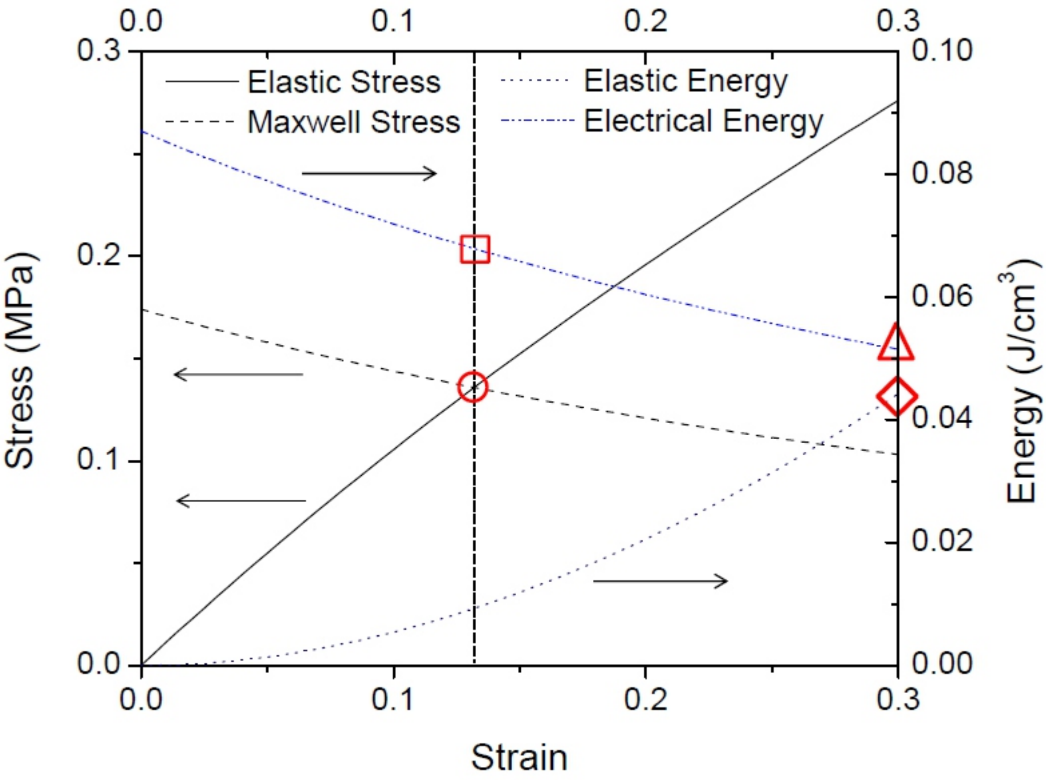

Figure 9.3: Visual derivation of the efficiency for a constant charge energy harvesting cycle with 30% strain for the intermediate elastomer in Figure 9.1 using a nominal bias field of 47.9 MV/m. The mechanical energy input into the system during stretching is marked by the red diamond, while the electrical energy input into the system is shown as the red triangle. If the mechanical stress is removed the material will relax until the Maxwell stress curve intersects the elastic stress curve (red circle). The electrical energy at this point is shown by the red square (max electrical energy). The electrical energy is then collected and the material is allowed to fully relax. The efficiency is taken as the difference between the max electrical energy and the input electrical energy divided by the input mechanical energy.

CHAPTER 10

Acrylic Interpenetrating Polymer Network Dielectric Elastomers for Energy Harvesting

In Chapter 6 it was shown that increasing material stiffness should increase the amount of energy that can be harvested with dielectric elastomers by suppressing the effects of Maxwell pressure-induced strains during the relaxation phase. Here, we test the energy harvesting capabilities of VHB-based interpenetrating polymer network elastomers (IPNs) with a trimethylolpropane trimethacrylate (TMPTMA) additive network. We explore the effects that increased additive content have on material stiffness and energy harvesting performance and compare the results with highly prestrained VHB4910 and VHB4905.

10.1 Materials

For this study we use 3Ms VHB4910 and 4905 acrylic elastomers as well as VHB4905-based IPN films. The IPN films were fabricated using trimethylolpropane trimethacrylate (TMPTMA) as an additive. The chemical structure of TMPTMA is shown in Figure 10.1. The IPN films were prepared by first prestraining a 3M VHB4905 film to 400x400% onto a rigid frame and spraying a solution of TMPTMA monomers with a thermally activated free radical initiator onto the film using an airbrush. The extent of prestrain was observed to vary from approximately 380x380% to 420x420% from sample to sample. The films were left overnight to allow the monomers to diffuse into the film and the solvent to evaporate. The monomers were polymerized in a vacuum oven at 80-85C for several hours. Upon removal, electrodes were applied to the films. The IPN films were used in their unrelaxed state. The IPN preparation process is described in more detail in Reference [172]. VHB4905 and 4910 films were prestrained by hand to varying degrees using an apparatus built in-house and electrodes were applied to the films.

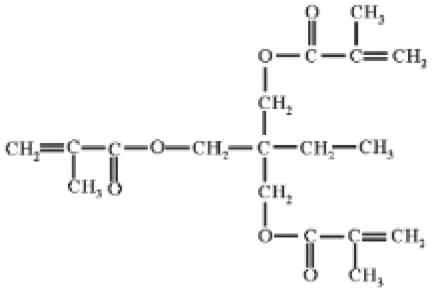

Figure 10.1: Chemical structure of TMPTMA.

Carbon nanotubes (CNTs) are used as the electrode material. CNTs were sprayed from a dispersion in chloroform using an airbrush at a concentration of 0.2mg/mL. A contact mask was used to define the shape of the electrodes.

10.2 Apparatus and Testing Procedure

The prestrained VHB films and IPN elastomer generators were cycled between high and low strain states using the diaphragm setup shown in Figure 10.2. The films were affixed to the air pressure chamber using layer of VHB4910 to ensure proper adhesion. A layer of rigid tape was applied around the active area of the film to ensure the deformation was isolated to the active area in the event that the film delaminated from the VHB4910 adhesion layer. Air was pumped into a separate air reservoir which was then used to pressurize and depressurize the air pressure chamber causing the film to deform to a high strain state and relax. The setup was arranged such that the air could be transferred quickly between the reservoir and pressure chamber allowing the material to relax quickly. As such, the rate of relaxation was defined primarily by the materials viscoelasticity and the sample geometry.

The generators were fabricated using unrelaxed IPN or prestrained VHB4905 and 4910 films and had a circular active area measuring 1" in diameter. The capacitance in the rest state was measured using a multimeter and the capacitance in the stretched state was calculated based on strain measurements. The thickness of the VHB samples was calculated based on the capacitance measurements and the dielectric constant of VHB acrylic measured from a sample of known thickness ($\epsilon_r = 4.1 \pm 0.1$). The thickness of the IPN samples was measured directly using a micrometer and the thickness measurement was used to infer the dielectric constant. A high voltage power supply, built in house, was used to supply voltage to the DE generator and a high voltage diode rated at 10 kV was used to prevent back-charging from the DE generator to the power supply. An Agilent DSO3202 oscilloscope connected across the DE generator using a high impedance step-down voltage probe was used to measure the voltage across the device. The vertical displacement of the film was measured using an Acuity AR200-50 laser displacement sensor and the pressure was measured using an analog pressure gauge. The area strain of the film was calculated using the following equation that assumes the film deforms in a spherical manner:

$$\lambda_A = \frac{H^2 + r^2}{r^2} \tag{10.1}$$

where H is the vertical deflection and r is the radius of the active area (0.5 inches). The stiffness of the films was determined from the pressure applied to deform the film and the deflection of the film. The strain on the film was calculated using equation 4 and the stress was calculated using the equation below normalized to take into account the variation in film thickness:

$$\sigma = \frac{pr}{2d} \tag{10.2}$$

—

where p is the pressure, r is the radius of the active area, and d is the thickness of the film, calculated as the thickness at rest divided by the area stretch. The pressure calculated using equation 5 is the stress normal to the plane of the film and not the real internal stress on the film.

All tests were performed using a constant charge energy harvesting cycle. The energy generated was calculated using equation 3. Energy density was calculated as the energy produced divided by the volume of the active elastomer film. The volume of the electrodes and packaging was not taken into account.

10.3 Results and Discussion

Table 10.1 lists the pertinent data for the films tested. Two VHB4905 films (denoted VHB4905-400 and VHB4905-300 for films prestrained 400x400% and 300x300% respectively) and two VHB4910 films (denoted VHB4910-400 and VHB4910-300 for films prestrained 400x400% and 300x300% respectively) were tested along with three IPN films with varying additive content. IPN4905-01 had the lowest additive content, followed by IPN4905-03 and IPN4905-02. The capacitance of IPN4905-3 is higher than the other two IPN samples due to some variability in the prestrain applied to the films.

The stress-strain data for the 7 samples is shown in Figure 10.3. As expected, increasing the prestrain on the VHB4905 and 4910 films increases the stiffness of the films. The incorporation of the rigid poly-(TMPTMA) additive network in the IPN films had the expected effect of increasing the stiffness in the composite film. The results indicate that the stiffness is tunable by varying the additive content. Interestingly enough, the VHB4910 films appear to be less stiff than their VHB4905 counterparts. The reason for this is unknown but may be due to batch-to-batch variability in the material from 3M.

The energy harvesting performance of the films is shown in Figure 10.4. The samples were tested at area strains of 75% (Figure 10.4a) and 50% (Figure 10.4b). These strain values are well within the safe operation window for VHB-based energy harvesters and are

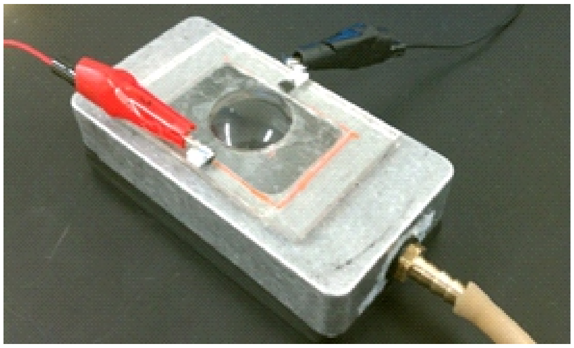

Figure 10.2: Diaphragm setup. The chamber pictured in the image was connected to an air reservoir that was used to pressurize and depressurize the pressure chamber quickly.

Table 10.1: Film Properties

Sample	**Prestrain**	**Dielectric Constant**	**Capacitance (nF)**	**Thickness (μm)**	**Active Volume (cm^3)**
VHB4905-400	400x400%	4.1	0.860	21	0.011
VHB4905-300	300x300%	4.1	0.558	33	0.017
VHB4910-400	400x400%	4.1	0.462	40	0.020
VHB4910-300	300x300%	4.1	0.280	66	0.033
IPN4905-01	400x400%	3.7	0.755	22	0.011
IPN4905-02	400x400%	3.6	0.652	25	0.013
IPN4905-03	400x400%	3.6	0.790	20	0.011

high enough to produce voltage peaks much larger than the system noise. The nominal field is taken as the applied bias voltage divided by the film thickness at rest.

As expected, the performance of the VHB samples increases with increasing prestrain, partly due to the increase in material stiffness and partly due to the decrease in viscoelasticity with prestrain. VHB4905 samples were observed to outperform their VHB4910 counterparts due in part to the increased stiffness of the VHB4905 samples, though geometrical and inertial factors arising from the increased thickness of the VHB4910 samples may play a role as well. We expect that the thicker film will relax more slowly due to the geometry of the test setup. It is also important to note that the peak in performance of the samples is shifted to higher bias fields for films with higher stiffness. This matches well with expectations that stiffer films will suppress Maxwell stress-induced strains during relaxation allowing for improved performance at higher bias fields.

The peak performance of the IPN films compares well with the highly prestrained VHB films. The IPN films show a further shift in peak performance to even higher bias fields as expected due to the increased stiffness of the films compared with the VHB elastomers. However, the performance gains resulting from the increased film stiffness are partially negated by increased losses due to an increase in viscoelasticity. We believe that increasing the additive content beyond a certain value has deleterious effects on the viscoelastic behavior the sample. The glass transition (T_g) of poly-TMPTMA is closer to room temperature than that of the VHB acrylic, so the peak in the mechanical loss factor of poly-TMPTMA is closer to room temperature. Increasing the additive content will therefore increase the loss factor of the composite material. This has the unfortunate effect of increasing the system damping and limiting the frequency of operation. The increased relaxation time for the stiffened IPN films will also result in increased losses due to leakage through the polymer films, which can be considerable at high bias fields. For VHB and IPN films the bulk electrical resistivity of the films is approximately 100 GΩ-m, as measured from the leakage current through a circular expansion actuator. Further performance increases for IPN films are expected if the increased viscoelasticity of the films can be reduced. This goal should be achievable with the use of a different additive or through the incorporation of a plasticizing agent.

Although the 400x400% prestrained VHB4905 film outperforms other samples, 75% of the film failed at or below 80 MV/m (bias for peak performance) after being cycled only a handful of times at that bias. The VHB films prestrained to 300x300% fared better while the IPN films appeared to be the most electromechanically stable. The additional stability should bode well for continuous long-term high-performance operation.

10.4 Conclusions

We have tested the energy harvesting capabilities of VHB-based IPN dielectric elastomers with varying additive content. We have shown that increasing the additive content increases the stiffness of the film which helps to mitigate the effects of Maxwell pressure-induced strains during the relaxation phase of the constant charge energy harvesting cycle and increase performance at high electrical bias fields. Compared to highly prestrained VHB4905 and VHB4910 films, the peak performance of the IPN films was shifted to higher bias fields. The overall performance of the IPN films was comparable with the highly prestrained VHB films. The performance gains achieved through the suppression of the Maxwell pressure-induced strains were partially mitigated by an increase in the viscoelasticity of the IPN films that contributes to a reduction in the relaxation speed of the films and increased parasitic losses due to damping and current leakage. It is expected that reducing the viscoelasticity of the IPN films through the use of a different additive or the incorporation of a plasticizing agent will further improve performance.

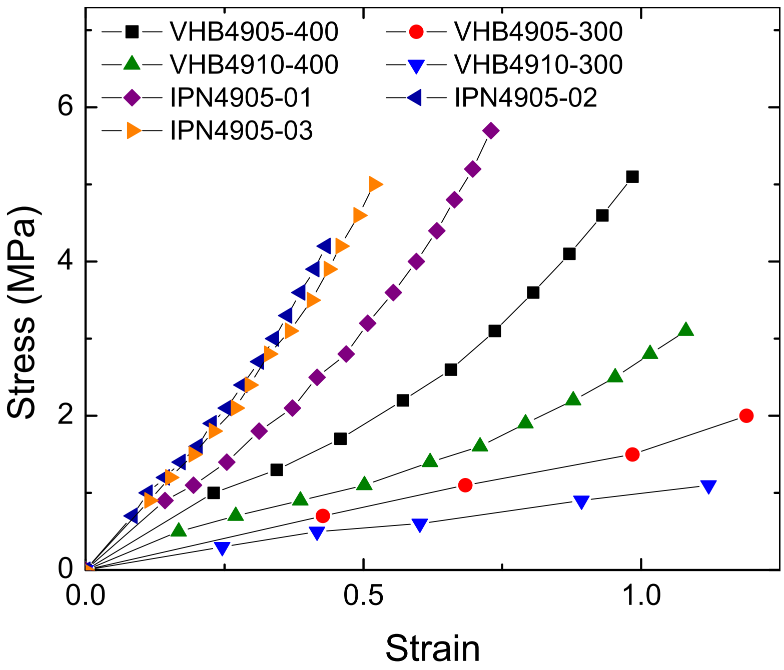

Figure 10.3: Normalized stress vs area strain for VHB4905 and 4910 samples of varying prestrain and IPN films with varying additive content.

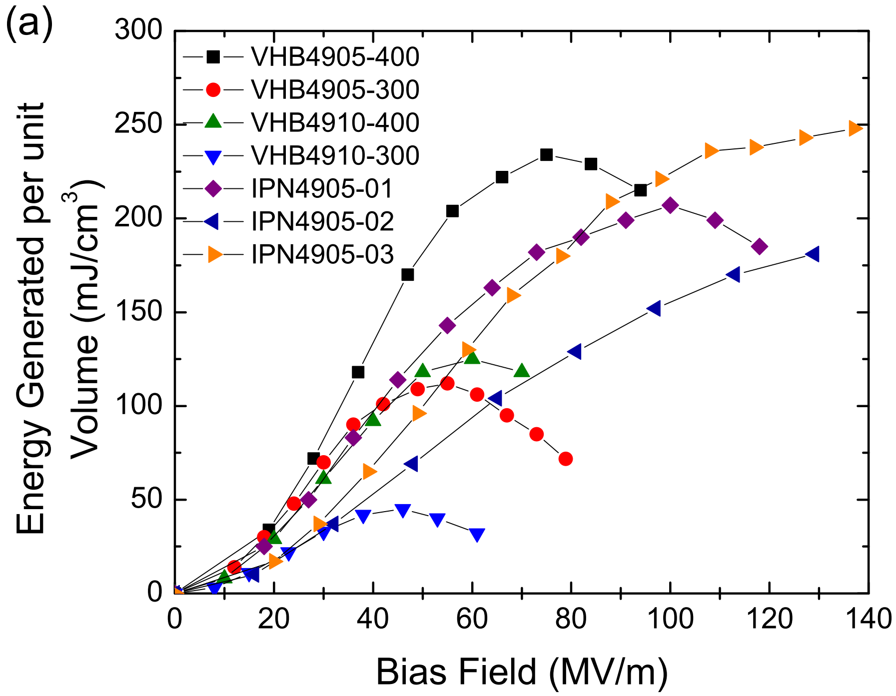

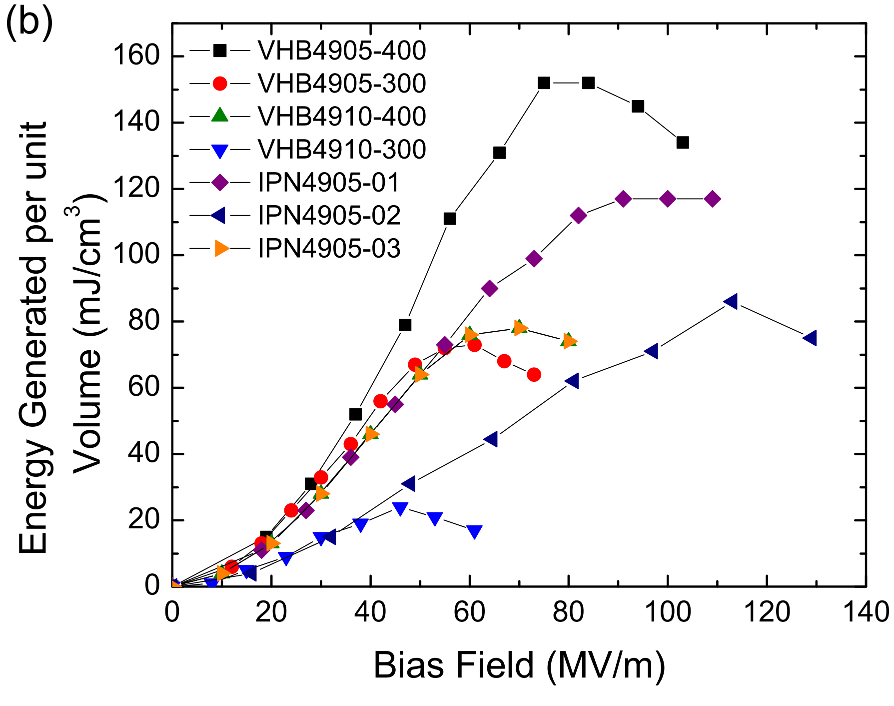

Figure 10.4: Energy generation data for (a) 75% strain and (b) 50% strain.

CHAPTER 11

Silicone TiO_2 Nanocomposite for Improved Energy Density

The VHB4910 series of acrylic elastomers have thus far demonstrated the highest energy density for energy harvesting, capable of producing up to 0.4 J/cm^3 ($\sim$0.4 J/g) for a single stretch-relaxation cycle for an applied mechanical strain of 100%. [331] However, the performance of these acrylic elastomers varies widely over the range of temperatures an energy harvesting device is expected to withstand and sees a drop in performance at higher levels of humidity. VHB4910 also suffers from moderate viscoelastic effects which limits the frequency range over which they can be driven. These fundamental issues place severe limitations on applications for which VHB4910 can be used.

Silicone materials, on the other hand, generally display good performance stability over relatively wide ranges of temperature, humidity, and frequencies. However, silicones generally lack high energy densities owing to their lower dielectric constant and breakdown field. Several reports have been published on preparing silicone composites with increased dielectric constant by the introduction of high permittivity or conductive fillers with the purpose of reducing the required electric fields for actuation (see Chapter 1). The results have been mixed as the addition of the fillers results in an unwanted increase in the material stiffness and, in some cases, in an increase in conductivity of the composite which has negative effects on the energy consumption of the materials. Opris et al. recently reported on a PDMS composite material with improved energy density and improved electrical properties. [197] Their material, however, still has a relatively low breakdown field and low permittivity.

For this study we use a high breakdown strength two part high temperature vulcanization (HTV) liquid silicone rubber (LSR), NuSil CF19-2186, which is the highest actuation energy density silicone found in the literature. [44, 307]. It is important to note that the actuation energy density (E_a) and energy generator energy density (E_g) (denoted as generator energy density hereafter) are different values. The actuation energy density is simply the elastic energy density due to actuation and is a function of the actuation strain and Maxwell pressure and is therefore highest for soft materials with high electrical breakdown strengths. For generator applications, Maxwell pressure induced strains are detrimental to performance as shown in previous chapters. The generator energy density depends primarily on the mechancal elastic energy density and applied electric field and is therefore highest for more rigid materials with high electrical breakdown strengths. The actuation energy density [44] and generator energy density are given by :

$$E_a = -pln\left(1+s_z\right) = -\epsilon_r\epsilon_0 E^2 \cdot ln\left(1+s_z\right) \tag{11.1}$$

$$E_g = \frac{1}{2} ZY \left(\frac{\left(\frac{-1+\sqrt{1+4Z}}{2Z}\right)^2}{\lambda_{3,M}^2} - 1 \right) \tag{11.2}$$

Where:

$$Z = \frac{\epsilon_r\epsilon_0}{Y} E^2 \frac{1}{\lambda_{3,M}^2}$$

In order to increase the generator energy density of the material, we add rutile TiO_2 nanoparticles ($\epsilon_r = 128$) functionalized with short PDMS chains which are dispersed into the polymer solution by ultrasonication at various loadings. In Chapter 3, we showed that the addition of these nanoparticles to a soft silicone host increase the permittivity as well as the stiffness of the elastomer while maintaining the same dielectric breakdown strength. These increases result in an improvement in the work density of the material while maintaining the same driving voltage. Here, the same procedure is used to synthesize a silicone with improved energy density for energy harvesting purposes. As we have previously shown, the energy density of a material increases with increasing stiffness while the efficiency of the material can be kept constant with a concomitant increase in the permittivity of the material.

Unlike various other successful techniques for increasing the permittivity and energy density of silicone elastomers, this approach does not influence the hydrophobicity of the material. The addition of dipoles or conductive fillers, for instance, makes the composite more polar thus attracting more moisture to the material which can influence performance. Our approach maintains the hydrophobicity of the material allowing it to be deployed with confidence in high moisture environments for applications such as wave energy harvesting.

11.1 Experimental

Samples were prepared by first dissolving the two parts of CF19-2186 silicone in Isopar G. Functionalized TiO_2 nanoparticles were then dispersed into part A of the CF19-2186 using a 100 W probe sonicator with a 50% duty cycle at 90% peak power using a 7mm probe for 10 minutes. The dispersion was then placed into a 400 W bath sonicator for 10 minutes before adding the part B CF19-2186 solution followed by bath sonication for an additional 5 minutes. The solutions were then allowed to cool at room temperature for 30 minutes and then drop cast onto poly(styrene sulfonate) (PSS) treated glass. Following solvent evaporation (∼6-8 hours at 45°C), the films were then heated to 180°C for >10 mins to cure the silicone.

COOH functionalized single wall carbon nanotubes (P3-SWCNTs) were dispersed in a combination of 80 vol.% isopropanol and 20 vol.% deionized water at a concentration of 0.4mg/mL in a bath sonicator for 1 hour then centrifuged at 8500 RPM for 20 mins to remove any SWCNT bundles. The SWCNT solution was spray deposited though a contact mask using a Pasche airbrush at 20 psi with a 3 working distance.

The mechanical properties were characterized using a TA Instruments RSAIII dynamic mechanical analysis machine (DMA). For tensile tests, planar dogbone shaped samples with a gauge length of 12 mm and gauge width of 2mm were used. Tensile tests were performed at a rate of 3.33 mm/s. Frequency sweeps were performed on samples with a width of 10 mm in the range of 0.1 to 20 Hz (limited by equipment).

Planar actuators were prepared by prestraining the films onto rigid frames and applying electrodes. The capacitance and dissipation factor of the actuators was measured using a G^WInstek LCR-819 LRC meter. Actuation tests were performed using a low voltage DC power supply and a Trek 10/10B-HS high voltage amplifier. LabView software was used to monitor the strain, monitored with the use of a digital USB microscope, and the output voltage, measured using a National Instruments USB-6009 data acquisition system.

11.2 Results and Discussion

The results for tensile tests are shown in Figure 11.1a while Figure 11.1b shows the results of frequency sweeps with an offset strain of 5%. As expected, the introduction of the nanoparticles to the silicone acts to reinforce the nanocomposite, increasing the modulus by 2.21 times for a loading of 20wt.% TiO_2. The loss tangent (tan δ) is also observed to increase, indicating a small increase in the viscoelasticity of the material. For comparison, the loss tangent for non-prestrained VHB4905 at 1Hz is 0.64 at room temperature.

Films were prestrained by stretches $\alpha_x = \alpha_x = 1.25$ and circular electrodes were patterned onto the film. The capacitance was measured at various frequencies and the relative permittivity was calculated based on the equation for capacitance:

$$C = \epsilon_r \epsilon_0 \frac{A}{d} \tag{11.3}$$

Where C is capacitance, ϵ_r is the relative permittivity, ϵ_0 is the permittivity of free space, A is the overlapping electrode area, and d is the film thickness. The change in relative permittivity is plotted in Figure 11.2 and is shown to increase with particle loadings, with a 31% increase at 5wt.% TiO_2 and a 58% increase at 20wt.% TiO_2. The dissipation factor measured at 1 kHz ranged from 0.016 for the pure material to 0.025 at 20wt.% TiO_2

(Table 11.1).

The same samples were used to determine the electric field strength of the elastomer films by subjecting them to actuation tests. The real electric field strength (E_b) was calculated as the applied voltage (V) over the instantaneous thickness (t_i) determined from the initial thickness (t_0) and area strain using the equation:

$$E_b = \frac{V}{t_i} = \frac{V}{t_0} \alpha_{x,a} \cdot \alpha_{y,a} \tag{11.4}$$

Where $\alpha_{x,a} = \alpha_{y,a}$ are the stretches due to actuation in the x and y directions and $\alpha_{x,a} \cdot \alpha_{y,a}$ is the area stretch due to actuation. Following previous results, higher prestrains should result in improvements to the dielectric breakdown strength as well as the energy density for energy harvesting. To determine if this is the case for the nanocomposite materials, additional samples were prestrained by $\alpha_{x,a} = \alpha_{y,a} = 1.50$ and were also tested.

Values for breakdown strength and actuation strain were observed to differ from sample to sample due to difficulties with processing. Improper homogenization of the composite prior to drop casting the films or the incorporation of foreign dust particles during the curing process as well as non-uniform film thickness resulting from improper leveling of the casting surface can result in poor performance values. The peak strain and electric field for the different TiO_2 concentrations at$\alpha_{x,a} = \alpha_{y,a} = 1.50$ and 1.25 are shown in Table 11.1 along with other pertinent data.

Results indicate that the electrical breakdown field remains very high (>200 for $\alpha_{x,a} = \alpha_{y,a} = 1.50$ and >120 for $\alpha_{x,a} = \alpha_{y,a} = 1.25$) for all TiO_2 contents. The maximum area strain decreases with increasing content due to the increased stiffness of the composites and the reduction in maximum field. The disparity between breakdown strength values for $\alpha_{x,a} = \alpha_{y,a} = 1.50$ is interest since the values for $\alpha_{x,a} = \alpha_{y,a} = 1.25$ are quite similar and the sample with 20wt.% TiO_2 content actually shows the highest breakdown strength at that prestrain. The maximum breakdown strength for the 10wt.% sample at $\alpha_{x,a} = \alpha_{y,a} = 1.50$

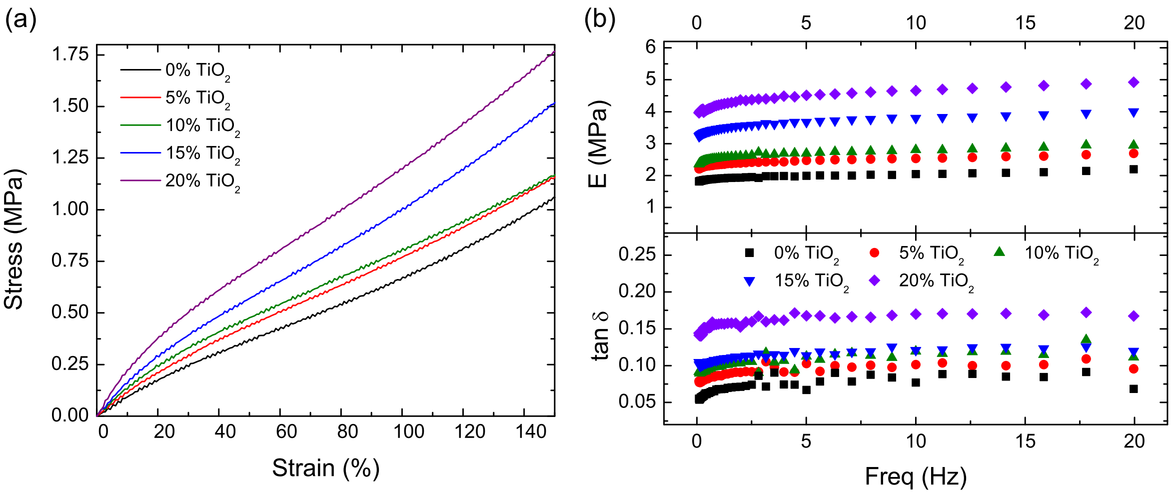

Figure 11.1: Mechanical properties of CF19-2186/TiO_2 nanocomposites for various TiO_2 loadings. The stiffness increases with increased TiO_2 content as expected due to the chain-pinning effects of the nanoparticles. The tan δ value is also observed to increase with increased TiO_2 loading; however, losses are still quite low.

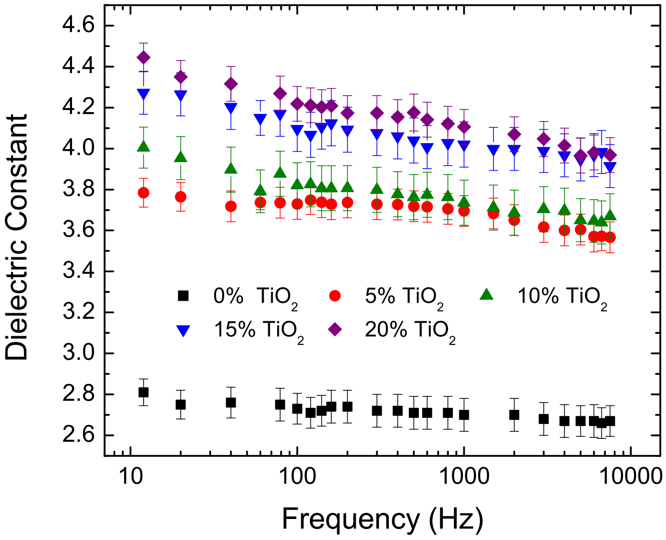

Figure 11.2: Dielectric constant of CF19-2186/TiO_2 nanocomposites for various TiO_2 loadings.

Table 11.1: Electrical and actuation properties of CF19-2186/TiO_2 nanocomposites with various TiO_2 loadings.

TiO_2 Content	**Dielectric Constant (100 Hz)**	**Dissipation Factor (1 kHz)**	**Max. Area Strain** ($\alpha_{x,a} = \alpha_{y,a} = 1.50$)	**Max. Breakdown Field** ($V/\mu m$) ($\alpha_{x,a} = \alpha_{y,a} = 1.50$)	**Max. Area Strain** ($\alpha_{x,a} = \alpha_{y,a} = 1.25$)	**Max. Breakdown Field** ($V/\mu m$) ($\alpha_{x,a} = \alpha_{y,a} = 1.25$)
0%	2.73	0.016	56%	370	27%	146
5%	3.73	0.017	42%	313	25%	141
10%	3.82	0.019	42%	355	23%	151
15%	4.10	0.018	16%	212	16%	123
20%	4.22	0.025	25%	225	17%	165

is also quite high. These results lead us to believe that relatively low observed breakdown strength for certain samples is the result of less-than-perfect homogenization. This conclusion is supported by the results from Chapter 3 where a similar approach is used with a different silicone base material and no decrease in the breakdown strength is observed up to TiO_2 loadings of 20wt.%.

Results of the actuation tests for $\alpha_{x,a} = \alpha_{y,a} = 1.50$ are shown in Figure 11.3a. The actuation curves all essentially overlap one another, a poor result for improving actuation but an ideal result for increasing energy density while maintaining the same efficiency and required operating field of the pure material. These results indicate that the increase in permittivity offset the increases in stiffness almost exactly. Figure 11.3b shows normalized stress-strain curves for the composite materials. The normalized values are those presented in Figure 11.1a divided by the modulus at 1Hz shown in Figure 11.1b. The inset in the figure shows an expanded view of the first 15% strain showing the values overlap in the expected linear range.

Based on the work shown in previous chapters, maintaining the same ratio of permittivity and stiffness should indicates the peak efficiency should occur for all materials near the same electric field value, thus the composite material does not reduce or increase the required electric field. Referring to Figure 11.3b, the normalized stress-strain response of the composite materials show that increasing the TiO_2 content has the effect of reducing the effective modulus at increasing strain values. Based on our previous theoretical analysis this should result in an increase in the energy harvesting efficiency for composites with higher TiO_2 content. It should be noted though that the loss tangent (Figure 11.1b) and dissipation (Table 11.1) also increase marginally with increasing TiO_2, so that any gains in efficiency from the reduced effective modulus at higher strains will be partially offset by increased parasitic losses.

In order to calculate the generator energy density for the composites, the modulus and $\tan \delta$ at $\alpha_{x,a} = \alpha_{y,a} = 1.50$ were measured using a DMA at a frequency of 1 Hz for samples

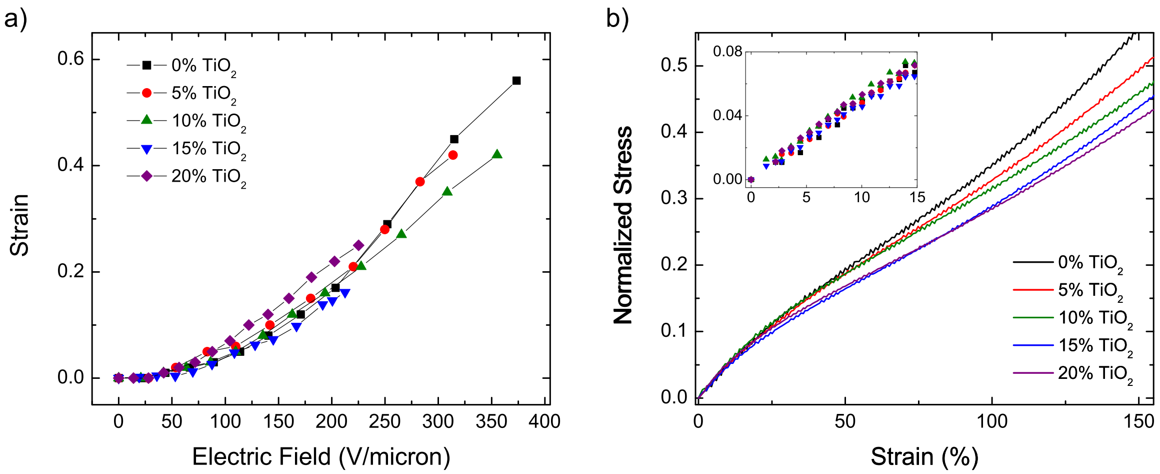

Figure 11.3: a) Actuation strain results for the CF19-2186/TiO$_2$ nanocomposites prestrained by $\alpha_{x,a} = \alpha_{y,a} = 1.50$. The actuation strain curves are essentially overlapped indicating that increases in permittivity offset by matching increases in modulus. b) Normalized stress-strain response for the nanocomposites showing that composites with increasing TiO$_2$ content display a larger reduction in effective modulus with increasing strain. The inset shows an expanded view of the first 15% strain representing the expected linear stress-strain region of the elastomers. In this region the normalized stress-strain curves overlap almost completely.

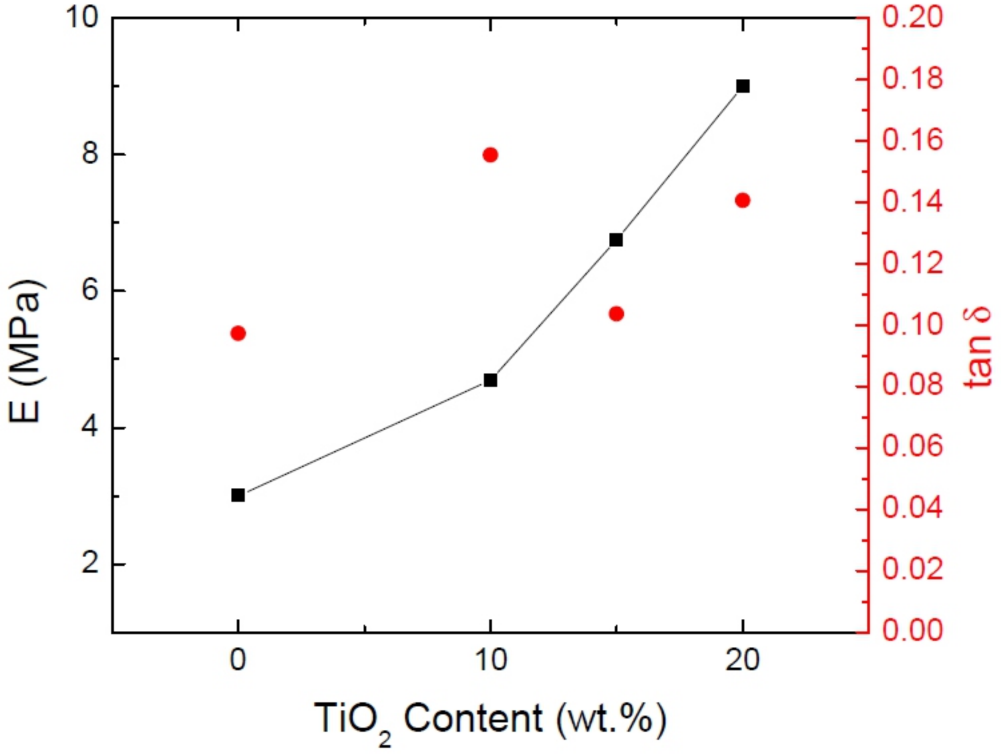

Figure 11.4: Modulus and tan δ values for CF19-2186/TiO_2 nanocomposites prestrained to $\alpha_{x,a} = \alpha_{y,a} = 1.50$.

with 0, 10, 15 and 20wt.% TiO_2 (Figure 11.4). As expected, the modulus increases with increased prestrain; however, the tan δ values remain approximately the same as for the fully relaxed samples.

Using these values and the values for breakdown field listed in Table 11.1 the generator energy density can be estimated using Equation 11.2 above for bias electrical field values up to the breakdown strength of the material. The results of the calculations are shown in Figure 11.5. As expected from previous analysis, the generator energy density increases with TiO_2 content due to an increase in the modulus and permittivity of the nanocomposites. An increase of over 3 times is possible at 20wt.% TiO_2. The values compare very favorably with highly prestrained VHB4910 and actually exceed the maximum reported energy density

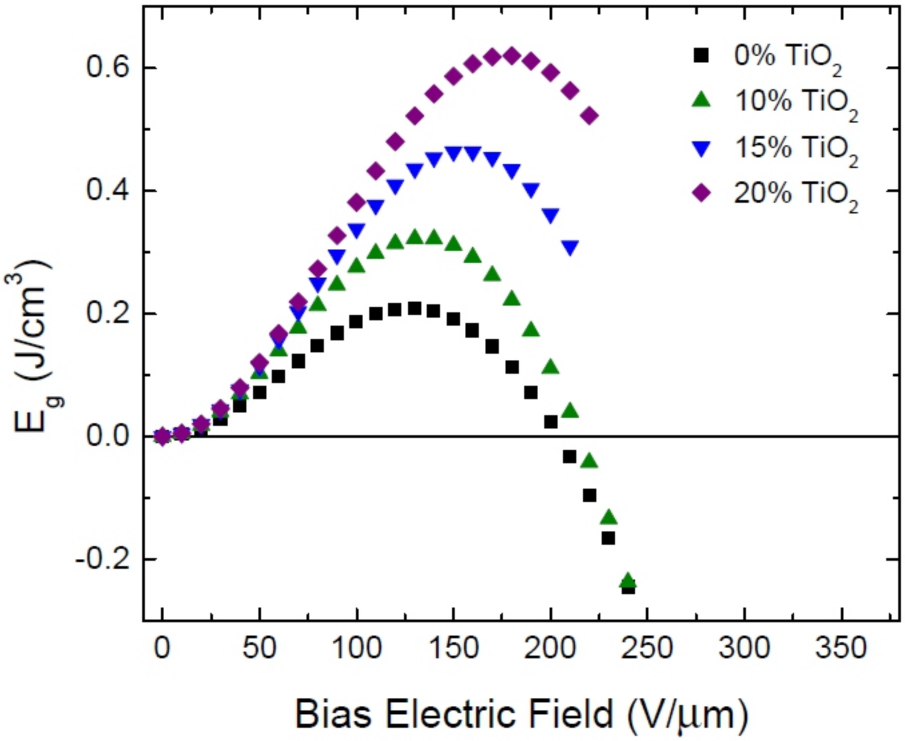

Figure 11.5: Calculated generator energy density for CF19-2186/TiO$_2$ nanocomposites stretched by 50% in area for bias electric field values up to the breakdown strength of the composite.

of VHB4910 despite being stretched to only 50% in area as compared to 100% for the case of the VHB4910 results. It is important to note, however, that these calculations are only an approximation and do not account for any parasitic loss mechanisms. Actual generator energy density values are expected to be lower but are still expected to exceed the performance of highly prestrained VHB at similar applied mechanical strains.

Referring to Figure 11.5, it should also be noted that the peak performance lies within the bounds of the measure maximum breakdown strength of all the composite materials, indicating that the reduction in maximum breakdown strength will not impact the performance of the nanocomposite materials.

11.3 Conclusions

High breakdown strength silicone-TiO_2 nanocomposite materials were successfully fabricated using Nusil CF19-2186 as the base silicone. The composite materials show an increase in the permittivity with increased TiO_2 content with only a marginal increase in the dissipation factor. The modulus of the composites also increases with increased TiO_2 content as the nanoparticles act to restrict chain motion. The $\tan \delta$ of the composite materials was also observed to increase marginally with increased TiO_2 content but remains low, indicating that viscoelastic losses should be minimal. The breakdown strength for the nanocomposites remained very high (> 200 V/μm for a prestrain of $\alpha_{x,a} = \alpha_{y,a} = 1.50$ and >120 V/μm for a prestrain of $\alpha_{x,a} = \alpha_{y,a} = 1.25$) and in some cases the breakdown strength of the nanocomposites exceed that of the pure base silicone. Generator energy density calculations show an improvement of over 3 times for a TiO_2 content of 20wt.% compared with the pure base silicone. The peak calculated energy density for the 20wt.% and 15wt.% TiO_2 samples, over 0.6 J/g and over 0.45 J/g respectively, exceed the measured value for highly prestrained VHB4905 (0.4 J/g) despite the fact that the applied strain for the nanocomposite calculations was only 50% in area compared to 100% in area in the case of the VHB4910 results. The calculations do not take into account any parasitic loss mechanisms and are based on a relatively simple model so experimental values are expected to be lower; however, it is expected that the performance of the nanocomposite should be capable of exceeding the performance of VHB4910 when mechanically strained to similar values.

CHAPTER 12

Silicone Carbon Nanotube Composite Electrodes for Energy Harvesting

One prevailing issue with dielectric elastomer generators obtaining electrodes that are capable of maintaining low resistance over a broad strain range and a large number of cycles. Additional requirements include low viscoelastic losses and the ability to operate over a relatively wide temperature range. Maintaining low resistance in the highly stretched state is important for reducing parasitic resistive losses that can act to reduce the net energy harvested from the system. In addition, low resistance will be beneficial for high frequency and large capacitance applications, since the time required to charge the elastic capacitor is equal to the product of electrode resistance and the active material capacitance.

A plethora of stretchable electrode technologies have been developed recently, including buckled electrode structures [215, 342], corrugated electrodes [214, 343], metallic nanowires and carbon nanotubes embedded in the surface of elastomers [313, 344] or in the bulk [345], and ion implanted electrodes [220, 223, 346] among others. However, these technologies fall short in terms of one or more of mechanical rigidity, lifetime, strain-rate dependence, and generally suffer from increases in resistance of several order of magnitude or complete loss of conductivity at large strains ($> 100\%$). Lipomi et al. recently reported on a skin-like carbon nanotube PDMS electrode fabricated by direct spray-coating on carbon nanotubes onto an activated PDMS film. [347] By cycling their electrodes at high strains, the baseline resistance is first observed to increase with strain for the first strain cycle, and then maintain this strain value thereafter for several thousand stretch-relaxation cycles. Their method involves programming the electrode via the reorientation and buckling of the deposited carbon nanotubes along the stretched direction. Following the initial stretching cycle, the carbon nanotubes retain that orientation, allowing the electrode to be stretched to high strains with only minimal increases in resistance.

Here, we demonstrate a silicone-single wall carbon nanotube (SWCNT) composite electrode that is capable of being stretched in excess of 150% strain and at strain rates up to 100%/s without any appreciable increase in resistance. The composite is also capable of being cycled at strains up to 120% for several thousands of cycles. An initial increase in the baseline resistance of under 10% is generally observed for the first stretch-relaxation cycle but this increase is then recovered over a number of subsequent cycles. The electrode remains locked into the surface of the silicone film and thus retains its as-deposited resistance value when stretched. The composite consists of a thin silicone film with SWCNT electrodes partially embedded within the surface. The material shows low viscoelastic losses across the expected operational frequency range and minimal changes in mechanical properties across a broad temperature range. Composite materials with electrodes embedded on both sides of the silicone film were tested as capacitive strain sensing and energy harvesting applications.

12.1 Composite Preparation

Samples were prepared by co-dissolving a room temperature vulcanizing (RTV) silicone and high temperature vulcanizing (HTV) silicone with an extended pot life in a common solvent. Thin films were prepared by drop casting the solution onto treated glass, allowing the RTV silicone to cure, peeling the film from the glass, stretching the film by 3.5 times in one direction and 1.25 times in the other direction and attaching it to a rigid frame. SWCNT electrodes were spray deposited along the highly stretched direction from a dispersion in isopropanol and water and the film was heat treated to cure the HTV silicone. The film was then released from the support frame and allowed to relax. A schematic representation of the process is shown in Figure 12.1.

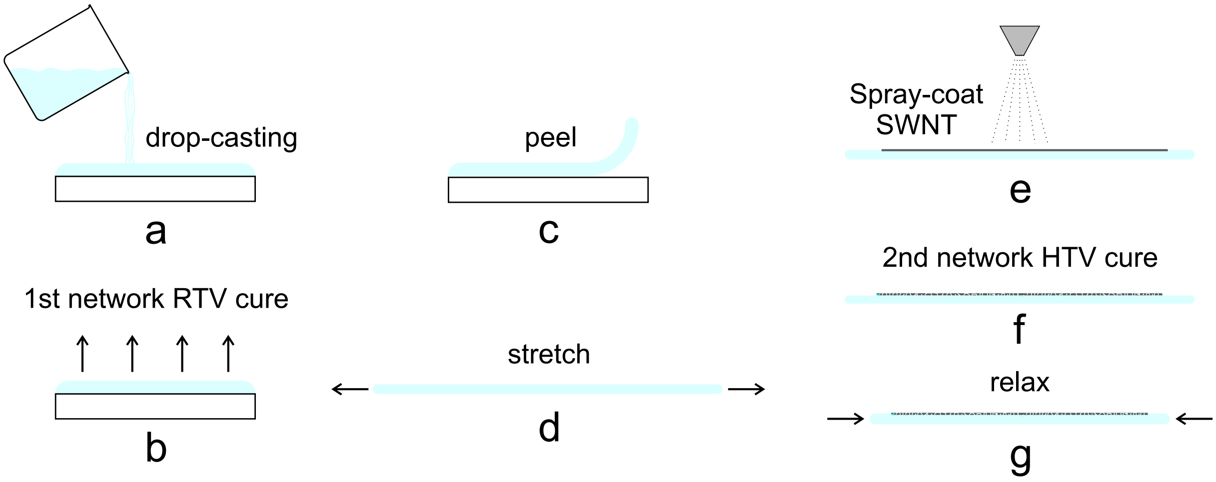

Figure 12.1: Schematic of the composite fabrication process. (a) An RTV and HTV silicone are dissolved in a co-solvent and drop-cast onto a treated glass substrate; (b) the solvent is allowed to evaporate and the RTV silicone is allowed to cure; (c) the film is removed from the substrate and (d) stretched onto a rigid frame; (e) SWCNTs are spray deposited onto the film from a dispersion in isopropanol and water; (f) the film is heat treated to cure the HTV silicone component; (g) the film is allowed to relax.

12.2 Experimental

12.2.1 Material Preparation

Dow Corning HSIII silicone was dissolved in an isoparafinic solvent (ExxonMobil Isopar G) at a concentration of 0.25g/mL and centrifuged to remove the pigment particles. Silpuran 6000/10 was dissolved in Isopar G at 0.25g/mL. Glass substrates were thoroughly cleaned by immersing in KOH/isopropanol bath for several hours followed by rinsing water, washing with detergent, rinsing with waster, rinsing with deionized water, drying, then wiping with isopropanol and acetone using a lint-free cloth. The glass was then treated with a poly(styrene-sulfonate) (PSS) solution in deionized water (5wt.%). P3-functionalized SWCNTs were dispersed in a mixture of isopropanol and water at a concentration of 0.2-0.4 mg/mL using a 400W bath sonicator for 2-3 hours. The SWCNT solution was then centrifuged to remove any nanotube bundles.

The HSIII and Silpuran 6000/10 solutions were mixed at a concentration of 15wt.% Silpuran. 83 NW curing agent was added to the solution at a 20:1 HSIII base to curing agent ratio. The resulting solution was drop cast onto the PSS-treated glass and the HSIII was allowed to cure for 2-3 days at room temperature. The partially cured films were then prestrained 250x25% onto a rigid metal frame. SWCNT electrodes were then spray deposited onto the sample using a Pasche airbrush at 20 psi. The sample was then heated in an over at 160C for 30 minutes to cure the Silpuran network. The films were then removed from the frame and allowed to relax.

12.2.2 Testing

For electrode cycling characterization a Zaber A-LSQ300A-E01 linear stage was used to strain the composite electrode and a Keithley 2000 multimeter and LabView software was used to monitor the resistance.

For capacitive sensing tests, samples were prepared by applying SWCNT electrodes onto both sides of the silicone film prior to curing the additive component with an overlapping region measuring 18mm in length and 5mm in width. The sample was loaded onto a Zaber A-LSQ300D-EO1 linear stage and the capacitance was monitored using an Agilent U1732C handheld LCR meter.

For capacitive energy harvesting tests, a high voltage source built in-house was used to supply voltage of the device through an in-house switching circuit controlled via LabView. The energy output was monitored by measuring the voltage drop over a 1 GΩ load resistor using an Agilent DSO3202A oscilloscope.

12.3 Mechanical Characterization

The mechanical properties of the composite were tested in the relaxed state. Results for a tensile test, frequency sweep and temperature sweep are shown in Figure 12.2. The material is very soft, even at large extension, reaching a stress value of just 1.08 MPa at a strain of 400%. The modulus at 1Hz is 286 kPa and the material shows a minor dependence on strain rate, with modulus increasing from 280 kPa at 0.1 Hz to 322 kPa at 10 Hz. The mechanical loss factor at 1 Hz is 0.067 and remains low across the range of frequencies tested indicating low viscoelasticity which is important for minimizing losses and improving performance repeatability and reliability. Modulus and viscoelasticity of the materials show relatively flat responses across the range of expected operating temperatures (-40 to 80°C). The modulus gradually increases from 315 kPa at -40°C to 383 kPa at 80°C while the mechanical loss factor decreases with temperature from 0.094 at -50°C to 0.066 at 80°C. The change in mechanical properties with temperature follows the expected trend for entropically elastic materials and is expected to have a negligible impact on the overall performance of a device made using this composite electrode.

12.4 Electrode Characterization

The resistance of the electrode was measured both before and after relaxation. A sheet resistance as low as 1.9kΩ/□ was obtained. No appreciable difference in this number was observed despite a reduction in electrode length of over 60% and an increase in the effective SWCNT density of 150%. This appears to indicate that the electrodes have been physically entangled or partially embedded in the silicone film in the high strain state.

The adhesion of the electrode material to the silicone was qualitatively determined by applying a piece of 3M Scotch tape to the conductive surface of the electrode and measuring the change in surface resistance. After several such tests no increase in the resistance was observed indicating good adhesion between the silicone and SWCNTs. For comparison, a

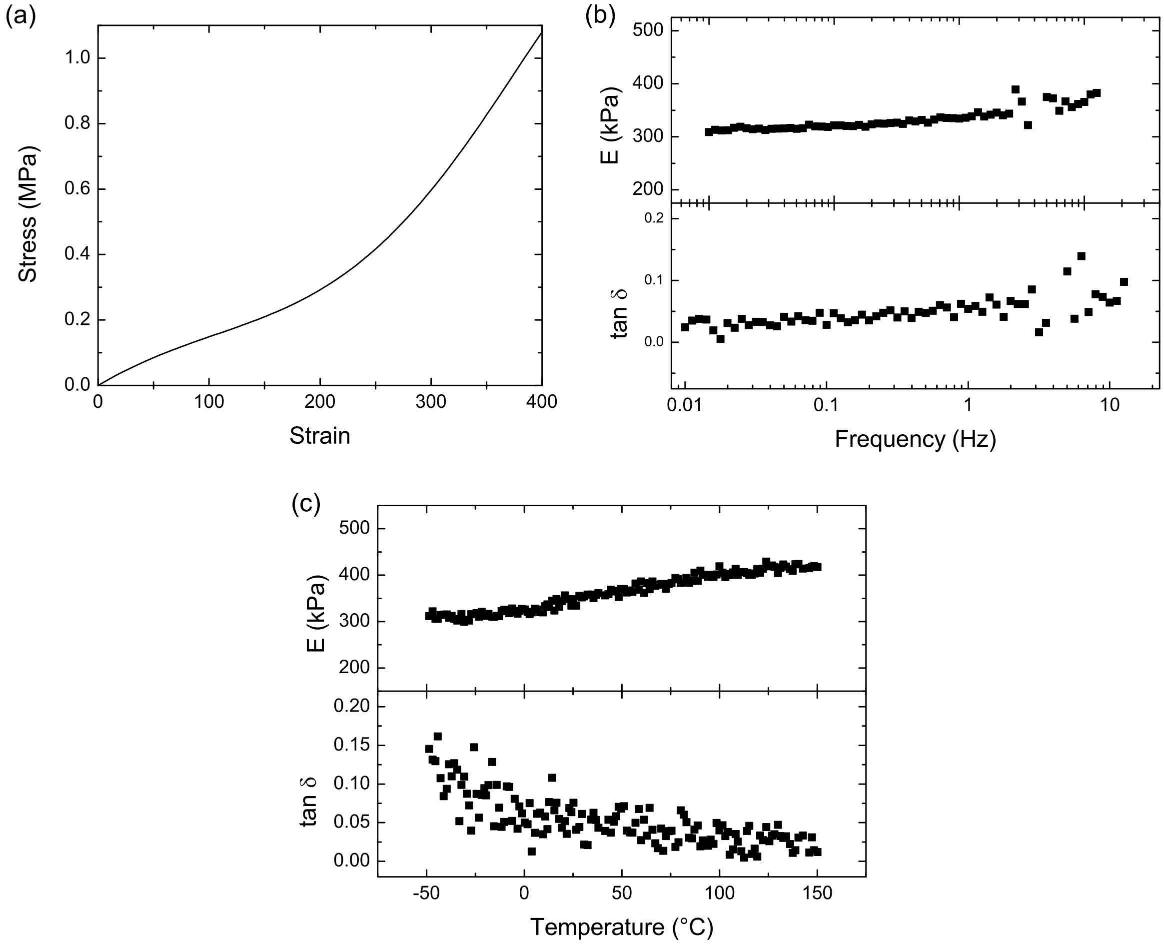

Figure 12.2: Mechanical properties of the composite material.

standard HSIII film with spray deposited electrodes was also tested; the majority of the electrode was removed resulting in a total loss of conductivity. The composite electrode was then subjected to longer term adhesion tests where the Scotch tape was left on the electrodes for several days. When peeled from the electrode surface, some of the electrodes were removed from the composite surface resulting in an increase in the electrode resistance by approximately an order of magnitude depending on the thickness of original SWCNT layer and the duration the tape was left on the electrode surface. This result indicates that enhanced van deer Waals force provided by physical entangling, instead of covalent bonding, should be considered the primary bonding force between the SWCNTs and the silicone host.

Scanning electron microscope (SEM) images of the sample were also taken to determine the surface and electrode morphology of the sample. Figure 12.3a shows the surface morphology of the composite; due to the fabrication process, the films surface shows non-uniform buckling with a feature size in the range of 10 μm. Figure 12.3b shows a high magnification image of the composite showing bundles of SWCNTs arranged in a pseudo-honeycomb pattern. White spots indicate the presence of silicone in and around the SWCNTs indicating that the nanotubes are at least partially locked into the surface layer of the silicone film.

Samples were prepared with a 15mm gap and 5 mm width and strained cyclically for 1000 cycles at 10% increments from 10-120% at a rate of 1 mm/s. Resistance measurements were taken in the stretched and relaxed states. Results for 10, 30, 60, 90 and 120% strains are shown in Figure 12.4. For all strains, the resistance in the stretched state is seen to increase between 5 and 10% for the first cycle while the baseline resistance in the relaxed state is also observed to increase by roughly 5% for 10, 60, and 120% strains and less than 3% for 30 and 90% strains. These initial increases are followed by a gradual relaxation. In the case of 10% strain, the final resistance after 1000 cycles in both the stretched and relaxed states is observed to decrease to 97% of the initial resistance value. At higher strains (30, 60, 90, and 120%) the final resistance in the stretched and relaxed states is found increased by less than 6% of the initial values. Based on these observations some level strain programming is

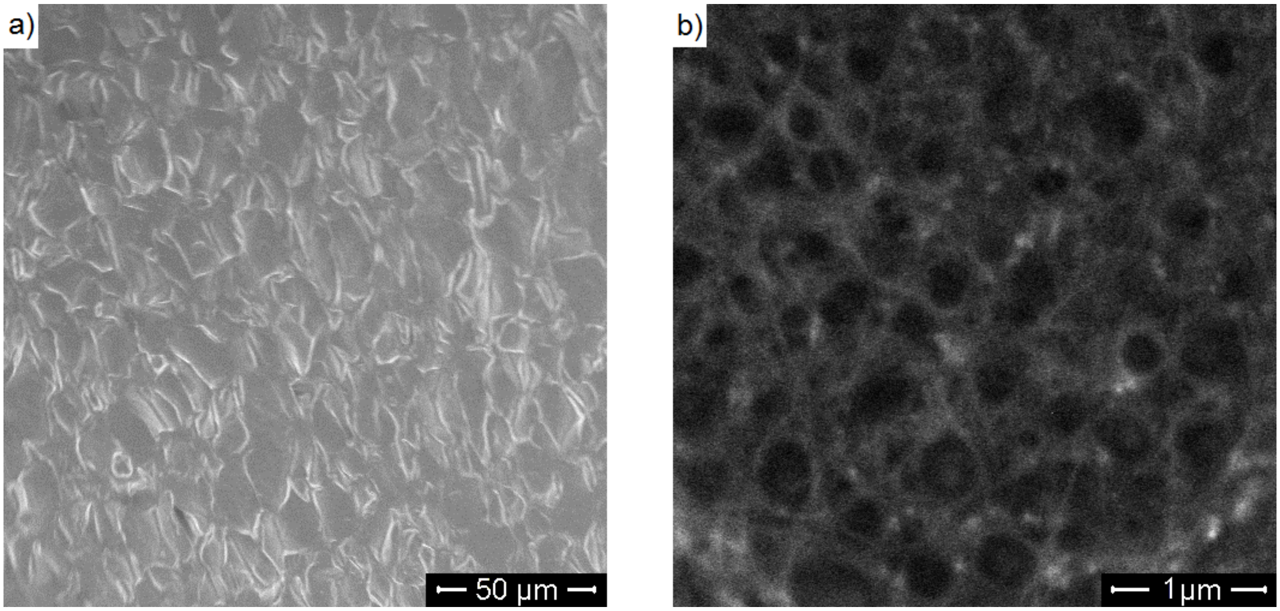

Figure 12.3: (a) Low magnification image of the surface of the composite showing its wrinkled morphology. (b) High magnification image of the SWCNTs on the surface of the composite. The SWCNTs bundles arrange themselves in a honeycomb like pattern. White spots in the image indicate the presence of silicone in and around the SWCNT bundles.

clear; however, the effects are much less pronounced than in the case of the results reported by Lipomi et al. and thus point to a different mechanism.

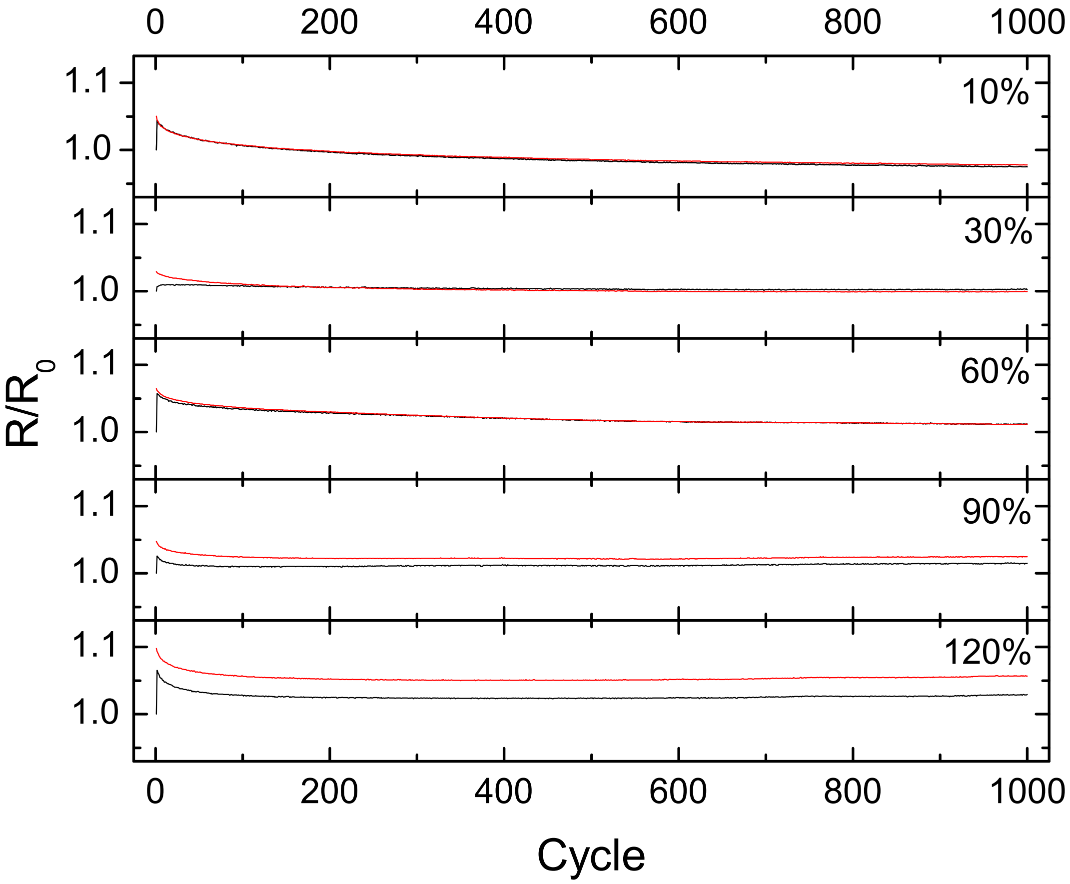

Figure 12.4: Resistance data for a sample being cyclically stretched for 1000 cycles to 10%, 30%, 60%, 90% and 120% strain. The two curves for each strain represent the resistance in the stretched (upper curve) and relaxed (lower curve) states. Below 90% strain, the curves essentially overlap indicating essentially no change in resistance with strain up to 90%.

In the case of the work of Lipomi et al. the carbon nanotubes are bonded by increased dipole forces due to plasma treating the surface of the PDMS film. The carbon nanotubes are free to reorient themselves on the surface of the PDMS and the morphology is able to change as the film is stretched and relaxed. For our composite material the situation is still not clear. One possible explanation could be related to the physically entangled SWCNT-silicone structure. During the curing process at elevated temperatures, the thermal diffusion rate of the oligomeric chains can be enhanced. [314] We believe that the uncured additive silicone resin diffuses into the deposited carbon nanotubes network and physically entangles them after curing. The carbon nanotubes are locked in the surface of silicone when the film relaxes. The orientation of the nanotubes will be limited by relaxation of the silicone chains. Because of this, very few new connections are made between carbon nanotubes, but very few of the original ones are lost. Therefore very small change in resistance can be observed before and after releasing from the supporting frame.

When the film is initially stretched from the fully relaxed state, the carbon nanotubes remain trapped by the additive silicone chains and therefore are able to retain the majority of the original electrical connections when the film is stretched. The initial small jump in resistance for the first strain cycle is likely due to some inhibition of chain movement in the additive network. If the nanotubes are entangled in the silicone chains, their movements will be tied together and the presence of the nanotubes is expected to have some influence on chain movement, likely retarding their motion. After a number of cycles at a particular strain the restricted chains are able to reach their equilibrium state which they maintain thereafter. This type of programming is therefore tied to restrictions in chain movement and not to reorientation of carbon nanotubes on the silicone surface.

In order to determine the effects of strain rate on the resistance change of the electrode, a sample was subjected to strain cycling at 100% strain at rates of 25%, 50% and 100% per second. Tests were run sequentially so that any effects due to programming at the previous strain rate are expected to remain for the following tests. The sample was cyclically strained for 1000 cycles at 25% per second and 2000 cycles for 50% and 100% per second (Figure 12.5). The results are similar for all strain rates, demonstrating a small increase ($\sim$10%) for the first cycle, followed by a gradual decrease in the resistance in both the stretched and relaxed states, and finally a plateau where the resistance stabilizes. Note, however, the relatively small initial increase at a strain rate of 50% per second; this is likely due to programming effects from running the test at 25% strain. At a strain rate of 100% per second the initial increase once more jumps to roughly 10% for both the stretched and relaxed state. At a strain rate of 100% per second the duration of time to reach the plateau region is also observed to increase but the overall increase in resistance is only 2% in the relaxed state and 4% in the stretched state. Two factors lead to the minimal strain rate dependence in our composite electrodes. Firstly, the silicone host itself has a very low mechanical loss factor so that its response to any mechanical loading/unloading is almost instant. Secondly, better bonding between SWCNTs and the silicone host allows the conductive network to responds rapidly to the mechanical input as well.

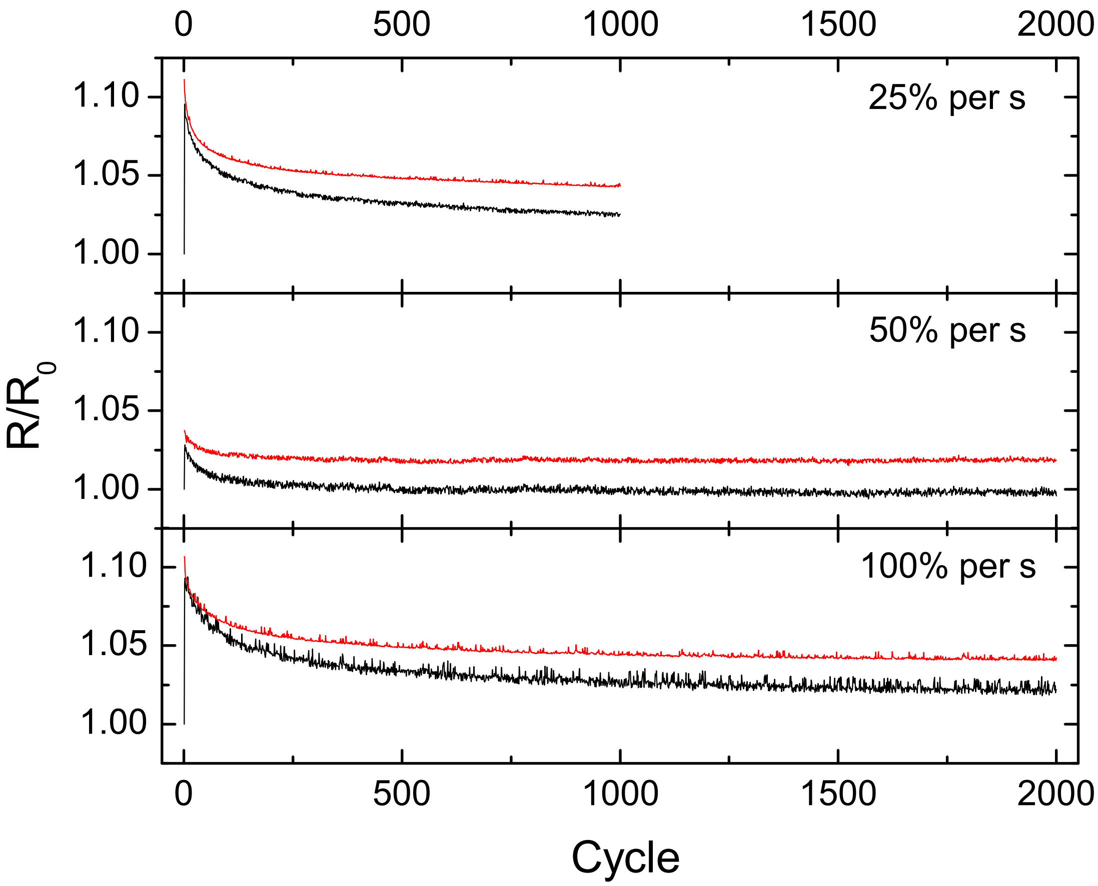

Figure 12.5: Resistance data for a sample being cyclically stretched to 100% strain at strain rates of 25%, 50% and 100% per second. The two curves for each strain rate represent the resistance in the stretched (upper curve) and relaxed (lower curve) states.

To determine the maximum strain the composite can withstand while maintaining conductivity, the films was stretched at a rate of 1 mm/s until loss of conductivity (Figure 12.6). The resistance does not increase appreciably up to >150% strain, after which it increases sharply. The electrode can be stretched up to its as-deposited length with essentially no change in resistance. This indicates that the majority of the original electrical connections between nanotubes are maintained. Once the length of the electrode exceeds its original length, the SWCNTs begin to be pulled apart, reducing the number of electrical connections resulting in a large increase in the resistance. At 200% the resistance increases to 30 times the initial value. The resistance continues to increase sharply beyond the values shown in Figure 12.6, with an increase of over 160 times at an extension of 225%.

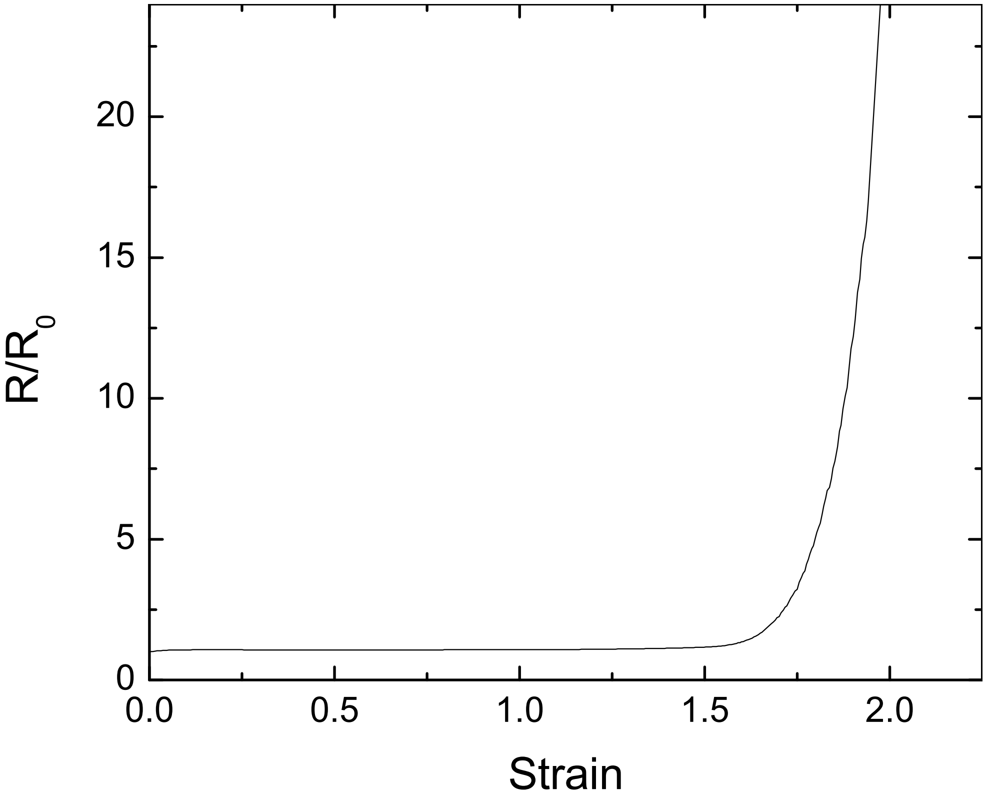

Figure 12.6: Resistance increase with strain. The strain remains essentially unchanged up to >150% strain after which the resistance increases sharply with strain.

12.5 Capacitive Sensing

In order to operate effectively as a capacitive energy harvester, it follows that a device should also operate well as a capacitive strain sensor. Indeed, owing to the negligible change in resistance up to 150% strain, the silicone-SCWNT composite should operate very well as a strain sensor.

Samples were prepared with overlapping electrodes sandwiching the silicone film. Elastomer materials have a Poisson ratio near 0.5, and are therefore essentially incompressible. When the material is stretched, the film will elongate in the stretch direction and compress in the thickness and width directions. If the dimensions of the film are chosen such that the width is much larger than the length, the compression in the width direction will be minimized resulting in a superlinear increase in capacitance with stretch. For strain sensing purposes, a linear response is optimal. Thus the dimensions of the electrode were chosen such that the electrode was longer that it was wide in order to maximize the linearity of the measurements. The sample was subjected to 100% strain over 10 cycles and shows excellent linearity and repeatability owing to the negligible increase in resistance with strain (Figure 12.7).

12.6 Energy Harvesting

To demonstrate the energy harvesting capabilities of our silicone-SWCNT composite, a sample was prepared with a width of 77 mm, a length of 26 mm, and a thickness of 88 μm. The dimensions of the sample help to minimize the compression of the elastomer in the width direction, resulting in a superlinear increase in capacitance (Figure 12.8a). In order to demonstrate the repeatability of this measurement, the sample was stretched by 100% strain over 10 cycles and capacitance was recorded at regular intervals. Figure 12.8b shows the relative change in capacitance along with strain over 10 cycles. With 100% applied strain, the capacitance increases by almost 3.5 times.

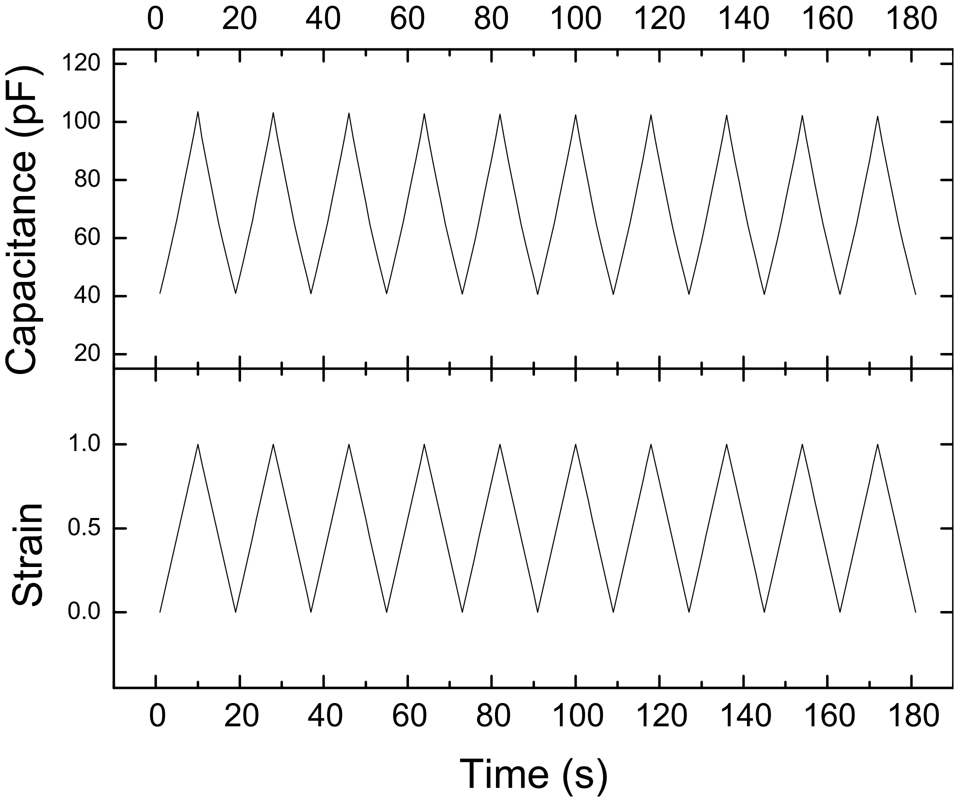

Figure 12.7: Capacitive sensing at 100% strain over 10 cycles.

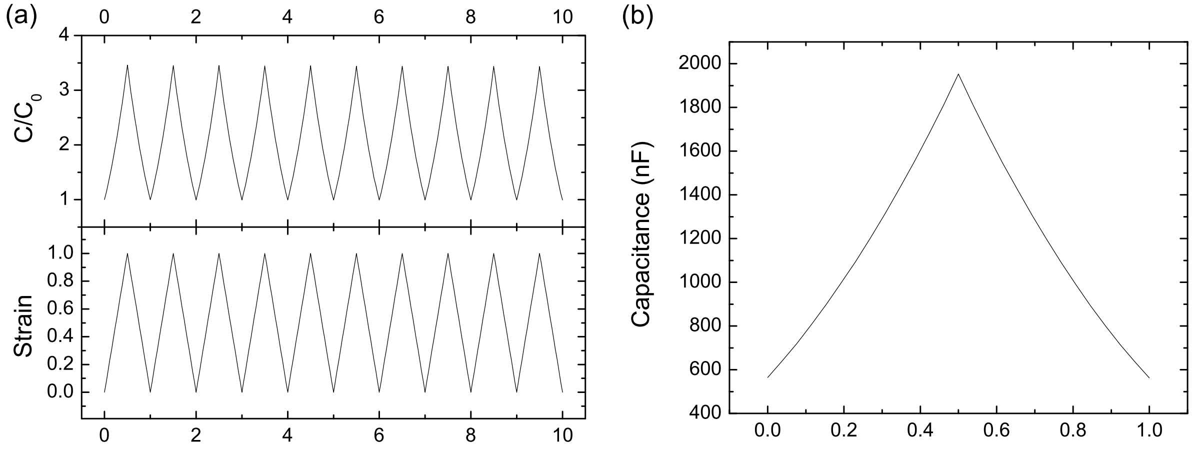

Figure 12.8: Capacitance cycling for capacitive energy harvester showing a superlinear increase in the capacitance with strain.

For energy harvesting tests, the sample was stretched to 50% strain at a rate of 100% strain per second. The sample was tested at various voltages and shows the expected increase in energy harvested with increased bias voltage. [331] The results, shown in Figure 12.9, indicate that approximately 7.5 mJ of energy can be harvested per cm^3 of active material at the peak voltage tested (1800 V). With a density of approximately $1g/cm^3$ and assuming an energy harvesting cycle frequency of 1 Hz we would need just over 130g of the material to produce 1 W of power.

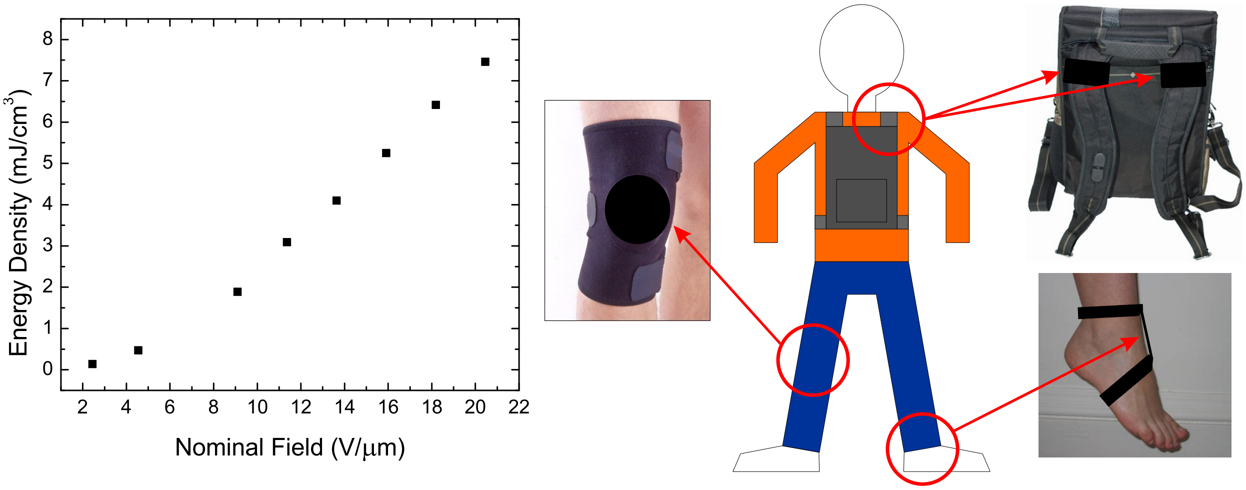

Figure 12.9: (Left)Capacitive energy harvesting results and (right) schematic of several concepts for energy harvesting from the human body.

Given the materials low stiffness, relatively high energy density and the ability to arrange it in a large number of configurations with different sizes, it could be used to harvest energy from a variety of sources on the human body. Regions of interest are the knee, that swings through an angle of 60° when walking, and the ankle and hip that both swing through over 20° during walking. [348]. Additional energy could be harvested at the shoulders or arms from natural arm swinging motions or by incorporating the material into the straps of a backpack or purse. The composite could also be incorporated into clothing or used as an external device.

12.7 Conclusions

We have developed a soft, flexible, and stretchable silicone-SWCNT composite that can withstand linear strains in excess of 150% without any appreciable change in resistance. The electrodes can be cycled over 1000 times at 120% strain with only a small (<10%) increase in resistance and over 5000 times at 100% strain with only a 5% increase in resistance. The electrodes also show strain rate independence and have been tested at strain rates ranging from 25% per second to as high as 100% per second with no clear deviation in the performance. If electrodes are patterned on both sides of the composite, it can be operated as a capacitive sensor and energy harvester. By selecting the appropriate device dimensions, the capacitance change is repeatable and can be made linear for sensor purposes or superlinear for energy harvesting purposes where a larger capacitance change results in larger energy gains. When operated as an energy harvester, the device can generate over 7 mJ of energy per cm^3 of active material when strained by 50%. The combination of softness, flexibility, high stretchability, low resistance changes, and relatively high energy density make this material suitable for harvesting energy from human motion.

CHAPTER 13

Applications for Dielectric Elastomer Generators

13.1 Concept for an Ocean Wave Energy Harvesters

Ocean waves presents a renewable, widely distributed, abundant source of clean energy. Tapping into this energy source could aid the US reducing the overall environmental impact caused by power station by reducing our reliance on coal, nuclear and other environmentally harmful sources. Harnessing clean energy from ocean waves along the US coasts could also reduce our dependence on foreign energy sources (such as oil from the Middle East), which can put the US at risk in the event of international turmoil.

Estimates of the total worldwide economically recoverable wave energy resource are in the range of 150 to 750 TWh/yr based on existing mature technologies as at 2003. [349] With further technical improvements this value could double or triple. [350] In the U.S., the total annual average wave energy off the coast at a depth of 60m has been estimated at 2100 TWh. [351] Analysis by the U.S. Electric Power Research Institute (EPRI) performed in 2003 estimates that the viable wave energy resource in the U.S. at 255 TWh per year. [352]

Several types of wave energy harvesters (WEHs) have been developed that can broadly be placed into 4 categories:

1. Terminators or oscillating water columns (OWCs) OWCs typically extend outward in the direction perpendicular to wave travel to capture more energy from incoming waves. Most OWC designs are on- or near-shore, however, floating devices exist that can be deployed offshore. OWCs capture wave energy using a column with trapped air

that extends underwater with a subsurface opening to allow water to enter and exit the column. The wave motion causes water in the column to rise and fall, which in turn forces air through a turbine to create electricity. Energetech [353] and the Japan Marine Science and Technology Center [354] have developed prototypes of offshore OWCs.

2. Attenuators Attenuators are long, multi-segmented floating devices oriented with their long edge parallel to the direction of wave travel. The relative motion of the individual segments results in flexing at the connection points between segments. The flexing motion can be used to drive hydraulic pumps or other converters. The McCabe wave pump [355] and the Pelamis by Pelamis Wave Power [356] are examples of attenuators that use hydraulic pumps.
3. Point absorbers Point absorbers are so named because they collect wave energy at a single point. A number of point absorbers have been packaged as buoys with one free floating component and second component that is either relatively immobile (i.e. fixed to the sea floor) or weighted such that its motion is out of phase with the motion of the floating component. The relative motion of the two components can be used to drive a pump or electromechanical generator. The PowerBuoy developed by Ocean Power Technologies [357] and the AquaBuOY developed by AquaEnergy Group, Ltd. [358] are examples of buoy-style point absorbers. The Archimedes Wave Swing is an example of another type of point absorber that relies on the relative motion of an air-filled cylinder that follows the vertical motion of the waves and a second cylinder that is fixed to the ocean floor to drive a linear electrical generator.
4. Overtopping devices Overtopping devices collect ocean water from waves into reservoirs and then use the water to drive turbines or other conversion devices. Water from waves that exceed the height of the reservoirs walls is collected. Some designs include wave reflecting arms that extend outward and concentrate the waves toward it, thereby increasing the effective wave height. Both onshore and offshore devices exist.

Examples of overtopping devices are the Wave Dragon^{TM} and WavePlane^{TM}.

The power rating of the aforementioned energy harvesters can vary widely based on the design of the device, location of the proposed installation, and purpose of the installation. Typical full-scale individual devices range in nameplate power rating from a few hundred kW to a few MW.

While the environmental impacts of WEHs are expected to be minimal, WEHs have yet to be adopted in many regions due to a few factors including:

1. Cost The capital cost for a wave energy park can be quite high, and depending on the nature of the installation, maintenance costs may also be high due to the difficulty in accessing and working on devices moored offshore.
2. Wear and risk of device failure Marine environments can be rather harsh. Rough seas and the corrosive environment may damage devices incorporating complex systems and moving parts.
3. Power transmission and conditioning Power transmission from a distributed source that lies miles off the coast could present difficulties and will result in some transmission losses. Additionally, conditioning power from a regular but unpredictable source presents difficulties.

While hydraulic, pneumatic, and electromechanical systems are mature and proven energy harvesting technologies, they are not without their limitations. Many of the systems can be relatively complex and consist of many moving parts that can become damaged in harsh conditions. Robust designs capable of withstanding marine environments will be expensive. Alternative approaches toward energy conversion may provide benefits over these mature technologies and open the door to newer, more effective WEH designs.

Due to their capacity to operate under high strain conditions and low to moderate frequencies at high energy densities and conversion efficiencies, DEs appear to be particularly suited to harvesting energy from ocean waves. Recently, SBR has reported the development of an attenuator type DE wave energy harvester wherein the walls of the device are made of

DE materials. [337] When a wave passes the device, it generates a pressure wave that strains the DE materials in the wall. SRI has also demonstrated ocean wave energy harvesting prototype devices based on DE materials. [324,326,332,335,336] Their device is a buoy-type point absorber that uses rolled DE tubes attached to a proof-mass. As the waves pass, the proof-mass moves out of phase with the rest of the buoy causing the DE tubes to stretch and contract.

Here we report on a pseudo-OWC type DE wave energy harvester. The basic device concept consists of a simple tubular column oriented perpendicular to the water surface, partially submerged in the water and anchored to the ocean floor. A dielectric elastomer film is affixed to the top end of the column. The device can be operated either as a standard OWC, allowing water to flow into and out of the submerged portion of the column, compressing the air trapped inside causing the DE film to deform, or as a pseudo-OWC, wherein no water is allowed to enter or leave the column and the difference in water height inside and outside the column as a wave passes by causes the trapped air in the column to change in pressure causing the DE film to deform. A conceptual rendering of the latter device is shown in Figure 13.1 where the DE is shown in yellow. The following will consider the case of the pseudo-OWC.

The passing of a wave of height (H) will generate a change in pressure of the air trapped in the column equal to $p = \rho g H$; where ρ is the density of ocean water (1020 kg/m^3) and g is the acceleration due to gravity. For typical wave heights ranging from 0.5 to 5m the pressure change is 5 to 50 kPa. As the film deforms, however, the volume (Vol) will increase, thus reducing the pressure change generated by the wave if the film deforms in the outward direction, or increasing the pressure change if the film deforms inward:

$$p = \rho \cdot g \cdot H \cdot \frac{Vol_0 + Vol_{DE}}{Vol_0} \tag{13.1}$$

Where the subscripts 0 and DE represent the free volume of the cylinder and the volume change due to the deformation of the DE film stack. Based on the work of Rosset et al., the

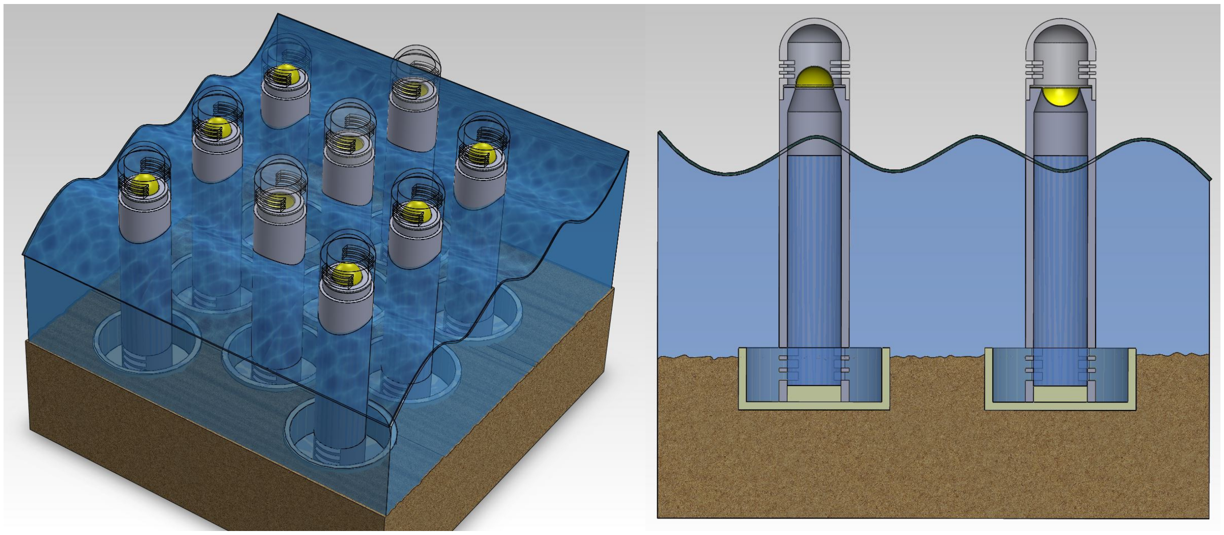

Figure 13.1: Pressure based pseudo-OWC DE WEH. As waves pass by the cylinders, the pressure differential inside and outside the tube varies. The pressure differential causes a stack of DE films to deform outward in the case of a positive wave height (or wave crest) and inward in the case of a negative wave height (or wave trough).

deformation of the DE film based on the pressure change can be derived from a modified version of the bulge test equation. [223] For the case of thin films where the thickness is much smaller than the radius, the balance between the biaxial stress in the film and the applied pressure can be derived from the case of a thin-walled spherical pressure vessel [359]:

$$\begin{aligned} \sigma 2\pi R t &= p\pi R^2 \\ p &= \frac{2\sigma t}{R} \end{aligned} \tag{13.2}$$

Where R is the radius of the pressure vessel and t is the thickness. For the case of a thin film being deformed into a spherical cap with height h, we can relate the radius of the film to the radius of the ”imaginary” pressure vessel geometrically by:

$$\begin{aligned} R^2 &= (R-h)^2 + r^2 \\ R &= \frac{h^2+r^2}{2h} \end{aligned} \tag{13.3}$$

As the film is deformed, the area increases by a factor λ_a, which is accompanied by a concomitant decrease in the film thickness (t) by a factor $\lambda_t = 1/\lambda_a$. Thus the thickness is given by:

$$t = t_0\lambda_t = \frac{t_0}{\lambda_a} = t_0\frac{A_0}{A_i} = t_0\frac{\pi r^2}{\pi\left(r^2+h^2\right)} = t_0\frac{r^2}{\left(r^2+h^2\right)} \tag{13.4}$$

The stress in the DE film can be broken down into two components: the stress due to deformation caused by the change in pressure, and the residual stress in the film due to prestrain ($_0$). Taking into account the hyperelastic nature of the DE films:

$$\sigma = \sigma\left(h, Y_e, c_i\right) + \sigma_0 \tag{13.5}$$

Under the assumption of a true biaxial strain state:

$$\sigma\left(h, Y_e, c_i\right) = 2\left(\lambda_a - 1/\lambda_a^2\right)\frac{\delta W}{\delta I_1} \tag{13.6}$$

Where:

$$\begin{aligned} I_1 &= \lambda_1^2 + \lambda_2^2 + \lambda_3^2 \\ &= 2\lambda_a + 1/\lambda_a^2 \end{aligned}$$

Combining the above equations, the relationship between pressure, stress, deformation, and radius becomes:

$$p = \frac{4t_0r^2\sigma\left(h, Y_e, c_i\right)}{r^2+h^2}h + \frac{4\sigma_0t_0r^2}{\left(r^2+h^2\right)^2}h \tag{13.7}$$

The strain (denoted s to prevent confusion with the dielectric constant) can then be calculated by:

$$s = \frac{h^2 + r^2}{r^2} \tag{13.8}$$

As the DE film is relaxing during an energy harvesting cycle, the voltage across the DE cannot be ignored; taking this into account, the equation becomes:

$$p = \frac{4t_0 r^2 \sigma\left(h, Y_e, c_i\right)}{r^2 + h^2} h + \frac{4\sigma_0 t_0 r^2}{\left(r^2 + h^2\right)^2} h - \frac{4\epsilon_0 \epsilon_r V^2}{t_0 r^2} h \tag{13.9}$$

Based on these equations it is possible to determine the strain state of the DE film for a given pressure and device dimensions. It also allows us to determine the scaling rules for the proposed design enabling estimates for large, grid-scale energy harvesters, and large wave heights to be determined from laboratory scale results.

Results will differ depending on the material system selected. We have selected prestrained VHB4905 for our laboratory-scale testing given the popularity of the material in the field, its ease of use, high energy density, and the ability to tune the material properties with prestrain. As shown in Chapter 10, higher prestrains result in higher energy density and thus larger energy gains; however, at a prestrain of 400x400%, VHB 4905 is more prone to rupture and has a poorer shelf life than films prestrained by 300x300%. It is also requires higher fields to operate at peak efficiency and is therefore more prone to electrical degradation and failure. Since this work deals with devices that will be deployed offshore, long lifetime takes precedence over energy density and a prestrain of 300x300% is therefore chosen.

Pressure-deflection data was collected for scaled versions of the design to determine what scaling relationships are valid experimentally. Tests were performed on samples with a diameter of 1 inch with 1 layer of VHB (D = 1, L = 1), a diameter of 2 inches with 1 layer of VHB (D = 2, L = 2), and a diameter of 1 inch with 2 layers of VHB (D = 1, L = 2) and the

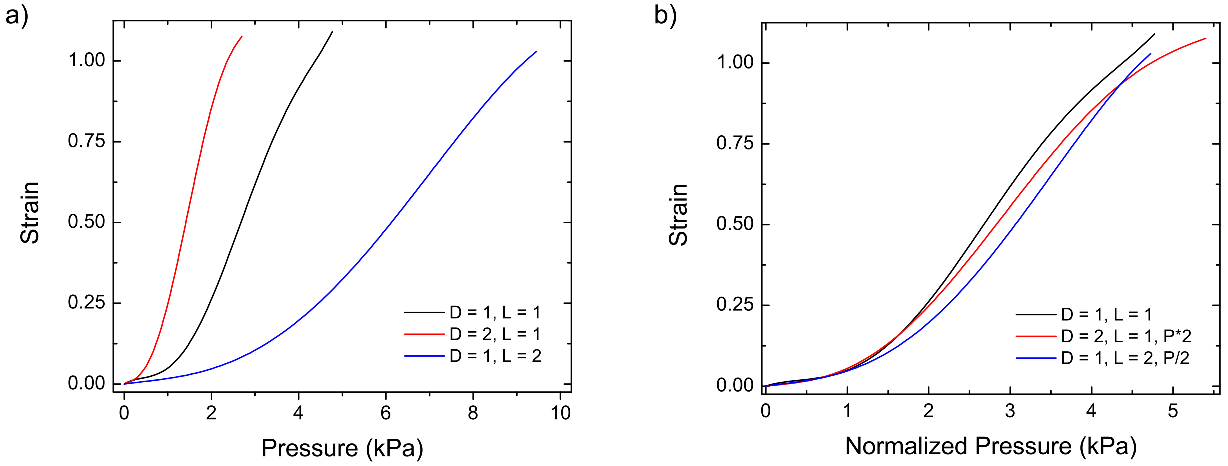

Figure 13.2: a) Pressure-strain curves for VHB4905 films prestrained 300x300% in a diaphragm configuration with diameters of 1 and 2 inches and 1 or 2 layers. b) Normalized pressure-strain curves where the measured pressure is doubled for the sample with a diameter of 2 and halved for the sample with two layers.

results are shown in Figure 13.2a. Based on the results of the analytical derivation above, the required pressure to strain the film should vary linearly with the thickness, and therefore the number of layers, and with the inverse of diameter. Thus, doubling the diameter is expected to cut the required pressure in half, and doubling the thickness is expected to double the required pressure. To determine if these scaling relationships are accurate, the experimentally measured pressure was doubled for the sample with a diameter of 2 inches and halved for the sample with 2 layers. The results, shown in Figure 13.2b, show that these ”normalized” curves are indeed very similar. Taking into account the viscoelasticity of the material, and therefore its strain rate dependent nature, it is safe to conclude that the values overlap within the expected bounds of experimental error.

Energy harvesting data was collected using a diaphragm setup on a single VHB4905 film prestrained 300x300% with a diameter of 2 inches. The device was tested at 25%, 50%, 75% and 100% strain by applying air pressuring by compressing and releasing an air reservoir attached to the diaphragm chamber. Voltage was supplied by a high voltage power supply

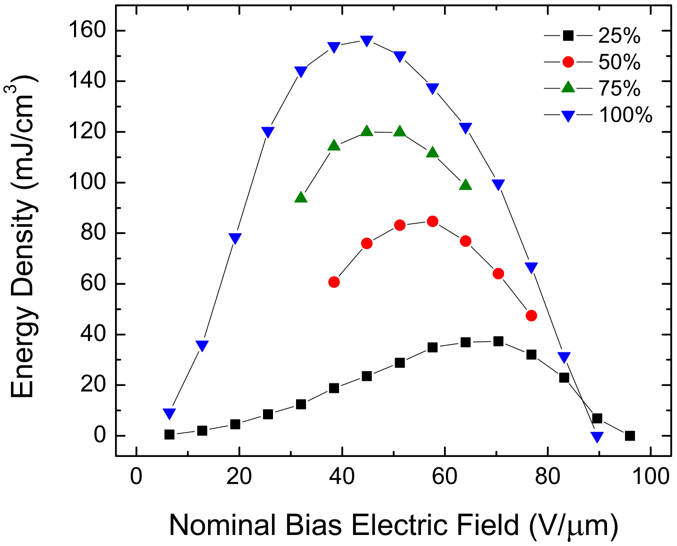

Figure 13.3: a) Pressure-strain curves for VHB4905 films prestrained 300x300% in a diaphragm configuration with diameters of 1 and 2 inches and 1 or 2 layers. b) Normalized pressure-strain curves where the measured pressure is doubled for the sample with a diameter of 2 and halved for the sample with two layers.

and the output voltage was monitored using an oscilloscope attached through the device using voltage converter with a 1000:1 step down ratio and an input impedance of 1 GΩ. Data for the complete range of viable nominal bias fields is shown for 25% and 100% strains while only data near the peak performance is shown for 50% and 75% strains (Figure 13.3).

These experimental results bring to light another interesting scaling relationship: the maximum energy that is harvested using this setup is essentially linearly dependent on the applied mechanical strain. It is also interesting to note that the peak energy density shifts from ∼70 V/μm and 25% strain to ∼45 V/μm at 100% strain. The shift to lower fields is caused by an increase in the potential on the film when the film is relaxed as strain, and thus the capacitance change, increases. At 100% strain, a peak voltage spike 4 times larger than the applied voltage. At 25% strain, the peak is only 1.56 times larger than the applied voltage. The increased spike in voltage results in an increase in Maxwell-pressure induced strains during relaxation when using a constant charge energy harvesting cycle, which results in lower performance at higher electric fields. This shift in performance must be considered when designing the energy harvesting circuitry for the system. Wave heights are expected to fluctuate over a relatively large range, so it may be prudent to design a system capable of measuring or predicting the wave height so that the appropriate bias voltage can be applied. Switching to a more complex energy harvesting cycle should result in improved energy gains but will also result in increased cost, complexity, and energy consumption.

Based on the results above, a device with a diameter of 2 m designed to reach 100% strain for a peak wave height of 5 m would require 787 layers of 300x300% prestrained VHB4905. The thickness of each layer is 31.25 μm, giving a total thickness of just 24.6 mm. The total volume of VHB4905 required would be 0.07726 m^3, or 77.26 kg of active material. Assuming an average wave height of 3 m and noting the non-linear pressure-strain response, the expected strain would be roughly 50% and the device would be able to provide 80 mJ/cm^3 of active material per incident wave. This amounts to 6.18 kJ of energy per incident wave per device. If we then assume a wave period of 10 s then each device is capable of producing 0.618 kW of power.

A scaled WEH prototype based on this concept is currently being developed. The prototype device consists of a simple 6” diameter poly(vinyl chloride) tube with a length of 4 feet. The dielectric elastomer films are stacked onto a rigid frame that is attached to the open end of the tube. A small pressure outlet has been drilled into the tube to monitor the pressure change inside the tube. Power is fed into the system using a high voltage capacitor rated at 1800 V and 22 μF and the output energy is stored in a separate high voltage capacitor rated at 5000 V and 1 μF. Alternating between the charging, open circuit, and discharging states is performed two high voltage Reed relays that are controlled via a digital acquisition system and LabView software. Waves are simulated by pumping water into and out of a small reservoir with a height of ∼2 feet. The net energy gain is calculated as the difference between the energy gained by the output capacitor and the energy lost by the input capacitor.

At this point the WEH prototype is still under development. Preliminary testing will be underway in the near future.

13.2 Concept for a Floor Tile Energy Harvesters

Another interesting potential application for DE energy harvesters is harvesting energy from human pedestrian and automotive traffic in a distributed manner. In regions of high pedestrian traffic, such as Bruin Walk or Ackerman Union at UCLA, floor tiles capable of harvesting energy could generate energy used to power lighting, displays, and other electronic equipment. Since the energy is being generated at the location and time that it will be used there are no losses associated with power transmission or long-term storage. In the event of a power outage or natural disaster, such a system could be used to power emergency lighting, emerging communication equipment, and provide additional energy to reserve power systems used to support vital resources at locations such as hospitals.

Floor tile energy harvesting systems based on piezoelectrics have already been demonstrated and field testing is underway. [360–362] Reviews thus far are positive. The primary issue with the piezoelectric systems is that they rely on rigid components to couple the force of the piezoelectric stacks effectively.

In similar work, SRI has also developed a heel-strike shoe sole energy harvester based on dielectric elastomers for military applications. [324, 326, 331, 332] They claim the device is capable of generating 1 J of energy per footstep.

We have developed several concept devices in order to determine their feasibility. The initial design consists of a "plunger" type device where the displacement of a top plate is couple to the dielectric elastomer through a gel material. The device consists of a rigid top plate with an array of cylindrical plungers attached to it and a bottom section consisting of two identical plates with arrays of holes matching the array of plungers on the top plate. A stack of DE films with electrodes patterned to form active regions at each hole location

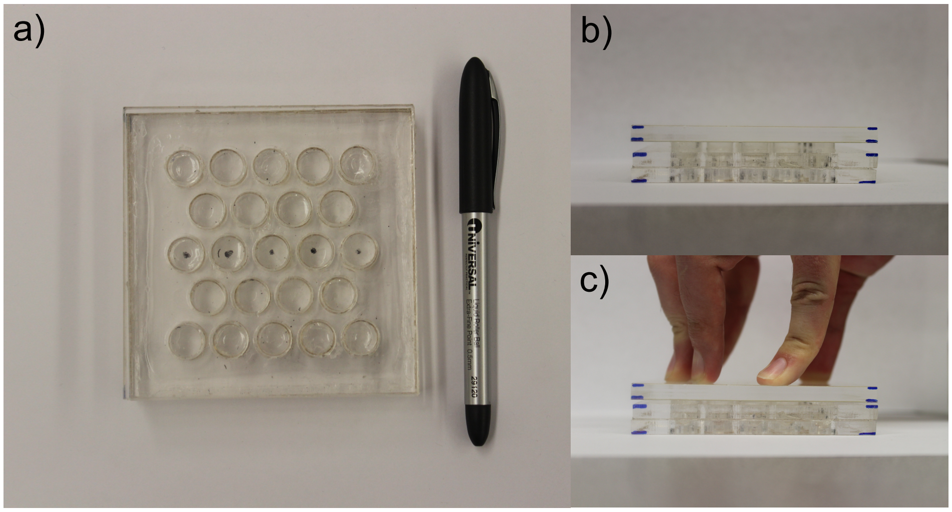

Figure 13.4: Concept for a rigid "plunger" type DE floor tile energy harvester showing a) a top view of the device, b) a side view of the device with no force applied and c) a side view of the device with a force applied causing a vertical deflection of approximately 0.5 mm

is placed between the two bottom plates and the holes in the upper bottom plate are filled with a coupling medium, in this case a silicone gel was used. The dimensions of the device can be tailored to maximize strain while minimizing vertical deflections. An image of a concept device with 1 cm wide plungers and no electrode material is shown in Figure 13.4. Figure 13.4b shows the device with no pressure applied and 13.4c shows the device with a force being applied. The deflection is approximately 5mm and generates close to 100% strain in the active sections of the DE stack.

While the design is capable of effectively coupling small deformations to relatively large strains, the design does not make use of the primary advantages of DE materials for this application: their conformability, stretchability, and maleability. The goal is thus to create a floor tile or shoe sole energy harvesting concept that is completely soft and/or flexible. Such a device could be incorporated into the entire sole of a shoe with no discernible change in the feel of the shoe. It could also be used in readily deployable large area mats that can be rolled up for storage and redeployed elsewhere when needed.

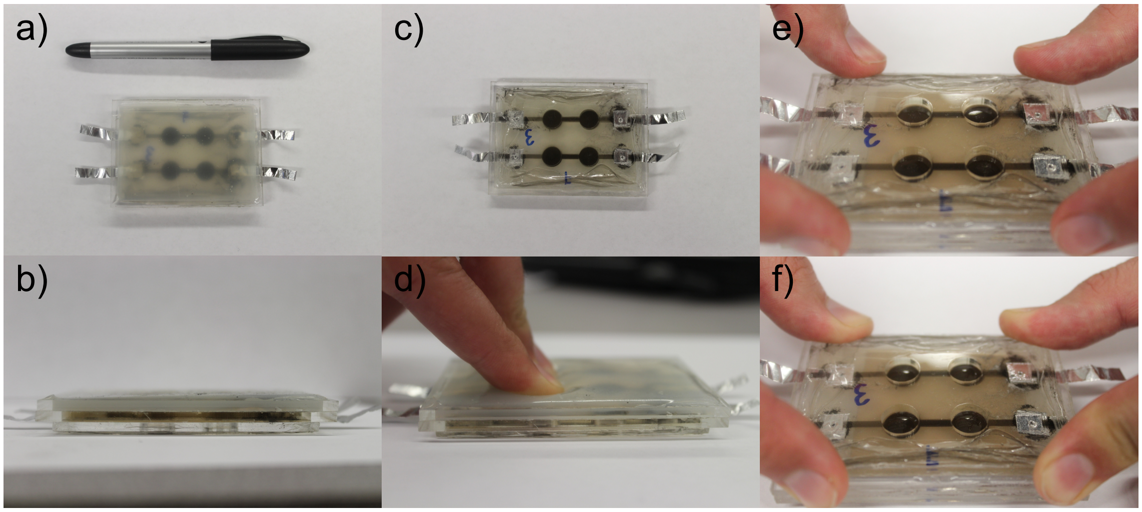

Figure 13.5: Concept for a "soft top" DE floor tile energy harvester showing a) a top view, b) side view, and c) bottom view of the device. d) shows how the soft top reacts to an applied force while e) and f) show the backside of the device with no force applied and with a force applied respectively.

The first step in realizing this type of design is to replace the rigid top plate and plunger components from the design in Figure 13.4. To do this, the "plungers" were replaced by a layer of silicone gel and the top layer is replaced by a semi-rigid silicone. Since the top surface of this design is "soft", it will be referred to as a "soft-top" floor tile energy harvester. A rigid bottom plate and reservoir for the silicone gel were retained in this design for ease of fabrication though only a single bottom plate was used in this design with the DE stack sitting on top of it. A prototype device using this design is shown in Figure 13.5. Figure 13.5e shows the backside of the device with no force applied while Figure 13.5f shows the device with a force applied. It is difficult to see in the image, but the active portions of the film are bulging upward when the force is applied and are lying flat when no force is applied.

In order to demonstrate the potential of such a design, a device with 3 active layers and 2 passive layers was fabricated and the capacitance change was measured when a load was applied to different regions of the device (Figure 13.6). The diameter of each active region is 1 cm. Force was applied either over a small circular area with the same diameter as one

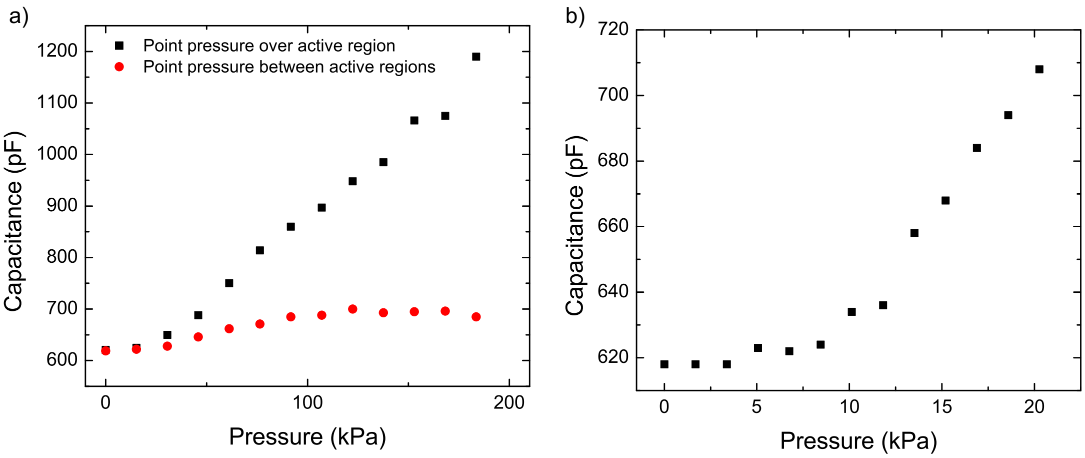

Figure 13.6: Applied pressure vs capacitance change for a "soft top" floor tile energy harvester. Pressure was applied using a small circular disk with the same diameter as the active regions as well as a square plate measuring 1.5" in length per side that allowed pressure to be applied across all active regions at the same time.

of the active regions or using a square top plate that covered all four active regions. As expected, the capacitance change is much higher in the case where the pressure is applied directly over an active region. In real scenarios the pressure is likely going to be placed over a large area. The results from Figure 13.6 show that in this case significant changes is capacitance are possible with low applied pressures.

Given the relative success of the "soft top" design, and entirely bendable floor tile generator was fabricated using a hard silicone rubber to replace the rigid plastic components. The hard silicone used had a similar feel as many athletic shoe soles. The resulting generator was capable of being bent and could be conformed to a curved surface. Image of the prototype device is shown in Figure 13.7.

This type of flexible device could be used as an energy harvesting floor tile capable of conforming to various surface morphologies. With some minor changes, the concept could also be used to make flexible energy harvesting shoe soles that cover the entirety of the sole and are thus capable of harvesting more energy than a simple heelstrike device.

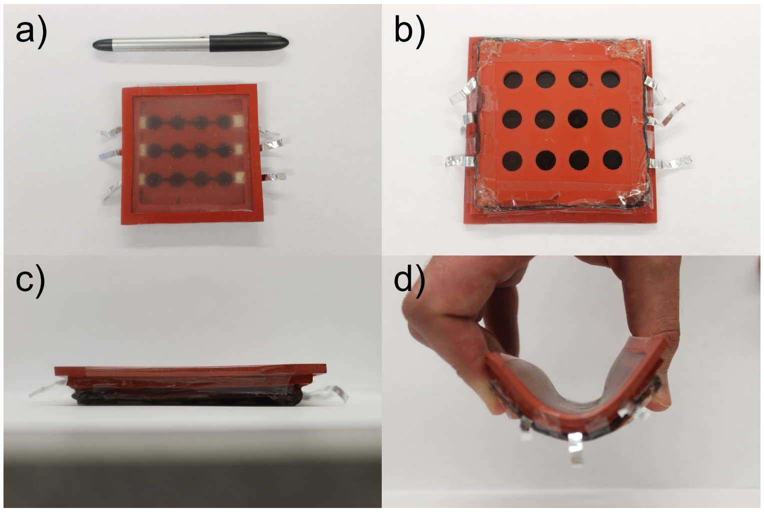

Figure 13.7: Concept for a completely "soft" and flexible DE floor tile energy harvester.

This work is still in the early conceptual phases and will require additional investigation that is beyond the scope of this dissertation.

13.3 Conclusions

Novel designs for a DE wave energy harvester and a DE floor tile or shoe sole energy harvester have been presented. The wave energy harvesting concept consists of a simple tube design where the tube is partially submerged in water with a DE stack at the open end. As waves pass by they generate a pressure differential between the inside and outside of the tube causing the DE stack to deform. Initial analysis shows that a 2 m wide device should be capable of producing 0.618 kW of power assuming an average wave height of 3 m and a wave period of 10 s.

Several floor tile concept concepts were introduced with varying levels of rigidity. A completely flexible design was also introduced that should allow for flexible energy harvesting floor tiles that can conform to various surfaces and could also be implemented as an energy harvesting shoe sole.

CHAPTER 14

Summary and Future Directions of this Work

14.1 Conclusions

The factors influencing the energy density and efficiency of dielectric elastomers were explored. It was found that the amount of energy that can be harvested from a DE generator increases with the applied strain and increases with the applied voltage up to a certain point before Maxwell pressure induced strains begin to dominate and the ability of the elastomer to relax is reduced. The amount of energy that can be harvested also increases with the stiffness of the material as more mechanical energy is put into the system. A high permittivity does not necessarily increase the amount of energy that can be harvested but it useful at reducing the required driving voltage, especially for stiff elastomers where the required fields may exceed the dielectric breakdown strength of the material. Low leakage currents and viscoelasticity contribute to lower parasitic losses and higher energy gains.

The efficiency of a DE generator is more complex. Additional analysis via an analytical derivation of the energy harvesting efficiency shows that the efficiency is dependent primarily on the shape of the stress-strain curve, the applied strain, and a lumped parameter that depends on the stiffness, permittivity, and the nominal electric field. A material that softens as it is stretched is capable of higher efficiencies than a material that stiffens as it is stretched. The efficiency generally decreases with increasing applied strain, though parasitic losses play a larger role at low strains. It is shown that beyond the general shape of the stess-strain curve, the stiffness and permittivity of the material do not affect the maximum efficiency that the material is capable of. A higher stiffness material simply requires a higher nominal electric field, and a higher permittivity reduced the electric field required. Thus, for materials with high permittivity or high breakdown strength, a stiff material would be beneficial as the amount of energy that can be harvested will increase, and the maximum efficiency can still be achieved.

Based on these analyses, the 3M VHB4910 series of elastomers was tested at different prestrains to vary the stiffness. Interpenetrating polymer network elastomers (IPNs) with increased stiffness were also fabricated using VHB4905 and a trifunctional acrylate additive. It was show that higher prestrains are capable of drastically increasing the amount of energy harvested due to an increase in the material stiffness and a decrease in the effective viscoelasticity of the elastomer. Stiffening of the elastomer via the IPN approach produced mixed results. The materials were indeed stiffened but at higher additive loadings the viscoelasticity of the material, and therefore the parasitic losses, increased. The result being that the maximum energy gains were shifted to higher electric fields, as expected in a stiffer material, but overall energy gains were hampered by losses and the performance of the IPN materials was not as good as the highly prestrained VHB.

Following these results, a silicone nanocomposite material was also tested for improved energy harvesting. Silicone materials generally have lower viscoelasticity than VHB acrylics, and higher bulk resistivity, contributing to lower losses. Silicones are also generally capable of operating over a wider temperature range and are not affected by moisture, making the more suitable for real applications where temperature and environmental conditions can vary widely. A high energy density silicone with a relatively high dielectric breakdown strength was chosen as the base material. PDMS coated rutile TiO_2 nanoparticles were added to the silicone host at various concentrations with the goal of increasing both the permittivity and stiffness of the material. Results show that the permittivity can be increased by 31% for a TiO_2 loading of just 5wt.% and up to 58% for a loading of 20wt.%. The stiffness increased by 23% at a 5wt.% loading and 121% at a 20wt.% loading. The dielectric breakdown field remained very high across all loadings. Mechanical and electrical loss factors increased slightly with the addition of the TiO_2 nanoparticles. Based on simple calculations, the generator energy density shows a 3 times increase for 20wt.% TiO_2 over the pure base material. Based on these calculations, it is expected that the nanocomposite can outperform highly prestrained VHB.

Very soft and flexible silicone-single wall carbon nanotube (SWNT) composite electrodes were presented based on the silicone interpenetrating polymer network (S-IPN) concept introduced in Section 1. The electrodes are capable of being stretched by over 150% linearly without an appreciable increase in the resistance. It was also demonstrated that the electrodes can be cycled several thousands of times with only a negligible increase in resistance. In fact, in the case of moderate strains, the baseline resistance was seen to decrease after 1000 cycles when compared to the original value. The composite electrodes are capable of operating as linear capacitive strain sensors with excellent linearity and repeatability. The capacitance change with strain can be made superlinear resulting in large capacitance swings for capacitive energy harvesting purposes. The soft silicone composite was capable of generating over 7 mJ/g of active material, and due to its compliance and low modulus should be ideal for use in minimally invasive energy harvesters for human motion.

Additional energy harvesting applications were explored with a focus on a floor tile or shoe sole energy harvester capable of harvesting energy from human foot traffic. The device can be made flexible for easy inclusion into the sole of a shoe or easy deployment in high-traffic areas. The top surface can also be made of a soft silicone allowing the devices to be used in areas such as playgrounds or gyms.

14.2 Future Work

14.2.1 Improved Materials for Energy Harvesting

In Chapter 11, a silicone nanocomposite material was presented with improved energy density for energy harvesting purposes. The material presents a good option for harvesting energy from abundant and high energy density sources such as ocean waves. While this is a step forward it is important to note that no single material will be useful for all applications. The soft silicone SWNT composite electrodes presented in Chapter 12 present a material option at the other end of the spectrum, designed for minimal user intrusiveness and very low parasitic losses, making it much more suitable for harvesting energy from human motion or for harvesting energy from low power density sources.

The results of Chapters 8 and 9 discussing the factors influencing the energy density and efficiency of DE generators can be used to design future specialty DEs for energy harvesting applications. The results from Chapter 9, in particular, should be useful for determining the ideal stress-strain response of a DE for applications where the force output and expected strain of the energy source are known.

14.2.2 Ocean Wave Energy Harvester

The concept for a pressure based pseudo-oscillating water column (OWC) DE energy harvester was presented in Chapter 13. Based on scaled down preliminary results it is expected that cost-effective large-scale utilities level ocean wave parks should be possible. Additional testing as well as materials and electronics development that were beyond the scope of this dissertation will be required.

14.2.3 Floor Tile/Shoe Sole Energy Harvester

The concept for a floor tile/shoe sole DE energy harvester was also presented in Chapter 13. The concept shows the potential for use as flexible and compliant floor tiles that can conform to curved surfaces or as energy harvesting shoe soles. Additional developmental work needs to be completed to determine the ideal DE material, the amount of DE material required, and the ideal structural material to allow for maximum power generation while maintaining good flexibility and conformability.

References

[1] Yoseph Bar-Cohen. *Electroactive Polymer (EAP) Actuators as Artificial Muscles - Reality, Potential and Challenges.* SPIE Press, 2 edition, 2004.

[2] J.D.W. Madden, N.A. Vandesteeg, P.A. Anquetil, P.G.A. Madden, A. Takshi, R.Z. Pytel, S.R. Lafontaine, P.A. Wieringa, and I.W. Hunter. Artificial muscle technology: physical principles and naval prospects. *IEEE Journal of Oceanic Engineering*, 29(3):706 – 728, 2004.

[3] Ron Pelrine, Roy Kornbluh, Jose Joseph, Richard Heydt, Qibing Pei, and Seiki Chiba. High-field deformation of elastomeric dielectrics for actuators. *Materials Science and Engineering: C*, 11(2):89 – 100, 2000.

[4] Roy D. Kornbluh, Ron Pelrine, Qibing Pei, Richard Heydt, Scott Stanford, Seajin Oh, and Joseph Eckerle. Electroelastomers: applications of dielectric elastomer transducers for actuation, generation, and smart structures. *Proceeding of SPIE*, 4698(1):254–270, 2002.

[5] J.M. Hollerbach, I.W. Hunter, and J. Ballantyne. *The Robotics Review 2*, chapter A comparative analysis of actuator technologies for robotics, pages 299 – 342. MIT Press, Cambridge, Mass., 1992.

[6] Honda Motor Company. http://world.honda.com/asimo/.

[7] T. Mirfakhrai, J.D. Madden, and R. Baughman. Polymer artificial muscles. *Materials Today*, 10:30, 2007.

[8] Michael H. Dickinson, Claire T. Farley, Robert J. Full, M. A. R. Koehl, Rodger Kram, and Steven Lehman. How animals move: An integrative view. *Science*, 288(5463):100–106, 2000.

[9] I. Hunter and S. Lafontaine. A comparison of muscle with artificial actuators. In *Tech. Dig. IEEE Solid State Sensors Actuators Workshop*, pages 178–185., 1992.

[10] Y. Bar-Cohen. Electro-active polymers: current capabilities and challenges. *Proceedings of SPIE*, 4695:1, 2002.

[11] Y. Bar-Cohen. Eap as artificial muscles: progress and challenges. *Proceeding of SPIE*, 5385:10, 2004.

[12] W.C. Roentgen. *Ser. Annual Physics and Chemistry Series 11(III)*, chapter About the Changes in Shape and Volume of Dielectrics Caused by Electricity., pages 771–786. JA Barth, Leipzig, Germany (in German)., 1880.

[13] Y Bar-Cohen. Electroactive polymers as artificial muscles: A review. *Journal of Spacecraft and Rockets*, 39:822–827, 2002.

[14] S Ashley. Artificial muscles. *Scientific American*, 289(4):52–59, 2003.

[15] RH Baughman. Playing nature's game with artificial muscles. *Science*, 308(5718):63–65, 2005.

[16] K. Meijer, M. Rosenthal, and R.J. Full. Muscle-like actuators? a comparison between three electroactive polymers. *Proceedings of SPIE*, 4329:7, 2001.

[17] T.R. Otero, J.L. Cascales, and A.J. Fernanez-Romero. Attempting a classification for electrical polymeric actuators. *Proceedings of SPIE*, 6524:65240L, 2007.

[18] D. Trivedi, C.D. Rahn, W.M. Kier, and I.D. Walker. Soft robotics: biological insipration, state of the art, and future research. *Appl Bionics Biomechanics*, 5:99, 2008.

[19] Zhongyang Cheng and Qiming Zhang. Field-activated electroactive polymers. *MRS Bulletin*, 33:183–187, 2008.

[20] A.M. Vinogradov. Accomplishments and future trends in the field of electroactive polymers. *Proceedings of the SPIE*, 6927:69270M, 2008.

[21] J.L. Pons. *Emerging actuator technologies: a micromechatronic approach*. Wiley, New Jersey, 2005.

[22] J.E. Huber, N.A. Fleck, and M.F. Ashby. The selection of mechanical actuators based on performance indices. *Proc. R. Soc. Lond. Ser. A*, 453:2185, 1997.

[23] S.G. Wax and R.R. Sands. Electroactive polymer actuators and devices. *Proceedings of SPIE*, 3669:2, 1999.

[24] John D. Madden. Mobile robots: Motor challenges and materials solutions. *Science*, 318(5853):1094–1097, 2007.

[25] Ravi Shankar, Tushar K. Ghosh, and Richard J. Spontak. Dielectric elastomers as next-generation polymeric actuators. *Soft Matter*, 3(9):1116–1129, 2007.

[26] Ailish O'Halloran, Fergal O'Malley, and Peter McHugh. A review on dielectric elastomer actuators, technology, applications, and challenges. *Journal of Applied Physics*, 104(7):071101, 2008.

[27] K.J. Kim and S. Tadokoro. *Electroactive polymers for robotic applications: artificial muscles and sensors*. Springer, London, 2007.

[28] M. Shahinpoor, K.J. Kim, and M. Mojarrad. *Artificial muscles: applications of advanced polymeric nanocomposites*. CRC Press Taylor & Francis Group, Boca Raton, 2007.

[29] F. Carpi and E. Smela. *Biomedical applications of electroactive polymer actuators.* Wiley, Chichester, 2009.

[30] M. Shahinpoor and K.J. Kim. Ionic polymer-metal composites: I. fundamentals. *Smart Materials and Structures*, 10:819, 2001.

[31] K.J. Kim and M. Shahinpoor. A novel method of manufacturing three-dimensional ionic polymer-metal composites (IPMCs) biomimetic sensors, actuators and artificial muscles. *Polymer*, 43:797, 2002.

[32] M. Shahinpoor. Mechanoelectrical phenomena in ionic polymers. *Math Mech Solids*, 8:281, 2003.

[33] X.L. Wang, I.K. Oh, J. Lu, J. Ju, and S. Lee. Biomimetic electro-active polymer based on sulfonated poly (styrene-ethylene-co-butylene-b-styrene). *Materials Letters*, 61:5117, 2007.

[34] S. Nemat-Nasser. Micromechanics of actuation of ionic polymer-metal composites. *Journal of Applied Physics*, 92:2899, 2002.

[35] M. Shahinpoor and K.J. Kim. Ionic polymer-metal composites: IV. Industrial and medical applications. *Smart Materials and Structures*, 14:197, 2005.

[36] K. Kaneto, M. Kaneko, Y. Min, and A.G. MacDiarmid. Artificial muscle-electromechanical actuators using polyaniline films. *Synth Met*, 71:2211, 1995.

[37] B.J. Akle, M.D. Bennett, and D.J. Leo. High-strain ionomeric-ionic liquid electroactive actuators. *Sensors and Actuators A*, 126:173, 2006.

[38] S. Nemat-Nasser and Y.X. Wu. Comparative experimental study of ionic polymer-metal composites with different backbone ionomers and in various cation forms. *Journal of Applied Physics*, 93:5255, 2003.

[39] K.J. Kim and M. Shahinpoor. Ionic polymer-metal composites: Ii. manufacturing techniques. *Smart Materials and Structures*, 12:65, 2003.

[40] Eamax Co. Japan. http://www.eamax.co.jp/.

[41] R. Kornbluh, R. Pelrine, Q. Pei, S. Oh, and J. Joseph. Ultrahigh strain response of field-actuated elastomeric polymers. *Proceedings of SPIE*, 3987:51, 2000.

[42] Zhibin Yu, Wei Yuan, Paul Brochu, Bin Chen, Zhitian Liu, and Qibing Pei. Large-strain, rigid-to-rigid deformation of bistable electroactive polymers. *Applied Physics Letters*, 95:192904, 2009.

[43] Z. Yu, X. Niu, P. Brochu, W. Yuan, H. Li, B. Chen, and Q. Pei. Bistable electroactive polymers (bsep): large-strain actuation of rigid polymers. *Proceedings of SPIE*, 7642:76420C, 2010.

[44] Ron Pelrine, Roy Kornbluh, Qibing Pei, and Jose Joseph. High-speed electrically actuated elastomers with strain greater than 100 *Science*, 287(5454):836–839, 2000.

[45] W. Kuhn, B. Hargitay, A. Katchalsky, and H. Eisenberg. Reversible dilation and contraction by changing the state of ionization of high polymer acid networks. *Nature (London)*, 165:514, 1955.

[46] A. Katchalsky and M. Zwick. Mechanochemistry and ion exchange. *Journal of Polymer Science*, 16:221, 1955.

[47] A. Fragala, J. Enos, A. Laconti, and J. Boyack. Electrochemical activation of a synthetic artificial muscle membrane. *Electrochim Acta*, 17:1507, 1972.

[48] Y. Osada. Conversion of chemical into mechanical energy by synthetic-polymers (chemomechanical systems). *Advances in Polymer Science*, 82:1, 1987.

[49] T. Tanaka. Phase-transitions in gels and a single polymer. *Polymer*, 20:1404, 1979.

[50] Y. Osada and M. Hasebe. Electrically activated mechanochemical devices using polyelectrolyte gels. *Chemistry Letters*, 9:1285, 1985.

[51] T. Shiga. Deformation and viscoelastic behavior of polymer gels in electric fields. *Advances in Polymer Science*, 134:131, 1997.

[52] P. Calvert and Z. Liu. Freeform fabrication of hydrogels. *Acta Metall Mater*, 46:2565, 1998.

[53] Z.S. Liu and P. Calvert. Multilayer hydrogels as muscle-like actuators. *Advanced Materials*, 12:288, 2000.

[54] B. Tondu, R. Emirkhanian, S. Mathé, and A. Ricard. A pH-activated artificial muscle using the McKibben-type braided structure. *Sensors and Actuators A*, 150:124, 2009.

[55] S. Iijima. Helical microtubules of graphitic carbon. *Nature*, 354:56, 1991.

[56] Ray H. Baughman, Anvar A. Zakhidov, and Walt A. de Heer. Carbon nanotubes–the route toward applications. *Science*, 297(5582):787–792, 2002.

[57] Ray H. Baughman, Changxing Cui, Anvar A. Zakhidov, Zafar Iqbal, Joseph N. Barisci, Geoff M. Spinks, Gordon G. Wallace, Alberto Mazzoldi, Danilo De Rossi, Andrew G. Rinzler, Oliver Jaschinski, Siegmar Roth, and Miklos Kertesz. Carbon nanotube actuators. *Science*, 284(5418):1340–1344, 1999.

[58] J.D.W. Madden, J.N. Barisci, P.A. Anquetil, G.M. Spinks, G.G. Wallace, R.H. Baughman, and I.W. Hunter. Fast carbon nanotube charging and actuation. *Advanced Materials*, 18(7):870–873, 2006.

[59] Tissaphern Mirfakhrai, Jiyoung Oh, Mikhail Kozlov, Eddie Chi Wah Fok, Mei Zhang, Shaoli Fang, Ray H Baughman, and John D W Madden. Electrochemical actuation of carbon nanotube yarns. *Smart Materials and Structures*, 16(2):S243, 2007.

[60] Min Kyoon Shin, Sun I. Kim, Seon Jeong Kim, Sung-Kyoung Kim, Haiwon Lee, and Geoffrey M. Spinks. Size-dependent elastic modulus of single electroactive polymer nanofibers. *Applied Physics Letters*, 89(23):231929, 2006.

[61] M. Hughes and G.M. Spinks. Multiwalled carbon nanotube actuators. *Advanced Materials*, 17(4):443–446, 2005.

[62] Ya-Li Li, Ian A. Kinloch, and Alan H. Windle. Direct spinning of carbon nanotube fibers from chemical vapor deposition synthesis. *Science*, 304(5668):276–278, 2004.

[63] Ray H. Baughman. Materials synthesis: Towering forests of nanotube trees. *Nature Nanotechnology*, 1(2):94–96, 2006.

[64] Ali E. Aliev, Jiyoung Oh, Mikhail E. Kozlov, Alexander A. Kuznetsov, Shaoli Fang, Alexandre F. Fonseca, Raquel Ovalle, Marcio D. Lima, Mohammad H. Haque, Yuri N. Gartstein, Mei Zhang, Anvar A. Zakhidov, and Ray H. Baughman. Giant-stroke, superelastic carbon nanotube aerogel muscles. *Science*, 323:1575–1578, 2009.

[65] R.H. Baughman, L.W. Shacklette, R.L. Elsebaumer, E.J. Plichta, and C. Becht. *Conjugated polymeric materials: opportunities in electronics, optoelectronics, and molecular electronics.* Kluwer, Dordrecht, 1990.

[66] R.H. Baughman, L.W. Shacklette, R.L. Elsebaumer, E.J. Plichta, and C. Becht. *Topics in molecular organization and engineering: molecular electronics*, volume 7. Kluwer, Dordrecht, 1991.

[67] R. H. Baughman. Conducting polymers in redox devices and intelligent materials systems. *Makromolekulare Chemie. Macromolecular Symposia*, 51(1):193–215, 1991.

[68] R.H. Baughman. Conducting polymer artificial muscles. *Synthetic Metals*, 78(3):339 – 353, 1996.

[69] Qibing Pei and Olle Inganäs. Conjugated polymers and the bending cantilever method: electrical muscles and smart devices. *Advanced Materials*, 4(4):277–278, 1992.

[70] Elisabeth Smela, Olle Inganäs, and Ingemar Lundström. Controlled folding of micrometer-size structures. *Science*, 268(5218):1735–1738, 1995.

[71] T.F. Otero, E. Angulo, J. Rodríguez, and C. Santamaría. Electrochemomechanical properties from a bilayer: polypyrrole / non-conducting and flexible material - artificial muscle. *Journal of Electroanalytical Chemistry*, 341:369 – 375, 1992.

[72] Timothy E. Herod and Joseph B. Schlenoff. Doping-induced strain in polyaniline: stretchoelectrochemistry. *Chemistry of Materials*, 5(7):951–955, 1993.

[73] Rachel Pytel, Edwin Thomas, and Ian Hunter. Anisotropy of electroactive strain in highly stretched polypyrrole actuators. *Chemistry of Materials*, 18(4):861–863, 2006.

[74] Qibing Pei and Olle Inganäs. Electrochemical applications of the bending beam method. 1. Mass transport and volume changes in polypyrrole during redox. *The Journal of Physical Chemistry*, 96(25):10507–10514, 1992.

[75] Qibing Pei and Olle Inganäs. Electrochemical applications of the bending beam method; a novel way to study ion transport in electroactive polymers. *Solid State Ionics*, 60(13):161 – 166, 1993.

[76] Qibing Pei and Olle Inganäs. Electrochemical applications of the bending beam method. 2. Electroshrinking and slow relaxation in polypyrrole. *The Journal of Physical Chemistry*, 97(22):6034–6041, 1993.

[77] Qibing Pei, O Inganäs, and I Lundstrom. Bending bilayer strips built from polyaniline for artificial electrochemical muscles. *Smart Materials and Structures*, 2(1):1, 1993.

[78] A. Mazzoldi, A. Della Santa, and D. De Rossi. *Polymer sensors and actuators*, chapter Conducting polymer actuators: properties and modeling, pages 207–244. Springer, Heidelberg, 1999.

[79] M. Cole and J.D. Madden. The effect of temperature exposure on polypyrrole actuation. *Materials Research Society Symposium Proceedings*, 889:105–110, 2006.

[80] Elisabeth Smela and Nikolaj Gadegaard. Surprising volume change in PPy(DBS): an atomic force microscopy study. *Advanced Materials*, 11(11):953–957, 1999.

[81] S. Hara, T. Zama, W. Takashima, and K. Kaneto. Artificial muscles based on polypyrrole actuators with large strain and stress induced electrically. *Polymer Journal*, 36:151, 2004.

[82] Susumu Hara, Tetsuji Zama, Wataru Takashima, and Keiichi Kaneto. Tris(trifluoromethylsulfonyl)methide-doped polypyrrole as a conducting polymer actuator with large electrochemical strain. *Synthetic Metals*, 156:351 – 355, 2006.

[83] G.M. Spinks, V. Mottaghitalab, M. Bahrami-Samani, P.G. Whitten, and G.G. Wallace. Carbon-nanotube-reinforced polyaniline fibers for high-strength artificial muscles. *Advanced Materials*, 18(5):637–640, 2006.

[84] T.W. Lewis, L.A.P. Kane-Maguire, A.S. Hutchison, G.M. Spinks, and G.G. Wallace. Development of an all-polymer, axial force electrochemical actuator. *Synthetic Metals*, 102:1317 – 1318, 1999.

[85] G.M. Spinks, G.G. Wallace, J. Ding, D. Zhou, B. Xi, T.R. Scott, and V.T. Truong. Ionic liquids and polypyrrole helix tubes: bringing the electronic Braille screen closer to reality. *Proceedings of SPIE*, 5051:372, 2003.

[86] P.F. Pettersson, E.W.H. Jager, and O. Inganäs. Surface micromachined polymer actuators as valves in PDMS microfluidic systems. In A. Dittmar and D. Beebe, editors, *1st international IEEE-EMBS special topic conference on microtechnologies in medicine and biology*, page 334. IEEE-EBMS, Lyon, France, 2000.

[87] A. Della Santa, A. Mazzoldi, and D. de Rossi. Steerable microcatheters actuated by embedded conducting polymer structures. *Journal of Intelligent Material Systems and Structures*, 7(3):292–300, 1996.

[88] Y. Takase, J. W. Lee, J. I. Scheinbeim, and B. A. Newman. High-temperature characteristics of nylon-11 and nylon-7 piezoelectrics. *Macromolecules*, 24(25):6644–6652, 1991.

[89] J. Su, Z. Y. Ma, J. I. Scheinbeim, and B. A. Newman. Ferroelectric and piezoelectric properties of nylon 11/poly(vinylidene fluoride) bilaminate films. *Journal of Polymer Science Part B: Polymer Physics*, 33(1):85–91, 1995.

[90] Qiong Gao and Jerry I. Scheinbeim. Dipolar intermolecular interactions, structural development, and electromechanical properties in ferroelectric polymer blends of nylon-11 and poly(vinylidene fluoride). *Macromolecules*, 33(20):7564–7572, 2000.

[91] Andrew J. Lovinger, G. T. Davis, T. Furukawa, and M. G. Broadhurst. Crystalline forms in a copolymer of vinylidene fluoride and trifluoroethylene (52/48 mol %). *Macromolecules*, 15(2):323–328, 1982.

[92] A.J. Lovinger. *Developments in crystalline polymers.* Applied Science Publishers, London, 1982.

[93] Andrew J. Lovinger, T. Furukawa, G. T. Davis, and M. G. Broadhurst. Curie transitions in copolymers of vinylidene fluoride. *Ferroelectrics*, 50(1):227–236, 1983.

[94] Y. Xu. *Ferroelectric materials and their applications.* North-Holland, Netherlands, 1991.

[95] C Huang, R Klein, F Xia, HF Li, QM Zhang, F Bauer, and ZY Cheng. Poly(vinylidene fluoride-trifluoroethylene) based high performance electroactive polymers. *IEEE Transactions on Dielectrics and Electrical Insulation*, 11:299–311, 2004.

[96] K. Tashiro, K. Takano, M. Kobayashi, Y. Chatani, and H. Tadokoro. Structural study on ferroelectric phase transition of vinylidene fluoride-trifluoroethylene copolymers (III) dependence of transitional behavior on VDF molar content. *Ferroelectrics*, 57(1):297–326, 1984.

[97] Q. M. Zhang, J. Zhao, T. Shrout, N. Kim, L. E. Cross, A. Amin, and B. M. Kulwicki. Characteristics of the electromechanical response and polarization of electric field biased ferroelectrics. *Journal of Applied Physics*, 77(6):2549 –2555, 1995.

[98] M. Eguchi. On the permanent electret. *Philosophical Magazine*, 49:178, 1925.

[99] G.M. Sessler, editor. *Electrets*, volume 1. Laplacian Press, 1998.

[100] S. Bauer. Piezo-, pyro- and ferroelectrets: soft transducer materials for electromechanical energy conversion. *Dielectrics and Electrical Insulation, IEEE Transactions on*, 13(5):953 –962, 2006.

[101] Siegfried Bauer, Reimund Gerhard-Multhaupt, and Gerhard M. Sessler. Ferroelectrets: soft electroactive foams for transducers. *Physics Today*, 57(2):37–43, 2004.

[102] Deliani Lovera, Holger Ruckdäschel, Andreas Göldel, Nico Behrendt, Thomas Frese, Jan K.W. Sandler, Volker Altstädt, Reiner Giesa, and Hans-Werner Schmidt. Tailored polymer electrets based on poly(2,6-dimethyl-1,4-phenylene ether) and its blends with polystyrene. *European Polymer Journal*, 43(4):1195 – 1201, 2007.

[103] Z.-Y. Cheng, R. S. Katiyar, X. Yao, and A. S. Bhalla. Temperature dependence of the dielectric constant of relaxor ferroelectrics. *Phys. Rev. B*, 57:8166–8177, 1998.

[104] Z.-Y. Cheng, Q. M. Zhang, and F. B. Bateman. Dielectric relaxation behavior and its relation to microstructure in relaxor ferroelectric polymers: High-energy electron irradiated poly(vinylidene fluoride-trifluoroethylene) copolymers. *Journal of Applied Physics*, 92:6749–6755, 2002.

[105] Q. M. Zhang, Vivek Bharti, and X. Zhao. Giant electrostriction and relaxor ferroelectric behavior in electron-irradiated poly(vinylidene fluoride-trifluoroethylene) copolymer. *Science*, 280(5372):2101–2104, 1998.

[106] Z.-Y. Cheng, T.-B. Xu, Vivek Bharti, Shexi Wang, and Q. M. Zhang. Transverse strain responses in the electrostrictive poly(vinylidene fluoride–trifluorethylene) copolymer. *Applied Physics Letters*, 74(13):1901–1903, 1999.

[107] SS Guo, XZ Zhao, QF Zhou, HLW Chan, and CL Choy. High electrostriction and relaxor ferroelectric behavior in proton-irradiated poly(vinylidene fluoride-trifluoroethylene) copolymer. *Applied Physics Letters*, 84:3349–3351, 2004.

[108] F. Xia, Z.-Y. Cheng, H.S. Xu, H.F. Li, Q.M. Zhang, G.J. Kavarnos, R.Y. Ting, G. Abdul-Sadek, and K.D. Belfield. High electromechanical responses in a poly(vinylidene fluoride-trifluoroethylene-chlorofluoroethylene) terpolymer. *Advanced Materials*, 14(21):1574–1577, 2002.

[109] Haisheng Xu, Z.-Y. Cheng, Dana Olson, T. Mai, Q. M. Zhang, and G. Kavarnos. Ferroelectric and electromechanical properties of poly(vinylidene-fluoride–trifluoroethylene–chlorotrifluoroethylene) terpolymer. *Applied Physics Letters*, 78(16):2360–2362, 2001.

[110] J. T. Garrett, C. M Roland, A. Petchsuk, and T. C. Chung. Electrostrictive behavior of poly(vinylidene fluoride-trifluoroethylene-chlorotrifluoroethylene). *Applied Physics Letters*, 83(6):1190–1192, 2003.

[111] Ambalangodage C. Jayasuriya, Adriana Schirokauer, and Jerry I. Scheinbeim. Crystal-structure dependence of electroactive properties in differently prepared poly(vinylidene fluoride/hexafluoropropylene) copolymer films. *Journal of Polymer Science Part B: Polymer Physics*, 39(22):2793–2799, 2001.

[112] M. Wegener, W. Kunstler, K. Richter, and R. Gerhard-Multhaupt. Ferroelectric polarization in stretched piezo- and pyroelectric poly(vinylidene fluoride-hexafluoropropylene) copolymer films. *Journal of Applied Physics*, 92(12):7442–7447, 2002.

[113] Bret Neese, Yong Wang, Baojin Chu, Kailiang Ren, Sheng Liu, Q. M. Zhang, Cheng Huang, and James West. Piezoelectric responses in poly(vinylidene fluoride/hexafluoropropylene) copolymers. *Applied Physics Letters*, 90(24):242917, 2007.

[114] Hui-Min Bao, Cheng-Liang Jia, Chang-Chun Wang, Qun-Dong Shen, Chang-Zheng Yang, and Q. M. Zhang. A type of poly(vinylidene fluoride-trifluoroethylene) copolymer exhibiting ferroelectric relaxor behavior at high temperature (∼100°C). *Applied Physics Letters*, 92(4):042903, 2008.

[115] F. Xia, H. Li, C. Huang, M.Y.M. Huang, H. Xu, F. Bauer, Z.Y. Cheng, and Q.M. Zhang. Poly(vinylidene-fluoride-trifluoroethylene) based high-performance electroactive polymers. *Proceedings of SPIE*, 5051:133, 2003.

[116] J. Su, K. Hales, and T.B. Xu. Composition and annealing effects on the response of electrostrictive graft elastomers. *Proceedings of SPIE*, 5051:191, 2003.

[117] J. Su, J.S. Harrison, T.L.S. Clair, Y. Bar-Cohen, and S. Leary. Electrostrictive graft elastomers and applications. *Materials Research Society Symposium Proceedings*, 600:131, 1999.

[118] M. Warner and M. Terentjev. *Liquid crystal elastomers.* Oxford Science Publications, 2003.

[119] P.G. de Gennes. Réflections sur un type de polymères nématiques. *Comptes Rendus de l'Académie des Sciences Série B*, 281:101–103, 1975.

[120] Pierre-Gilles de Gennes. Un muscle artificiel semi-rapide. *Comptes Rendus de l'Académie des Sciences - Series IIB*, 324(5):343 – 348, 1997.

[121] Donald L. Thomsen, Patrick Keller, Jawad Naciri, Roger Pink, Hong Jeon, Devanand Shenoy, and Banahalli R. Ratna. Liquid crystal elastomers with mechanical properties of a muscle. *Macromolecules*, 34(17):5868–5875, 2001.

[122] H. Wermter and H. Finkelmann. Liquid crystalline elastomers as artificial muscles. *e-Polymers*, 13:1, 2001.

[123] Min-Hui Li and Patrick Keller. Artificial muscles based on liquid crystal elastomers. *Philosophical Transactions of the Royal Society A: Mathematical, Physical and Engineering Sciences*, 364(1847):2763–2777, 2006.

[124] W Lehmann, H Skupin, C Tolksdorf, E Gebhard, R Zentel, P Kruger, M Losche, and F Kremer. Giant lateral electrostriction in ferroelectric liquid-crystalline elastomers. *Nature*, 410:447–450, 2001.

[125] P.G. de Gennes. *Polymer liquid crystals*, chapter Mechanical properties of nematic polymers, pages 115–131. Academic Press, New York, 1982.

[126] J. F. D'Allest, P. Maïssa, A. ten Bosch, P. Sixou, A. Blumstein, R. Blumstein, J. Teixeira, and L. Noirez. Experimental evidence of chain extension at the transition temperature of a nematic polymer. *Phys. Rev. Lett.*, 61:2562–2565, 1988.

[127] M. H. Li, A. Brûlet, P. Davidson, P. Keller, and J. P. Cotton. Observation of hairpin defects in a nematic main-chain polyester. *Phys. Rev. Lett.*, 70:2297–2300, 1993.

[128] M.H. Li, A. Brûlet, J. P. Cotton, P. Davidson, C. Strazielle, and P. Keller. Study of the chain conformation of thermotropic nematic main chain polyesters. *J. Phys. II France*, 4(10):1843–1863, 1994.

[129] Walter Lehmann, Lutz Hartmann, Friedrich Kremer, Peter Stein, Heino Finkelmann, Holger Kruth, and Stefan Diele. Direct and inverse electromechanical effect in ferroelectric liquid crystalline elastomers. *Journal of Applied Physics*, 86(3):1647–1652, 1999.

[130] Norbert Leister, Walter Lehmann, Uwe Weber, Dieter Geschke, Friedrich Kremer, Peter Stein, and Heino Finkelmann. Measurement of the pyroelectric response and of the thermal diffusivity of microtomized sections of 'single crystalline' ferroelectric liquid crystalline elastomers. *Liquid Crystals*, 27(2):289–297, 2000.

[131] Susanta Sinha Roy, Walter Lehmann, Elisabeth Gebhard, Christian Tolksdorf, Rudolf Zentel, and Friedrich Kremer. Inverse piezoelectric and electrostrictive response in freely suspended flc elastomer film as detected by interferometric measurements. *Molecular Crystals and Liquid Crystals*, 375(1):253–268, 2002.

[132] DK Shenoy, DL Thomsen, A Srinivasan, P Keller, and BR Ratna. Carbon coated liquid crystal elastomer film for artificial muscle applications. *Sensors and Actuators A*, 96(2-3):184–188, 2002.

[133] H. Skupin, F. Kremer, S. V. Shilov, P. Stein, and H. Finkelmann. Time-resolved FTIR spectroscopy on structure and mobility of single crystal ferroelectric liquid crystalline elastomers. *Macromolecules*, 32(11):3746–3752, 1999.

[134] C Huang, QM Zhang, and A Jakli. Nematic anisotropic liquid-crystal gels - Self-assembled nanocomposites with high electromechanical response. *Advanced Functional Materials*, 13(7):525–529, 2003.

[135] H. Finkelmann and M. Shahinpoor. Electrically controllable liquid crystal elastomer-graphite composite artificial muscles. *Proceedings of SPIE*, 4695:459, 2002.

[136] S.V. Ahir, A.R. Tajbakhsh, and E.M. Terentjev. Self-assembled shape-memory fibers of triblock liquid-crystal polymers. *Advanced Functional Materials*, 16(4):556–560, 2006.

[137] Jawad Naciri, Amritha Srinivasan, Hong Jeon, Nikolay Nikolov, Patrick Keller, and Banahalli R. Ratna. Nematic elastomer fiber actuator. *Macromolecules*, 36(22):8499–8505, 2003.

[138] Martin Chambers, Heino Finkelmann, Maja Remskar, Antoni Sanchez-Ferrer, Bostjan Zalar, and Slobodan Zumer. Liquid crystal elastomer-nanoparticle systems for actuation. *J. Mater. Chem.*, 19:1524–1531, 2009.

[139] Christopher M. Spillmann, Banahalli R. Ratna, and Jawad Naciri. Anisotropic actuation in electroclinic liquid crystal elastomers. *Applied Physics Letters*, 90(2):021911, 2007.

[140] David M. Walba, Hong Yang, Richard K. Shoemaker, Patrick Keller, Renfan Shao, David A. Coleman, Christopher D. Jones, Michi Nakata, and Noel A. Clark. Main-Chain Chiral Smectic Polymers Showing a Large Electroclinic Effect in the SmA* Phase. *Chemistry of Materials*, 18(19):4576–4584, 2006.

[141] Ronald E. Pelrine, Roy D. Kornbluh, and Jose P. Joseph. Electrostriction of polymer dielectrics with compliant electrodes as a means of actuation. *Sensors and Actuators A: Physical*, 64(1):77 – 85, 1998.

[142] I. Krakovsky, T. Romijn, and A. Posthuma de Boer. A few remarks on the electrostriction of elastomers. *Journal of Applied Physics*, 85:628 –629, 1999.

[143] R. Díaz-Calleja, M. J. Sanchis, and E. Riande. Effect of an electric field on the bifurcation of a biaxially stretched incompressible slab rubber. *European Physical Journal E*, 30(4):417–426, 2009.

[144] N. Goulbourne, E. Mockensturm, and M. Frecker. A Nonlinear Model for Dielectric Elastomer Membranes. *Journal of Applied Mechanics*, 72:899, 2005.

[145] M Wissler and E Mazza. Modeling and simulation of dielectric elastomer actuators. *Smart Materials and Structures*, 14:1396–1402, 2005.

[146] G. Kofod. *Dielectric elastomer actuators*. PhD thesis, The Technical University of Denmark, 2001.

[147] M Wissler and E Mazza. Modeling of a pre-strained circular actuator made of dielectric elastomers. *Sensors and Actuators A*, 120:184–192, 2005.

[148] P. Sommer-Larsen, G. Kofod, M.H. Shridhar, M. Benslimane, and P. Gravesen. Performance of dielectric elastomer actuators and materials. *Proceedings of SPIE*, 4695:158, 2002.

[149] E. Yang, M. Frecker, and E. Mockensturm. Viscoelastic model of dielectric elastomer membranes. *Proceedings of SPIE*, 5759:82, 2005.

[150] Jean-Sbastien Plante and Steven Dubowsky. On the performance mechanisms of dielectric elastomer actuators. *Sensors and Actuators A: Physical*, 137(1):96 – 109, 2007.

[151] Michael Wissler and Edoardo Mazza. Electromechanical coupling in dielectric elastomer actuators. *Sensors and Actuators A*, 138:384–393, 2007.

[152] H.W. Hwang, C.J. Kim, S.J. Kim, H. Wang, N.C. Park, and Y.P. Park. Preisach modeling of dielectric elastomer eap actuator. *Proceedings of SPIE*, 6927:692726, 2008.

[153] Xuanhe Zhao and Zhigang Suo. Electrostriction in elastic dielectrics undergoing large deformation. *Journal of Applied Physics*, 104:123530, 2008.

[154] J. W. Fox and N. C. Goulbourne. On the dynamic electromechanical loading of dielectric elastomer membranes. *Journal of the Mechanics and Physics of Solids*, 56:2669–2686, 2008.

[155] J.W. Fox and N.C. Goulbourne. Nonlinear dynamic characteristics of dielectric elastomer membranes. *Proceedings of SPIE*, 6927:69271P, 2008.

[156] R. Kornbluh, R. Pelrine, J. Joseph, R. Heydt, Q. Pei, and S. Chiba. High-field electrostriction of elastomeric polymer dielectrics for actuation. *Proceedings of SPIE*, 3669:149, 1999.

[157] Jinxiong Zhou, Wei Hong, Xuanhe Zhao, Zhiqian Zhang, and Zhigang Suo. Propagation of instability in dielectric elastomers. *International Journal of Solids and Structures*, 45:3739–3750, 2008.

[158] Mickael Moscardo, Xuanhe Zhao, Zhigang Suo, and Yuri Lapusta. On designing dielectric elastomer actuators. *Journal of Applied Physics*, 104(9):093503, 2008.

[159] Jean-Sebastien Plante and Steven Dubowsky. Large-scale failure modes of dielectric elastomer actuators. *International Journal of Solids and Structures*, 43(25-26):7727–7751, 2006.

[160] Xuanhe Zhao, Wei Hong, and Zhigang Suo. Electromechanical hysteresis and coexistent states in dielectric elastomers. *Physical Review B*, 76(13):134113, 2007.

[161] R. Díaz-Calleja, E. Riande, and M. J. Sanchis. On electromechanical stability of dielectric elastomers. *Applied Physics Letters*, 93(10):101902, 2008.

[162] Jinsong Leng, Liwu Liu, Yanju Liu, Kai Yu, and Shouhua Sun. Electromechanical stability of dielectric elastomer. *Applied Physics Letters*, 94(21):211901, 2009.

[163] R. Pelrine, R. Kornbluh, J. Joseph, and S. Chiba. Electrostriction of polymer films for microactuators. In *IEEE Tenth Annual International Workshop on MEMS*, page 238, 1997.

[164] R. Pelrine, R. Kornbluh, and G. Kofod. High-strain actuator materials based on dielectric elastomers. *Advanced Materials*, 12(16):1223 – 1225, 2000.

[165] Q. M. Zhang, J. Su, Chy Hyung Kim, R. Ting, and Rodger Capps. An experimental investigation of electromechanical responses in a polyurethane elastomer. *Journal of Applied Physics*, 81(6):2770–2776, 1997.

[166] L. Petit, B. Guiffard, L. Seveyrat, and D. Guyomar. Actuating abilities of electroactive carbon nanopowder/polyurethane composite films. *Sensors and Actuators A: Physical*, 148(1):105 – 110, 2008.

[167] F. Carpi, A. Mazzoldi, and D. De Rossi. High-strain dielectirc elastomer actuation. *Proceedings of SPIE*, 5051:419, 2003.

[168] Ravi Shankar, Tushar K. Ghosh, and Richard J. Spontak. Electromechanical response of nanostructured polymer systems with no mechanical pre-strain. *Macromolecular Rapid Communications*, 28(10):1142–1147, 2007.

[169] Ravi Shankar, Tushar K. Ghosh, and Richard J. Spontak. Electroactive nanostructured polymers as tunable actuators. *Advanced Materials*, 19(17):2218+, 2007.

[170] Kwangmok Jung, Ja Choon Koo, Jae-do Nam, Young Kwan Lee, and Hyouk Ryeol Choi. Artificial annelid robot driven by soft actuators. *Bioinspiration and Biomimetics*, 2(2):S42–S49, 2007.

[171] S.M. Ha, W. Yuan, Q. Pei, R. Pelrine, and S. Stanford. Interpenetrating polymer networks for high-performance electroelastomer artificial muscles. *Advanced Materials*, 18(7):887–891, 2006.

[172] Soon Mok Ha, Wei Yuan, Qibing Pei, Ron Pelrine, and Scott Stanford. Interpenetrating networks of elastomers exhibiting 300electrically-induced area strain. *Smart Materials and Structures*, 16(2):S280, 2007.

[173] S.M. Ha, I.S. Park, M. Wissler, R. Pelrine, S. Stanford, K.J. Kim, G. Kovacs, and Q. Pei. High electromechanical performance of electroelastomers based on interpenetrating polymer networks. *Proceedings of SPIE*, 6927:69272C, 2008.

[174] G Kofod, P Sommer-Larsen, R Kronbluh, and R Pelrine. Actuation responsee of polyacrylate dielectric elastomers. *Journal of Intelligent Material Systems and Structures*, 14(12):787–793, 2003.

[175] G. Kofod, R. Kornbluh, R. Pelrine, and P. Sommer-Larsen. Actuation response of polyacrylate dielectric elastomers. *Proceedings of SPIE*, 4329:141, 2001.

[176] R. Palakodeti and M.R. Kessler. Influence of frequency and prestrain on the mechanical efficiency of dielectric electroactive polymer actuators. *Materials Letters*, 60:3437 – 3440, 2006.

[177] H.R. Choi, K. Jung, N.H. Chuc, M. Jung, I. Koo, J. Koo, J. Lee, J. Lee, J. Nam, M. Cho, and Y. Lee. Effects of prestrain on behavior of dielectric elastomer actuator. *Proceedings of SPIE*, 5759:283, 2005.

[178] Patrick Lochmatter, Gabor Kovacs, and Michael Wissler. Characterization of dielectric elastomer actuators based on a visco-hyperelastic film model. *Smart Materials and Structures*, 16(2):477–486, 2007.

[179] Q Pei, R Pelrine, S Stanford, R Kornbluh, and M Rosenthal. Electroelastomer rolls and their application for biomimetic walking robots. *Synthetic Metals*, 135(1-3, Part 1, SI):129–131, 2003.

[180] N. C. Goulbourne, E. M. Mockensturm, and M. I. Frecker. Electro-elastomers: Large deformation analysis of silicone membranes. *International Journal of Solids and Structures*, 44(9):2609–2626, 2007.

[181] P. Lochmatter and G. Kovacs. Design and characterization of an active hinge segment based on soft dielectric EAPs. *Sensors and Actuators A*, 141(2):577–587, 2008.

[182] Patrick Lochmatter, Gabor Kovacs, and Silvain Michel. Characterization of dielectric elastomer actuators based on a hyperelastic film model. *Sensors and Actuators A*, 135(2):748–757, 2007.

[183] Eric M. Mockensturm and Nakhiah Goulbourne. Dynamic response of dielectric elastomers. *International Journal of Non-Linear Mechanics*, 41(3):388 – 395, 2006.

[184] Michael Wissler and Edoardo Mazza. Mechanical behavior of an acrylic elastomer used in dielectric elastomer actuators. *Sensors and Actuators A*, 134:494–504, 2007.

[185] Guggi Kofod. The static actuation of dielectric elastomer actuators: how does prestretch improve actuation? *Journal of Physics D - Applied Physics*, 41(21), 2008.

[186] Giuseppe Gallone, Federico Carpi, Danilo De Rossi, Giovanni Levita, and Augusto Marchetti. Dielectric constant enhancement in a silicone elastomer filled with lead magnesium niobate-lead titanate. *Materials Science and Engineering: C Materials Science and Engineering C*, 27(1):110–116, 2007.

[187] Z. Zhang, L. Liu, J. Fan, K. Yu, L. Shi, and J. Leng. New silicone dielectric elastomers with a high dielectric constan. *Proceedings of SPIE*, 6926:692610, 2008.

[188] P. Lotz, M. Matysek, P. Lechner, M. Hamann, and H.F. Schlaak. Dielectric elastomer actuators using improved thin film processing and nanosized particles. *Proceedings of SPIE*, 6927:692723, 2008.

[189] J.P. Szabo, J.A. Hiltz, C.G. Cameron, R.S. Underhill, J. Massey, B. White, and J. Leidner. Elastomeric composites with high dielectric constant for use in maxwell stress actuators. *Proceedings of SPIE*, 5051:180, 2003.

[190] F Carpi and D De Rossi. Improvement of electromechanical actuating performances of a silicone dielectric elastomer by dispersion of titanium dioxide powder. *IEEE Transactions on Dielectrics and Electrical Insulation*, 12(4):835–843, 2005.

[191] M Razzaghi-Kashani, N Gharavi, and S Javadi. The effect of organo-clay on the dielectric properties of silicone rubber. *Smart Materials and Structures*, 17(6):065035, 2008.

[192] X.Q. Zhang, M. Wissler, B. Jaehne, R. Broennimann, and G. Kovacs. Effects of crosslinking, prestrain, and dielectric filler on the electromechanical response of a new silicone and comparison with acrylic elastomer. *Proceedings of SPIE*, 5385:78, 2004.

[193] Wijittra Wichiansee and Anuvat Sirivat. Electrorheological properties of poly(dimethylsiloxane) and poly(3,4-ethylenedioxy thiophene)/poly(stylene sulfonic acid)/ethylene glycol blends. *Materials Science and Engineering: C*, 29(1):78 – 84, 2009.

[194] L. Z. Chen, C. H. Liu, C. H. Hu, and S. S. Fan. Electrothermal actuation based on carbon nanotube network in silicone elastomer. *Applied Physics Letters*, 92(26):263104, 2008.

[195] Bjoern Kussmaul, Sebastian Risse, Guggi Kofod, Remi Wache, Michael Wegener, Denis N. McCarthy, Hartmut Krueger, and Reimund Gerhard. Enhancement Of Dielectric Permittivity And Electromechanical Response In Silicone Elastomers: Molecular Grafting Of Organic Dipoles To The Macromolecular Network. *Advanced Functional Materials*, 21(23):4589–4594, 2011.

[196] Martin Molberg, Daniel Crespy, Patrick Rupper, Frank Nueesch, Jan-Anders E. Manson, Christiane Loewe, and Dorina M. Opris. High Breakdown Field Dielectric Elastomer Actuators Using Encapsulated Polyaniline as High Dielectric Constant Filler. *Advanced Functional Materials*, 20(19):3280–3291, 2010.

[197] Dorina M. Opris, Martin Molberg, Christian Walder, Yee Song Ko, Beatrice Fischer, and Frank A. Nueesch. New Silicone Composites for Dielectric Elastomer Actuator Applications In Competition with Acrylic Foil. *Advanced Functional Materials*, 21(18):3531–3539, 2011.

[198] Q. Pei, R. Pelrine, M. Rosenthal, S. Stanford, H. Prahlad, and R. Kornbluh. Recent progress on electroelastomer artificial muscles and their application for biomimetic robots. *Proceedings of SPIE*, 5385:41, 2004.

[199] G. Mathew, J. M. Rhee, C. Nah, and D. J. Leo. Effects of silicone rubber on properties of dielectric acrylate elastomer actuator. *Polymer Engineering & Science*, 46(10):1455–1460, 2006.

[200] S.M. Ha, W. Yuan, Q. Pei, R. Pelrine, and S. Stanford. New high-performance electroelastomer based on interpenetrating polymer networks. *Proceedings of SPIE*, 6168:616808, 2006.

[201] S.M. Ha, M. Wissler, R. Pelrine, S. Stanford, G. Kovacs, and Q. Pei. Characterization of electroelastomers based on interpenetrating polymer networks. *Proceedings of SPIE*, 6524:652408, 2007.

[202] Han Zhang, Lukas Düring, Gabor Kovacs, Wei Yuan, Xiaofan Niu, and Qibing Pei. Interpenetrating polymer networks based on acrylic elastomers and plasticizers with improved actuation temperature range. *Polymer International*, 59(3):384–390, 2010.

[203] Hristiyan Stoyanov, Matthias Kollosche, Sebastian Risse, Denis N. McCarthy, and Guggi Kofod. Elastic block copolymer nanocomposites with controlled interfacial interactions for artificial muscles with direct voltage control. *Soft Matter*, 7(1):194–202, 2011.

[204] Ravi Shankar, Tushar K. Ghosh, and Richard J. Spontak. Mechanical and actuation behavior of electroactive nanostructured polymers. *Sensors and Actuators A*, 151(1):46–52, 2009.

[205] C.G. Cameron, R.S. Underhill, M. Rawji, and J.P. Szabo. Conductive filler: elastomer composites for maxwell stress actuator applications. *Proceedings of SPIE*, 5385:51, 2004.

[206] JD Nam, SD Hwang, HR Choi, JH Lee, KJ Kim, and S Heo. Electrostrictive polymer nanocomposites exhibiting tunable electrical properties. *Smart Materials and Structures*, 14(1):87–90, 2005.

[207] C Huang, QM Zhang, G deBotton, and K Bhattacharya. All-organic dielectric-percolative three-component composite materials with high electromechanical response. *Applied Physics Letters*, 84(22):4391–4393, 2004.

[208] B Guiffard, L Seveyrat, G Sebald, and D Guyomar. Enhanced electric field-induced strain in non-percolative carbon nanopowder/polyurethane composites. *Journal of Physics D: Applied Physics*, 39(14):3053, 2006.

[209] QM Zhang, HF Li, M Poh, F Xia, ZY Cheng, HS Xu, and C Huang. An all-organic composite actuator material with a high dielectric constant. *Nature*, 419(6904):284–287, 2002.

[210] K. Jung, J.H. Lee, M.S. Cho, J.C. Koo, J. Nam, Y.K. Lee, and H.R. Choi. Development of enhanced synthetic rubber for energy efficient polymer actuators. *Proceedings of SPIE*, 6168:61680N, 2006.

[211] Kwangmok Jung, Joonho Lee, Misuk Cho, Ja Choon Koo, Jae-do Nam, Youngkwan Lee, and Hyouk Ryeol Choi. Development of enhanced synthetic elastomer for energy-efficient polymer actuators. *Smart Materials and Structures*, 16(2):S288–S294, 2007.

[212] Huu Chuc Nguyen, Vu Thuy Doan, JongKil Park, Ja Choon Koo, Youngkwan Lee, Jae do Nam, and Hyouk Ryeol Choi. The effects of additives on the actuating performances of a dielectric elastomer actuator. *Smart Materials and Structures*, 18(1):015006, 2009.

[213] Federico Carpi, Piero Chiarelli, Alberto Mazzoldi, and Danilo De Rossi. Electromechanical characterisation of dielectric elastomer planar actuators: comparative evaluation of different electrode materials and different counterloads. *Sensors and Actuators A: Physical*, 107(1):85 – 95, 2003.

[214] M. Benslimane and P. Gravesen. Mechanical properties of dielectric elastomer actuators with smart metallic compliant electrodes. *Proceedings of SPIE*, 4695:150, 2002.

[215] Stephanie Perichon Lacour, Sigurd Wagner, Zhenyu Huang, and Z. Suo. Stretchable gold conductors on elastomeric substrates. *Applied Physics Letters*, 82(15):2404–2406, 2003.

[216] J.H. Lalli, S. Hannah, M. Bortner, S. Subrahmanyan, J. Mecham, B. Davis, and R.O. Claus. Self-assembled nanostructured conducting elastomeric electrodes. *Proceedings of SPIE*, 5385:290, 2004.

[217] A.B. Hill, R.O. Claus, J.H. Lalli, J.B. Mecham, B.A. Davis, R.M Goff, and S. Subrahmanyan. Metal rubber electrodes for active polymer devices. *Proceedings of SPIE*, 5759:246, 2005.

[218] R.O. Claus, R.M Goff, M. Homer, A.B. Hill, and J.H. Lalli. Ultralow modulus electrically conducting electrode materials. *Proceedings of SPIE*, 6168:61681O, 2006.

[219] R. Delille, M.Urdaneta, K. Hsieh, and E. Smela. Novel compliant electrodes based on platinum salt reduction. *Proceedings of SPIE*, 6168:61681Q, 2006.

[220] S. Rosset, M. Niklaus, P. Dubois, and H.R. Shea. Mechanical characterization of a dielectric elastomer microactuator with ion-implanted electrodes. *Sensors and Actuators A: Physical*, 144(1):185 – 193, 2008.

[221] S. Rosset, M. Niklaus, V. Stojanov, A. Felber, P. Dubois, and H.R. Shea. Ion-implanted compliant and patternable electrodes for miniaturized dielectric elastomer actuators. *Proceedings of SPIE*, 6927:69270W, 2008.

[222] S. Rosset, M. Niklaus, P. Dubois, and H.R. Shea. Performance characterization of miniaturized dielectric elastomer actuators fabricated using metal ion implantation. In *Micro Electro Mechanical Systems, 2008. MEMS 2008. IEEE 21st International Conference on*, pages 503 –506, jan. 2008.

[223] Samuel Rosset, Muhamed Niklaus, Philippe Dubois, and Herbert R. Shea. Metal ion implantation for the fabrication of stretchable electrodes on elastomers. *Advanced Functional Materials*, 19(3):470–478, 2009.

[224] W. Yuan, T. Lam, J. Biggs, L. Hu, Z. Yu, S.M. Ha, D. Xi, M.K. Senesky, G. Grüner, and Q. Pei. New electrode materials for dielectric elastomer actuators. *Proceedings of SPIE*, 6524:65240N, 2007.

[225] T. Lam, H. Tran, W. Yuan, Z. Yu, S.M. Ha, R. Kaner, and Q. Pei. Polyaniline nanofibers as a novel electrode material for fault-tolerant dielectric elastomer actuators. *Proceedings of SPIE*, 6927:69270O, 2008.

[226] W. Yuan, L. Hu, S.M. Ha, T. Lam, G. Grüner, and Q. Pei. Self-clearable carbon nanotube electrodes for improved performance of dielectric elastomer actuators. *Proceedings of SPIE*, 6927:69270P, 2008.

[227] W. Yuan, L.B. Hu, Z.B. Yu, T. Lam, J. Biggs, S.M. Ha, D.J. Xi, B. Chen, M.K. Senesky, G. Grüner, and Q. Pei. Fault-tolerant dielectric elastomer actuators using single-walled carbon nanotube electrodes. *Advanced Materials*, 20(3):621–625, 2008.

[228] Liangbing Hu, Wei Yuan, Paul Brochu, George Gruner, and Qibing Pei. Highly stretchable, conductive, and transparent nanotube thin films. *Applied Physics Letters*, 94(16):161108, 2009.

[229] Wei Yuan, Paul Brochu, Soon Mok Ha, and Qibing Pei. Dielectric oil coated single-walled carbon nanotube electrodes for stable, large-strain actuation with dielectric elastomers. *Sensors and Actuators A*, 155(2):278–284, 2009.

[230] R. Kornbluh, R. Pelrine, and J. Joseph. Elastomeric dielectric artificial muscle actuators for small robots. In *Proceedings of the 3rd IASTED international conference*

on robotics and manufacturing. Cancun, Mexico, pages 1–6. ACTA Press, Calgary, Alberta, June 1995.

[231] R. Kornbluh, R. Pelrine, J. Eckerle, and J. Joseph. Electrostrictive polymer artificial muscle actuators. In *Proceedings of the 1998 IEEE international conference on robotics and automation. Leuven, Belgium*, pages 2147–2154. IEEE Press, Piscataway, NJ, May 1998.

[232] F. Carpi, D. De Rossi, R. Kornbluh, R. Pelrine, and P. Sommer-Larsen, editors. *Dielectric elastomers as electromechanical transducers: fundamentals, materials, devices, models and applications of an emerging electroactive polymer technology.* Elsevier Ltd., Oxford, 2008.

[233] H. Choi, S. Ryew, K. Jung, J. Jeon, H. Kim, J. Nam, A. Takanishi, R. Maeda, K. Kaneko, and K. Tanie. Biomimetic actuator based on dielectric polymer. *Proceedings of SPIE*, 4695:138, 2002.

[234] H.R. Choi, K.M. Jung, J.W. Kwak, S.W. Lee, H.M. Kim, J.W. Jeon, and J.D. Nam. Multiple degree-of-freedom digital soft actuator for robotic applications. *Proceedings of SPIE*, 5051:262, 2003.

[235] M.Y. Jung, N.H. Chuc, J.W. Kim, I.M. Koo, K.M. Jung, Y.K. Lee, J.D. Nam, H.R. Choi, and J.C. Koo. Fabrication and characterization of linear motion dielectric elastomer actuators. *Proceedings of SPIE*, 6168:616824, 2006.

[236] N.C.S. Goulbourne. Cylindrical dielectric elastomer actuators reinforced with inextensible fibers. *Proceedings of SPIE*, 6168:61680A, 2006.

[237] P. Lochmatter and G. Kovacs. Concept study on active shells driven by soft dielectric eap. *Proceedings of SPIE*, 6524:65241O, 2007.

[238] H. Wang and J. Zhu. Implementation and simulation of a cone dielectric elastomer actuator. *Proceedings of SPIE*, 7266:726607, 2008.

[239] J. Lenarcic and P. Wenger, editors. *Advances in robot kinematics: analysis and design.* Springer Science + Business Media B.V., Berlin, 2008.

[240] Y. Liu, L. Shi, L. Liu, Z. Zhang, and J. Leng. Inflated dielectric elastomer actuator for eyeball's movements: fabrication, analysis and experiments. *Proceedings of SPIE*, 6927:69271A, 2008.

[241] H. Prahlad, R. Pelrine, R. Kornbluh, P. von Guggenberg, S. Chhokar, and J. Eckerle. Programmable surface deformation: thickness-mode electroactive polymer actuators and their applications. *Proceedings of SPIE*, 5759:102, 2005.

[242] F. Carpi and D. De Rossi. Dielectric elastomer cylindrical actuators: electromechanical modelling and experimental evaluation. *Materials Science and Engineering: C*, 24(4):555 – 562, 2004.

[243] G. Kofod, M. Paajanen, and S. Bauer. New design concept for dielectric elastomer actuators. *Proceedings of SPIE*, 6168:61682J, 2006.

[244] Guggi Kofod, Werner Wirges, Mika Paajanen, and Siegfried Bauer. Energy minimization for self-organized structure formation and actuation. *Applied Physics Letters*, 90(8):081916, 2007.

[245] B. O'Brien, E. Calius, S. Xie, and I. Anderson. An experimentally validated model of a dielectric elastomer bending actuator. *Proceedings of SPIE*, 6927:69270T, 2008.

[246] J.S. Plante, L.M. Devita, and S. Dubowsky. A road to practical dielectric elastomer actuators based robotics and mechatronics: discrete actuation. *Proceedings of SPIE*, 6524:652406, 2007.

[247] N. Bonwit, J. Heim, M. Rosenthal, C. Duncheon, and A. Beavers. Design of commercial applications of epam technology. *Proceedings of SPIE*, 6168:616805, 2006.

[248] R. Zhang, P. Lochmatter, A. Kunz, and G. Kovacs. Spring roll dielectric elastomer actuators for a portable force feedback glove. *Proceedings of SPIE*, 6168:61681T, 2006.

[249] Q. Pei, M. Rosenthal, R. Pelrine, S. Stanford, and R. Kornbluh. Multifunctional electroelastomer roll actuators and their application for biomimetic walking robots. *Proceedings of SPIE*, 5051:281, 2003.

[250] Q Pei, M Rosenthal, S Stanford, H Prahlad, and R Pelrine. Multiple-degrees-of-freedom electroelastomer roll actuators. *Smart Materials and Structures*, 13(5):N86–N92, 2004.

[251] N.H. Chuc, J. Park, D.V. Thuy, H.S. Kim, J. Koo, Y. Lee, J. Nam, and H.R. Choi. Linear artificial muscle actuator based on synthetic elastomer. *Proceedings of SPIE*, 6524:65240J, 2007.

[252] F Carpi, A Migliore, G Serra, and D De Rossi. Helical dielectric elastomer actuators. *Smart Materials and Structures*, 14(6):1210–1216, 2005.

[253] F. Carpi and D. De Rossi. Contractile dielectric elastomer actuator with folded shape. *Proceedings of SPIE*, 6168:61680D, 2006.

[254] Federico Carpi, Claudio Salaris, and Danilo De Rossi. Folded dielectric elastomer actuators. *Smart Materials and Structures*, 16(2):S300–S305, 2007.

[255] Federico Carpi and Danilo De Rossi. Bioinspired actuation of the eyeballs of an android robotic face: concept and preliminary investigations. *Bioinspiration and Biomimetics*, 2(2):S50–S63, 2007.

[256] F. Carpi and D. De Rossi. Contractile folded dielectric elastomer actuators. *Proceedings of SPIE*, 6524:65240D, 2007.

[257] H.F. Schlaak, M. Jungmann, M. Matysek, and P. Lotz. Novel multilayer electrostatic solid state actuators with elastic dielectric. *Proceedings of SPIE*, 5759:121, 2005.

[258] M. Matysek, P. Lotz, K. Flittner, and H.F. Schlaak. High-precision characterization of dielectric elastomer stack actuators and their material parameters. *Proceedings of SPIE*, 6927:692722, 2008.

[259] Sohil Arora, Tushar Ghosh, and John Muth. Dielectric elastomer based prototype fiber actuators. *Sensors and Actuators A-Physical*, 136(1):321–328, 2007.

[260] Colin G. Cameron, Jeffrey P. Szabo, Stephen Johnstone, Jason Massey, and Jacob Leidner. Linear actuation in coextruded dielectric elastomer tubes. *Sensors and Actuators A*, 147(1):286–291, 2008.

[261] G. Kofod, H. Stoyanov, and R. Gerhard. Multilayer coaxial fiber dielectric elastomers for actuation and sensing. *Applied Physics A*, 102(3):577–581, 2011.

[262] G. Kovacs and L. Düring. Contractile tension force stack actuator based on soft dielectric eap. *Proceedings of SPIE*, 7287:72870A, 2009.

[263] G. Kovacs, S.M. Ha, S. Michel, R. Pelrine, and Q. Pei. Study on core free rolled actuator based on soft dielectric. *Proceedings of SPIE*, 6927:69270X, 2008.

[264] D. Hanson and V. White. Converging the capabilities of eap artificial muscles and the requirements for bio-inspired robotics. *Proceedings of SPIE*, 5385:29, 2004.

[265] Gabor Kovacs, Patrick Lochmatter, and Michael Wissler. An arm wrestling robot driven by dielectric elastomer actuators. *Smart Materials and Structures*, 16(2):S306–S317, 2007.

[266] F. Carpi and D. De Rossi. Eyeball pseudo-muscular actuators for an android face. *Proceedings of SPIE*, 5759:16, 2005.

[267] F. Carpi, G. Fantoni, P. Guerrini, and D. De Rossi. Buckling dielectric elastomer actuators and their use as motors for the eyeballs of an android face. *Proceedings of SPIE*, 6168:61681A, 2006.

[268] Elaine Biddiss and Tom Chau. Dielectric elastomers as actuators for upper limb prosthetics: Challenges and opportunities. *Medical Engineering and Physics*, 30(4):403–418, 2008.

[269] Steven Dubowsky, Samuel Kesner, Jean-Sebastien Plante, and Penelope Boston. Hopping mobility concept for search and rescue robots. *Industrial Robot: An International Journal*, 35(3):238–245, 2008.

[270] R. Pelrine, P. Sommer-Larsen, R. Kornbluh, R. Heydt, G. Kofod, Q. Pei, and P. Gravesen. Applications of dielectric elastomer actuators. *Proceedings of SPIE*, 4329:335, 2001.

[271] K. Jung, H. Nam, Y. Lee, and H. Choi. Micro inchworm robot actuated by artificial muscle actuator based on nonprestrained dielectric elastomer. *Proceedings of SPIE*, 5385:357, 2004.

[272] R. Pelrine, R. Kornbluh, Q. Pei, S. Stanford, S. Oh, and J. Eckerle. Dielectric elastomer artificial muscle actuators: toward biomimetic motion. *Proceedings of SPIE*, 4695:126, 2002.

[273] P. Lochmatter, G. Kovacs, and P. Ermanni. Design and characterization of shell-like actuators based on soft dielectric electroactive polymers. *Smart Materials and Structures*, 16(4):1415–1422, 2007.

[274] O. Khatib, V. Kumar, and G.J. Pappas, editors. *Experimental robotics: the 11th international symposium*, volume 54. Springer Tracts in Advanced Robotics, 2009.

[275] R. Heydt, R. Kornbluh, J. Eckerle, and R. Pelrine. Sound radiation properties of dielectric elastomer electroactive polymer loudspeakers. *Proceedings of SPIE*, 6168:61681M, 2006.

[276] S. Chiba, M. Waki, R. Kornbluh, and R. Pelrine. Extending applications of dielectric elastomer artificial muscle. *Proceeding of SPIE*, 6524:652424, 2007.

[277] M. Aschwanden and A. Stemmer. Low voltage, highly tunable diffraction grating based on dielectric elastomer actuators. *Proceedings of SPIE*, 6524:65241N, 2007.

[278] M. Aschwanden, D. Niederer, and A. Stemmer. Tunable transmission grating based on dielectric elastomer actuators. *Proceedings of SPIE*, 6927:69271R, 2008.

[279] H. Kim, J. Park, N.H. Chuc, H.R. Choi, J.D. Nam, Y. Lee, H.S. Jung, and J.C. Koo. Development of dielectric elastomer driven micro-optical zoom lens system. *Proceedings of SPIE*, 6524:65241V, 2007.

[280] S. Lee, K. Jung, J. Koo, S. Lee, H. Choi, J. Jeon, J. Nam, and H. Choi. Braille display device using soft actuator. *Proceedings of SPIE*, 5385:368, 2004.

[281] K. Ren, S. Liu, M. Lin, Y. Wang, and Q.M. Zhang. A compact electroactive polymer actuator suitable for refreshable braille display. *Proceedings of SPIE*, 6524:65241G, 2007.

[282] Ig Mo Koo, Kwangmok Jung, Ja Choon Koo, Jae-Do Nam, Young Kwan Lee, and Hyouk Ryeol Choi. Development of soft-actuator-based wearable tactile display. *IEEE Transactions on Robotics*, 24(3):549 –558, 2008.

[283] F. Carpi, A. Mannini, and D. De Rossi. Elastomeric contractile actuators for hand rehabilitation splints. *Proceedings of SPIE*, 6927:692705, 2007.

[284] F. Carpi, A. Khanicheh, C. Mavroidis, and D. De Rossi. Silicone made contractile dielectric elastomer actuators inside 3-tesla mri environment. In *2008 IEEE/RSJ international conference on intelligent robots and systems, Nice, France*, pages 137–142, Sept 2008.

[285] Federico Carpi, Azadeh Khanicheh, Constantinos Mavroidis, and Danilo De Rossi. MRI compatibility of silicone-made contractile dielectric elastomer actuators. *IEEE-ASME Transactions on Mechatronics*, 13(3):370–374, 2008.

[286] K. Tadakuma, L.M. Devita, J.S. Plante, Y. Shaoze, and S. Dubowsky. The experimental study of precision parallel manipulator with binary actuation: with application to mri cancer treatment. In *2008 IEEE international conference on robotics and automation, Pasadena, CA, USA*, pages 2503–2508, May 2008.

[287] Feng Xia, Srinivas Tadigadapa, and Q.M. Zhang. Electroactive polymer based microfluidic pump. *Sensors and Actuators A: Physical*, 125(2):346 – 352, 2006.

[288] Y.Y. Jhong, C.M. Huang, C.C. Hseih, and C.C. Fu. Improvemen of viscoelastic effects of dielectric elastomer actuator and its application for valve devices. *Proceedings of SPIE*, 6524:65241Y, 2007.

[289] C. Bolzmacher, J. Biggs, and M. Srinivasan. Flexible dielectric elastomer actuators for wearable human-machine interfaces. *Proceedings of SPIE*, 6168:616804, 2006.

[290] S. Michel, C. Dürager, M. Zobel, and E. Fink. Electroactive polymers as a novel actuator technology for lighter-than-air vehicles. *Proceedings of SPIE*, 6524:65241Q, 2007.

[291] S. Michel, A. Bormann, C. Jordi, and E. Fink. Feasibility studies for a bionic propulsion system of a blimp based on dielectric elastomers. *Proceedings of SPIE*, 6927:69270S, 2008.

[292] Wen-Pei Yang and Lien-Wen Chen. The tunable acoustic band gaps of two-dimensional phononic crystals with a dielectric elastomer cylindrical actuator. *Smart Materials and Structures*, 17(1):015011, 2008.

[293] Wen-Pei Yang, Liang-Yu Wu, and Lien-Wen Chen. Refractive and focusing behaviours of tunable sonic crystals with dielectric elastomer cylindrical actuators. *Journal of Physics D: Applied Physics*, 41(13):135408, 2008.

[294] Liang-Yu Wu, Mei-Ling Wu, and Lien-Wen Chen. The narrow pass band filter of tunable 1d phononic crystals with a dielectric elastomer layer. *Smart Materials and Structures*, 18(1):015011, 2009.

[295] Markus Beck, Reto Fiolka, and Andreas Stemmer. Variable phase retarder made of a dielectric elastomer actuator. *Optics Letters*, 34(6):803–805, 2009.

[296] M. Beck, M. Aschwanden, and A. Stemmer. Sub-100-nanometre resolution in total internal reflection fluorescence microscopy. *Journal of Microscopy*, 232(1):99–105, 2008.

[297] Artificial Muscle Incorporated. Vivitouch, www.vivitouch.com/.

[298] M. Kollosche, J. Zhu, Z. Suo, and G. Kofod. Complex interplay of nonlinear processes in dielectric elastomers. *Phys. Rev. E*, 85:051801, 2012.

[299] Xuanhe Zhao and Zhigang Suo. Theory of dielectric elastomers capable of giant deformation of actuation. *Physical Review Letters*, 104:178302, 2010.

[300] S. J. A. Koh, T. Li, J. Zhou, X. Zhao, W. Hong, J. Zhu, and Z. Suo. Mechanisms of Large Actuation Strain in Dielectric Elastomers. *J. Polym. Sci. Part B-Polym. Phys.*, 49(7):504–515, 2011.

[301] T. Lu, J. Huang, C. Jordi, G. Kovacs, R. Huang, D. R. Clarke, and Z. Suo. Dielectric elastomer actuators under equal-biaxial forces, uniaxial forces, and uniaxial constraint of stiff fibers. *Soft Matter*, 8(22):6167–6173, 2012.

[302] M. Kollosche and G. Kofod. Electrical failure in blends of chemically identical, soft thermoplastic elastomers with different elastic stiffness. *Appl. Phys. Lett.*, 96(7):071904, 2010.

[303] H. Stoyanov, P. Brochu, X. Niu, E. Della Gaspera, and Q. Pei. Dielectric elastomer transducers with enhanced force output and work density. *Appl. Phys. Lett.*, 100(26):262902, 2012.

[304] C Huang and QM Zhang. Enhanced dielectric and electromechanical responses in high dielectric constant all-polymer percolative composites. *Advanced Functional Materials*, 14(5):501–506, 2004.

[305] Hristiyan Stoyanov, Matthias Kollosche, Denis N. McCarthy, and Guggi Kofod. Molecular composites with enhanced energy density for electroactive polymers. *Journal of Materials Chemistry*, 20(35):7558–7564, 2010.

[306] Bai-Xiang Xu, Ralf Mueller, Markus Klassen, and Dietmar Gross. On electromechanical stability analysis of dielectric elastomer actuators. *Applied Physics Letters*, 97(16):162908, 2010.

[307] Paul Brochu and Qibing Pei. Advances in dielectric elastomers for actuators and artificial muscles. *Macromolecular Rapid Communications*, 31(1):10–36, 2010.

[308] Hristiyan Stoyanov, Denis Mc Carthy, Matthias Kollosche, and Guggi Kofod. Dielectric properties and electric breakdown strength of a subpercolative composite of carbon black in thermoplastic copolymer. *Applied Physics Letters*, 94(23):232905, 2009.

[309] Zhigang Suo and Jian Zhu. Dielectric elastomers of interpenetrating networks. *Applied Physics Letters*, 95(23):232909, 2009.

[310] Yingying Zhang, Chris J. Sheehan, Junyi Zhai, Guifu Zou, Hongmei Luo, Jie Xiong, Y. T. Zhu, and Q. X. Jia. Polymer-embedded carbon nanotube ribbons for stretchable conductors. *Advanced Materials*, 22(28):3027–3031, 2010.

[311] Zhigang Suo. Theory of dielectric elastomers. *Acta Mechanica Solida Sinica*, 23(6, 1):549–578, 2010.

[312] Soo Jin Adrian Koh, Tiefeng Li, Jinxiong Zhou, Xuanhe Zhao, Wei Hong, Jian Zhu, and Zhigang Suo. Mechanisms of Large Actuation Strain in Dielectric Elastomers. *Journal of Polymer Science Part B*, 49(7):504–515, 2011.

[313] Zhibin Yu, Xiaofan Niu, Zhitian Liu, and Qibing Pei. Intrinsically stretchable polymer light-emitting devices using carbon nanotube-polymer composite electrodes. *Advanced Materials*, 23(34):3989–+, 2011.

[314] Eugene Helfand and Yukiko Tagami. Theory of the interface between immiscible polymers. ii. *The Journal of Chemical Physics*, 56(7):3592–3601, 1972.

[315] Steven R Anton and Henry A Sodano. A review of power harvesting using piezoelectric materials (2003-2006). *Smart Materials and Structures*, 16(3):R1, 2007.

[316] H.A. Sodano, D.J. Inman, and G. Park. A review of power harvesting from vibration using piezoelectric materials. *The Shock and Vibration Digest*, 36:197–205, 2004.

[317] J.P. Lynch and K.J. Loh. A summary review of wireless sensors and sensor networks for structural health monitoring. *The Shock and Vibration Digest*, 38:91–128, 2006.

[318] Jonathan Granstrom, Joel Feenstra, Henry A Sodano, and Kevin Farinholt. Energy harvesting from a backpack instrumented with piezoelectric shoulder straps. *Smart Materials and Structures*, 16(5):1810, 2007.

[319] Joel Feenstra, Jon Granstrom, and Henry Sodano. Energy harvesting through a backpack employing a mechanically amplified piezoelectric stack. *Mechanical Systems and Signal Processing*, 22(3):721 – 734, 2008.

[320] Yoseph Bar-Cohen and Qiming Zhang. Electroactive polymer actuators and sensors. *MRS Bulletin*, 33(3):173–181, 2008.

[321] K. Ren, Y. Liu, H.F. Hofmann, and Q. Zhang. An investigation of energy harvesting using electrostrictive polymers. *MRS Proceedings*, 889:889–W01–05, 2006.

[322] Q. Zhang and H. Hofmann. Harvesting electric energy during walking with a backpack: Physiological, ergonomic, biomechanical, and electromechanical materials, devices, and system considerations. *Pentagon Report*, page A378824, 2005.

[323] Kailiang Ren, Yiming Liu, H. Hofmann, Q. M. Zhang, and John Blottman. An active energy harvesting scheme with an electroactive polymer. *Applied Physics Letters*, 91(13):132910, 2007.

[324] R.D. Kornbluh, R. Pelrine, H. Prahlad, A. Wong-Foy, B. McCoy, S. Kim, J. Eckerle, and T. Low. Dielectric elastomers: stretching the capabilities of energy harvesting. *MRS Bulletin*, 37:246, 2012.

[325] C. Graf and J. Maas. Energy harvesting cycles based on electro active polymers. *Proceedings of SPIE*, 7642:7642120, 2010.

[326] R. D. Kornbluh, R. Pelrine, H. Prahlad, A. Wong-Foy, B. McCoy, S. Kim, J. Eckerle, and T. Low. From boots to buoys: promises and challenges of dielectric elastomer energy harvesting. *Proceeding of SPIE*, 7976:797605, 2011.

[327] Thomas McKay, Benjamin O'Brien, Emilio Calius, and Iain Anderson. Self-priming dielectric elastomer generators. *Smart Materials and Structures*, 19(5):055025, 2010.

[328] Thomas McKay, Benjamin O'Brien, Emilio Calius, and Iain Anderson. An integrated, self-priming dielectric elastomer generator. *Applied Physics Letters*, 97(6):062911, 2010.

[329] Thomas G. McKay, Benjamin M. O'Brien, Emilio P. Calius, and Iain A. Anderson. Soft generators using dielectric elastomers. *Applied Physics Letters*, 98(14):142903, 2011.

[330] Benjamin M. O'Brien, Emilio P. Calius, Tokushu Inamura, Sheng Q. Xie, and Iain A. Anderson. Dielectric elastomer switches for smart artificial muscles. *Applied Physics A*, 100(2, SI):385–389, 2010.

[331] Ron Pelrine, Roy D. Kornbluh, Joseph Eckerle, Philip Jeuck, Seajin Oh, Qibing Pei, and Scott Stanford. Dielectric elastomers: generator mode fundamentals and applications. *Proceeding of SPIE*, 4329:148 – 156, 2001.

[332] Seiki Chiba, Mikio Waki, Roy Kornbluh, and Ron Pelrine. Current status and future prospects of power generators using dielectric elastomers. *Smart Materials and Structures*, 20(12):124006, 2011.

[333] R. Pelrine, R. Kornbluh, J. Eckerle, and Q. Pei. Electroactive polymer thermal electric generators, 2003.

[334] C. Jean-Mistral, S. Basrour, and J.J. Chaillout. Dielectric polymer: scavenging energy from human motion. *Proceedings of SPIE*, 6927:692716, 2008.

[335] S. Chiba, M. Waki, R. Kornbluh, and R. Pelrine. Innovative power generators for energy harvesting using electroactive polymer artificial muscles. *Proceedings of SPIE*, 6927:692715, 2008.

[336] R. Kornbluh, R. Pelrine, H. Prahlad, S. Chiba, J. Eckerle, B. Chavez, S. Stanford, and T. Low. Wave powered generation using electroactive polymers, 2007.

[337] P. Jean, A. Wattez, G. Ardoise, C. Melis, R. Van Kessel, A. Fourmon, E. Barrabino, J. Heemskerk, and J.P. Queau. Standing wave tube electro active polymer wave energy converter. *Proceedings of SPIE*, 8340:83400C, 2012.

[338] Y.H. Iskandarani, R.W. Jones, and E. Villumsen. Modeling and experimental verification of a eielectric polymer energy scavenging cycle. *Proceedings of SPIE*, 7287:72871Y, 2009.

[339] Soo Jin Adrian Koh, Xuanhe Zhao, and Zhigang Suo. Maximal energy that can be converted by a dielectric elastomer generator. *Applied Physics Letters*, 94(26):262902, 2009.

[340] Yanju Liu, Liwu Liu, Zhen Zhang, Yang Jiao, Shouhua Sun, and Jinsong Leng. Analysis and manufacture of an energy harvester based on a Mooney-Rivlin-type dielectric elastomer. *EPL*, 90(3):36004, 2010.

[341] Gyungsoo Kang, Kyung-Soo Kim, and Soohyun Kim. Analysis of the efficiency of a dielectric elastomer generator for energy harvesting. *Review of Scientific Instruments*, 82(4):046101, 2011.

[342] Stephanie P. Lacour, Donald Chan, Sigurd Wagner, Teng Li, and Zhigang Suo. Mechanisms of reversible stretchability of thin metal films on elastomeric substrates. *Applied Physics Letters*, 88(20):204103, 2006.

[343] C. Jordi, A. Schmidt, G. Kovacs, S. Michel, and P. Ermanni. Performance evaluation of cutting-edge dielectric elastomers for large-scale actuator applications. *Smart Materials and Structures*, 20(7):075003, 2011.

[344] Sungryul Yun, Xiaofan Niu, Zhibin Yu, Weili Hu, Paul Brochu, and Qibing Pei. Compliant silver nanowire-polymer composite electrodes for bistable large strain actuation. *Advanced Materials*, 24:1321–1327, 2012.

[345] Tsuyoshi Sekitani, Yoshiaki Noguchi, Kenji Hata, Takanori Fukushima, Takuzo Aida, and Takao Someya. A rubberlike stretchable active matrix using elastic conductors. *Science*, 321(5895):1468–1472, 2008.

[346] Samuel Rosset, Muhamed Niklaus, Philippe Dubois, and Herbert R. Shea. Large-stroke dielectric elastomer actuators with ion-implanted electrodes. *Journal of Microelectromechanical Systems*, 18(6):1300–1308, 2009.

[347] Darren J. Lipomi and Zhenan Bao. Stretchable, elastic materials and devices for solar energy conversion. *Energy and Environmental Science*, 4(9):3314–3328, 2011.

[348] Raziel Riemer and Amir Shapiro. Biomechanical energy harvesting from human motion: theory, state of the art, design guidelines, and future directions. *Journal of NeuroEngineering and Rehabilitation*, 8(1):22, 2011.

[349] European Thematic Network on Wave Energy. Results from the work of the european thematic network on wave energy, erk5-ct-1999-20001, 2000-2003. available at www.wave-energy.net., 2003.

[350] T.W. Thorpe. A brief review of wave energy, etsu report r-122. Technical report, United Kingdom Department of Trade and Industry, 1999.

[351] R. Bedard, G. Hagerman, M. Previsic, O. Siddiqui, R. Thresher, and B. Ram. Final summary report, project definition study, offshore wave power feasibility demonstration project, epri global wp 009 us rev. 2. Technical report, EPRI, 2005.

[352] G. Hagerman and R. Bedard. E2i epri specification, guidelines for preliminary estimation of power production by offshore wave energy conversion devices, epri global wp 001 us rev. 1. Technical report, EPRI, 2003.

[353] Energetech. Press release: Enegetech wave energy success, oct. 2005. http://www.zulenet.com/electriceco/energetech.html, 2005.

[354] Japan Marine Science and Technology Center (JAMSTEC). Offshore floating wave energy device mighty whale. http://www.jamstec.go.jp/jamstec-e/tech/now6.html, 2006.

[355] International Energy Agency (IEA). The iea ocean energy systems newsletter issue 2, september 22, 2003. http://www.iea-oceans.org/publications.asp?id=2, 2003.

[356] Pelamis. http://www.pelamiswave.com/.

[357] Ocean Power Technologies (OPT). http://www.oceanpowertechnologies.com/.

[358] A. Weinstein, G. Fredrikson, M.J. Parks, and K. Nielsen. Aquabuoy - the offshore wave energy converter numerical modeling and optimization. In *OCEANS '04. MTTS/IEEE TECHNO-OCEAN '04*, volume 4, pages 1854 –1859 Vol.4, nov. 2004.

[359] M.K. Small and W.D. Nix. Analysis of the accuracy of the bulge test in determining the mechanical properties of thin films. *Journal of Materials Research*, 7:1553–1563, 1992.

[360] SoundPower. http://www.soundpower.co.jp/products/products1.html.

[361] PaveGen. http://www.pavegen.com/.

[362] PowerLeap. http://powerleap.net/.